The University of Nottingham

UNITED KINGDOM · CHINA · MALAYSIA

Department of Chemical and Environmental Engineering

INVESTIGATION ON SYNTHESIS AND PROCESS CONTROL OF MICROPOROUS PARTICLE MATERIAL

By

XIANI HUANG

Thesis submitted to the University of Nottingham for the degree of

Doctor of Philosophy

March 2019

Dedication

To my husband, Dr. Hangfu YANG, my parents and my parents-in-law, they give me love, support and encouragement. To my lovely two sons, Zijing YANG and Jingqiu YANG, they motivate me to finish my PhD study.

Acknowledgements

I would like to express my gratitude to my supervisor, Professor Xiaogang Yang, for his consistent help, encouragement and patient guidance during my whole PhD study. Prof. Yang has encouraged me to use the mathematical modelling in conjunction with the experimental approaches to solve the problem of synthesis of various particle materials, especially lithium battery positive electrode precursor materials, and he has repeatedly emphasised the importance of interdisciplinary interactive study in the field of material science, chemical reactive engineering and fluid dynamics. These important ideas have greatly expanded my version and deepen my understanding to the knowledge of materials manufacturing.

I would like to thank all the members of the FAST group, Dr Guang Li, Dr Jie Yang, Dr Yiyi Wu, Dr Luming Chen, Dr Collins Ezeh, Dr Bin Dong, Dr Weibin Shi, Mr Chenyang Xue, Ms Lu Liu, Mr. Bin Li, Ms Xinyue Cai, Ms Yanqing Guo, Ms Shanshan Long, and Ms Lulu Wang for their assistance and pleasurable discussions in many cases.

I also want to express my gratitude to all the laboratory technician in Faculty of Science and Engineering at the UNNC, in particular Mrs Carey Tao, Mrs Helen Xu, Mrs Jane Zhang, Mr John Zhu and Mr Julian Zhu, Mr Jason Wang, and Ms Kate Yuan who have provided me the technical support in conducting my experiments.

Finally, I especially would like to thank my husband, Dr Hangfu Yang, for his understanding and full support through the duration of this project.

My sincere thanks are also gone to the financial supports through the PhD scholarship of the International Doctoral Innovation Centre (IDIC) of the University of Nottingham Ningbo China, National Natural Science Foundation of China (NSFC) (Grant No. 21576141) and Zhejiang Provincial Natural Science Foundation (Grant No. LY15B060001).

Abstract

With the increasing demands for portable electronic devices and the use of electrical vehicles (EVs) for green transport, the application of high energy density Lithium-ion batteries (LIBs) has been widely recognised. As an important part of Lithium-ion battery, $LiNi_xCo_yMn_{1-x-y}O_2$ (NCM) cathode material, especially high nickel NCM material, has attracted much attention due to high capacity, low cost, good cycling stability and safety. Today, the preparation process of $LiNi_xCo_yMn_{1-x-y}O_2$ is commercial and mature. The synthesis conditions of high nickel material are harsh and its surface activity is high, plus, its long synthesis time, which restricts its popularization and application. Hence, developing a simple and cost-effective method instead of the traditional preparation way is urgently needed.

In this work, a Lobed Taylor-Couette reactor (LTC) has been applied to synthesize the NiCoMn hydroxide, a precursor of $LiNi_xCo_yMn_{1-x-y}O_2$cathodic material used in batteries. A steady state is attained when the reaction time is about 3~4 times of the mean residence time. The effect of shear rate on the agglomerate shape and sizes of the hydroxides was studied. It was found that the particle size decreases with increasing from low shear rate to high shear rate while the morphology of particles changes from irregular to spherical-like in shapes. The molar ratio of NH_3/MSO_4 (0.4~1) would be desirable for getting spherical precursors. A relation correlating turbulent energy dissipation rate and the molar ratio of NH_3/MSO_4 is proposed for estimation of the particle sizes.

Following the study on synthesis of the NiCoMn hydroxide, the electrochemical performances of synthesised$LiNi_{0.6}Co_{0.2}Mn_{0.2}O_2$ cathode materials were evaluated. Calcination of $(Ni_{0.6}Co_{0.2}Mn_{0.2})(OH)_2$ with LiOH at a proper temperature leads to a high tap-density of materials. The effect of various parameters such as stirring speed and molar ratio of NH_3/MSO_4 on the electrochemical performances of $LiNi_{0.6}Co_{0.2}Mn_{0.2}O_2$was investigated. It has been revealed from the present study that our developed material has been demonstrated to have good electrochemical stability.

Based on the preceding studies, numerical simulation to predict the electrochemical performance of $LiNi_{0.6}Co_{0.2}Mn_{0.2}O_2$ during the discharge process was performed. In the simulations, an electrochemical Pseudo 2D model with modifications was adopted, taking the electrochemical reactions into consideration. The effects of calendaring and particle sizes on the physical and electrochemical property of $LiNi_{0.6}Co_{0.2}Mn_{0.2}O_2$ cathode were investigated using this model. The simulation results indicate that the estimated porosity by fitting the experimental data, which was used in the model, shows consistency for numerical simulation of electrochemical properties of the LIBs. Meanwhile, the simulation results have illustrated that decreasing the particle size of active materials can be beneficial to the enhancement of diffusion of the solid phase, characterized by an increase in the diffusion coefficient (Ds).

The material doping was also explored, aiming to improve the electrochemical performance of $LiNi_{0.6}Co_{0.2}Mn_{0.2}O_2$ cathode material. The effects of the Mg doping for Ni on the structure and the electrochemical properties of

$Li(Ni_{0.6}Co_{0.2}Mn_{0.2})O_2$ samples are assessed. The use of the Rietveld refinement has shown that addition of a small amount of Mg will be beneficial to the lowering of the bonding distance of Li-O and M-O and increasing the structural stability of the material, thus to the improvement of the electrochemical performances of $Li(Ni_{0.6}Co_{0.2}Mn_{0.2})O_2$.

Table of Contents

List of Figures

List of Tables

List of Abbreviations and Symbols

Symbols

A	Surface area of the electrode [cm^2]
A_1	Cross-sectional area of the inner cylinder [mm^2]
a	Cell parameter of the crystal [Å]
C	Particle strength coefficient
c	Cell parameter of the crystal [Å]
c'	Original solution concentration, mol L^{-1}
c^*	Equilibrium saturation concentration, mol L^{-1}
c_l	Concentration of lithium ions in the electrolyte phase [mol m^{-3}]
c_s	Concentration of lithium in the active material particles of the electrode [mol m^{-3}]
$c_{s,max}$	Maximum lithium concentration in the solid phase [mol m^{-3}]
$c_{s,surf}$	Lithium-ion concentration at the particle surface [mol m^{-3}]
D_l	Li-ion diffusion coefficient in the electrolyte phase [$m^2 s^{-1}$]
D_s	Li-ion diffusion coefficient of NMC [$m^2 s^{-1}$]
D_g	Grain size of the crystal [nm]
D	Diffusion coefficient of $NiCl_2$ solution [m^2 s^{-1}]
d	Equivalent gap width [mm]
$dmax$	Agglomerate particle size [µm]
$f_\pm$	Average molar activity coefficient
F	Faraday constant, 96485 [C mol^{-1}]
G	Shear rate [s^{-1}]
i_s	Electrical current density in the solid phase [Ah]
i_l	Electrical current density in the solid phase [Ah]
I_{app}	Applied current of 1D computational domain [Ah]
K	Constant of Debye-Scherrer's formula
K_{agg}	Aggregation rates [$m^3 s^{-1}$]

K_{break}	Breakage rates [m^3s^{-1}]
L	Thickness of electrode coating [μm]
L_{LTC}	Length of reactor [mm]
m	Order of Reaction
m_s	Weight of the active material [mg]
n	Molar ratio of NH_3/MSO_4
P	Power input (W)
P_i	Precursor prepared at different conditions
P_1	Perimeter of the inner cylinder [mm]
r	Radial coordinate inside a spherical particle [μm]
r	Chemical reaction rate
R	Universal gas constant, 8.314 [J $mol^{-2}K^{-1}$]
R	Reynolds number ratio
R_1	Radius of sectors[mm]
R_2	Radius of the outer cylinder[mm]
R_{eq}	Equivalent radius of the inner cylinder [mm]
Re	Reynolds number, dimensionless
Re_c	Critical Reynolds number, dimensionless
S_a	Volume-specific surface area [m^{-1}]
t_+	Transferring number of lithium ions
T	Absolute temperature [K]
V	Total volume of the electrode [μm^3]
V_l	Volume of electrolyte [μm^3]
V_s	Volume of active material [μm^3]
S	Relative Supersaturation (c'/c^*), dimensionless
s	Stable particle size exponent
Sc	Schmidt number, dimensionless
t_m	Characteristic time for micromixing [ms]
V_{LTC}	Volume of reactor [ml]

Greek Letters

η	Reactor radius ratio [R_{eq}/R_2]
ω	Angular velocities [rad s^{-1}]
f	Friction factor
μ	Dynamic viscosity of the fluid [Pa·S]
ν	Kinematic viscosity of the fluid
λ	Kolmogorov length [μm]
λ'	Wavelength of the X-ray radiation [Å]
β	Full width half maximum
σ	Absolute Supersaturation, dimensionless
ε	Energy dissipation rate [m^2 s^{-3}]
ε_l	Porosity of electrolyte
ε_l	Volume fraction of electrolyte relative to the volume of the bulk electrode
ε_s	Volume fraction of the solid phase relative to the volume of the bulk electrode
β	Bruggeman porosity exponent
α_a	Anodic charge transfer coefficients
α_c	Cathodic charge transfer coefficients
η	Local surface potential [V]
σ_s	Electrical conductivity [S m^{-1}]
φ_s	Potential in the solid phase [V]
φ_l	Potential in the electrolyte phase (V)
ρ_L	Suspension density [g cm^{-3}]
ρ_s	Density of the active material [g cm^{-3}]
k_0	Reaction rate constant [$m^{2.5}mol^{-0.5}s^{-1}$]
κ_l	Ionic conductivity of the electrolyte [S m^{-1}]

Abbreviations

LCO	Lithium cobalt oxide
LCP	Lithium cobalt phosphate
LFP	Lithium iron phosphate

LFSF	Lithium iron fluoro-sulphate
LMO	Lithium manganese oxide
LTC	Lobed Taylor-Couette reactor
LTS	Lithium titanium sulphide
NCA	Nickel cobalt aluminium oxide
NCM	Nickel cobalt manganese oxide
NCM333	$LiNi_{1/3}Co_{1/3}Mn_{1/3}O_2$
NCM523	$LiNi_{0.5}Co_{0.2}Mn_{0.3}O_2$
NCM622	$LiNi_{0.6}Co_{0.2}Mn_{0.2}O_2$
PSD	Particle size distribution
DMC	Dimethyl carbonate
EC	Ethylene carbonate
LIBs	Lithium-ion batteries
NMP	N-methyl pyrrolidinone
HEVs	Hybrid electric vehicles
P2D	Pseudo-two-dimensional
OCP	Open circuit potential

Chapter 1

Introduction

1.1 Background

1.1.1 Overview

Crystallisation is of great importance in the chemical industry for separation, purification and powder synthesis. During industrial crystallisation, precipitation is a common method to prepare powder materials. Generally, it involves primary and secondary particle formation processes, nucleation and crystal growth and particle agglomeration/breakage, respectively. All such processes have a determining effect on the final product quality, product shape and particle size distribution (PSD). Primary nucleation is promoted by agitation; the agitation process facilitates the formation of secondary nucleation. The particle aggregation is strongly influenced by the physic-chemical properties of the reaction and the hydrodynamic conditions imposed during the process. These conditions induced by shear rate are considered key parameters for most crystallisation processes, depending on the type and geometry of the mixing tank (Sung *et al*., 2000, Richter *et al*., 2008), stirring shape and speed (Torbacke and Rasmuson 2001). Additionally, the mass transfer process is controlled by the hydrodynamic conditions of the suspension.

Mixing on a molecular scale (micro-mixing) plays an important role in several precipitation chemical reactions. Micro-mixing refers to the viscous-convective defamation process along with the molecular diffusion process (Duan *et al*., 2016). It increases the selectivity of competitive reactions, where the reaction rate of interest is limited by diffusion. Generally, diffusion is the final step that generates molecular homogeneity. A poor micro-mixing process will bring about a series of by-products, increasing the cost of higher purification and process economy.

The micro-mixing process was directly affected by the hydrodynamic atmosphere. During the agglomeration process, hydrodynamics in the conventional stirred tank reactor (CSTR), characterised by the occurrence of turbulence, was chaotic, accompanied by fast kinetic precipitation. Generally, this makes it difficult to keep the size of synthesised precursors with a narrow distribution when applying the traditional bulk mode in the mixing. Consequently, the agglomerate size, size distribution and morphology of the synthesised particles are difficult to predict.

The Taylor-Couette reactor has typical flow features such as narrow shear rate distribution, absence of high shear regions compared to the CSTR reactor, limited flow patterns and easily adjusted mean residential time. It has been used in many engineering areas such as precipitation, filtration, catalytic reactions and bioreactor applications.

1.1.2 Lithium Battery Materials

Introduced by Sony in the 1990’s, the lithium-ion batteries (LIBs) technology has developed for over 20 years. As shown in Figure 1–1, LIBs deliver higher specific energy and power as compared to batteries like nickel (Ni)-metal hydride, Ni-cadmium (Cd) and lead (Pb)–acid owing to low molecular weight and a smaller radius. Thus, it shows potential application prospect in the portable electronics market and in power tools equipment (Dunn et al., 2011). Moreover, it is regarded as a better choice as the next generation energy tools like in hybrid electric vehicles (HEVs) and plug-in hybrids (PHEVs) (Armand and Tarascon, 2008). Long-term stability, high-energy density and safety are the common goals to be considered for the development of LIBs.

To achieve a better electrode, research advances in the LIBs' field occurred through controlling the particle size and adjusting the composition, structure and morphology (Aricò *et al*., 2005). Additionally, reaction mechanisms and materials systems are being considered as important parts for future development. Materials focused on Li nickel-rich oxide made via eco-efficient processes are receiving increased attention (Tarascon, 2010).

1.2 Research Aims and Objectives

1.2.1 Research Aims

The present work is aimed at the synthesis of nickel-rich precursor for the lithium cathode material with a lobed Taylor-Couette reactor (LTC). By controlling the shear rate of LTC and chemical conditions, various particle sizes of $(Ni_{0.6}Co_{0.2}Mn_{0.2})(OH)_2$ hydroxide can be obtained. Thereafter, the electrochemical performances of $LiNi_{0.6}Co_{0.2}Mn_{0.2}O_2$ based on the above hydroxide are to be evaluated, followed by a pseudo-two-dimensional (P2D) model to simulate the discharge process of the $LiNi_{0.6}Co_{0.2}Mn_{0.2}O_2$ cathode material. Considering the shortcomings of the material, this work focuses on metal doping on $LiNi_{0.6}Co_{0.2}Mn_{0.2}O_2$ to improve its electrochemical performance.

1.2.2 Research Objectives

The research objectives of this dissertation are organised as follows:

Chapter 2 provides a summary of the primary and secondary processes involved in the crystallisation process, mixing process, the general application of chemical reactors and recent development in the field of the lithium cathode material.

Chapter 3 portrays a study of the effects of different operating parameters such as the shear rate, molar ratio of NH_3/MSO_4, pH on the size, particle size distribution (PSD) and morphologies of investigated particles. Furthermore, a correlation on predicting the particle size between the turbulent energy dissipation rate and molar ratio of NH_3/MSO_4 is proposed.

Chapter 4 is a study of physical and electrochemical properties for the spherical $LiNi_{0.6}Co_{0.2}Mn_{0.2}O_2$ cathode material. This was synthesised by a mixture of the calcined precursor with LiOH at high-temperature calcination. Particularly, the effect of stirring speed, calcination temperature, and the molar ratio of NH_3/MSO_4 on its electrochemical performances was evaluated in depth.

Chapter 5 studies the calendaring effects on the physical and electrochemical properties of the $LiNi_{0.6}Co_{0.2}Mn_{0.2}O_2$ cathode material. A P2D model was built to simulate the electrochemical reactions during the discharge process.

Chapter 6 studies $LiNi_{0.6-x}Co_{0.2}Mn_{0.2}Mg_xO_2$ (x=0, 0.02, 0.04 and 0.06) samples prepared in a Lobed Taylor-Couette reactor by co-precipitation and high-temperature solid state method. The effects of the Mg doping for Ni on the structure and the electrochemical properties of samples are characterized by XRD, SEM and electrochemical measurements.

Chapter 7 outlines the summarised results with suggestions for future work.

References

ARICÒ, A. S., BRUCE, P., SCROSATI, B., TARASCON, J.-M. & SCHALKWIJK, W. V. 2005. Nanostructured materials for advanced energy conversion and storage devices. Nature Materials, 4, 366-377.

ARMAND, M. & TARASCON, J.-M. 2008. Building better batteries. Nature, 451, 652-657.

DUAN, X., FENG, X., YANG, C. & MAO, Z.-S. 2016. Numerical simulation of micro-mixing in stirred reactors using the engulfment model coupled with CFD. Chemical Engineering Science, 140, 179-188.

DUNN, B., KAMATH, H. & TARASCON, J.-M. 2011. Electrical energy storage for the grid: a battery of choices. Science, 334, 928-935.

PACHAURI, R. K. & REISINGER, A., EDS. Climate Change 2007: Synthesis Report. Core Writing Team, IPCC, Geneva, Switzerland.

RICHTER, O., HOFFMANN, H. & KRAUSHAAR-CZARNETZKI, B. 2008. Effect of the rotor shape on the mixing characteristics of a continuous flow Taylor-vortex reactor. Chemical Engineering Science, 63, 3504-3513.

SUNG, M.-H., CHOI, I.-S., KIM, J.-S. & KIM, W.-S. 2000. Agglomeration of yttrium oxalate particles produced by reaction precipitation in semi-batch reactor. Chemical Engineering Science, 55, 2173-2184.

TARASCON, J. M. 2010. Key challenges in future Li-battery research. Philosophical Transactions of the Royal Society A, 368, 3227-3241.

TORBACKE, M. & RASMUSON, Å. C. 2001. Influence of different scales of mixing in reaction crystallization. Chemical Engineering Science, 56, 2459-2473.

Figures

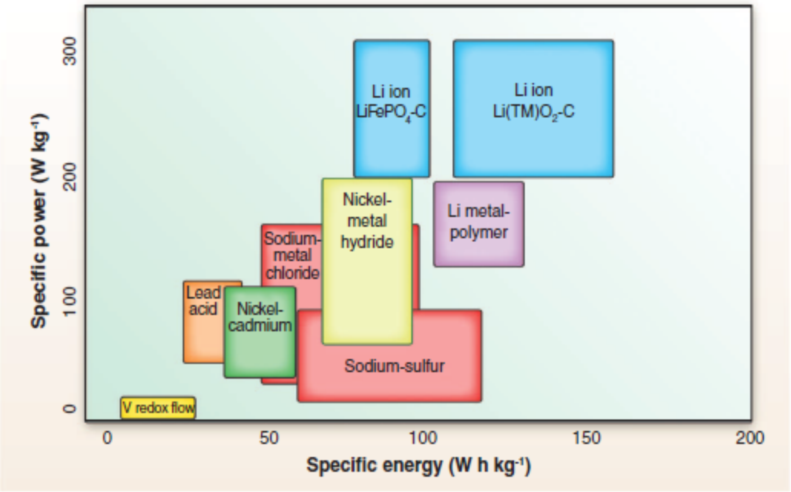

Figure 1-1. Gravimetric power and energy densities for different rechargeable batteries (Dunn *et al*., 2011) © 2011, American Association for the Advancement of Science

Chapter 2

Current Status of Synthesis and Process Control of Microporous Particle Material

2.1 Crystallisation Kinetics

2.1.1 Nucleation

Crystal nuclei is a tiny crystal particle formed by molecules, atoms and ions in a supersaturated solution, an essential in the crystallisation process. Nucleation is where nuclei (seeds) act as templates for crystal growth. The nucleation rate is that at which a number of particles are formed in solution in a stipulated time. The primary kinetic factor determines the particle size distribution of the crystal. There are two – primary and secondary nucleation – for particle formation during the industrial crystallisation. Primary refers to the formation of the first nucleus; secondary nuclei are crystal nuclei produced from a pre-existing crystal (Botsaris, 1976). Primary nucleation is the case without the presence of other crystalline matter. Homogeneous nucleation occurs when nuclei form uniformly throughout the parent phase and is a spontaneous process. Heterogeneous nucleation forms at structural levels inhomogeneities (container surfaces, impurities, grain boundaries and/or dislocations).

The produced nuclei are gathered in the vicinity of crystals present in a supersaturated system, referred to as the secondary nucleation process. Thus, we may consider a simple scheme as follows (shown in Figure 2-1).

The free energy change (ΔG) associated with the formation of a nucleus, developed by Volmer and Weber (Volmer and Weber, 1925), can be written as below:

$$\Delta G = \Delta G_s + \Delta G_v \qquad (2\text{–}1)$$

Where ΔG_s is the surface excess free energy of the interface separating the parent and the product phases and ΔG_v is the volume excess free energy change per unit volume, expressed as a negative quantity.

For a spherical nucleus:

$$\Delta G = 4\pi r^2 \sigma - \frac{4}{3}\pi r^3 \Delta G_v \qquad (2\text{–}2)$$

Where σ is interfacial energy. The Eq. 2–2 is plotted as Figure 2–2.

The net free energy change increases with the increase in size and decreases for further increase in the size of the nucleus. The size of the critical nucleus is obtained when the free energy change is maximum. Thus, we set $\frac{d}{dr}\Delta G = 0$; radius (r*) of critical nucleus $\mathrm{r}^* = \frac{2\delta}{G_v}$. Using the Gibbs-Thomson relation, the rate of nucleation (J) is expressed as follows:

$$\mathrm{J} = \mathrm{J}_0 \exp\left[\frac{-16\pi\sigma^3\Omega^2}{3\mathrm{k}^3\mathrm{T}^3(\ln \mathrm{S})^2}\right] \qquad (2\text{–}3)$$

Where J_0 is the pre-exponential factor. Eq. 2–3 indicates the rate of nucleation is determined by temperature T, the degree of supersaturation S and interfacial energy σ.

2.1.2 Crystal Growth

In the process of precipitation, crystal growth refers to the deposition of solute ions or molecules on the crystal surface – it is one of the main processes that increase crystal size. In a supersaturated solution, once a stable crystal nucleus is formed, the crystal growth process begins. Till date, several types of research have focused on the mechanism, their study including two-dimensional nucleation growth, spiral dislocation growth and diffusion control growth. Based on these growth models, a series of crystal growth kinetic models have been established. We have list three typical mechanisms of crystal growth below.

Surface energy theory: In 1878, Gibbs argued that the growth of crystal should satisfy a basic principle: the total free energy of crystal at a constant temperature and pressure in equilibrium should be at a minimum data for a given volume. However, for the case of the liquid droplet, the atoms or molecules were randomly dispersed, whereas, for a solid, the atoms or molecules were dispersed regularly in a lattice structure. Thus, this theory has its own limitations (Gibbs, 1948). In 1901, Wulff developed Gibbs's theory, suggesting that the final shape of the crystal at an equilibrium state is related to the free energy of each face. He suggested that the growth rate of the crystal was proportional to specific surface energies of the faces. That implies that a high index faces grow faster than one of a low index. In practice, the crystal always has difficulty in maintaining its geometrical similarity. The biggest disadvantage of this theory is that it cannot explain the supersaturation and solution movement of crystal growth rate (Wulff, 1901).

Adsorption layer theory: Volmer first proposed an adsorption layer of solute atoms or molecules existing on the surface of the crystal. It was believed that the concentration of the solution in the adsorption layer was different from the concentration of the solute in the liquid phase. When the units of the crystalline substance reached the surface of the crystal, it did not immediately enter the crystal lattice and only lost one degree of freedom to diffuse on the crystal's surface. The adsorption layer of crystal growth unit was thus not tightly packed at the interface. Moreover, a dynamic balance was established between the layer and the bulk solution. The thickness of the adsorption layer did not exceed 10 μm – at times, only 1 nm. The concentration of the bulk solution in the adsorption layer play an important role in the process of secondary nucleation and crystal growth (Volmer, 1939).

Diffusion-reaction theory: This is proposed based on the following assumptions: (a) There is a concentration gradient in the vicinity of a growing surface; (b) The growth is a reverse process of dissolution. The crystal growth is divided into two steps: (1) Solute-diffusion process. The substance to be crystallised is transferred from the bulk of the fluid phase to the solid phase by diffusion through a stationary liquid layer. (2) Surface-reaction process. The solute reaches the surface of the crystal and grows on its lattice plane. It releases heat during the crystallisation process. And the released crystallisation heat is transferred back to the solution. Concentration differences are the driving force of these two stages (Whitjey, 1897).

2.1.3 Aggregation/breakup

In agitated suspension, secondary processes, such as agglomeration/aggregation and breakup/re-disperse, can have a vital effect on the final crystal form, shape and particle size distribution (PSD). Agglomeration takes place when the motion of two or more solutions allow them to aggregate sufficiently, with enough time to let them facilitate growth and intergrowth of an agglomerative bond (Figure 2–3).

This is a common phenomenon during the reaction precipitation. After aggregation, a solution is formed between the crystals, which determines the forces combining the crystallites together. This solution is quite different from the bulk solution, where it has molecular thin layers (Michael Brunsteiner *et al.*, 2005). Conversely, breakup refers to the breakage process of aggregates and agglomerates. Agitation is an important factor in agglomeration that determines the collision of particles and crystals (Masy and Cournil, 1991). The agglomeration behaviour was observed in the reaction of yttrium oxalate, benzoic acid and europium oxalate (Sung *et al.*, 2000, Åslund and Rasmuson, 1992, Kim *et al.*, 2004). Since the turbulent agitation enhances the particle collision frequency, the particle agglomeration was promoted at a low agitation speed, while the agglomerate size was decreased for an agitation speed beyond a certain value.

2.2 Mixing

Reaction crystallisation is commonly used in the field of inorganic compounds such as carbonate and barium sulphate (Jung *et al*., 2003, Cafiero *et al*., 2002). The rate of chemical reaction is quite fast; the reactant concentrations of the product changes are from moderate to low content. Hence, the supersaturation at the feed point is quite high and significantly dependent on the mixing conditions. Thus, when the rate of nucleation and crystal growth are high, the final PSD will be influenced by the mixing conditions during the process.

There are three different scales of mixing processes: macromixing, mesomixing, and micromixing, for each chemical process. Macromixing refers to the composition homogeneity at the macroscopic scale of the complete mixing vessel. It usually implies the initial phase when the two liquids contact. It is realised through the macroscopic convective turbulent transport of different materials and shear, chaotic flow and vortex motion. Macromixing refers to the distribution process of one fluid with an average composition, uniform without changing the local concentration and reducing the size of regions of uniform composition. Mesomixing appears after macromixing. It is not commonly used and lumped into macromixing. Meso-mixing involves the disintegration of liquid elements from an initial, macroscopic scale towards the Kolmogorov scale (Villermaux and Falk, 1994; Bourne, 2003; Wenzel and Górak, 2018). Finally, micromixing describes the mixing of two liquids in a molecular level process. It provides an ideal environment for chemical reactions, providing a close operation condition. Baldyga*et al*. developed an

Engulfment deformation diffusion (EDD) model to analyse the micro-mixing process. The EDD model is proposed on the basis of turbulence theory. They believed that the micro-mixing process consists of three typical processes: engulfment, deformation and diffusion (Figure 2-4). The fluid elements are in the form of lamellar structure. Due to the motion of vortices, the striation of fluid elements is formed by engulfment. At the scales smaller than the Kolmogorov scale, the small fluid elements are deformed, such that the unsteady molecular diffusion can take place within the deforming slabs or laminated structures, embedded within the energy dissipating vortices. The diffusion itself is a slow process; it could be enhanced within the turbulent mixing process. For some fast reactions, the characteristic reaction time is necessary to achieve molecular diffusion on the order of milliseconds. Thus, the diffusion process could be accelerated by viscous-convective deformation and the shrinkage of fluid elements. The researchers believed that the effects of deformation and molecular diffusion were negligible when the Schmidt number was lower than 4000. Furthermore, they simplified the EDD model to the E model, including rate-controlling engulfment (Baldyga and Bourne, 1984, Baldyga and Bourne, 1989a; Baldyga and Bourne, 1989b; Bakldyga *et al*., 1995).

Many chemical reactions are fast relative to mixing so that conversion occurs before the reagent homogenisation is achieved. In such cases, concentration gradients until molecular scale considerably affect the final product properties and the way of contacting reagents appears to be a crucial parameter. Thus, particular attention should be paid to the choice of the mixing device to control the micro-mixing process.

2.3 Taylor-Couette (TC) Reactor

Taylor-Couette flow has been studied extensively since 1923 due to its nonlinear dynamics. Figure 2–5 shows the typical schematic diagram of the TC reactor. It is a unique hydrodynamic fluid device created by gaps between two co-axially positioned cylinders along the cylindrical axis. The outer cylinder of the TC reactor is fixed; the inner cylinder is rotated. The flow regimes undergo a series of changes as the rotational speed of the inner cylinder increases. Beyond a critical Reynolds number, pure azimuthal Couette flow is transformed into the Taylor vortex flow (TVF), wavy vortex flow (WVF), MWVF and total turbulence (Nemri *et al.*, 2013; Nemri *et al.*, 2016). The critical condition is given by the Reynolds number (Re) based on width *e*, the angular velocity of the inner cylinder ω, the inner diameter R_i and the kinematic fluid viscosity ν. It could be defined as follows:

$$R_e = \frac{\omega e R_i}{\nu} \tag{2-4}$$

Transport properties of the Taylor-Couette flow have been determined and modelled by experimental and numerical studies. Kataoka et al. were the first to propose a single parameter model for the TVF regime (Kataoka *et al.*, 1975). Using the residence time distribution (RTD) measurements, they found plug flow considered as a well-mixed batch vessel and no transfer with adjacent vortices. Later, their studies showed that axial dispersion became independent of the molecular diffusion coefficient and increased with the axial flow-rate (Kataoka *et al*., 1977, Kataoka *et al*., 1975). The model of continuous stirred tank reactor (CSTR) and one-parameter model were established to determine the correlations between axial dispersion coefficient Dx and Reynolds number (Re) in terms of axial Reynold number (Re_{ax}) and the tangential one (Kataoka and Takigawa, 1981, Enokida *et al*., 1989). A direct numerical simulation (DNS) (shown in Figure 2-6) was carried out by Nemri *et al*. to study the mixing and axial dispersion in Taylor-Couette flow patterns (Nemri *et al*., 2013, Nemri *et al*., 2016). The DNS results show that the deformation of the vortex is induced by the azimuthal wave. The wavy perturbation breaks the stream surface between neighbouring vortices, thus enabling fluid bundles to cross the boundary. The combination of intra-vortex and inter-vortex mixing is enhanced by axial dispersion.

Comparing with traditional stirred tank reactors, a big advantage of the TC reactor is its absence of high shear regions. The TC reactor has been used for several decades. Currently, it is used in areas of ultrafiltration, slurry filtration, polymerisation of styrene and vinyl acetate (Holeschovsky and Cooney, 1991; Choi *et al*., 1999; Kataoka *et al*., 1995). Additionally, a Taylor vortex is used for chemical and biological reactions. Sczechowski *et al*., Sengupta *et al*., Dutta and Ray developed a Taylor vortex reactor for heterogeneous photocatalysis for water purification; they showed an outstanding photo-efficiency in the reactor (Sczechowski, 1995; Sengupta *et al*., 2001; Dutta and

Ray, 2004). Zougari found that the gas-liquid interfacial area and organic solid deposition could be enhanced in the use of the Taylor vortex reactor (Zougari *et al*., 2006). Nguyen *et al*. compared the mass transfer coefficient in different reactors. As shown in Figure 2–7, the mass transfer coefficients in the Taylor vortex crystalliser was 4–5 times higher than those with a turbulent eddy (Nguyen *et al*., 2011). Jung *et al*. studied its utilisation in crystallisation. Their results demonstrated that the Taylor reactor is beneficial to crystallisation processes of nucleation, growth, phase transformation and agglomeration/breakage. In the gas-liquid reaction crystallisation of calcium carbonate, they found that the high shear rate induced by the TC reactor could enhance the mass transfer rate of CO_2-$Ca(OH)_2$ reaction, increasing the rotational speed of the inner cylinder (Jung *et al*., 2000). The morphologies of calcium carbonate were also related to the mass transfer rate of CO_2 and the concentration of calcium hydroxide (Kang *et al*., 2003). The morphology of crystal shifts from rhombohedral structure to a spindle or needle-shaped structure due to excess calcium ions, increasing the $Ca(OH)_2$ concentration and decreasing the interfacial transport rate. Kim *et al.* synthesised a series of Ni-rich precursors ($(Ni_{0.90}Co_{0.05}Mn_{0.05})(OH)_2$) used as a precursor for lithium cathode materials. They found the particle size of the precursor was influenced by parameters such as the rotational speed of the inner cylinder, mean residence time and concentration of NH_3H_2O solution; the highest tap density of the agglomerates was 2.13 g cm^{-3}. Furthermore, they compared the influence of gap size between the inner and outer cylinder of the TC reactor on the particle size, since these parameters affected the fluid shear and stability of the Taylor vortex flow (Kim *et al*., 2011; Mayra and Kim, 2015).

Some limitations in the TC reactor also appear when it is operated in the laminar flow regime; the intra-vortex mixing shows some deficiencies in the mixing in the core of the vortexes. Moreover, it is easy to concentrate the dispersed phase in the core of the vortexes due to the presence of regions of low velocity. Based on these limitations, a series of studies have been carried out. Soos first proposed a classical TC reactor with a lobed cross-section to study the effect on the distribution of the shear rate (Soos *et al*., 2007). It was found that the long tails in the high shear rate region of the ST units and the low shear rate present in the classical TC units were removed. The narrowest $\gamma/<\gamma>$ distributions were obtained when the ratio of the largest gap d_{max} to smallest gap d_{min} were in the range of 2 to 3. Li *et al.* investigated the use of specific profiles of the cross section for the inner cylinder in the TC reactor to deform the Taylor vortices, effectively reducing the regions of low velocity and shear rate in the TC reactor (Figure 2-8) (Li *et al*., 2015a). They used a Reynolds stress model to simulate the highly turbulent rotating flows.

The dimensionless torque G obtained from the modified TC reactor is considered much smaller than the classical ones. Snyder and Mullin *et al.* suggested that the inner or outer cylinder with a square cross-section could affect the final flow patterns and the mixing intensity of reactors in the vortexes (Mullin and Lorenzen, 1985; Snyder, 1968).

2.4 Lithium Cathode Material

In the past decades, the Li-ion batteries have expanded application from consumer electronics to other areas such as the automotive industry. The development of automotive technology has been experienced from Hybrid (HV) to a plug-in hybrid (PHEV) to fully electric (EV). The slow rate of the EV market is restricted by key factors like cost-to-range ratio and charging time. The driving ranges of over 300 miles make it possible to guarantee the success of EVs. The request for an extended driving range has urged scientists to develop novel electrode active materials, particularly for cathode materials (Myung *et al*., 2016; Scrosati and Garche, 2010; Nitta *et al*., 2015).

The commonly-used cathode materials are compound materials ($Li(Ni_{1/3}Co_{1/3}Mn_{1/3})O_2$, $LiCoO_2$, $LiMn_2O_4$, $LiFePO_4$ et al.) with reversible Li intercalation/deintercalation ability (Hu *et al*., 2013; Julien and Mauger, 2013; Xu *et al*., 2012). Since these compound materials are stable in air and have a high redox potential, they are often used as the preferred cathode material for lithium-ion batteries. The voltage and specific capacity of commonly used cathode materials are shown in Figure 2-9, where LCO is ‘lithium cobalt oxide’, LMO is ‘lithium manganese oxide’, NCM is for ‘nickel cobalt manganese oxide’, NCA is ‘nickel cobalt aluminium oxide’, LCP is ‘lithium cobalt phosphate’, LFP is ‘Lithium iron phosphate’, LFSF is ‘Lithium iron fluoro-sulphate’ and LTS is ‘lithium titanium sulphide’.

The ideal cathode material should have the following characteristics:

(a) High redox potential and an output voltage

(b) High specific capacity and good cycle performance

(c) High diffusion coefficient (quickly charged and discharged)

(d) Good chemical stability

(e) Cheap

2.4.1 Fundamentals of the Li-ion Rechargeable Battery

The Li-ion battery utilises the reversible electrochemical reactions to convert and store electrochemical energy. The fundamentals of a working Li-ion battery is illustrated in Figure 2-10. (Kraytsberg and Ein-Eli, 2012). The negative electrode (anode) is a graphitic carbon that supports Li ions in its layers, the positive electrode (cathode) is a Li metal-oxide material. On the process of charging, Li ions de-intercalate from the layered oxide compounds via solid-state diffusion and intercalate into the graphite layers. The electrodes are separated by a separator and Li ions are transported through the electrolyte. The Li-ion approaches the electrode/electrolyte interface and diffuses through the electrolyte. During the discharge process, the whole transportation of Li ions is reversed. During Li intercalation/deintercalation, charge distribution inside the host structure is changed; furthermore, the overall charge transition results in electron flow in the external circuit. The electron passes through the anode or cathode particles and their interfaces by the outside current collector and migrates via the external circuit to power a device (Tang *et al.*, 2015).

The electrode reaction of a typical lithium nickel or cobalt (M) battery can be expressed as follows:

Positive electrode reaction: $LiMO_2 \longrightarrow Li_{1-x}MO_2 + xLi^+ + xe$ (2–5)

Negative electrode reaction: $nC + xLi^+ + xe \longrightarrow Li_xC_n$ (2–6)

Whole battery reaction: $nC + LiMO_2 \longrightarrow Li_{1-x}MO_2 + Li_xC_n$ (2–7)

2.4.2 Layered Oxides

There are three choices for the development of cathode materials: layered $LiMO_2$ (M = Ni, Mn, Co) (Mizushima *et al.*, 1980), spinel $LiMn_2O_4$(Thackeray *et al.*, 1983) and olivine $LiFePO_4$ (Padhi *et al.*, 1997a). Each has its own merits and demerits. Among them, the layered lithium metal oxides with the highest potential capacity (current up to ~180 mAh g^{-1}) have garnered much attention in recent times and will be discussed in the following sections.

$LiCoO_2$: In 1980, Mizushima *et al.* first suggested the $LiCoO_2$(LCO) material. It had desirable features including high discharge potential, low molecular weight, high energy capacity, good charge/discharge performance, relative ease of synthesis and treatment and stable and high discharge voltage, making it the earliest and one of the most commonly used cathode materials for commercial LIBs (Mizushima *et al.*, 1980). LCO is in the form of α-$NaFeO_2$ structure, a distorted rock-salt structure where the cations order in alternating (111) planes (Figure 2-11a). The Co-located in octahedral sites occupy alternating layers and form a hexagonal symmetry. Due to the high redox value of the Co^{4+}/Co^{3+} couple, LCO has a high operational voltage of 4 V. The theoretical capacity of LCO is approximately 274 mAh g^{-1}, making it as a very attractive cathode material.

The major drawbacks of LCO cathodes are high cost, environmental hazard, low thermal stability and fast capacity fade at high current rates or during deep cycling. LCO cathodes are expensive because of the high cost of Co, while low thermal stability refers to the exothermic release of oxygen when a lithium metal oxide cathode is heated above a certain point, resulting in a runaway reaction where the cell can burst into flames (Dahn *et al.*, 1994; Nitta *et al.*, 2015).

LiNiO₂: Unlike Cobalt, Ni is less expensive and is environmentally friendly. $LiNiO_2$ has a similar structure to LCO. Nickel has a higher energy density than cobalt; 50% of lithium ions can be transferred between the anode and cathode for cobalt at the maximum voltage of a typical battery (4.7 V), while 70% of lithium ions can be mobilised for nickel at only 4.2 V. The $LiNiO_2$ (LNO) has a theoretical specific capacity of 275 mAh g^{-1}. However, the development of LNO still suffers from the following drawbacks: First, it experiences difficulty in the preparation of well-ordered $LiNiO_2$ material. Ni^{3+} ions are not stable at high temperatures in $LiNiO_2$. It cannot be overlooked that the presence of Ni^{2+} in $LiNiO_2$ and half of other materials may occupy the lithium sites between $<NiO_2>$ layer space. Additionally, the radius of Ni^{2+} (0.83 Å) is larger than that of Li^+ (0.74 Å); the mobility of Li^+ will be reduced and weaken its electrochemical properties (Li *et al.*, 1992; Kalyani and Kalaiselvi, 2005; Rougier *et al.*, 1996). Second, $LiNiO_2$ with $R\overline{3}m$ layered structure and $Fm3m$ rock salt-type structure coexisted in the material. The latter forms an electrochemical that is inactive in comparison with the former one (Kraytsberg and Ein-Eli, 2012). Thus, it should develop available routes to bypass the obstacles. Third, $Li_{1-x}NiO_2$ suffers from several successive phase transformations accompanied by volume changes, which results in material integrity and degrades the cycling stability and high-voltage capability. Unstable Ni^{4+} exists in Li_xNiO_2 ($x<<1$); it will reduce to Ni^{3+} at elevated temperatures. The transition of Ni^{4+} to Ni^{3+} exhibits a change of lattice structure, accompanied by oxygen loss. This leads to serious health issues (Yamada *et al*., 1995; Guilmard *et al*., 2003; Dahn *et al*., 1994).

<u>$LiMnO_2$</u>: Compared to Co or Ni, $LiMnO_2$ is a promising material, being cheaper and less toxic. The layered $LiMnO_2$ was prepared almost two decades ago (Armstrong and Bruce, 1996). Due to performance limitations such as low capacity, the difficulty of mass production and power charge/discharge performance, especially at high temperatures, $LiMnO_2$ has hindered widespread commercialisation (Gu *et al*., 2013).

<u>$LiMO_2$</u>: Lithium nickel cobalt manganese oxide ($LiNi_xMn_yCo_zO_2$, $x+y+z=1$) is a promising class of cathode materials with a theoretical specific capacity of 278 mAh g^{-1} and a sloped potential ranging from 3.7–5.0 V vs Li/Li^+ (Nykvist and Nilsson, 2015; Wandt *et al*., 2018). It integrates features of $LiCoO_2$, $LiNiO_2$ and $LiMnO_2$for their high capacity, good cycling stability, low cost and safety. Ni provides high capacity. Co could increase the electronic conductivity of the material, which provides an excellent rate capability. Mn is attributed to maintaining its cycling stability and performance (Liang *et al*., 2014). The new bond model is shown in Figure 2-12 and reveals that the bond strength of

Ni^{2+}/Mn^{4+} and Ni^{3+}/Mn^{4+} are stronger than those of Co^{2+}/Mn^{4+} and Co^{3+}/Mn^{4+}. Thus, Ni-rich cathode material (Ni>0.5) is popular for the development of high rate LIBs' application (Liang *et al*., 2016).

2.4.3 Spinel Oxides

Relative to layered oxide, Spinel $LiMn_2O_4$ is lower in cost, environmentally friendly and more abundant. The structure of $LiMn_2O_4$ is shown in Figure 2-11b. Li occupies the tetrahedral 8a sites, Mn occupies the octahedral 16d sites and O is located at the 32e sites. Its unique 3D structure makes $LiMn_2O_4$ perfect for high rate Li-ion application (Julien and Massot, 2003). However, a big disadvantage for $LiMn_2O_4$ is its capacity fading problems – the phase transformation from cubic spinel to tetragonal rock-salt structure (Thackeray *et al*., 1998). The Jahn-Tell effect causes structural distortion, which results in severe attenuation of capacity (Li *et al*., 2009). Manganese dissolution is believed to be the main cause of capacity degradation (Tang *et al*., 2014). The theoretical capacity of $LiMn_2O_4$ is 148 mAh g^{-1}. Practically, the discharge capacity of $LiMn_2O_4$ is approximately 120 mAh g^{-1}. Doping and surface coating are two important methods to improve the cycle stability and electrochemical performances of materials. Due to the low capacity of the material, Li-ion diffusivity and electronic conductivity, it is mainly used in power tools with lower energy density and cost.

2.4.4 Olivine Polyanions

In 1997, Goodenough et al. first reported the olivine $LiFePO_4$ structure cathode material (Padhi *et al.,* 1997). It is a safety, high thermal stability induced and environmentally compatible; furthermore, it is low-cost material compared to layered and spinel materials. The structure of $LiFePO_4$ is shown in Figure 2-11c. It is an orthorhombic lattice structure with a space group Pnma. The framework of $LiFePO_4$ consists of corner-shared FeO_6 octahedra and edge-shared LiO_6 octahedra. The FeO_6 octahedra and PO_4 tetrahedra are in contact with each other by sharing oxygen vertices in the b-c planes (Zhang, 2011). The theoretical capacity of $LiFePO_4$ is 170 mAh g^{-1} (Franger *et al.*, 2002). The improved stability of $LiFePO_4$ is owed to the strong bonding of Fe-O and P-O. Currently, $LiFePO_4$ has been commercialised and is successfully used in the areas of EVs. However, the main problem of $LiFePO_4$ is its poor rate capability limited by the 1D Li-ion transport channels and the low Li-ion diffusivity and electron conductivity (Zhang, 2011). Three main research directions such as size tailoring, doping and surface modifications have been proposed to improve the electrochemical performances of $LiFePO_4$.

2.5 Nickel Rich Based NCM Cathode Material

2.5.1 Nickel Rich Cathode Material

The layered cathode material, especially Ni-rich ones like NCM and NCA, has attracted much attention owed to its high reversible capacity, rate capability and low cost. Currently, the commercial material of NCM members includes $LiNi_{1/3}Co_{1/3}Mn_{1/3}O_2$ (NCM333) (Deng *et al.*, 2010) and $LiNi_{0.5}Co_{0.2}Mn_{0.3}O_2$ (NCM523) (Noh and Cho, 2012). With further room for improvement the capacity, the development of Ni-rich materials ($Ni \geq 0.6$) are required urgently. These relevant studies include preparation methods (Liang *et al.*, 2014; Lu *et* *al*., 2013; Zhang *et al*., 2010; Fu *et al*., 2014; Yue *et al*., 2011), particle size and morphology (Atsumi *et al*., 2001; Nie *et al*., 2015; Xia *et al*., 2015) on the electrochemical performance of the studied materials.

The co-precipitation method is a common preparation process for the industrial production of cathode materials. It could synthesise the precursor with spherical morphology and elements uniform at an atomic level. Liang et al. systematically studied the effect of co-precipitation conditions like temperature, pH value, stirring speed, or chelating agent concentration on the preparation of the $Ni_{0.6}Co_{0.2}Mn_{0.2}(OH)_2$ precursor. They obtained the precursor with a tap-density of 1.94 g cm^{-3} by controlling the optimal synthetic condition (Liang *et al*., 2014). Spray drying is another useful method to prepare cathode materials using element mixing at an atomic level (Yue *et al*., 2011). Li *et al*. synthesised the $Ni_{0.6}Co_{0.2}Mn_{0.2}(OH)_2$ precursor with a tiny, quasi-spherical structure using the ultrasonic spray pyrolysis method. The materials prepared thus had a pure phase and exhibited good structural ordering (Li *et al*., 2015b). Other methods, such as the solid state reaction method, combustion method and solvothermal method, were also researched (Fu *et al*., 2014). However, these have not been detailed within this study. Figure 2-13 shows the typical morphology of NCM precursors prepared by different methods.

To clarify the role of each transition metal in NCM, Noh *et al*. studied the effects of Ni on the electrochemical performance and the structural and thermal stabilities of $Li[Ni_xCo_yMn_z]O_2$ (x=1/3, 0.5, 0.6, 0.7, 0.8 and 0.85). From Figure 2-14, $LiNi_{1/3}Mn_{1/3}Mn_{1/3}O_2$ shows the best capacity retention and thermal stability, but with the lowest discharge capacity. $LiNi_{0.85}Co_{0.075}Mn_{0.075}O_2$ has the lowest capacity retention as well as thermal stability, although its discharge capacity is the largest. The chief reason for capacity retention is overall volume expansion of the electrode and structural transition, to a spinel-like structure (Noh *et al*., 2013).

Alternately, NCM materials' discharge capacity can be increased by increasing the upper cut-off voltage to over 4.3V. However, fast deterioration of battery is apparent, if the upper cut-off voltage crosses 4.5V owed to an increase of charge transfer resistance caused by HF attack (Park *et al*., 2004; Liu *et al*., 2014; Yano *et al*., 2015; Wolff-Goodrich *et al*., 2015). A suitable electrolyte is needed to develop a high voltage Li battery (Gallus *et al*., 2014). Furthermore, oxygen release is a problem that leads to thermal runaway of the battery, especially at an overcharged state (Konishi *et al*., 2011). Recently, Wandt *et al*. first showed that highly reactive singlet oxygen ($^1O_2$) is released when charging NCM to a SOC beyond 80%, providing significant evidence for the reaction between singlet oxygen and the electrolyte to be a chemical reaction, as shown in Figure 2-15.They argued that the prevention of chemical side reactions with $^1O_2$ were likely of key importance for the development of reversible high-energy density batteries based on the NCM cathodes (Wandt *et al*., 2018).

Overall, the main research obstacles for Ni-rich materials include the following three aspects: (a) The high reactivity of Ni^{4+} at the end of the charging process, leading to low thermal stabilities and side reaction on the cathode side with the electrolyte; (b) Li/Ni mixing results in the disorder structure, producing an inactive rock salt phase on the particle surface; (c) The microcracks of material during the charge and discharge process.

2.5.2 Doping

Metal ions doping has proved to be an effective way to improve the electrochemical properties of the lithium cathode material. Doping could improve the structural stability of high nickel cathode materials reported in many kinds of literature. The general mechanisms are divided into the following two aspects:

(1) Doping could help reduce Ni^{2+} ions' migration from the position of 3b (transition metal) to 3a (lithium). It stabilises the valence state of Ni^{2+} or increases the electrostatic repulsion between transition metal layers, making the transition of Ni^{2+} to lithium layer difficult (Abdellahi *et al*., 2016, Cai *et al*., 2012).

(2) Moreover, it can improve the bond energy between metal ions and oxygen, improving the structural stability and reducing oxygen evolution (Kang and Ceder, 2006; Ceder *et al*., 1997).

The common substitution metals in the literature included Mg (Liao *et al*., 2008), Al (Belharouak *et al*., 2006), Zn (Chen *et al*., 2009), Fe (Reimers *et al*., 1993), Ti and Cr (Li *et al*., 2012) have been widely studied.

Mg: It is generally accepted that the Mg substitution could reduce cation mixing; it acts as a pillar to improve structural stability (Liao *et al*., 2008). It could lead to the alleviation of phase change during lithium-ion insertion and extraction; the thermal stability could be enhanced at every de-lithiated state (Kim *et al*., 2006). These characteristics have a positive effect on the final electrochemical performances of electrodes. Thus, the addition of Mg has attracted great attention. The literature reported that the addition of Mg into $LiCoO_2$ material could improve its conductivity. Owed to the similar radius of Mg^{2+} (0.72 Å) and Li (0.76 Å), Mg^{2+} could enter the vacancy of the Li-ion; this does not take place in the redox reaction during the charge/discharge process. The crystal structure is less affected by severe shrinkage of the interlayer spacing upon lithium deintercalation. These structural aspects endorse the significant improvement of cycling behaviour (Figure 2-16).

Al: Aluminium is another common metal doped in cathode materials. In some cases, the addition of Al could improve the retention capacity of the electrode materials during the cycling process; in other cases, it may recede the decreased capacity. The improvement capacity of electrode materials is by improved electrode kinetics, structural modifications and microstructural effects. While for some cases, the capacity degradation is chiefly because Al^{3+} cannot be further oxidised. So, the transition metal ion being replaced with aluminium represents one less oxidisable ion (Guilmard *et al*., 2003; Woo *et al*., 2009; Dahn *et al*., 1994a; Liu *et al*., 2009). The proportion of Al doping is mainly concentrated below 5%, since a higher amount of Al will lead to its capacity loss. However, Jo *et al*. reported that the rate capacity of $LiNi_{0.81}Co_{0.1}Al_{0.09}O_2$ is 155 mAh g^{-1} at 10 C with a cut-off voltage of 3.0-4.5 V. Additionally, it has improved thermal stability and electrochemical performances at a high temperature of 60°C, as shown in Figure 2-17. By optimising the contents of the doped element, a sample with better performance can be synthesised with lesser inert elements (Jo *et al*., 2014).

Furthermore, several studies have been carried out to evaluate the electrochemically active element, like Fe or Cr on the electrochemical performances of materials. Fe is a low cost, eco-friendly and resource-abundant element in nature. Compared to other materials, the electrochemical performances of materials doped by Fe is not improved obviously (Reimers *et al.*, 1993). Fe doping will reduce the discharge capacity of Li-nickel rich cathode material owed to the improved oxidation potential of the Ni^{2+} element (Pardo *et al*., 2000). Zinc doping for Ni in $LiCo_{0.3}Ni_{0.4}Mn_{0.3}O_2$ has been shown to improve the high rate discharge capacity and thermal stability due to its prevention of structural transformation (Chen *et al*., 2009). Ti doping has shown to improve the crystal structure in or reduce the dissolution of the electrode. Wilcox et al. found that Ti substitution Co in $Li(Ni_{1/3}Co_{1/3}Mn_{1/3})O_2$ could lead to the formation of a high rate and capacity-positive electrode (Wilcox *et al*., 2009). The DFT results show that Ti substitution could reduce the structural distortions during de-lithiation and suppress the formation of rock-like salt phase at high voltage (Markus *et al*., 2014).

To summarise, most research published today are based on improving the structural stability of materials during the charge/discharge process. After doping, the material could form a solid solution in the layered structure. When the Ni element is oxidised into Ni^{4+}, this could improve the stability of the transition metal layer, thus inhibiting the change of the irreversible phase in a high de-lithium state. The variation of the cell constant is also inhibited, such that the electrochemical performances could be improved obviously.

2.5.3 Surface Coating

The surface coating is another effective way to improve the electrochemical performances and thermal stability of cathode materials. Since these materials corrode and dissolute in the liquid electrolyte during the charging and discharging process, resistive reaction layers will be formed on their surface. Oxide acts as an interfacial stabiliser, which could protect the material from dissolution. Metal oxides or other materials like Al_2O_3, ZnO, ZrO_2, TiO_2, V_2O_5, $Al(OH)_3$, $AlPO_4$ and AlF_3, have been reported to be effective coating materials (Guo *et al*., 2009; Li *et al*., 2006; Ahn *et al*., 2007; Park *et al*., 2008; Chen *et al*., 2014). The relevant surface coating techniques include sol-gel, solid state reaction, pulsed laser deposition, chemical vapour deposition (CVD) and physical vapour deposition (PVD) (Figure 2-18). Kalluri*et al.* summarised in detail the merits and demerits of these surface coating technology in a recent progress report (Kalluri *et al*., 2017). A recent study (shown in Figure 2-19) reveals that the presence of Al_2O_3 coated on the $Li_{1.2}Ni_{0.2}Mn_{0.6}O_2$ could suppress the structures from a layered to a spinel phase transition. For the particle without coating, the valence of Mn appears after 40 charge/discharge cycles, while the coated sample demonstrates a negligible Mn loss (Yan *et al*., 2015). Li *et al*. employed the method of atomic layer deposition (ALD) to coat $LiNi_{1/3}Co_{1/3}Mn_{1/3}O_2$ with a solid-state electrolyte – $LiTaO_3$. The results show that a proper thickness of coating could be beneficial in preventing cathode material dissolution into the electrolyte and maintain the microstructure of NMC (Li *et al*., 2014).

2.5.4 Concentration Gradient

The surface of the high-nickel cathode material is relatively active; there are many problems during the production, storage and charge/discharge of Li ions. Contrary to the layered material NCM, the NCM cathode with a concentration gradient can make use of the advantages of each element (Ni, Co and Mn) without compromising energy density or safety. A core-shell or concentration gradient cathode materials consist of an outer shell with a high Mn content, providing good thermal stability and an inner core with high Ni content facilitating high discharge capacity (Figure 2-20). Sun *et al*. synthesised core-shell NCM particles (shown in Figure 2-21) that delivered the discharge capacity of 215 mAh g^{-1}, maintaining 90% capacity retention after 1000 cycles, where the Ni concentration decreased linearly while Mg concentration increased gradually from the centre to the outer layers (Sun *et al*., 2012). Recently, Kim *et al*. prepared a highly stable $LiNi_{0.6}Co_{0.2}Mn_{0.2}O_2$ cathode exploiting polystyrene beads (PSBs) cluster as a sacrificial template, which incorporated co-precipitation (Kim *et al*., 2017). As shown in Figure 2-22, the pore-space and concentration gradient were formed with reduced Ni oxidation state during the thermal decomposition of the PSBs. It reduces unstable trivalent nickel ions to stable divalent nickel ions. To balance the charge neutrality, the oxidation state of Ni was induced in the diffusion of the transition metal ions from the surface to the core, thus facilitating the formation of concentration gradients in the cathode materials. This specific structure had good cycle stability at a voltage of 4.45 V without any electrolyte additive; it retained 5% higher discharge capacity after 250 cycles in comparison to the pristine NCM.

2.6 Modelling Studies of Li-ion Battery Performance

The electrical performance of the Li-ion battery is dependent on the preparation condition where each cell is exposed. The mass flux of Li-ions is based on three transport phenomena: the migration, diffusion and convection. In the Battery Management System (BMS) of electrical vehicles, modelling the battery performances usually rested on batteries' past experimental data to predict future states. To optimise cell design parameters, more attention should be paid to develop an accurate battery model able to predict battery performance at different cell levels. Generally, the Li-ion battery model could be divided into two parts (Figure 2-23): the empirical and electrochemical model. We have reviewed three typical types of modelling with various complexities and capabilities, aiming at simulating Li-ion cells under normal conditions.

Equivalent circuit models (ECM): This model utilises the electrical circuit component and relatively few parameters to study the dynamic process of the Li battery. Figure 2-24 shows the model of electrical behaviour: an open-circuit voltage source is connected with resistors or capacitors. The cell voltage can be simulated from the ECM. Under a constant-current condition, Verbrugge and Conell derived the time-dependent cell voltage as follows (Verbrugge and Conell, 2002)

$$V(t) = \frac{Q(0)}{C} e^{-t/R_2C} + V_0 - IR_1 - IR_2(1 - e^{-t/R_2C}) \qquad (2\text{-}8)$$

Where $Q(0)$ is the nominal capacity, V_o is the nominal state of charge (SOC) dependent cell open-circuit voltage, R_1 is all Ohmic resistant components and R_2 is the faradic non-linear components in the circuit. Eq. 2-8 can be used to calculate the cell voltage change at various rates. Thus, a simulated voltage versus SOC (or time) discharge curve for a specific rate can be obtained.

The main feature of the ECM lies in its simple implementation and fast calculation. Hence, it has been widely used in the Battery Management System (BMS) and vehicle power management control. However, since the ECM is empirical in nature, it experiences difficulty in providing insights into the electrochemical process inside the battery, such that its physical parameters cannot be determined. Furthermore, it cannot update the characteristics of the battery when it ages. Thus, these models cannot work properly on the BMS system after several charge/discharge cycles (Bizeray *et al.*, 2015; Seaman *et al.*, 2014; Northrop *et al.*, 2014).

Pseudo-two-Dimensional models: The porous structure of the electrode is believed to be a chief characteristic of the Li-ion battery. The complex geometry of the inner porous structure makes it difficult to predict battery performance. In 1975, Newman and Tiedemann developed a porous electrode theory for battery application with a macroscopic description. The governing equations were derived based on material balance, electroneutrality and the conservation of charge balance (Newman and Tiedemann, 1975). Doyle *et al.* developed a pseudo-two-dimensional (P2D) electrochemical model for Li-ion battery simulation combining porous electrode theory and concentrated solution theory (Doyle *et al.*, 1993). Most current Li-ion models are derived from these theories, where electrochemical reaction and the prediction of the battery performance is done mathematically under various operating conditions with higher accuracy. Figure 2-25 shows a simplified 1D model to describe the charge/discharge and species transport in the solid and electrolyte phases. The main description equation of the P2D model is listed in Table 1 (Xu and Wang, 2017). The main features of the equations involve the following aspects: the solid phase Li^+ ions' concentration (c_s), the liquid phase Li^+ ions' concentration (c_l), the solid phase potential, the liquid phase potential and the pore wall flux of Li^+ ions in the electrode.

Numerous studies have been conducted to test and validate model accuracy (Newman and Tiedemann, 1975; Doyle and Newman, 1996; Darling and Newman, 1997; Darling and Newman, 1998). The effort has been on studying the effects of design parameters such as electrode thickness, particle size and porosity by coupling the P2D model on battery performance. For instance, Yang *et al*. proposed an electrochemical-thermal Li-ion battery model to investigate the charging polarisation characteristics. The influence factors such as $LiPF_6$ concentration and particle radius were evaluated on its polarisation properties (Yang *et al*., 2016). Appiah et al. proposed a non-linear least squares technique to study the effect of cathode thickness and porosity on Li transport. They found that thicker electrodes with a lower porosity require a longer time for discharge than thinner electrodes with higher porosity (Appiah *et al*., 2016). Some researchers presented 3D microstructure-based models to model battery performance (Stephenson *et al*., 2011). To estimate porosity, Meyer *et al*. investigated that controlling the compaction process can determine a performance-optimised pore structure in LIBs. There is exponential relation between the porosities of electrodes and the applied line load (shown in Figure 2-26) (Meyer *et al*., 2017).

Although the P2D model is relatively accurate and in good agreement with experimental data, it is not suitable for real-time applications. It usually takes hours to spatially discretise the system. Thus, a simplified P2D battery should be developed for a fast and reliable estimation of the Li-ion battery.

Single particle model (SPM): Compared to the P2D model, the SPM is described from a series of ordinary differential equations and assumes that both electrodes are composed of spherical particles with same size and shape; the current distribution is uniform across the electrodes (Li *et al*., 2017). Thus, it provides quick responses for Li-ion battery simulation but is unsuitable for simulating high discharge rates and thick electrodes.

References

ABDELLAHI, A., URBAN, A., DACEK, S. & CEDER, G. 2016. Understanding the effect of cation disorder on the voltage profile of Lithium transition-metal oxides. *Chemistry of Materials,* 28**,** 5373-5383.

AHN, D., LEE, J.-G., LEE, J. S., KIM, J., CHO, J. & PARK, B. 2007. Suppression of structural degradation of $LiNi_{0.9}Co_{0.1}O_2$ cathode at 90°C by $AlPO_4$-nanoparticle coating. *Current Applied Physics,* 7**,** 172-175.

APPIAH, W. A., PARK, J., SONG, S., BYUN, S., RYOU, M.-H. & LEE, Y. M. 2016. Design optimization of $LiNi_{0.6}Co_{0.2}Mn_{0.2}O_2$/graphite lithium-ion cells based on simulation and experimental data. *Journal of Power Sources,* 319**,** 147-158.

ARMSTRONG, A. R. & BRUCE, P. G. 1996. Synthesis of layered $LiMnO_2$ as an electrode for rechargeable lithium batteries. Nature, 381**,** 499-500.

ÅSLUND, B. L. & RASMUSON, Å. C. 1992. Semibatch reaction benzoic crystallization of acid. *AIChE Journal,* 38**,** 328-342.

ATSUMI, T., NAKATA, Y., KOBAYAKAWA, K., NEGISHI, K., YAMAZAKI, N. & SATO, Y. 2001. Particle size effect of $LiCoO_2$ powders on discharge performance of lithium ion batteries. *Electrochemistry Communications,* 69**,** 603-607.

BALDYGA, J., PODGÓRSKA, W. & POHORECKI, R. 1995. Mixing-precipitation model with application to double feed semibatch precipitation. *Chemical Engineering Science,* 50**,** 1281-1300.

BALDYGA, J. & BOURNE, J. R. 1984. A Fluid Mechanical Approach to Turbulent Mixing and Chemical Reaction Part I Inadequacies of Available Methods. *Chemical Engineering Communications,* 28**,** 231-241.

BALDYGA, J. & BOURNE, J. R. 1989a. Simplification of micromixing calculations. I. derivation and application of new model. *The Chemical Engineering Journal,* 42**,** 83-92.

BALDYGA, J. & BOURNE, J. R. 1989b. Simplification of micromixing calculations. II. new applications. *The Chemical Engineering Journal,* 42**,** 93-101.

BELHAROUAK, I., LU, W., VISSERS, D. & AMINE, K. 2006. Safety characteristics of $Li(Ni_{0.8}Co_{0.15}Al_{0.05})O_2$ and $Li(Ni_{1/3}Co_{1/3}Mn_{1/3})O_2$. *Electrochemistry Communications,* 8**,** 329-335.

BIZERAY, A. M., ZHAO, S., DUNCAN, S. R. & HOWEY, D. A. 2015. Lithium-ion battery thermal-electrochemical model-based state estimation using orthogonal collocation and a modified extended Kalman filter. *Journal of Power Sources,* 296**,** 400-412.

BOTSARIS, G. D. 1976. Secondary nucleation - A review. In: Mullin J.W. (eds) *Industrial Crystallization*. Springer, Boston, **3**-22.

BOURNE, J. R. 2003. Mixing and the selectivity of chemical reactions. *Organic Process Research & Development,* 7**,** 471-508.

BRUNSTEINER, M., JONES, A. G., PRATOLA, F., PRICE, S. L. & SIMONS, S. J. R. 2005. Toward a molecular understanding of crystal agglomeration. Crystal Growth & Design, 5, 3-16.

CAFIERO, L. M., BAFFI, G., CHIANESE, A. & JACHUCK, R. J. J. 2002. Process intensification: precipitation of barium sulfate using a spinning disk reactor. *Industrial & Engineering Chemistry Research,* 41**,** 5240-5246.

CAI, L., LIU, Z., AN, K. & LIANG, C. 2012. Probing Li-Ni cation disorder in $Li_{1-x}Ni_{1+x-y}Al_yO_2$ cathode materials by neutron diffraction. *Journal of The Electrochemical Society,* 159**,** A924-A928.

CEDER, G., AYDINOL, M. K. & KOHAN, A. F. 1997. Application of first-principles calculations to the design of rechargeable Li-batteries. *Computational Materials Science* 8**,** 161-169.

CHEN, Y., CHEN, R., TANG, Z. & WANG, L. 2009. Synthesis and characterization of Zn-doped $LiCo_{0.3}Ni_{0.4-x}Mn_{0.3}Zn_xO_2$ cathode materials for lithium-ion batteries. *Journal of Alloys and Compounds,* 476**,** 539-542.

CHEN, Y., ZHANG, Y., CHEN, B., WANG, Z. & LU, C. 2014. An approach to application for $LiNi_{0.6}Co_{0.2}Mn_{0.2}O_2$ cathode material at high cutoff voltage by TiO_2 coating. *Journal of Power Sources,* 256**,** 20-27.

CHOI, C. K., PARK, J. Y., PARK, W. C. & KIM, J. J. 1999. A study on dynamic separation of silica slurry using a rotating membrane filter: 2. modelling of cake formation. *Journal of Membrane Science,* 157**,** 177-187.

DAHN, J. R., FULLER, E. W., OBROVAC, M. & SACKEN, U. V. 1994. Thermal stability of $LixCoO_2$, $LixNiO_2$ and λ-MnO_2 and consequences for the safety of Li-ion cells. *Solid State Ionics,* 69**,** 265-270.

DARLING, R. & NEWMAN, J. 1997. Modeling a porous intercalation electrode with two characteristic particle sizes. *Journal of The Electrochemical Society,* 144**,** 4201-4208.

DARLING, R. & NEWMAN, J. 1998. Modeling side reactions in composite $LiMn_2O_4$ electrodes. *Journal of The Electrochemical Society,* 145**,** 990-998.

DENG, C., ZHANG, S., FU, B. L., YANG, S. Y. & MA, L. 2010. Synthetic optimization of nanostructured $Li[Ni_{1/3}Mn_{1/3}Co_{1/3}]O_2$ cathode material prepared by hydroxide coprecipitation at 273K. *Journal of Alloys and Compounds,* 496**,** 521-527.

DOYLE, M., FULLER, T. F. & NEWMAN, J. 1993. Modeling of galvanostatic charge and discharge of the Lithium/polymer/insertion cell. *Journal of The Electrochemical Society,* 140**,** 1526-1533.

DOYLE, M. & NEWMAN, J. 1996. Comparison of modeling predictions with experimental data from plastic Lithium ion cells. *Journal of The Electrochemical Society,* 143**,** 1890-1903.

DUTTA, P. K. & RAY, A. K. 2004. Experimental investigation of Taylor vortex photocatalytic reactor for water purification. *Chemical Engineering Science,* 59**,** 5249-5259.

ENOKIDA, Y., NAKATA, K. & SUZUKI, A. 1989. Axial turbulent diffusion in fluid between rotating coaxial cylinders. *AIChE Journal,* 35**,** 1211-1214.

FRANGER, S., LE CRAS, F., BOURBON, C. & ROUAULT, H. 2002. $LiFePO_4$ synthesis routes for enhanced electrochemical performance. *Electrochemical and Solid-State Letters,,* 5**,** A231-A233.

FU, C., LI, G., LUO, D., LI, Q., FAN, J. & LI, L. 2014. Nickel-rich layered microspheres cathodes: lithium/nickel disordering and electrochemical performance. *ACS Applied Materials & Interfaces,* 6**,** 15822-15831.

GALLUS, D. R., SCHMITZ, R., WAGNER, R., HOFFMANN, B., NOWAK, S., CEKIC-LASKOVIC, I., SCHMITZ, R. W. & WINTER, M. 2014. The influence of different conducting salts on the metal dissolution and capacity fading of NCM cathode material. *Electrochimica Acta,* 134**,** 393-398.

GIBBS, J. W. 1948. Collected Works. Thermaldynamics, Yale University Press, New Haven, I.

GU, M., BELHAROUAK, I., ZHENG, J., WU, H., XIAO, J., GENC, A., AMINE, K., THEVUTHASAN, S., BAER, D. R., ZHANG, J.-G., BROWNING, N. D., LIU, J. & WANG, C. 2013. Formation of the spinel phase in the layered composite cathode used in Li-ion batteries. *ACS Nano*, 7**,** 760-767.

GUILMARD, M., CROGUENNEC, L. & DELMAS, C. 2003. Thermal stability of Lithium nickel oxide derivatives. part II: $Li_xNi_{0.70}Co_{0.15}Al_{0.15}O_2$ and $LixNi_{0.90}Mn_{0.10}O_2$ (x=0.50 and 0.30) comparison with $Li_xNi_{1.02}O_2$ and $Li_xNi_{0.89}Al_{0.16}O_2$. *Chemistry of Materials,* 15**,** 4484-4493.

GUO, R., SHI, P., CHENG, X. & SUN, L. 2009. Effect of ZnO modification on the performance of $LiNi_{0.5}Co_{0.25}Mn_{0.25}O_2$ cathode material. *Electrochimica Acta,* 54**,** 5796-5803.

HOLESCHOVSKY, U. B. & COONEY, C. L. 1991. Quantitative description of ultrafiltration in a rotating filtration device. *AIChE Journal,* 37**,** 1219-1226.

HU, M., PANG, X. & ZHOU, Z. 2013. Recent progress in high-voltage lithium ion batteries. *Journal of Power Sources*, 237**,** 229-242.

JO, M., NOH, M., OH, P., KIM, Y. & CHO, J. 2014. A new high power $LiNi_{0.81}Co_{0.1}Al_{0.09}O_2$ cathode material for Lithium-ion batteries. *Advanced Energy Materials,* 4**,** 1301583-1301590.

JOKAR, A., RAJABLOO, B., DÉSILETS, M. & LACROIX, M. 2016. Review of simplified pseudo-two-dimensional models of lithium-ion. *Journal of Power Sources*, 327**,** 44-55.

JULIEN, C. M. & MASSOT, M. 2003. Lattice vibrations of materials for Lithium rechargeable batteries I. Lithium manganese oxide spinel. *Materials Science and Engineering: B*, 97**,** 217-230.

JULIEN, C. M. & MAUGER, A. 2013. Review of 5-V electrodes for Li-ion batteries: status and trends. *Ionics*, 19**,** 951-988.

JUNG, T., KIM, W.-S. & CHOI, C. K. 2003. Effect of nonstoichiometry on reaction crystallization of calcium carbonate in a couette-Taylor reactor. *Crystal Growth & Design,* 4**,** 491-495.

JUNG, W. M., KANG, S. H., KIM, W.-S. & CHOI, C. K. 2000. Particle morphology of calcium carbonate precipitated by gas-liquid reaction in a Couette-Taylor reactor. *Chemical Engineering Science*, 55**,** 733-747.

KALLURI, S., YOON, M., JO, M., PARK, S., MYEONG, S., KIM, J., DOU, S. X., GUO, Z. & CHO, J. 2017. Surface engineering strategies of layered $LiCoO_2$ cathode material to realize high-energy and high-voltage Li-ion cells. *Advanced Energy Materials,* 7**,** 1601507-1601527.

KALYANI, P. & KALAISELVI, N. 2005. Various aspects of $LiNiO_2$ chemistry: a review. *Science and Technology of Advanced Materials,* 6**,** 689-703.

KANG, K. & CEDER, G. 2006. Factors that affect Li mobility in layered Lithium transition metal oxides. *Physical Review B,* 74**,** 094105-094111.

KANG, S. H., LEE, S. G., JUNG, W. M., KIM, M. C., KIM, W.-S., CHOI, C. K. & FEIGELSON, R. S. 2003. Effect of Taylor vortices on calcium carbonate crystallization by gas–liquid reaction. *Journal of Crystal Growth,* 254**,** 196-205.

KATAOKA, K., DOI, H., HONGO, T. & FUTAGAWA, M. 1975. Ideal plug flow properties of Taylor vortex flow. *Journal of Chemical Engineering of Japan,* 8**,** 472-476.

KATAOKA, K., DOI, H. & KOMAI, T. 1977. Heat mass transfer in taylor vortex flow with constant axial flow rates. *International Journal of Heat and Mass Transfer,* 20**,** 57-63.

KATAOKA, K., OHMURA, N., KOUZU, M., SIMAMURA, Y. & OKUBO, M. 1995. Emulsion polymerization of styrene in a continuous taylor vortex flow reactor. *Chemical Engineering Science,* 50**,** 1409-1416.

KATAOKA, K. & TAKIGAWA, T. 1981. Intermixing over cell boundary between taylor vortices. *AIChE Journal,* 27**,** 504-508.

KIM, G.-H., MYUNG, S.-T., KIM, H.-S. & SUN, Y.-K. 2006. Synthesis of spherical $Li[Ni_{(1/3-z)}Co_{(1/3-z)}Mn_{(1/3-z)}Mgz]O_2$ as positive electrode material for lithium-ion battery. *Electrochimica Acta,* 51**,** 2447-2453.

KIM, J.-M., CHANG, S.-M., CHANG, J. H. & KIM, W.-S. 2011. Agglomeration of nickel/cobalt/manganese hydroxide crystals in couette–Taylor crystallizer. *Colloids and Surfaces A: Physicochemical and Engineering Aspects,* 384**,** 31-39.

KIM, J., CHO, H., JEONG, H. Y., MA, H., LEE, J., HWANG, J., PARK, M. & CHO, J. 2017. Self-induced concentration gradient in nickel-rich cathodes by sacrificial polymeric bead clusters for high-energy Lithium-ion batteries. *Advanced Energy Materials,* 7**,** 1602559-1602566.

KIM, W.-S., KIM, W.-S., KIM, K.-S., KIM, J.-S. & WARD, M. D. 2004. Crystal agglomeration of europium oxalate in reaction crystallization using double-jet semi-batch reactor. *Materials Research Bulletin,* 39**,** 283-296.

KONISHI, H., YUASA, T. & YOSHIKAWA, M. 2011. Thermal stability of $Li_{1-y}Ni_xMn_{(1-x)/2}Co_{(1-x)/2}O_2$ layer-structured cathode materials used in Li-Ion batteries. *Journal of Power Sources,* 196**,** 6884-6888.

KRAYTSBERG, A. & EIN-ELI, Y. 2012. Higher, stronger, better…a review of 5 volt cathode materials for advanced Lithium-ion batteries. *Advanced Energy Materials,* 2**,** 922-939.

LI, D., KATO, Y., KOBAYAKAWA, K., NOGUCHI, H. & SATO, Y. 2006. Preparation and electrochemical characteristics of $LiNi_{1/3}Mn_{1/3}Co_{1/3}O_2$ coated with metal oxides coating. *Journal of Power Sources,* 160**,** 1342-1348.

LI, G., YANG, X. & YE, H. 2015a. CFD simulation of shear flow and mixing in a taylor–couette reactor with variable cross-section inner cylinders. *Powder Technology,* 280**,** 53-66.

LI, J., LOTFI, N., LANDERS, R. G. & PARK, J. 2017. A single particle model for Lithium-ion batteries with electrolyte and stress-enhanced diffusion physics. *Journal of The Electrochemical Society,* 164**,** A874-A883.

LI, L.-J., WANG, Z.-X., LIU, Q.-C., YE, C., CHEN, Z.-Y. & GONG, L. 2012. Effects of chromium on the structural, surface chemistry and electrochemical of layered $LiNi_{0.8-x}Co_{0.1}Mn_{0.1}Cr_xO_2$. *Electrochimica Acta,* 77**,** 89-96.

LI, T., LI, X., WANG, Z., GUO, H., PENG, W. & ZENG, K. 2015b. Electrochemical properties of $LiN_{i0.6}Co_{0.2}Mn_{0.2}O_2$ as cathode material for

Li-ion batteries prepared by ultrasonic spray pyrolysis. *Materials Letters,* 159**,** 39-42.

LI , W., REIMERS, J. N. & DAHN, J. R. 1992. Crystal structure of $Li_xNi_{2-x}O_2$ and a lattice-gas model for the order-disorder transition. *Physical Review B,* 46**,** 3236-3246.

LI, X., LIU, J., BANIS, M. N., LUSHINGTON, A., LI, R., CAI, M. & SUN, X. 2014. Atomic layer deposition of solid-state electrolyte coated cathode materials with superior high-voltage cycling behavior for lithium ion battery application. *Energy & Environmental Science,* 7**,** 768-778.

LI, X., XU, Y. & WANG, C. 2009. Suppression of Jahn–teller distortion of spinel $LiMn_2O_4$ cathode. *Journal of Alloys and Compounds,* 479**,** 310-313.

LIANG, C., KONG, F., LONGO, R. C., KC, S., KIM, J.-S., JEON, S., CHOI, S. & CHO, K. 2016. Unraveling the origin of instability in Ni-rich $LiNi_{1-2x}Co_xMn_xO_2$ (NCM) cathode materials. *The Journal of Physical Chemistry C,* 120**,** 6383-6393.

LIANG, L., DU, K., PENG, Z., CAO, Y., DUAN, J., JIANG, J. & HU, G. 2014. Co–precipitation synthesis of $Ni_{0.6}Co_{0.2}Mn_{0.2}(OH)_2$ precursor and characterization of $LiNi_{0.6}Co_{0.2}Mn_{0.2}O_2$ cathode material for secondary lithium batteries. *Electrochimica Acta,* 130**,** 82-89.

LIAO, P.-Y., DUH, J.-G. & SHEU, H.-S. 2008. Structural and thermal properties of $LiNi_{0.6-x}Mg_xCo_{0.25}Mn_{0.15}O_2$ cathode materials. *Journal of Power Sources,* 183**,** 766-770.

LIU, L., SUN, K., ZHANG, N. & YANG, T. 2009. Improvement of high-voltage cycling behavior of $Li(Ni_{1/3}Co_{1/3}Mn_{1/3})O_2$ cathodes by Mg, Cr, and Al substitution. *Journal of Solid State Electrochemistry,* 13**,** 1381-1386.

LIU, T., GARSUCH, A., CHESNEAU, F. & LUCHT, B. L. 2014. Surface phenomena of high energy $Li(Ni_{1/3}Co_{1/3}Mn_{1/3})O_2$/graphite cells at high temperature and high cutoff voltages. *Journal of Power Sources,* 269**,** 920-926.

LU, H., ZHOU, H., SVENSSON, A. M., FOSSDAL, A., SHERIDAN, E., LU, S. & VULLUM-BRUER, F. 2013. High capacity $Li[Ni_{0.8}Co_{0.1}Mn_{0.1}]O_2$ synthesized by sol–gel and co-precipitation methods as cathode materials for lithium-ion batteries. *Solid State Ionics,* 249-250**,** 105-111.

MARKUS, I. M., LIN, F., KAM, K. C., ASTA, M. & DOEFF, M. M. 2014. Computational and experimental investigation of Ti substitution in $Li_1(Ni_xMn_xCo_{1-2x-y}Ti_y)O_2$ for Lithium ion batteries. *Journal of Physical Chemistry Letters,* 5**,** 3649-3655.

MASY, J. C. & COURNIL, M. 1991. Using a turbidimetric method to study the kinetics of agglomeration of potassium sulphate in a liquid medium. *Chemical Engineering Science,* 46**,** 693-701.

MAYRA, Q.-P. & KIM, W.-S. 2015. Agglomeration of Ni-rich hydroxide in reaction crystallization: effect of taylor vortex dimension and intensity. *Crystal Growth & Design,* 15**,** 1726-1734.

MEYER, C., BOCKHOLT, H., HASELRIEDER, W. & KWADE, A. 2017. Characterization of the calendering process for compaction of electrodes for lithium-ion batteries. *Journal of Materials Processing Technology,* 249**,** 172-178.

MIZUSHIMA, K., JONES, P. C., WISEMAN, P. J. & GOODENOUGH, J. B. 1980. $LixCoO_2$ ($0<x<1$): A new cathode material for batteries of high energy density. *Materials Research Bulletin,* 4**,** 783-789.

MULLIN, T. & LORENZEN, A. 1985. Bifurcation phenomena in flows between a rotating circular cylinder and a stationary square outer cylinder. *Journal of Fluid Mechanics,* 157**,** 289-303.

MYUNG, S.-T., MAGLIA, F., PARK, K.-J., YOON, C. S., LAMP, P., KIM, S.-J. & SUN, Y.-K. 2016. Nickel-rich layered cathode materials for automotive lithium-ion batteries: achievements and perspectives. *ACS Energy Letters,* 2**,** 196-223.

NEMRI, M., CHARTON, S. & CLIMENT, E. 2016. Mixing and axial dispersion in Taylor–couette flows: the effect of the flow regime. *Chemical Engineering Science,* 139**,** 109-124.

NEMRI, M., CLIMENT, E., CHARTON, S., LANOË, J.-Y. & ODE, D. 2013. Experimental and numerical investigation on mixing and axial dispersion in taylor–couette flow patterns. *Chemical Engineering Research and Design,* 91**,** 2346-2354.

NEWMAN, J. & TIEDEMANN, W. 1975. Porous-electrode theory with battery applications. *AlChE Journal,* 21**,** 25-41.

NGUYEN, A.-T., KIM, J.-M., CHANG, S.-M. & KIM, W.-S. 2011. Phase transformation of guanosine 5-monophosphate in continuous couette−Taylor crystallizer: experiments and numerical modeling for kinetics. Industrial & Engineering Chemistry Research, 50**,** 3483-3493.

NIE, M., XIA, Y.-F., WANG, Z.-B., YU, F.-D., ZHANG, Y., WU, J. & WU, B. 2015. Effects of precursor particle size on the performance of $LiNi_{0.5}Co_{0.2}Mn_{0.3}O_2$ cathode material. *Ceramics International,* 41**,** 15185-15192.

NITTA, N., WU, F., LEE, J. T. & YUSHIN, G. 2015. Li-ion battery materials: present and future. *Materials Today,* 18**,** 252-264.

NOH, H.-J., YOUN, S., YOON, C. S. & SUN, Y.-K. 2013. Comparison of the structural and electrochemical properties of layered Li[NixCoyMnz]O_2 (x=1/3, 0.5, 0.6, 0.7, 0.8 and 0.85) cathode material for Lithium-ion batteries. *Journal of Power Sources,* 233**,** 121-130.

NOH, M. & CHO, J. 2012. Optimized synthetic conditions of $LiNi_{0.5}Co_{0.2}Mn_{0.3}O_2$ cathode materials for high rate Lithium batteries via Co-precipitation method. *Journal of The Electrochemical Society,* 160**,** A105-A111.

NORTHROP, P. W. C., SUTHAR, B., RAMADESIGAN, V. S. S., SHRIRAM, BRAATZ, R. D. & SUBRAMANIAN, V. R. 2014. Efficient simulation and reformulation of Lithium-ion battery models for enabling electric transportation. *Journal of The Electrochemical Society,* 161**,** E3149-E3157.

NOYES, A. A. & WHITNEY, W. R. 1897. The rate of solution of solid substances in their own solutions. Solution of Solid Substances, 16, 930-934.

NYKVIST, B. & NILSSON, M. 2015. Rapidly falling costs of battery packs for electric vehicles. Nature Climate Change, 5, 329-332.

PADHI, A. K., NANJUNDASWAMY, K. S. & GOODENOUGH, J. B. 1997. Phospho-olivines as positive-electrode materials for rechargeable Lithium batteries. *J. Electrochem. Soc.,,* 144**,** 1188-1194.

PARK, B. C., KIM, H. B., MYUNG, S. T., AMINE, K., BELHAROUAK, I., LEE, S. M. & SUN, Y. K. 2008. Improvement of structural and electrochemical properties of AlF_3-coated $Li[Ni_{1/3}Co_{1/3}Mn_{1/3}]O_2$ cathode materials on high voltage region. *Journal of Power Sources,* 178**,** 826-831.

PARK, S. H., YOON, C. S., KANG, S. G., KIM, H. S., MOON, S. I. & SUN, Y. K. 2004. Synthesis and structural characterization of layered $Li[Ni_{1/3}Co_{1/3}Mn_{1/3}]O_2$ cathode materials by ultrasonic spray pyrolysis method. *Electrochimica Acta,* 49**,** 557-563.

PRADO, G., ROUGIER, A., FOURNèS, L. & DELMAS, C. 2000. Electrochemical behavior of iron-substituted lithium nickelate. Journal of Electrochemical Society, 147, 2880-2887.

REIMERS, J. N., ROSSEN, E., JONES, C. D. & DAHN, J. R. 1993. Structure and electrochemistry of $Li_xFe_yNi_{1-y}O_2$. Solid State Ionics, 61**,** 335-344.

ROUGIER, A., GRAVEREAU, P. & DELMAS, C. 1996. Optimization of the composition of the $Li_{1-z}Ni_{1+z}O_2$ electrode materials: structural, magnetic and electrochemical studies. *Journal of The Electrochemical Society,* 143**,** 1168-1175.

SCROSATI, B. & GARCHE, J. 2010. Lithium batteries: status, prospects and future. *Journal of Power Sources,* 195**,** 2419-2430.

SCZECHOWSKI, J. G., KOVAL, C. A. & NOBLE, R. D. 1995. A Taylor vortex reactor for heterogeneous photocatalysis. Chemical Engineering Science, 50, 3163-3173.

SEAMAN, A., DAO, T.-S. & MCPHEE, J. 2014. A survey of mathematics-based equivalent-circuit and electrochemical battery models for hybrid and electric vehicle simulation. *Journal of Power Sources,* 256**,** 410-423.

SENGUPTA, T. K., KABIR, M. F. & RAY, A. K. 2001. A Taylor vortex photocatalytic reactor for water purification. *Industrial & Engineering Chemistry Research,* 40**,** 5268-5281.

SNYDER, H. A. 1968. Experiments on rotating flows between noncircular cylinders. *Physics of Fluids,* 11**,** 1606-1611.

SOOS, M., WU, H. & MORBIDELLI, M. 2007. Taylor-couette unit with a lobed inner cylinder cross section. *AIChE Journal,* 53**,** 1109-1120.

STEPHENSON, D. E., WALKER, B. C., SKELTON, C. B., GORZKOWSKI, E. P., ROWENHORST, D. J. & WHEELER, D. R. 2011. Modeling 3D microstructure and ion transport in porous Li-ion battery electrodes. *Journal of The Electrochemical Society,* 158**,** A781-A789.

SUN, Y.-K., CHEN, Z., NOH, H.-J., LEE, D.-J., JUNG, H.-G., REN, Y., WANG, S., YOON, C. S., MYUNG, S.-T. & AMINE, K. 2012. Nanostructured high-energy cathode materials for advanced lithium batteries. *Nature materials,* 11**,** 942-947.

SUNG, M.-H., CHOI, I.-S., KIM, J.-S. & KIM, W.-S. 2000. Agglomeration of yttrium oxalate particles produced by reaction precipitation in semi-batch reactor. *Chemical Engineering Science,* 55**,** 2173-2184.

TANG, D., SUN, Y., YANG, Z., BEN, L., GU, L. & HUANG, X. 2014. Surface structure evolution of $LiMn_2O_4$ cathode material upon charge/discharge. *Chemistry of Materials,* 26**,** 3535-3543.

TANG, Y., ZHANG, Y., LI, W., MA, B. & CHEN, X. 2015. Rational material design for ultrafast rechargeable lithium-ion batteries. *Chemical Society Reviews,* 44**,** 5926-5940.

THACKERAY, M. M., DAVID, W. I. F., BRUCE, P. G. & GOODENOUGH, J. B. 1983. Lithium insertion into manganese spinels. *Materials research bulletin,* 18**,** 461-472.

THACKERAY, M. M., SHAO-HORN, Y., KAHAIAN, A. J., KEPLER, K. D., SKINNER, E., VAUGHEY, J. T. & HACKNEY, S. A. 1998. Structural fatigue in spinel electrodes in high voltage (4 V) Li/$Li_xMn_2O_4$ cells. *Electrochemical and Solid-State Letters,* 1**,** 7-9.

VERBRUGGE, M. W. & CONELL, R. S. 2002. Electrochemical and thermal characterization of battery modules commensurate with electric vehicle integration. *Journal of The Electrochemical Society,* 149**,** A45-A53.

VILLERMAUX, J. & FALK, L. 1994. A generalized mixing model for initial contacting of reactive fluids. *Chemical Engineering Science,* 49**,** 5127-5140.

VOLMER, M. 1939. Kinetic der Phasenbildung, Steinkopff, Leipzig.

VOLMER M. & WEBER A., 1925. Nucleus formation in supersaturated sturctures.*Physical Chemistry,* 119**,** 227-301.

WANDT, J., FREIBERG, A. T. S., OGRODNIK, A. & GASTEIGER, H. A. 2018. Singlet oxygen evolution from layered transition metal oxide cathode materials and its implications for lithium-ion batteries. *Materials Today,* 21**,** 825-833.

WENZEL, D. & GÓRAK, A. 2018. Review and analysis of micromixing in rotating packed beds. *Chemical Engineering Journal,* 345**,** 492-506.

WILCOX, J., PATOUX, S. & DOEFF, M. 2009. Structure and Electrochemistry of $LiNi_{1/3}Co_{1/3-y}M_yMn_{1/3}O_2$ (M=Ti, Al, Fe) positive electrode materials. *Journal of The Electrochemical Society,* 156**,** A192-A198.

WOLFF-GOODRICH, S., LIN, F., MARKUS, I. M., NORDLUND, D., XIN, H. L., ASTA, M. & DOEFF, M. M. 2015. Tailoring the surface properties of $LiNi_{0.4}Mn_{0.4}Co_{0.2}O_2$ by titanium substitution for improved high voltage cycling performance. *Physical Chemistry Chemical Physics,* 17**,** 21778-21781.

WOO, S.-W., MYUNG, S.-T., BANG, H., KIM, D.-W. & SUN, Y.-K. 2009. Improvement of electrochemical and thermal properties of $Li[Ni_{0.8}Co_{0.1}Mn_{0.1}]O_2$ positive electrode materials by multiple metal (Al, Mg) substitution. *Electrochimica Acta,* 54**,** 3851-3856.

WULFF, G. 1901. Zur frage der geschwindigkeit des wachstums und der auflösung der Krystallflachen. Z. Krystallographie und Mineralogie, 34**,** 449.

XIA, Y.-F., NIE, M., WANG, Z.-B., YU, F.-D., ZHANG, Y., ZHENG, L.-L., WU, J. & KE, K. 2015. Structural, morphological and electrochemical investigation of $LiNi_{0.6}Co_{0.2}Mn_{0.2}O_2$ cathode material synthesized in different sintering conditions. *Ceramics International,* 41**,** 11815-11823.

XU, B., QIAN, D., WANG, Z. & MENG, Y. S. 2012. Recent progress in cathode materials research for advanced lithium ion batteries. *Materials Science and Engineering: R: Reports,* 73**,** 51-65.

XU, M. & WANG, X. 2017. Electrode thickness correlated parameters estimation for a Li-ion NMC battery electrochemical model. ECS Transactions, 77, 491-507.

YAMADA, S., FUJIWARA, M. & KANDA, M. 1995. Synthesis and properties of $LiNiO_2$ as cathode material for secondary batteries. *Journal of Power Sources,* 54**,** 209-213.

YAN, P., NIE, A., ZHENG, J., ZHOU, Y., LU, D., ZHANG, X., XU, R., BELHAROUAK, I., ZU, X., XIAO, J., AMINE, K., LIU, J., GAO, F., SHAHBAZIAN-YASSAR, R., ZHANG, J.-G. & WANG, C.-M. 2015. Evolution of lattice structure and chemical composition of the surface reconstruction layer in $Li_{1.2}Ni_{0.2}Mn_{0.6}O_2$ cathode material for Lithium ion batteries. *Nano Letters,* 15**,** 514-522.

YANG, F., QIAO, Y., GAO, B., DUAN, P. & ZHU, Y. 2016. Investigation on Li-ion battery charging polarization characteristics and influence factors. *Ionics,* 22**,** 1603-1610.

YANO, A., AOYAMA, S., SHIKANO, M., SAKAEBE, H., TATSUMI, K. & OGUMI, Z. 2015. Surface structure and high-voltage charge/discharge characteristics of Al-oxide coated $LiNi_{1/3}Co_{1/3}Mn_{1/3}O_2$ cathodes. *Journal of The Electrochemical Society,* 162**,** A3137-A3144.

YUE, P., WANG, Z., PENG, W., LI, L., CHEN, W., GUO, H. & LI, X. 2011. Spray-drying synthesized $LiNi_{0.6}Co_{0.2}Mn_{0.2}O_2$ and its electrochemical performance as cathode materials for lithium ion batteries. *Powder Technology,* 214**,** 279-282.

ZHANG, W.-J. 2011. Structure and performance of $LiFePO_4$ cathode materials: a review. *Journal of Power Sources,* 196**,** 2962-2970.

ZHANG, X., JIANG, W. J., MAUGER, A., QILU, GENDRON, F. & JULIEN, C. M. 2010. Minimization of the cation mixing in $Li_{1+x}(NMC)_{1-x}O_2$ as cathode material. *Journal of Power Sources,* 195**,** 1292-1301.

ZOUGARI, M., JACOBS, S., RATULOWSKI, J., HAMMAMI, A., BROZE, G., FLANNERY, M., STANKIEWICZ, A. & KARAN, K. 2006. Novel organic solids deposition and control device for live-oils: design and applications. *Energy & Fuels,* 20**,** 1656-1663.

Figures

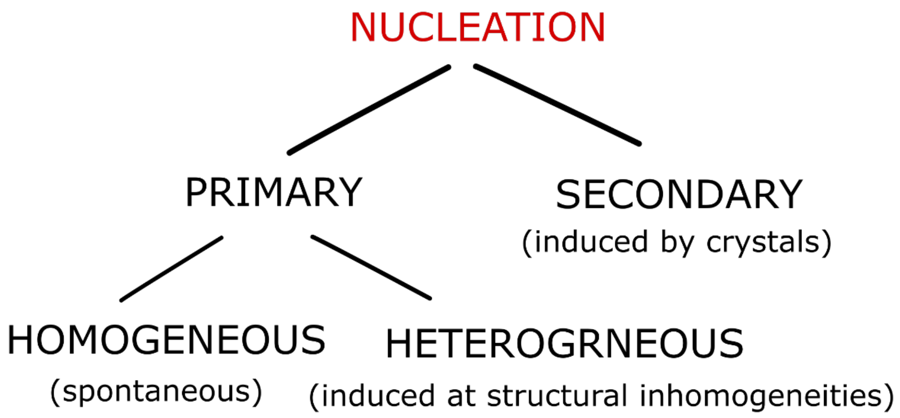

Figure 2-1. A simple scheme of nucleation

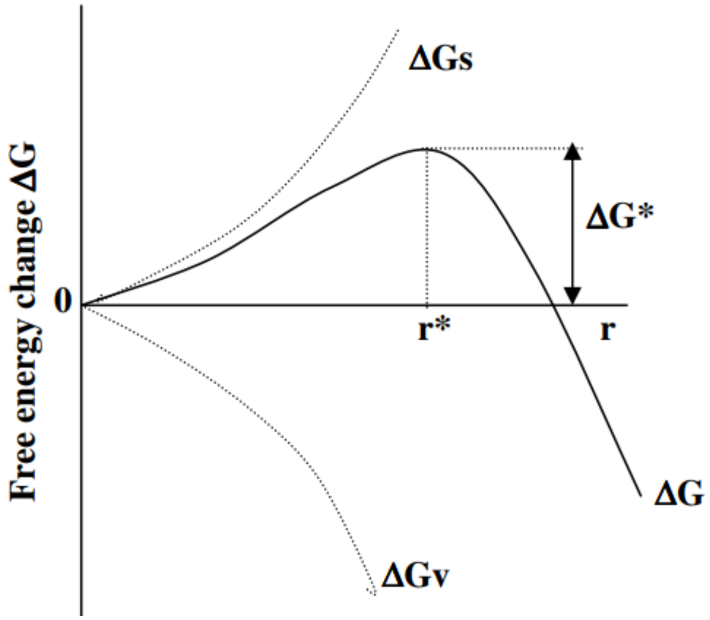

Figure 2-2. Curve showing the dependence of the change in surface energy (ΔG_s), volume energy (ΔG_v) and the net free energy (ΔG) on radius (r) of the nucleus (Volmer and Weber, 1925).

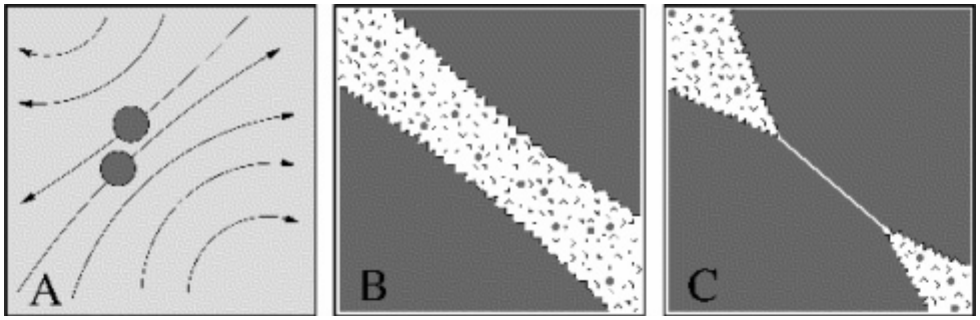

Figure 2-3. The stages of crystal agglomeration (A) approach of two crystals on a macroscopic length scale, (B) aggregation, where for separations below several nanometers, the microscopic structure of the solvent, solute, and impurities affect the interaction between the crystals, and (C) a solid agglomerative bond forms between the particles (Brunsteiner*et al*., 2005) © 2005 American Chemical Society

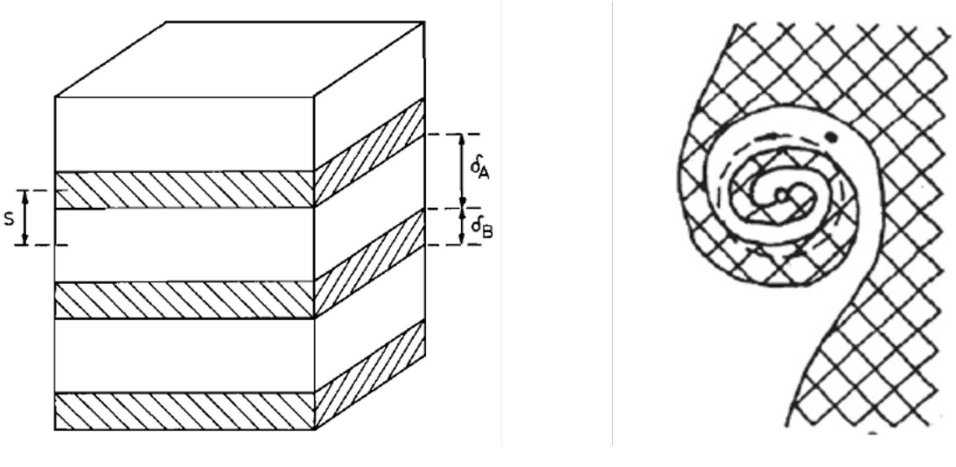

Figure 2-4. Schematic of mechanistic micro-mixing model: (a) Lamellar structure consisting of layers of A and B rich solutions; (b) Engulfment model (Baldyga and Bourne, 1984) © Taylor & Francis

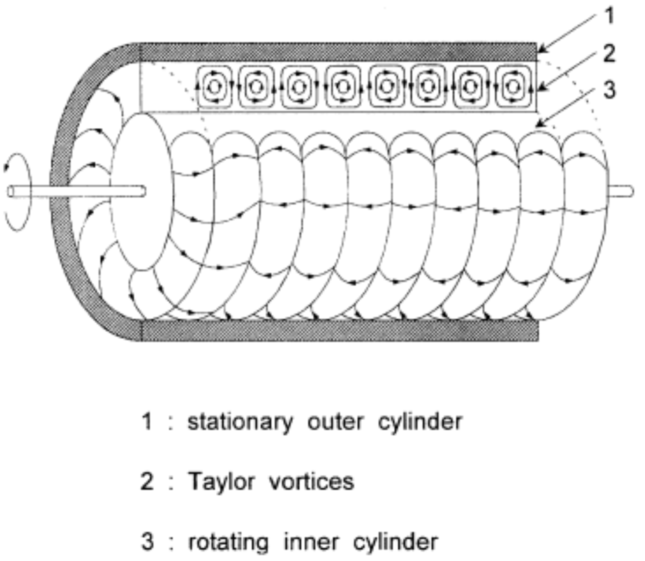

Figure 2-5. Schematic diagram of Taylor vortices in Taylor-Couette reactor(Jung *et al*., 2000) © 1999 Elsevier Science B.V.

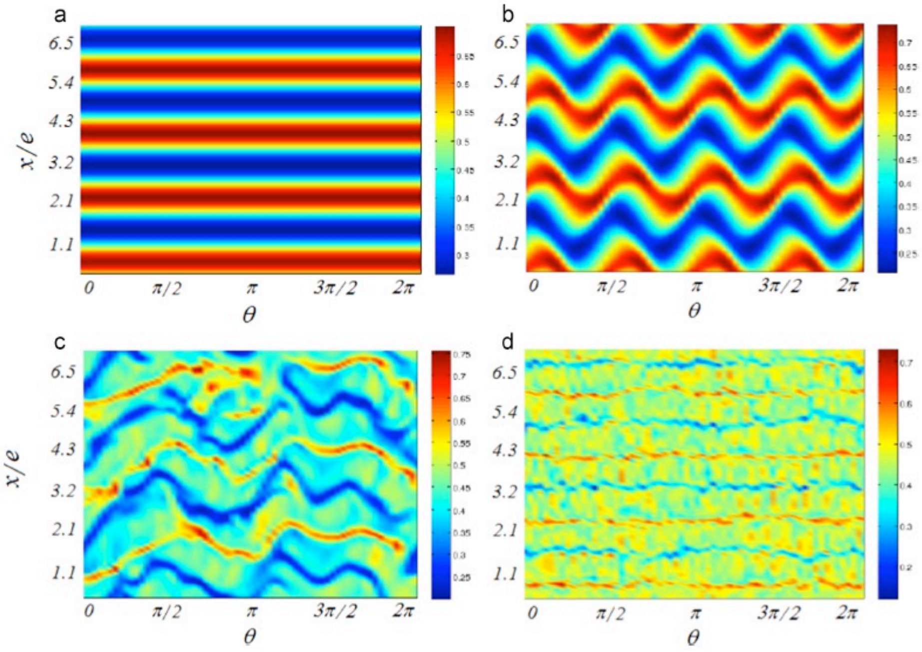

Figure 2-6. DNS visualization of the flow regimes achieved in the small-gap column (η=0.85)-Isocontours of the axial velocity in the middle of the gap $r = (1 + \eta)/2$. (a) Re=140 (TVF). (b) Re=200 (WVF). (c) Re=800 (MWVF).(d) Re=3500 (TTVF) (Nemri *et al*., 2016) © 2015 Elsevier Ltd.

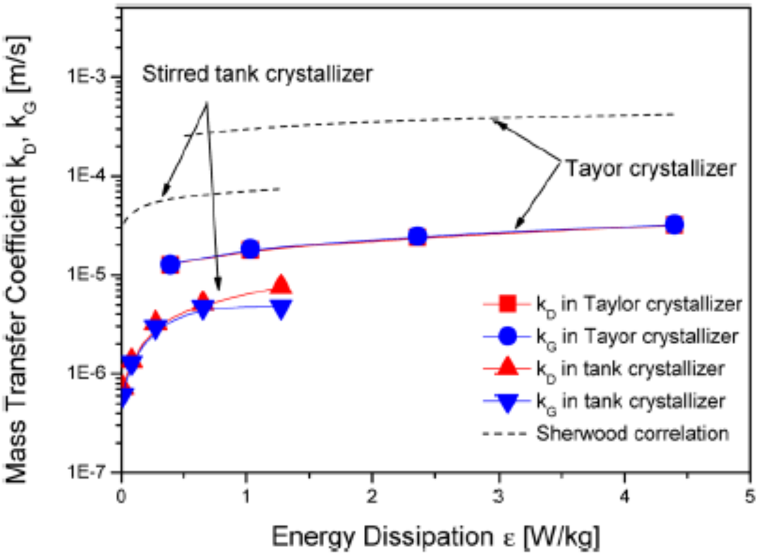

Figure 2-7. Comparison of mass transfer coefficients in Taylor vortex and stirred tank crystallizers for estimating turbulent motion effectiveness (Nguyen *et al*., 2011) © 2011, American Chemical Society

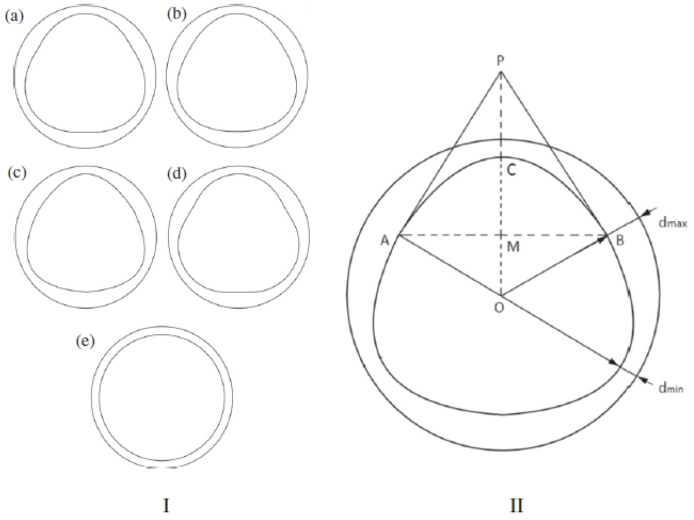

Figure 2-8. Schematic of cross section of the TC reactor using different inner cylinder composed of different cross-section profiles. I: (a) Case A: new modified TC with e=0.35, (b) Case B: new modified TC with e=0.4, (c) Case C: new modified TC with e=0.5, (d) Case D: lobed TC reported in literature; (e) Case E: classical TC, II: definition of cross-section profile of the inner cylinder for the new modified TC reactor(Li *et al*., 2015a) © 2015 Elsevier B.V.

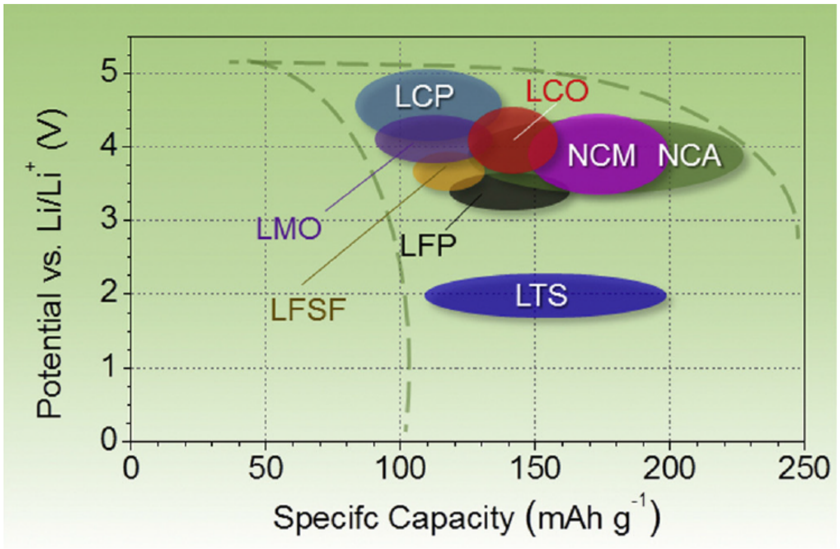

Figure 2-9. Comparison of voltage and capacity for cathode materials (Nitta *et al.*, 2015) © 2014 The Authors

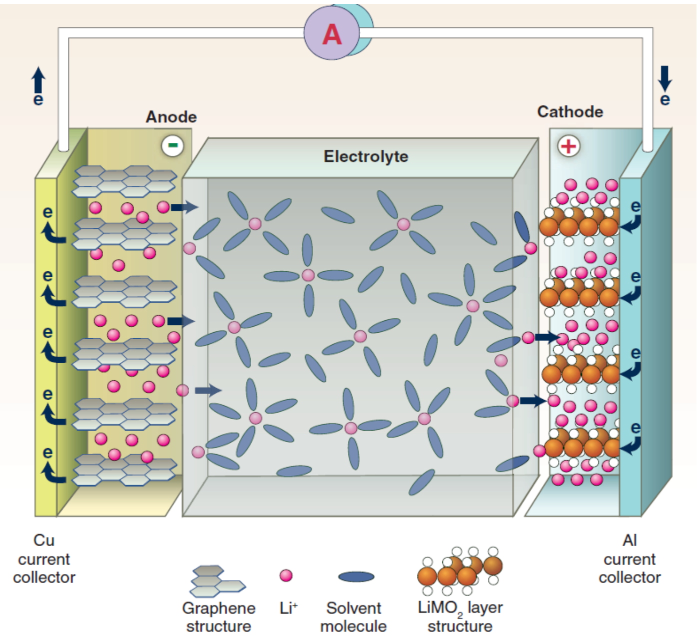

Figure 2-10. Schematic of a LIBs (Kraytsberg and Ein-Eli, 2012) © 2012 WILEY - VCH Verlag GmbH & Co. KGaA

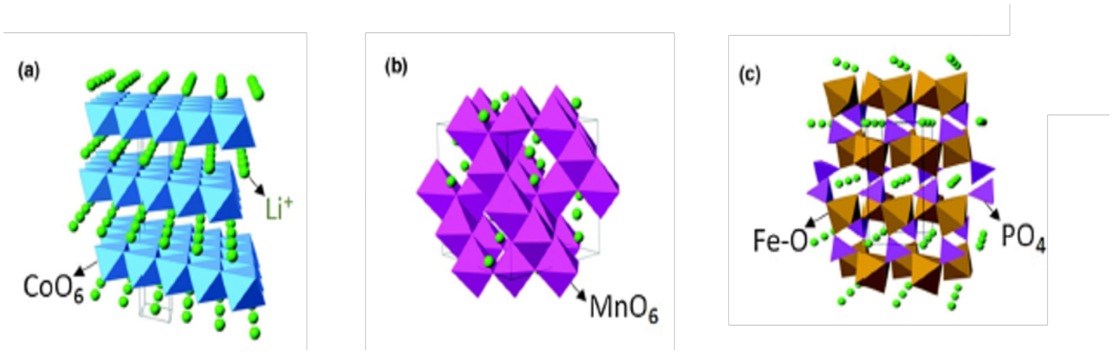

Figure 2-11. Crystal structures of (a) layered $LiCoO_2$; (b) spinel $LiMn_2O_4$; (c) olivine $LiFePO_4$(Nitta *et al*., 2015) © 2014 The Authors

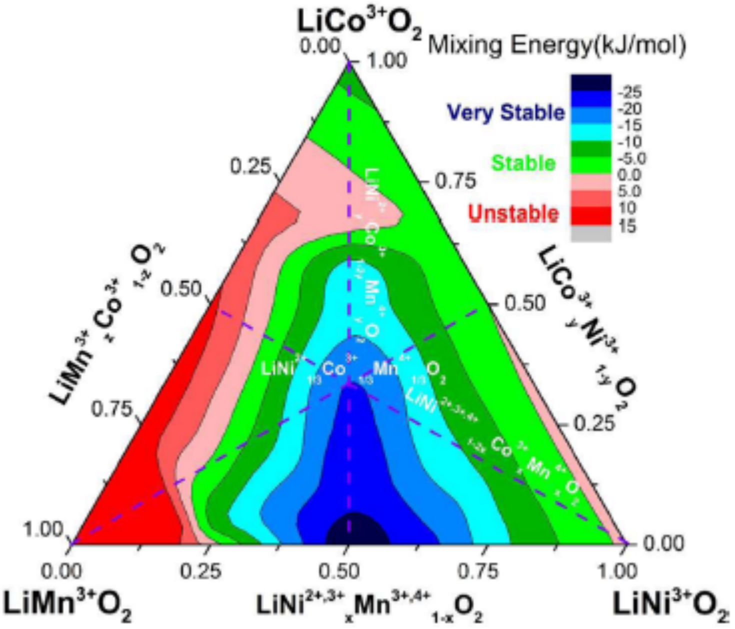

Figure 2-12. Mixing energy predicted from present bonding model for the solid solution $LiTMO_2$ (TM = Ni, Co, Mn) phase triangle (Liang *et al*., 2016) © 2016, American Chemical Society

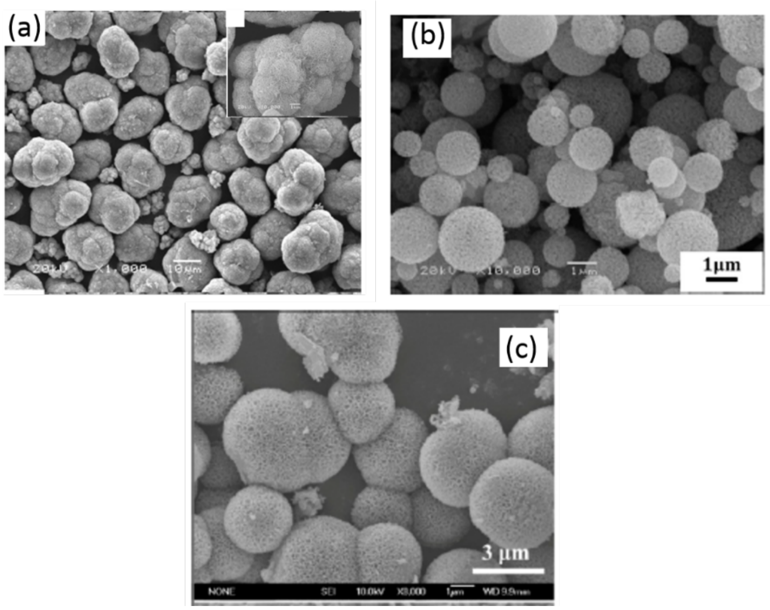

Figure 2-13. SEM images of (a) $Ni_{0.6}Co_{0.2}Mn_{0.2}(OH)_2$ precursors prepared by co-precipitation method; (b) $Ni_{0.6}Co_{0.2}Mn_{0.2}(OH)_2$ precursors prepared byultrasonic spray pyrolysis; (c)$Ni_{0.7}Co_{0.15}Mn_{0.15}(OH)_2$ precursors prepared by solvothermal method (Liang *et al*., 2014) © 2014 Elsevier Ltd. (Li *et al*., 2015b) © 2015 Elsevier B.V.

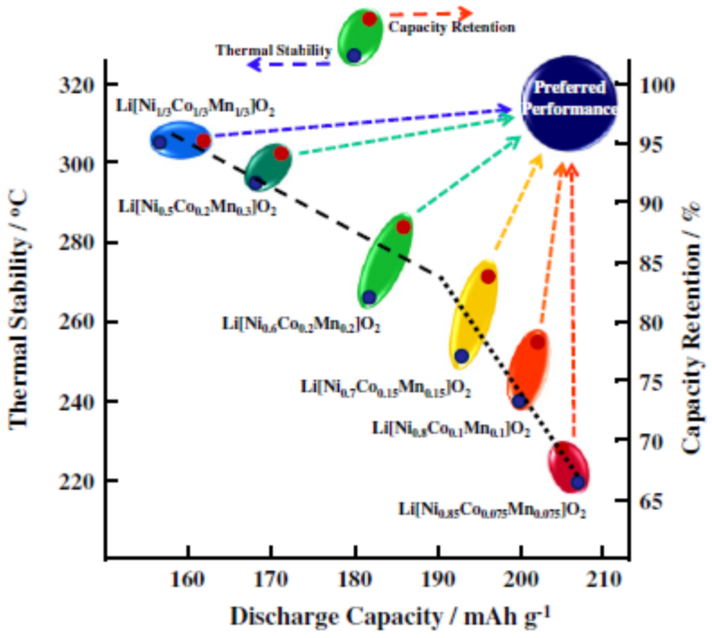

Figure 2-14. The relation between discharge capacity, thermal stability and capacity retention of $Li/Li(Ni_xCo_yMn_z)O_2$ (x=1/3, 0.5, 0.6, 0.7, 0.8, and 0.85) (Noh *et al*., 2013) © 2013 Elsevier B.V.

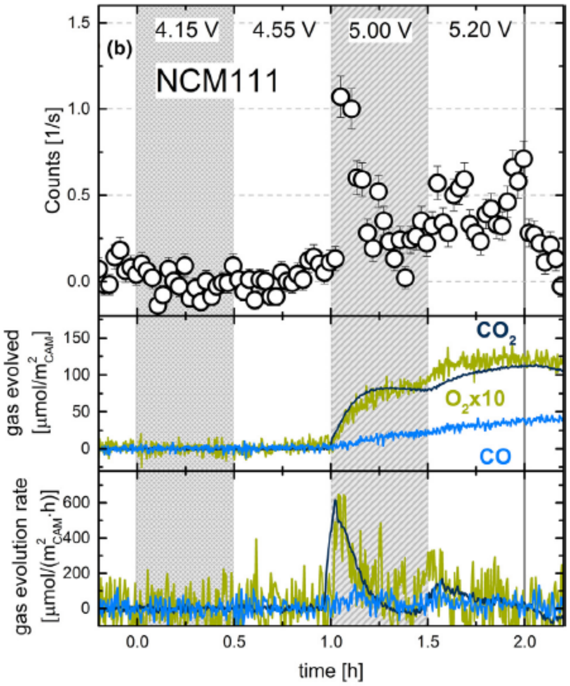

Figure 2-15. Middle panels shows the evaluation of O_2, CO_2, and CO measured by on-line electrochemical mass spectrometry (OEMS) (Wandt *et al.*, 2018) © 2018 Elsevier Ltd

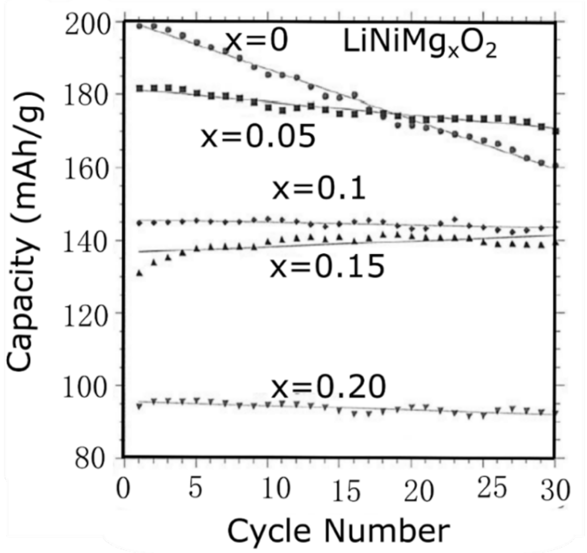

Figure 2-16. Plot of the capacity vs. cycle number of the first 30 cycles for the five synthesized compounds with different Mg cation additions (Chang *et al.*, 2000) © 2000 ECS - The Electrochemical Society

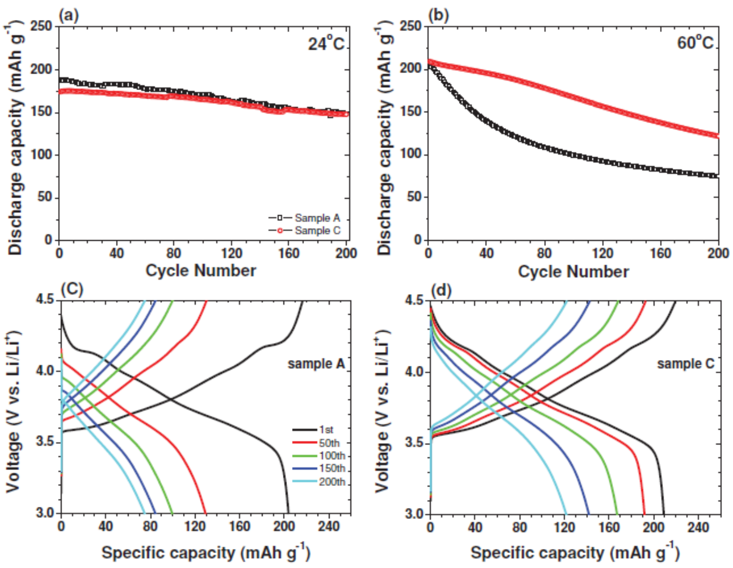

Figure 2-17. Plots of discharge capacity vs. cycle number of $LiNi_{0.89}Co_{0.11}O_2$ (black squares) and $LiNi_{0.81}Co_{0.1}Al_{0.09}O_2$ (red circles) at a) 24 °C and b) 60 °C at a rate of 1C. Corresponding voltage profiles for c) $LiNi_{0.89}Co_{0.11}O_2$ and d) $LiNi_{0.81}Co_{0.1}Al_{0.09}O_2$ at 60 °C measured after 1 st , 50 th , 100 th , 150 th , and 200 th cycles(Jo *et al*., 2014) © 2014 WILEY‐VCH Verlag GmbH & Co. KGaA

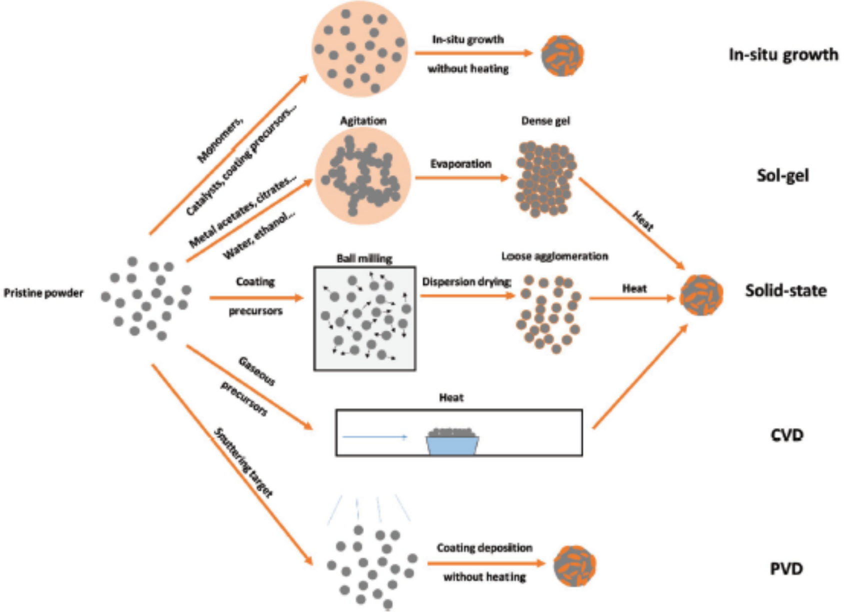

Figure 2-18. Schematic diagram summarizing conventional coating techniques (Kalluri *et al*., 2017) © 2018 WILEY-VCH Verlag GmbH & Co. KGaA, Weinheim

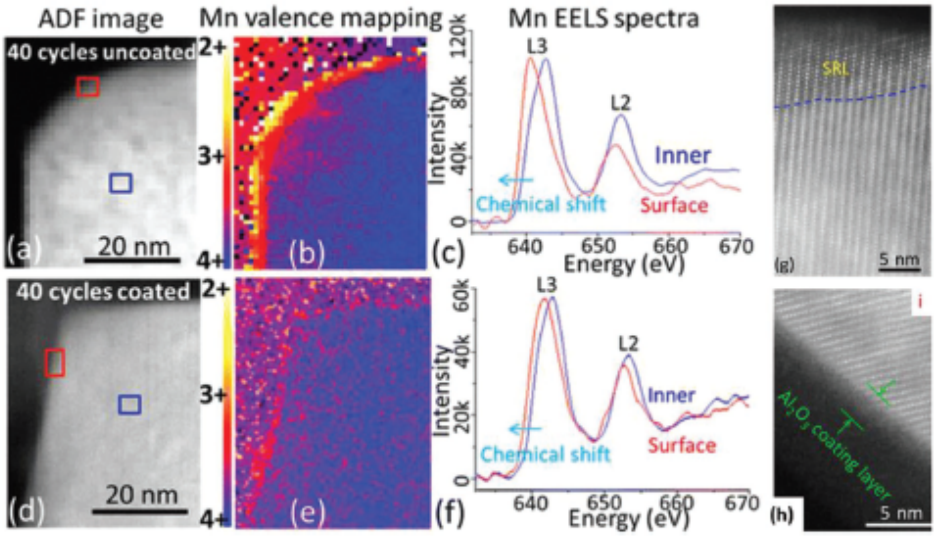

Figure 2-19. STEM-EELS study of $Li_{1.2}Ni_{0.2}Mn_{0.6}O_2$ and Al_2O_3 coated $Li_{1.2}Ni_{0.2}Mn_{0.6}O_2$ and their corresponding lattice images (Yan *et al*., 2015) © 2018 WILEY-VCH Verlag GmbH & Co. KGaA, Weinheim

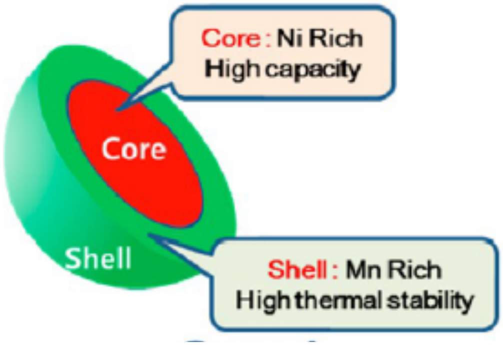

Figure 2-20. Schematic drawings of a core−shell structure(Myung *et al*., 2016) © 2017, American Chemical Society

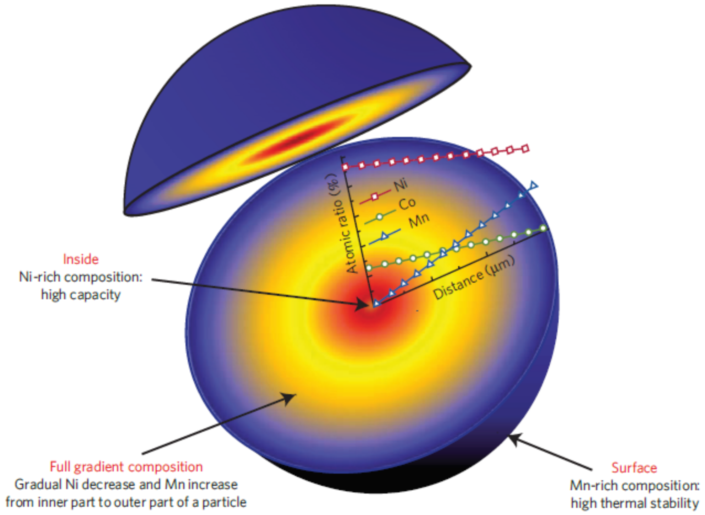

Figure 2-21. Schematic diagram of the FCG lithium transition-metal oxide particle (Sun *et al*., 2012) © 2012, Springer Nature

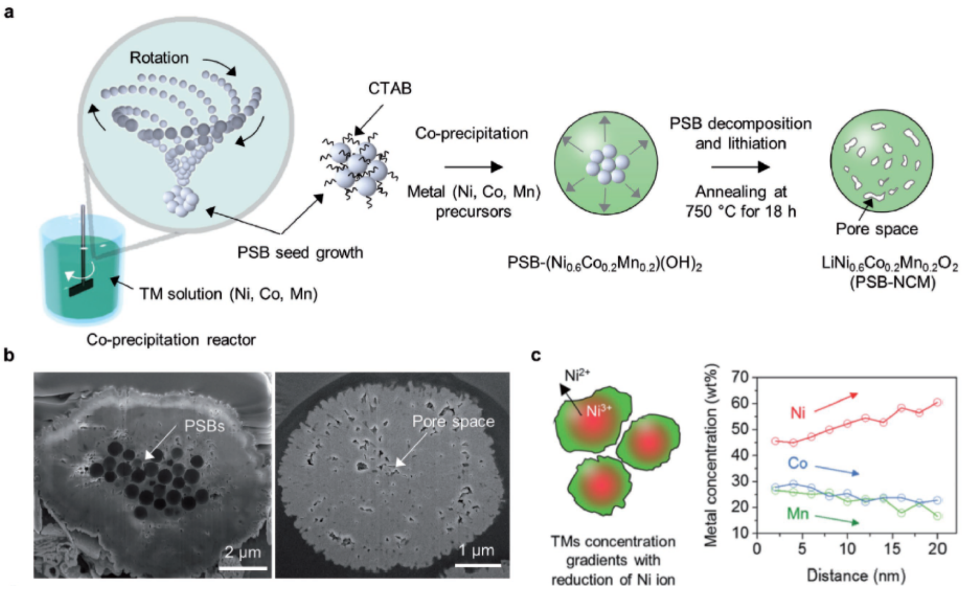

Figure 2-22. Porous nickel-rich cathode with self-induced concentration gradient. a) Schematic for the synthetic method for the PSB-NCM. b) Cross sectioned SEM images of the PSB-NCM before and after lithiation. c) Schematic of the primary particle of the PSB-NCM with its EDX result (Kim *et al*., 2017) © 2017 WILEY‐VCH Verlag GmbH & Co. KGaA

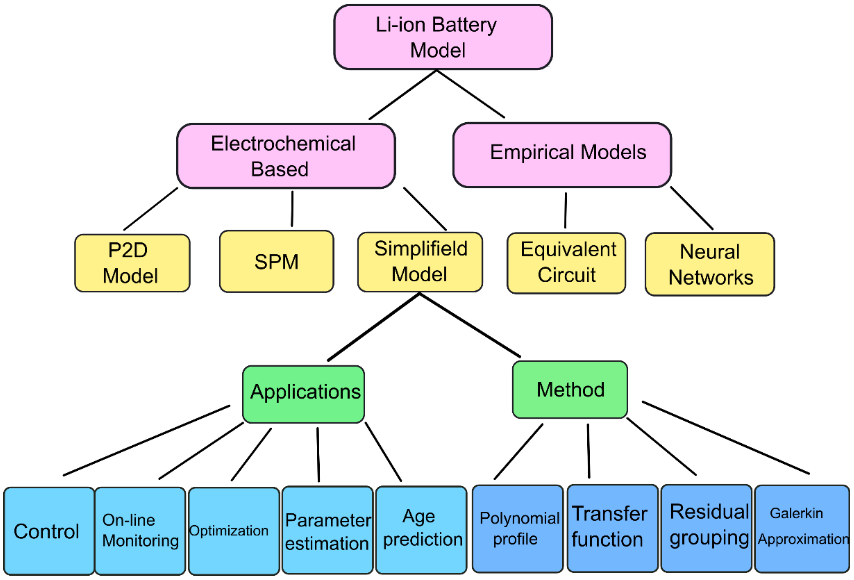

Figure 2-23. The general classification of Li-ion battery models

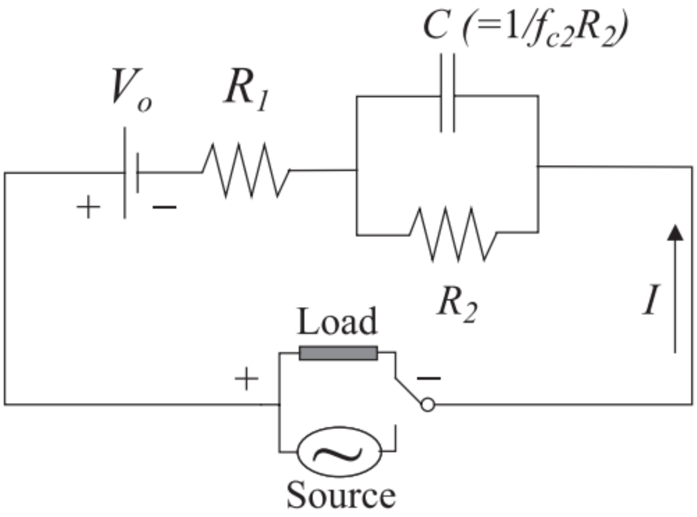

Figure 2-24. The equivalent circuit model (Bor Yann Liawa *et al*., 2004)

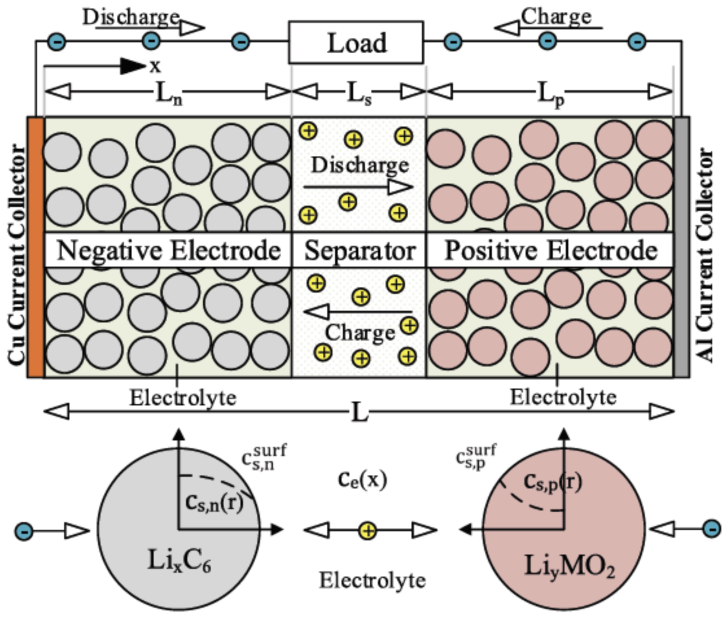

Figure 2-25. The Li-ion battery P2D model(Jokar *et al*., 2016) © 2016 Elsevier B.V.

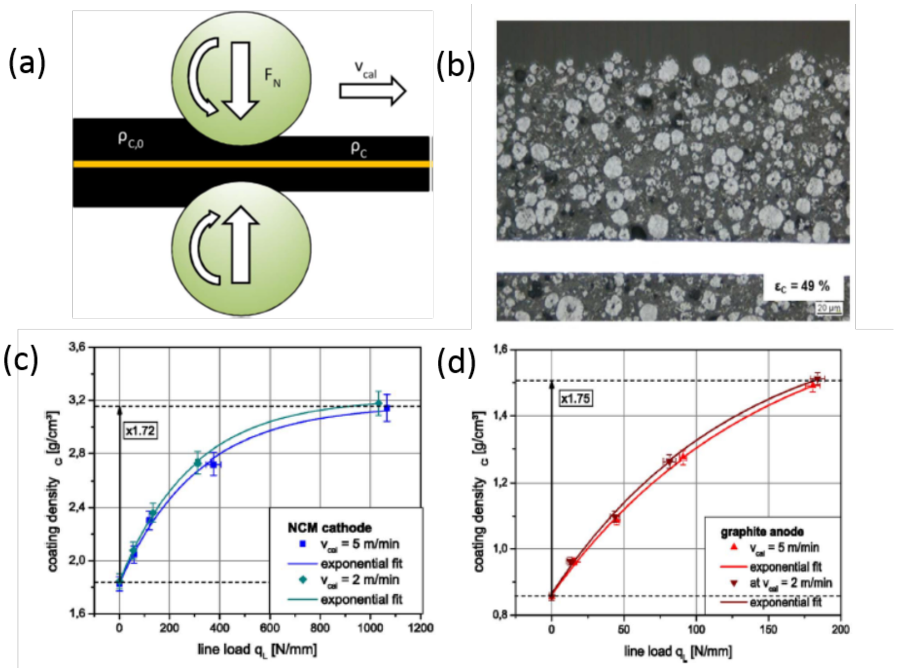

Figure 2-26. (a) Sketch of the calendering process; (b) SEM images of cross section of NCM cathode; (c) Increase of the coating density of NCM cathodes; (d) Increase of the coating density of graphite anodes(Meyer *et al*., 2017). © 2017 Elsevier B.V.

Tables

Table 2-1. The governing equation of P2D model (Xu and Wang, 2017)

Process	**Governing equations**	**Eq.**
Solid phase diffusion	$\frac{\partial C_s}{\partial t} = \frac{D_s}{r^2}\frac{\partial}{\partial r}(r^2\frac{\partial C_s}{\partial r})$	(2-9)
	$\varepsilon_l\frac{\partial c_l}{\partial t} = \frac{\partial}{\partial t}\left(D_l{\varepsilon_l}^{\beta}\frac{\partial c_l}{\partial x}\right) + \frac{1-t_+}{F}j_n$	(2-10)
Electrochemical reaction kinetic	$j_n = Fk_0c_l^{\alpha_a}(c_{s,max} - c_{s,surf})^{\alpha_a}c_{s,surf}^{\alpha_c}\left\{exp\left(\frac{\alpha_aF\eta}{RT}\right) - exp\left(\frac{-\alpha_cF\eta}{RT}\right)\right\}$	(2-11)
	$\eta = \varphi_s - \varphi_l - U_{eq} - j_nR_{film}$	(2-12)
Charge conservation		
	$i_s = \sigma_s\varepsilon_s^{\beta_s}\frac{\partial\varphi_s}{\partial x}$	(2-13)
	$i_l = k_{l,eff}\frac{\partial\varphi_l}{\partial x} + k_{D,eff}\frac{\partial lnc_l}{\partial x}$	(2-14)
	$k_{l,eff} = k_l\varepsilon_l^{\beta}$	(2-15)
	$k_{D,eff} = \frac{2RTk_{l,eff}}{F}(t_+ - 1)(1 + \frac{\partial lnf_{\pm}}{\partial c_l})$	(2-16)

Chapter 3

Preparation of Spherical-like $(Ni_{0.6}Co_{0.2}Mn_{0.2})(OH)_2$ Precursor Using a Lobed Taylor-Couette reactor: Effect of shear rate, Molar ratio of NH_3/MSO_4 and pH on Precursor Particle Size and Morphology

Summary

The proceeding literature review (Chapter 2) has clearly illustrated that the application of Taylor reactor is able to prepare the nickel-rich precursors with controllable size. This chapter will investigate the use of Taylor-Couette flow reactor with a lobed inner cylinder (LTC) to prepare $(Ni_{0.6}Co_{0.2}Mn_{0.2})(OH)_2$ hydroxide precursor with a uniform and spherical morphology. Effects of hydrodynamics and physico-chemical conditions on the agglomerate shape and sizes of the particles are investigated. It was found that a steady state is attained when the reaction time is about 3~4 times of the mean residence time. Changes in the morphology of precursors take place when the shear rate increases from 855 s^{-1} to 1707 s^{-1}, corresponding to the Reynolds number $Re=5.1\times10^3-2.1\times10^4$, where irregularly shaped agglomerate particles gradually change into spherical-like ones. Further increasing the shear rate results in the reduction in the particle size, likely attributing to the enhancement of the agglomeration and breakage process. The tap density 1.94 g cm^{-3} of sample particles were obtained through controlling the shear rate. It was also revealed that when the molar ratio of NH_3/MSO_4 increases from 0.2 to 0.8, the synthesized particles size increases. Beyond this ratio range, the particle size decreases, indicating the

influence of the chelating reaction by the level of supersaturation. The formation of spherical particles is also optimized by changing the pH from 11.4~11.6. As a result, a relation correlating turbulent energy dissipation rate and the molar ratio of NH_3/MSO_4 is proposed for estimation of the particle sizes.

3.1 Introduction

With increased demand for power consumption and the longer driving range of electric vehicles, the synthesis of $Ni_xCo_yMn_{1-x-y}(OH)_2$ precursor for Lithium cathode materials has become crucial for the realization of these requirements. Precursor materials having uniform properties and spherical-like shape is preferred due to its relatively high packing density and specific surface area that processes better electrochemical properties as a cathodic material (Thai *et al*., 2015; Kim *et al*., 2011). Co-precipitation process is a common method for the synthesis of $Ni_xCo_yMn_{1-x-y}(OH)_2$ precursor as this process has the features of simple operation and easy to realize mass production with relatively low cost. The process consists of several basic steps that include nucleation, growth, aggregation and break-up (Farahani *et al*., 2017). The nucleation and growth are closely related to local supersaturation of solution. The secondary process such as aggregation and break-up can be affected by the collision between particles and the shear stresses acting on the particle surfaces. While the particle aggregation is strongly influenced by the physico-chemical properties of the reaction and the hydrodynamics involved in the process, physico-chemical conditions, especially for chemical conditions, mainly refer to the interaction function of reagents. They are related to types and concentration of reagents, pH, temperature, pressure among others (Jung *et al*., 2010; Bubakova *et al*., 2013). Hydrodynamics is characterized by the shear taking place in the mixed volume and strongly depends on the type and geometry of the mixing devices (Sung *et al*., 2000, Richter *et al*., 2008), stirring shape and speed

(Torbacke and Rasmuson 2001). Controlling the flow dynamics of feed mixing will be beneficial to the control of the particle properties such as particle size, morphology and crystallinity, significantly influencing the quality of the final product (Aljishi *et al*., 2013). However, hydrodynamics in conventional stirred tank reactor (CSTR), usually characterized by the occurrence of turbulence, during the agglomeration process are chaotic accompanying by the fast kinetic precipitation. This makes very difficult to keep the size of synthesized precursors with a narrow distribution when applying the traditional bulk mode in the mixing. Consequently, the agglomerate size, size distribution and morphology of the synthesized particles are difficult to be predicted.

A Taylor–Couette (TC) reactor has typical flow features such as narrow shear rate distribution, the absence of high shear regions in comparison with CSTR reactor, limited flow patterns and easily adjusted mean residential time (Li *et al*., 2015). Various powders such as yttrium oxalate (Sung *et al*., 2000), $CaCO_3$(Kang *et al*., 2003), Ni-rich precursor and its derivative materials (Mayra and Kim, 2015; Thai *et al*., 2015; Kim and Kim, 2017) were synthesized by using the TC reactor. Kim et al synthesized a series of Ni-rich precursors ($(Ni_{0.90}Co_{0.05}\,Mn_{0.05})(OH)_2$) by using the traditional Taylor-Couette reactor, i.e the inner cylinder being circular and concentric. They found that the particle size of the precursor was influenced by those parameters such as rotational speed of the inner cylinder, mean residence time and concentration of NH_3H_2O solution. They have obtained the tap density of 2.13 g cm^{-3} of the agglomerates. They also studied the influence of gap size between the inner and outer cylinder of TC reactor on the particle size, as the gap will affect the fluid shear and stability of the Taylor vortices (Kim *et al*., 2011; Mayra and Kim, 2015). Although the use of TC reactors can achieve the notable improvement when comparing with the CSTR in terms of the broadness of shear rate distribution, they still suffer from several limitations. When the particles are involved in the two-phased systems in TC reactors, there is an accumulation of the dispersed phase in the regions of low velocities in those Taylor vortex cores, resulting in the mean residence time of dispersed phase longer than that of the continuous phase (Soos *et al*., 2007). Such segregation process is not desirable for practical synthesis of particles.

In order to prevent such segregation process, various methods have been attempted such as using eccentrically assembly of the inner cylinder, changing the rotational speed of both cylinders or utilizing a non-circular cross-section of the inner cylinder (Snyder, 1968; Lopez and Marques, 2002; Cole, 1967). It was revealed from these studies thata Taylor-Couette reactor with a lobed inner cylinder (LTC) can effectively reduce the formation of low shear rate region (Soos *et al*., 2007) and improve the mixing effect of intra-vortices. The shear flow and mixing effect in a Taylor-Couette reactor with variable cross-section inner cylinders have been investigated in the research group where the authors of the current work are based. The simulation results have indicated that the regions of low shear rate can be effectively reduced through changing the traditional inner cylinder to lobed inner cylinder (Li *et al*., 2015). Hence, it is believed that the adoption of the lobed TC reactor can effectively reduce the region of low velocities, producing the particles of $Ni_xCo_yMn_{1-x-y}(OH)_2$ precursor with narrow size distribution. In return, the electrochemical properties of the synthesized precursor particle materials can be improved. To the best of our knowledge, the synthesis of the $Ni_{0.6}Co_{0.2}Mn_{0.2}(OH)_2$ precursor (NCM622) by using the LTC reactor is not yet reported in the open literature. In the present work, an LTC reactor is utilized to synthesize NCM622 precursor of the Lithium cathode materials. The effects of different operating parameters such as the shear rate, molar ratio of NH_3/MSO_4, pH on the size, particle size distribution (PSD) and morphologies of particles are investigated. A correlation on predicting the particle size between turbulent energy dissipation rate and the molar ratio of NH_3/MSO_4 will be proposed.

3.2 Experimental

3.2.1 Synthesis Method

NCM622precursor was prepared by the co-precipitation method in the LTCreactor. The schematic diagram of the preparation apparatus is shown in Figure 3-1. The metal sulfate solution was prepared using $NiSO_4\cdot 6H_2O$ (>98%, Jinchuan Group co., LTD), $MnSO_4\cdot H_2O$ (>96%, Shanghai nanwei chemicals co., Ltd), $CoSO_4\cdot 7H_2O$ (>98%, Sinopharm Chemical Reagent Co., Ltd) as raw materials. The molar ratio of nickel sulfate, cobalt sulfate, and manganese sulfate in the feed solution was kept constant at 0.6:0.2:0.2 and its feed concentration was always fixed at 2 mol L^{-1}. 4 M of Sodium hydroxide (>96%, Tianjin zhiyuan chemicals co., Ltd) was used as hydroxyl reactant and a certain content of ammonia (25~28%, Sinopharm Chemical Reagent Co., Ltd) was used as chelating agent for crystallization of NCM622 precursor. All the reagents were in industry grade and were used without further purification. Before reaction, the LTC reactor was initially filled with distilled water and the reaction temperature was kept at 55°C. During the reaction, the metal sulfate solution, sodium hydroxide and ammonia were continuously injected using peristaltic pump through three ports located at the front axial part of the reactor. The mean residence time of aggregates or agglomerates was maintained to be 60 mins. After the reaction, the final precipitate was filtered using a vacuum pump and washed by distilled water several times until pH=7. The precipitate was then dried in a circulation oven at 80°C overnight. All the samples prepared at different conditions are listed in Table 3-1 and labelled as Pi (i=1, 2, 3,…,). Here, the suspension density ρ_L is approximately 1.1 g cm^{-3}, the change of the suspension density can be ignored as the suspension condition varies. The dynamic viscosity of the fluid, μ, is 0.003 Pa·S, giving the kinematic viscosity ν to be 2.73×10^{-6}.

3.2.2 LTC Reactor and Adopted Mixing Conditions

The LTC reactor is composed of two concentric cylinders, where the inner cylinder is rotated at different angular velocities ω and the outer cylinder is stationary. The volume of the reactor, V_{LTC}, is approximately 630 ml. The cross-section profile of the inner cylinder consists of three arcs that have the same radius R_1 (47.5 mm) and each is eccentrically offset from the axis, corresponding to 120°C. These arcs are connected tangentially by straight lines. The equivalent radius of the inner cylinder R_{eq} is defined and estimated by

$$R_{eq} = \frac{4A_1}{P_1} \tag{3-1}$$

where A_1 is the cross sectional area of the inner cylinder, and P_1 is the perimeter of the inner cylinder. R_{eq} is estimated 53.8 mm and the radius R_2 of the outer cylinder is 60 mm, which gives the equivalent gap width d of the reactor around 6.2 mm and the radius ratio of $\eta=R_{eq}/R_2=0.897$. The length L_{LTC} of the reactor is 160 mm. The LTC reactor is placed horizontally so that the effect of hydrostatic pressure can be disregarded. A servo motor was used to drive and control the rotation of the inner cylinder.

Following the previous studies on Taylor reactors, the flow regime in such reactor is characterized by the Reynolds number, defined by

$$Re = \frac{\omega R_{eq} d}{\nu} \tag{3-2}$$

Where ω is angular velocity, ν is the kinematic viscosity, and d is the gap width. The critical Reynold number (Re_c) can be estimated (Mayra and Kim, 2015):

$$Re_c = 41.2\left(\frac{d}{R_{eq}}\right)^{-0.5} + 27.2\left(\frac{d}{R_{eq}}\right)^{0.5} + 2.8\left(\frac{d}{R_{eq}}\right)^{1.5} \tag{3-3}$$

As the flow in the LTC reactor is likely turbulent based on the Reynolds number, the shear rate which dominates the particle motion can be evaluated by

$$G = \sqrt{\frac{\varepsilon}{\nu}} \tag{3-4}$$

The mean turbulent energy dissipation rate ε in the Taylor vortex flow is estimated using Eq. 3-5 (Mayra and Kim, 2015):

$$\langle\varepsilon\rangle = \frac{P}{\rho_L V_{LTC}} = \frac{\pi L_{LTC} R_{eq}^4 \omega^3 f}{V_{LTC}} \qquad (3\text{-}5)$$

where P is the power input to the reactor, which can be considered to be balanced the energy dissipation due to the turbulence. L_{LTC} and V_{LTC} are the axial length and volume of reactor respectively, f is the friction factor which can be estimated using the following relation:

$$f = 0.80Re^{-0.53}(\frac{d}{R_{eq}})^{0.35} \qquad (3\text{-}6)$$

The transition of flow regimes is experienced from Laminar Couette flow → Taylor vortex flow (TVF) → wavy vortex flow (WVF) → turbulent vortex flow → turbulence (Nemri *et al.*, 2013). These changes can be characterized according to the Reynold number ratio of $R = R_e/R_{ec}$.

As the flow regimes in the reactor in the current study are falling into the turbulent regime, the turbulent eddies that contribute to the dissipation can be characterized by the Kolmogorov length λ, which can be estimated based on the micromixing turbulent energy dissipation rate ε and the kinematic viscosity ν:

$$\lambda = (\frac{\nu^3}{\varepsilon})^{1/4} \qquad (3\text{-}7)$$

Table 3-2 lists the values of the shear rate, angular velocities, Reynolds numbers and Reynold number ratios and Kolmogorov length λ for the condition of the rotational speed varying from 100 to 1500 rpm. It is now generally accepted that when the Reynolds number ratio R is about 35, the flow regime changes from wavy vortex flow to turbulent vortex flow while R greater than 100 indicates the flow to be fully turbulence (Ehrl *et al*., 2010; Bubakova *et al*., 2013). As the rotational speed adopted is higher than 400 rpm (R=29.4) in the present study, the turbulent vortex flow should become dominant in most of the cases. Further increase in the rotational speed (greater than 1100 rpm, R=107.7), the flow regime will be fully turbulence.

3.2.3 Material Characterization

XRD analyses were conducted in a Bruker-AXS D8 advance powder diffractometer using Cu-Ka radiation (λ=1.5418 Å) and a power of 40 kv×20 Ma, where diffraction pattern was recorded in the range 2θ=10-80 ° with a step size of 0.01°. The morphologies of synthesized powders were measured by using SEM produced from ZEISS ZIGMA 174C CZ. A particle size analyser (Bettersize 2000 Intelligent Laser Particle Size Analyzer, Bettersize instruments Ltd.) was used to determine the particle size and size distribution of aggregates. The typical particle sizes are labelled as D_{10}, D_{50} and D_{90}, respectively. D_{10} is the diameter at which 10% of the sample particles have smaller particles than this diameter while D_{50}, known as “mass median diameter”, is the diameter which divides the sample particles greater or smaller than this diameter. D_{90} is also defined in the same way. In our system, the size of D_{90} is used to approximate the largest agglomerate size that can be obtained. ICP-MS (NexiON 300X) was used to confirm the metal compositions of

NCM622 precursors. The tap density of particles was measured by putting a known mass of powder in a vertical tube and tapping for 15 mins on a lab bench. The volume after tapping the powder was determined and the tap density was calculated. Each measurement has been reproduced three times.

3.3 Results and Discussion

3.3.1 Effect of Shear Rate on Particle Size, Size Distribution and Morphology

Figure 3-2 shows the transient behaviour of agglomeration process affected by the shear rate. It has been recognized that the crystal nucleation and growth process directly depend on the supersaturation in solution. At the beginning of the reaction, the high local concentration of solution results in a high supersaturation, in which small primary particles are formed (Jung et al., 2000). These primary particles tend to form large aggregates but they are experiencing the local shear caused by turbulent eddies with Kolmogorov length scales. Once the crystal growth is curbed by the shear acting on the particles, the sizes of aggregates, for example, characterized by D_{90}, may gradually decrease until a relatively constant size is achieved. In our system, it was found that a steady state is approached when the reaction time is about 3-4 times of the mean residence time. The time needed for the particle to reach a steady size seems to be dependent on the shear rate. As shown in Figure 3-2, the particle size becomes stable after the test was carried out four hours for cases P5 (shear rate of 1707 s^{-1}) and P7 (2983 s^{-1}). While for case P9 (4376 s^{-1}), the size of the particle becomes stable after three hours. This may be attributed to the fact that higher shear rate can promote the mass transfer and is beneficial to the molecular growth but the strong shear action can also rip off the materials from the particle surface. This can be evidenced by the reduction of the time for the particle to reach its stable size. When the shear rate increases from 1707 s^{-1} to 4376 s^{-1}, the final size of the particles decreases. This observation is also in agreement with Kim's et al study (Thai et al., 2015). The particle size and the morphology of NCM622 precursors prepared by LTC reactor depend strongly on the fluid dynamic conditions. The shear rate in the LTC could influence particle size and affect the formation of spherical particles.

One of the hydrodynamics features for the LTC reactor is that Taylor vortices in the reactor are undergoing the deformation, the vortices in circumferential direction changes, which enhances the turbulent kinetic energy generation and turbulent energy dissipation but reduces the regions of low Reynolds shear stresses. Consequently, this allows the particles to undergo an environment with a slightly high shear rate but more uniform distribution on shear rates, being beneficial to the synthesis of particles (Li *et al*., 2015). The morphology of NCM622 prepared at different shear rates by the LTC reactor is characterized by using the SEM as shown in Figure 3-3. When the samples were prepared at the shear rate of 855 s^{-1} (shown in Figure 3-3a), the size of the particle is relatively large and the shape is irregular. When the shear rate increases to 1127 s^{-1}, the particle (shown in Figure 3-3b) has the tendency of evolutions into spherical-like morphology although their surfaces look loose. Further increase in the shear rates greater than 1707 s^{-1} (Figures 3-3c-g), the particles tend to be much more spherical-like and compact. The morphology changes can be related to the changes in flow regimes during the hydrodynamic process which is characterized by different shear rates. As mentioned earlier, Taylor vortex flow appears in the LTC reactor when the shear rate is higher than 855 s^{-1} as listed in Table 3-2. Further increasing the shear rate to 1707 s^{-1}, the collisions among crystals will be intensified. When the shear rate is greater than 2328 s^{-1}, the flow regime has changed from typical Taylor vortex flow to turbulent Taylor vortex flow, which will further enhance collisions among crystals. With increasing shear induced by turbulent eddies, very fine particles are detached or re-dispersed by the rip off of the formed agglomerate surface, thus a spherical-like shape of the particle can be formed. This phenomenon can also be explained in more detail by the hydrodynamics (CFD results) in the reactor with a lobbed inner cylinder. Figure 3-4 shows the turbulent kinetic energy and turbulent energy dissipation distributions in the cutting cross-section of the lobbed inner cylinder. It becomes clear that the high turbulent kinetic energy generation occurs just behind the smallest gap along the perimeter of the inner cylinder. This turbulent kinetic energy generation is due to a sudden expansion with a moving surface (counted from the location of the smallest gap where a time-dependent separation vortex takes place. As a result, the enhanced turbulence can be observed. Such enhanced turbulence will push the particles move towards the core of the Taylor vortices and benefit for the agglomeration process during the preparation. Furthermore, there is no a remarkable difference in the mean shear rate increase for different rotational speeds as shown in Figures 3-4a-d. Turbulent energy dissipation shown in

Figure 3-4 is also significantly enhanced in the vicinity of the lobed inner cylinder.

The XRD patterns of NCM622precursors are displayed in Figure 3-3h. It can be seen from the figure that the precursor is similar to the typical spectrum of $Ni(OH)_2$ (PDF # 14-0117). All the diffraction lines are indexed to a hexagonal structure with a space group of $P\overline{3}m1$.The crystal lattice parameters of the layered are calculated. The calculated unit cell parameters for P1 are $\boldsymbol{a}$ = 3.1293 **Å,** $\boldsymbol{c}$= 4.5851 **Å.** Similarly, the corresponding peaks of NCM622 powder particles for different shear rates are almost the same as those of P1 but a small shift in peaks towards the right side of the spectrum is observed for the case of P1 compared to the standard powder, which may indicate a small crystalline size is obtained in the present study.

The crystalline size of particles (shown in Table 3-3) is calculated by using the Debye-Scherrer's formula,

$$D_g = \frac{\mathrm{K}\lambda'}{\beta cos\theta} \tag{3-8}$$

where D_g is the grain size, K is a constant equal to 0.89, λ' is the wavelength of the X-ray radiation (1.5418Å), β is the full width half maximum and θ is the angle of diffraction. To estimate the mean particle size, four peaks with high intensities have been used for each calculation. It can be concluded that all the crystalline sizes estimated are in the range of 10-13 nm and increasing the shear rate has no significant impact on the mean crystallite size.

It has been recognized that the particle size distribution may change significantly with the reactor configurations and the mixing intensity generated in the reactors, characterized by the overall macro and micro-mixing (Kang et al., 2003). Figure 3-5 presents particle size distribution (PSD) at a low shear rate as shown in Figure 3-5a and high shear rate (Figure 3-5b). The particles have a broad size distribution when the shear rate of 154 s^{-1} is applied while such distribution becomes narrow when the shear rate increases from 154 s^{-1} to 1127s^{-1}. When the shear rate is in the range of 1707 and 2328 s^{-1}, the PSD was found to have little change as can be seen from Figure 3-4b. Further increase of the shear rate from 2983 s^{-1} to 4376 s^{-1}, the particle size was found to have narrow distribution and particle size scattering decreases. The narrowest PSD is obtained when the shear rate of 4376 s^{-1} is applied.

The effect of the shear rate on particle size when the preparation attains the steady during experiments can be inferred from Figure 3-6. The size change in D_{10}, D_{50} and D_{90} as a function of the shear rate looks very similar. When the shear rate is 154 s^{-1}, the aggregated particle is large and this may be attributed to the low collision rate at the low shear rate, resulting in a loose aggregation. When the shear rate increases from 154 s^{-1} to 1127 s^{-1}, particle break-up may surpass aggregation due to the enhanced shear, thus causing the size of the particle to decrease. This can be seen from Figures 3-3a and 3-3b. However, the aggregated particle becomes irregular in shapes and the particles are likely to change into smaller compact pieces of the aggregates. When the shear rate further increases from 1127 s^{-1} to 1707 s^{-1}, the aggregated particle size increases again. An explanation is that the process of formation of particles has very likely evolved from aggregation into agglomeration because a very strong shear weakens aggregation. In contrast, the formed particle looks loose from the SEM images as shown in Figure 3-3c at a low shear rate as the aggregation is the main mechanism for the formation of particles. With significant increase in the shear rate, the particles tend to be more compact but accompanied by size decrease.

In general, the precipitation involves a series of simultaneous and rapid reaction processes. These rapid reaction processes include the formation of primary particles caused by nucleation. When these primary particles aggregate due to the collision and shear action in the mixing taking place in the TC reactor, the macromixing may be mainly affected by the Taylor vortices while the aggregated particles will strongly interact with the turbulent eddies that have the Kolmogorov length scale with a very short typical time scale. According to the study of Baldyga and Bourne (Bałdyga and Bourne, 1984; Bałdyga *et al.*, 1995), the micromixing process is supposed to be dominated by the engulfment caused by eddy entrapping where the reactants are engulfed and the mass transfer can encourage the aggregation when the Schmidt number, Sc, is smaller than 4000. Based on the Schmidt number, Sc, definition:

$$\mathrm{S}_C = \frac{\nu}{D} \tag{3-9}$$

we can estimate the diffusion coefficient of $NiCl_2$ solution with $D(NiCl_2)= 2.44\times10^{-9}\ m^2\ s^{-1}$ so that the corresponding Sc can be calculated (Salmoni *et al.*, 1987). It was found that the calculated Sc is 1120. Thus, an engulfment-deformation-diffusion (EDD) model can be used to estimate the characteristic time t_m for micromixing, interpreted as unsteady molecular diffusion by engulfment of the turbulent eddies. The characteristic incorporation time for aggregated particles can be related to the local rate of turbulent energy dissipation ε and the kinematic viscosity *v*, given by

$$t_m \approx 12(\nu/\varepsilon)^{1/2} \tag{3-10}$$

Such typical micromixing times were reported to be 3–40 ms in stirred tanks and about 8 ms in centrifugal pumps (Carpenter, 2001) and 6-8 ms for the TC reactor with a chemical reaction system (Judat *et al.*, 2004). Figure 3-6 shows the calculated micromixing time as a function of the shear rate in our current study. As the shear rate increases, the micromixing time exhibits a tendency of exponential decrease. The micromixing time of 77 ms at the shear rate of 154 s^{-1} reduces to 7 ms at the shear rate of 1707 s^{-1}. The micromixing time changes slightly with a further increase in the shear rate ranging from 1707 s^{-1} to 4376 s^{-1}. Consequently, the change of particle size is not remarkable. LTC reactor can have improved micromixing characteristics due to the intensification of the turbulence as this will further reduce the dissipation eddy size and reduce the micro-mixing time.

The above phenomena can be further interpreted here. On micromixing, the reactants contact at a molecular scale while a continuous crystallization process is still going on in LTC reactor. Small primary particles produced by nucleation and growth are entrapped inside of eddies through the engulfment of solutions at the Kolmogorov length scale. As shown in Table 3-2, the Kolmogorov length scale λ decreases as an increase of the shear rate. At the high shear rate, the size of Kolmogorov scale eddies decreases, which may benefit the increase of the surface contact area of materials with these eddies (Baldyga *et al.*, 1995). The particles experience a series of processes that can be described nuclei generation in the turbulent eddies following by a secondary transport process in the Taylor vortices where the particles are further undergoing aggregation, breakage, ageing and ripening (Cafiero *et al.*, 2002). As shown in Table 3-2, the shear rate is enhanced with the increase of rotational speed. As a result, the strong shear rate suppresses the aggregation of small particles, resulting in the particle size to be more uniform.

The tap density of the particles prepared at a different shear rate is shown in Figure 3-7. The tap density of the particles at low shear rates of 154 ~ 1127 s^{-1} is in the range of 0.93 ~ 1.32 g cm^{-3}. With an increase in the shear rate from 1707 s^{-1} to 3668 s^{-1}, the particles become spherical and tap density slightly increases from 1.86 g cm^{-3} to 1.94 g cm^{-3} as the particle gets more compact. On the contrary, when the shear rate further increases to 4376 s^{-1}, the tap density decreases to 1.79 g cm^{-3}.

3.3.2 Effect of Molar Ratio of NH_3/MSO_4 on Particle Size, Size Distribution and Morphology

NH_3H_2O concentration or the molar ratio of NH_3/MSO_4 is one of the critical factors for the formation of spherical NCM series hydroxide particles as it is closely related to the supersaturation (Liang *et al.*, 2014; Cheralathan *et al.*, 2010). NH_3H_2O acts as a chelating agent for the metal hydroxide reaction and provides a slow supply of supersaturation after the initial nucleation of particles when compared to the fast and direct reaction of the metal sulphate with sodium hydroxide. The general reaction scheme of a metal hydroxide is suggested for the present study as follows:

$$\mathrm{M^{2+}} + m\mathrm{NH_3} \rightarrow [\mathrm{M(NH_3)}_m]^{2+} \tag{3-11}$$

$$[\mathrm{M(NH_3)}_m]^{2+} + 2\mathrm{OH^-} \Leftrightarrow \mathrm{M(OH)_2} + \mathrm{mNH_3} \tag{3-12}$$

$$\text{Whole reaction: } \mathrm{M^{2+}} + 2\mathrm{OH^-} \Leftrightarrow \mathrm{M(OH)_2} \tag{3-13}$$

where M^{2+} represents the metal ion of nickel, cobalt and manganese.

As reported in previous studies, an attempt was tried to control the particle size and shape of the precursors by varying the amount of NH_4OH. In order to synthesize homogenously mixed ternary spherical-like precursor, the different molar ratio of NH_3/MSO_4 was used in our experiments. Figure 3-8 shows the effect of the molar ratio of NH_3/MSO_4 on the particle size of NCM622 precursor. It can be seen that the sizes of NCM622 precursor increase as the molar ratio of NH_3/MSO_4 increases from 0.2 to 0.8. When the molar ratio of NH_3/MSO_4 is 0.2, the particles characterised by D_{10}, D_{50}, D_{90} sizes are 0.85, 1.92 and 3.64 μm, respectively. While the molar ratio of NH_3/MSO_4 is 0.8, the sizes of D_{10}, D_{50}, D_{90} are 3.03, 5.45 and 8.5 μm. This can be interpreted from the chemical reaction rate, evaluated by:

$$\mathrm{r} = \mathrm{k}[\mathrm{M}^{2+}][\mathrm{NH}_3]^{m} \quad (\mathrm{m}=1\sim6) \tag{3-14}$$

As the molar ratio of NH_3/MSO_4 increases from 0.2 to 0.8, the chemical reaction rate of forming $[\mathrm{M}(\mathrm{NH}_3)_m]^{2+}$ increases. As can be seen from equations (3-11) and (3-12), ammoniac mixed transition metal-ligand will be formed first. This ligand is usually unstable and will react with alkaline to form the final precursor. As the chemical reaction rate of NH_3/MSO_4 increases, more $[\mathrm{M}(\mathrm{NH}_3)_m]^{2+}$ ligand will convert to form the precursor. This gives rise to the number of precursors in a given time with increase in the particle size. As the molar ratio of NH_3/MSO_4 is further increased to 1, the particle size starts to decrease. This indicates that the ability of $[\mathrm{M}(\mathrm{NH}_3)_m]^{2+}$ ligand transforming to final precursor is limited. A certain amount of M^{2+} will in the form of $[\mathrm{M}(\mathrm{NH}_3)_m]^{2+}$ and leads to the incomplete precipitation.

SEM images of NCM622 precursor prepared at a different molar ratio of NH_3/MSO_4 are shown in Figure 3-9. The precursor prepared at a molar ratio of 0.2 (see Figure 3-9a) consists of small primary particles and looks irregular. Other precursors prepared at the molar ratio of 0.4, 0.6, 0.8 and 1.0 have good integrity and sphericity. However, cracks can be observed on the particles for the case of the molar ratio of NH_3/MSO_4 of 0.8 and 1 as shown in Figure 9d and 9e. These observations demonstrate that the presence of ammonia plays an important role in promoting the formation of dense spherical precursors. As the small-sized secondary precursors are produced by the agglomeration of primary particles through their Brownian motion. They experience a series of nucleation and growth, agglomeration, breakup and ripening (Park *et al*., 2008). It is also speculated that the high shear rate produced by Taylor vortices in the LTC reactor effectively promotes the collision among the particles but the hydrotalcite-like compounds have lower integrity of particles compared with carbonate co-precipitation precursor (Zhang *et al*., 2010). This causes the precursors produced with a high molar ratio of NH_3/MSO_4 easily to form cracks.

3.3.3 Effect of pH on Particle Size, Size Distribution and Morphology

For the synthesis of homogenously mixed precursor materials, pH is the other essential parameter to affect the final product as Ni, Co, Mn participated for precipitation have different solubility, in particular, Ni ions prefer a high pH to form the complex while Co and Mn ions require a low pH. Thus, the optimal pH value taken in precipitation to form spherical-like particles will be different according to their concentration ratio. For example, for $Ni_{1/3}Co_{1/3}Mn_{1/3}(OH)_2$ (NCM 333) particles and $Ni_{0.5}Co_{0.2}Mn_{0.3}(OH)_2$ (NCM 523), the optimal pH value was found to around 11.0. For a high composition of Ni-rich hydroxide $Ni_{0.9}Co_{0.05}Mn_{0.05}(OH)_2$ (NCM 955), the optimal pH value is usually at 12.0 (Thai *et al*., 2015, Noh and Cho, 2012). Figure 3-10a shows the particle size and size distribution of NCM622 precursors prepared at three different pH values. It was found that a uniform particle distribution when the pH falls into the ranges of 11.0~11.2 and 11.4~11.6. While pH at 10.0~10.5 and 12.2~12.5 will yield narrower particle size distributions compared with the other two examples. When pH is in the range of 12.2~12.5, two dispersed peaks were observed to take place in the particle size distribution, indicating that the particle size for the condition that particles are prepared at high pH value exhibits two modes of strong aggregation. The data for $D_{10}/D_{50}/D_{90}$ of NCM622 precursors obtained when the preparation attains steady state are shown in Figure 3-10b. It was found that when pH changes from 11.0~11.2 to 11.4~11.6, the measured D_{50} has almost the same value of 3.50 μm but the measured D_{10} decreases from 1.79 to 0.85 μm while D_{90} increases from 5.58 to 6.08 μm. This indicates that an increase in the pH within a certain range can result in a decrease in the particle size as more small aggregates are formed. For lower pH values of 10.0~10.5 and 12.2 ~12.5, the particle size measured by $D_{10}/D_{50}/D_{90}$ is 0.55, 1.26 and 2.26μm, and 0.51, 1.08 and 2.03μm, respectively.

The SEM images of NCM622 precursor prepared at different pH are shown in Figure 3-11. For samples of P14 and P16 (See Figures 3-11a and 3-11b), the shapes of the secondary particle are irregular, indicating the conditions of low pH and high pH not suitable for producing spherical-like particles. When the pH is in the range of 11.0~11.6, the shape of particles exhibits the form of quasi-spherical like morphology. The metal compositions of NCM622 precursors are also confirmed by the use of ICP-MS analysis. It was found that metal composition of the precursor is well consistent with the composition ratio of 0.6:0.2:0.2 (Ni:Co:Mn) when pH is in the range of 11.4~11.6 as can be seen from Table 4. Thus, it can be concluded that the range of pH used for the preparation of NCM622 precursor should be 11.4~11.6.

3.3.4 Prediction of Particle Size

The formation of NCM precursor is a typical precipitation and crystallization process. During precipitation, the aggregate particles may break up due to particle collision and then re-dispersion under the action of turbulent shear to form the agglomerates. Although all the steps have an effect on the final crystal size and size distribution, crystal nucleation only takes place in a short time and produce large quantities of small primary grains. The XRD results analyzed in the preceding section have shown that increasing the shear rate has no significant impact on the mean crystallite size. Thus, we only consider the aggregate size change in our system to be mainly influenced by aggregation and break-up process.

If the aggregation process is dominated by particle collision and adhesion, it can be speculated that the breakage process is mainly caused by turbulent shear force so that the aggregation and breakage rates will be closely related to the turbulent energy dissipation (Sung *et al.*, 2000), which can be described by

$$K_{agg} \propto \varepsilon^{1/2} \tag{3-15}$$

$$K_{break} \propto \varepsilon \tag{3-16}$$

The net rate of the agglomerate size can be expressed as the sum of the particle aggregation and breakage rates, given by

$$\frac{\mathrm{dL}}{\mathrm{d}t} = k_1\varepsilon^{1/2} - k_2\varepsilon \tag{3-17}$$

Camp and Stein (1943) also proposed that the aggregation rate K_{agg} is proportional to the square root of the mean energy dissipation. It should be noted here that relations (3-15) to (3-17) did not account for any effects of supersaturation on the precipitation process. In fact, supersaturation σ is an important factor to affect the formation of the crystals in precipitation reaction as indicated in the classical nucleation theory. Considering the effects of supersaturation and power input, Rudolf *et al*. (2000) have modelled the final size of calcium oxalate by correlating turbulent energy dissipation and supersaturation. In their experiment, the agglomerate rate was found to be expressed as:

$$K_{agg} = (k_1 + k_2\varepsilon^{1/2} - k_3\varepsilon)\sigma^2 \tag{3-18}$$

They also provided the estimation for breakage rate, given by

$$K_{break} = k_4\varepsilon\sigma^{-2} \tag{3-19}$$

According to Parker et al. (1971) and Jarvis et al. (2005), the agglomerate particle size (d_{max}) can be estimated in terms of the average shear rate of the fluid motion (G), given by

$$d_{max} = CG^{-s} \tag{3-20}$$

where C is the particle strength coefficient and s is the stable particle size exponent, both of which are related to the physical properties of the materials.

As the LTC reactor has specific flow patterns, i.e Taylor vortices, the growth process of particles will be directly affected by both the shear due to Taylor vortices and the turbulent eddies embedded in Taylor vortices during the operation of the LTC reactor. Particles formed by agglomeration are continuously under the action of materials removed by the local shear due to the particle interaction with the turbulent eddies in the collision process. We can argue that the shear rate directly affects the aggregation process of particle more than it does for the breakage process. It is thus assumed that the net rate of the agglomerate size (D_{50}) can be expressed as the joint contributions from the particle aggregation and supersaturation σ, or

$$D_{50} = k_1 G^{-k_2} \sigma^{k_3} \tag{3-21}$$

In equation (3-21), $D_{50,}$ a mass median diameter, is the diameter at which 50% of a sample's mass is comprised of smaller particles. It is used to represent our typical size of particles. k_1 is the particle strength coefficient andk_2 is the stable particle size exponent mentioned by Parker et al. k_3 is the kinetic order of supersaturation.

The supersaturation is mainly related to the concentrations of NH_3H_2O. As briefly discussed in section 3.3.2, when the concentration of NH_3H_2O is low, chelation of NH_3H_2O is quite weak and the combination between NH_3H_2O and metal sulfate ions may be also weak, which results in the effective control of co-precipitation reaction to being difficult and the supersaturation of reaction and the nucleation rate becomes large. As a result, the supersaturation of reaction decreases and the growth rate of crystal increases as the concentration of NH_3H_2O increases. Consequently, the shapes of the produced precursor become irregular. When the concentration of NH_3H_2O is too high, the nickel ions are dissolved out into the ammonia solutions again. This indicates that there exists a proper supersaturation for the formation of the NCM622 precursor. The supersaturation σ based on the molar ratio of NH_3/MSO_4 (n) should be accounted for in our case, i.e

$$\sigma = k_4 n^{-k_5} \tag{3-22}$$

The detailed calculation is shown in Appendix A. Based on these considerations, the typical particle size (D_{50}) can be predicted by using the following relation

$$D_{50} = T_1 \varepsilon^{-T_2} \mathrm{n}^{T_3} \tag{3-23}$$

Where T_1 is the particle strength coefficient, T_2 is the stable particle size exponent related to materials and T_3 is kinetic order of supersaturation.

The estimated D_{50} as the function of turbulent energy dissipation ε and the molar ration and our experimental data are shown in Figure 3-12. It can be seen from the figure that the proposed correlation (equation (3-24)) for prediction of agglomerate size (D_{50}) based on turbulent energy dissipation and molar ratio of NH_3/MSO_4 is in the range of the experimental data.

$$D_{50} = 9.08 \varepsilon^{-0.178} \mathrm{n}^{0.4} \tag{3-24}$$

With caution, it is considered that the relation given by equation (3-24) is reliable for evaluation of particle size when the turbulent energy dissipation and the molar ratio of NH_3/MSO_4 are obtainable.

3.4 Conclusions

The $Ni_{0.6}Co_{0.2}Mn_{0.2}(OH)_2$ precursor has been prepared using the LTC reactor. The size and morphology of the prepared particles are controlled through modulating the shear rate, the molar ratio of NH_3/MSO_4 and pH. The current has demonstrated that an effective method for realisation of controllable preparation of the particle size and spherical-like precursors used as Lithium cathode material is feasible, which may be beneficial to the improvement of the electrochemical properties of the precursor materials. The conclusions reached as the results of the current study are as follows:

(1) It was found that the particle size decreases with increasing the shear rate. It was observed that the particle size increases when aggregation changes into agglomeration, corresponding to a lower shear rate being changed to higher shear rate.

(2) The micromixing in the LTC reactor can be intensified with increasing the local shear rate, which can be realized by adjusting the lobed inner cylinder rotational speed. Consequently, the morphology of particle also changes from irregular to spherical-like and synthesized particles become compact at a high shear rate.

(3) The particle size and size distribution are also influenced by the molar ratio of NH_3/MSO_4. NH_3H_2O, a chelating agent in the reaction, can provide a slow supply of supersaturation during the co-precipitation process. An appropriate molar ratio of NH_3/MSO_4 (0.4~1) would be desirable for getting spherical precursors.

(4) A correlation between turbulent energy dissipation and the molar ratio of NH_3/MSO_4 is proposed and it can be provided for estimation of the synthesised particle size.

References

ALJISHI, M. F., RUO, A.C., PARK, J. H., NASSER, B., KIM, W.S. & JOO, Y. L. 2013. Effect of flow structure at the onset of instability on barium sulfate precipitation in Taylor–Couette crystallizers. *Journal of Crystal Growth,* 373**,** 20-31.

BAŁDYGA, J. & BOURNE, J. R. 1984. A Fluid Mechanical Approach to Turbulent Mixing and Chemical Reaction Part I Inadequacies of Available Methods. *Chemical Engineering Communications,* 28**,** 231-241.

BAŁDYGA, J., PODGóRSKA, W. & POHORECKI, R. 1995. Mixing-precipitation model with application to double feed semibatch precipitation. *Chemical Engineering Science,* 50**,** 1281-1300.

BUBAKOVA, P., PIVOKONSKY, M. & FILIP, P. 2013. Effect of shear rate on aggregate size and structure in the process of aggregation and at steady state. *Powder Technology,* 235**,** 540-549.

CAMP, T. R. & STEIN, P. C. 1943. Velocity gradients and internal work in fluid motion. *Boston Society of Civil Engineers,* 30**,** 219-237.

CARPENTER, K. J. 2001. Chemical reaction engineering aspects of fine chemicals manufacture. *Chemical Engineering Science,* 56**,** 305-322.

CHERALATHAN, K. K., KANG, N. Y., PARK, H. S., LEE, Y. J., CHOI, W. C., KO, Y. S. & PARK, Y.K. 2010. Preparation of spherical $LiNi_{0.80}Co_{0.15}Mn_{0.05}O_2$ lithium-ion cathode material by continuous co-precipitation. *Journal of Power Sources,* 195**,** 1486-1494.

COLE, J. A. 1967. Taylor vortices with eccentric rotating cylinders. *Nature,* 216**,** 1200-1202.

EHRL, L., SOOS, M., WU, H. & MORBIDELLI, M. 2010. Effect of flow field heterogeneity in coagulators on aggregate size and structure. *AIChE Journal,* 56**,** 2573-2587.

FARAHANI, H. B., SHAHROKHI, M. & DEHKORDI, A. M. 2017. Experimental investigation and process intensification of barium sulfate nanoparticles synthesis via a new double coaxial spinning disks reactor. *Chemical Engineering and Processing: Process Intensification,* 115**,** 11-22.

JARVIS, P., JEFFERSON, B., GREGORY, J. & PARSONS, S.A. 2005. A review of floc strength and breakage, Water Research, 39**,** 3121–3137.

JUDAT, B., RACINA, A. & KIND, M. 2004. Macroand Micromixing in a Taylor-Couette Reactor with Axial Flow and their Influence on the Precipitation of Barium Sulfate. *Chemical Engineering & Technology,* 27**,** 287-292.

JUNG, W.M., HOON K. S., KIM, K.S., KIM, W.S. & KYUN C. C. 2010. Precipitation of calcium carbonate particles by gas–liquid reaction: Morphology and size distribution of particles in Couette-Taylor and stirred tank reactors. *Journal of Crystal Growth,* 312**,** 3331-3339.

JUNG, W. M., KANG, S. H., KIM, W.S. & CHOI, C. K. 2000. Particle morphology of calcium carbonate precipitated by gas-liquid reaction in a couette-taylor reactor. *Chemical Engineering Science,* 55**,** 733-747.

KANG, S. H., LEE, S. G., JUNG, W. M., KIM, M. C., KIM, W.S., CHOI, C. K. & FEIGELSON, R. S. 2003. Effect of Taylor vortices on calcium carbonate crystallization by gas–liquid reaction. *Journal of Crystal Growth,* 254, 196-205.

KIM, J.E. & KIM, W.S. 2017. Synthesis of core–shell particles of nickel–manganese–cobalt hydroxides in a continuous couette-taylor crystallizer. *Crystal Growth & Design,* 17, 3677-3686.

KIM, J.M., CHANG, S.M., CHANG, J. H. & KIM, W.S. 2011. Agglomeration of nickel/cobalt/manganese hydroxide crystals in couette–taylor crystallizer. *Colloids and Surfaces A: Physicochemical and Engineering Aspects,* 384, 31-39.

CAFIERO, L. M., BAFFI, G., CHIANESE A. & JACHUCK, R. J. J. 2002. Process intensification: precipitation of barium sulfate using a spinning disk reactor. Industry & Engineering Chemistry Research., 41, 5240-5246.

LI, G., YANG, X. & YE, H. 2015. CFD simulation of shear flow and mixing in a taylor–couette reactor with variable cross-section inner cylinders. *Powder Technology,* 280, 53-66.

LIANG, L., DU, K., PENG, Z., CAO, Y., DUAN, J., JIANG, J. & HU, G. 2014. Co–precipitation synthesis of $Ni_{0.6}Co_{0.2}Mn0_{.2}(OH)_2$ precursor and characterization of $LiNi0_{.6}Co_{0.2}Mn_{0.2}O_2$ cathode material for secondary lithium batteries. *Electrochimica Acta,* 130, 82-89.

LOPEZ, J. M. & MARQUES, F. 2002. Modulated taylor-couette flow: onset of spiral modes. *Theoretical andComputational Fluid Dynamics,* 16, 59-69.

MAYRA, Q.P. & KIM, W.S. 2015. Agglomeration of Ni-rich hydroxide in reaction crystallization: effect of taylor vortex dimension and intensity. *Crystal Growth & Design,* 15, 1726-1734.

NEMRI, M., CLIMENT, E., CHARTON, S., LANOë, J.Y. & ODE, D. 2013. Experimental and numerical investigation on mixing and axial dispersion in taylor–couette flow patterns. *Chemical Engineering Research and Design,* 91, 2346-2354.

NOH, M. & CHO, J. 2012. Optimized synthetic conditions of $LiNi_{0.5}Co_{0.2}Mn_{0.3}O_2$ cathode materials for high rate lithium batteries via co-precipitation cethod. *Journal of The Electrochemical Society,* 160, A105-A111.

SALMONI, P.R., HOWELLS,W.S. & MILLS, R. 1987. The dynamics of water molecules in ionic solution. II. Quasi-elastic neutron scattering and tracer diffusion studies of the proton and ion dynamics in concentrated Ni^{2+}, Cu^{2+} and Nd^{3+} aqueous solutions. Journal of Physics C: Solid State Physics, 20, 5727-5747.

PARKER, D.S., KAUFMAN, W.J., & JENKINS, D. 1971. Physical conditioning of activated sludge floc. *Water Pollution Control Federation,* 43, 1817–1833.

PARK, S. H., KANG, S. H., BELHAROUAK, I., SUN, Y. K. & AMINE, K. 2008. Physical and electrochemical properties of spherical

$Li_{1+x}(Ni_{1/3}Co_{1/3}Mn_{1/3})_{1-x}O_2$ cathode materials. *Journal of Power Sources,* 177**,** 177-183.

RICHTER, O., HOFFMANN, H. & KRAUSHAAR-CZARNETZKI, B. 2008. Effect of the rotor shape on the mixing characteristics of a continuous flow Taylor-vortex reactor. *Chemical Engineering Science,* 63**,** 3504-3513.

ZAUNER, R.& JONES, A. G. 2000. Determination of nucleation, growth, agglomeration and disruption kinetics from experimental precipitation data: the calcium oxalate system. *Chemical Engineering Science,* 55**,** 4219-4232.

SNYDER, H. A. 1968. Experiments on rotating flows between noncircular cylinders. *Physics of Fluids,* 11**,** 1606-1611.

SOOS, M., WU, H. & MORBIDELLI, M. 2007. Taylor-Couette unit with a lobed inner cylinder cross section. *AIChE Journal,* 53**,** 1109-1120.

SUNG, M.H., CHOI, I.S., KIM, J.S. & KIM, W.S. 2000. Agglomeration of yttrium oxalate particles produced by reaction precipitation in semi-batch reactor. *Chemical Engineering Science,* 55**,** 2173-2184.

THAI, D. K., MAYRA, Q.P. & KIM, W.S. 2015. Agglomeration of Ni-rich hydroxide crystals in Taylor vortex flow. *Powder Technology,* 274**,** 5-13.

TORBACKE, M. & RASMUSON , Å. C. 2001. Influence of different scales of mixing in reaction crystallization. *Chemical Engineering Science,* 56**,** 2459-2473.

ZHANG, S., DENG, C., FU, B. L., YANG, S. Y. & MA, L. 2010. Synthetic optimization of spherical $Li[Ni_{1/3}Mn_{1/3}Co_{1/3}]O_2$ prepared by a carbonate co-precipitation method. *Powder Technology,* 198**,** 373-380.

Figures

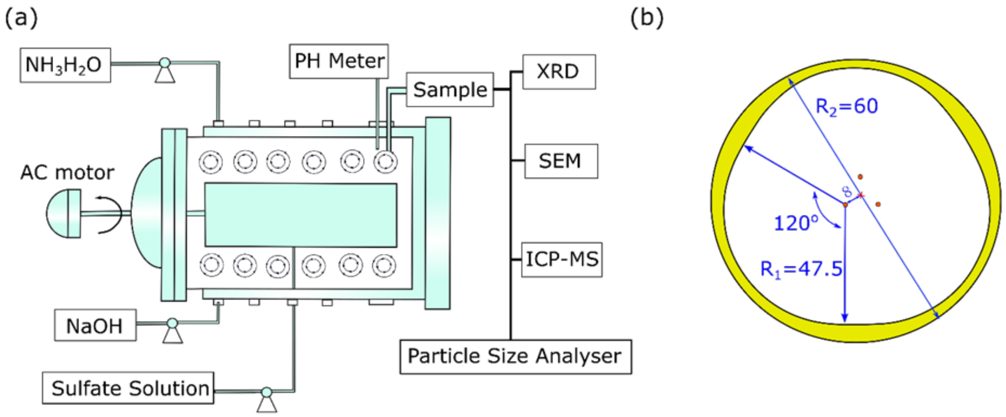

Figure 3-1. Schematic diagram of (a) experimental system used for reaction crystallization of NCM622 precursor and (b) Inner structure of lobed Taylor-Couette unit (LTC)

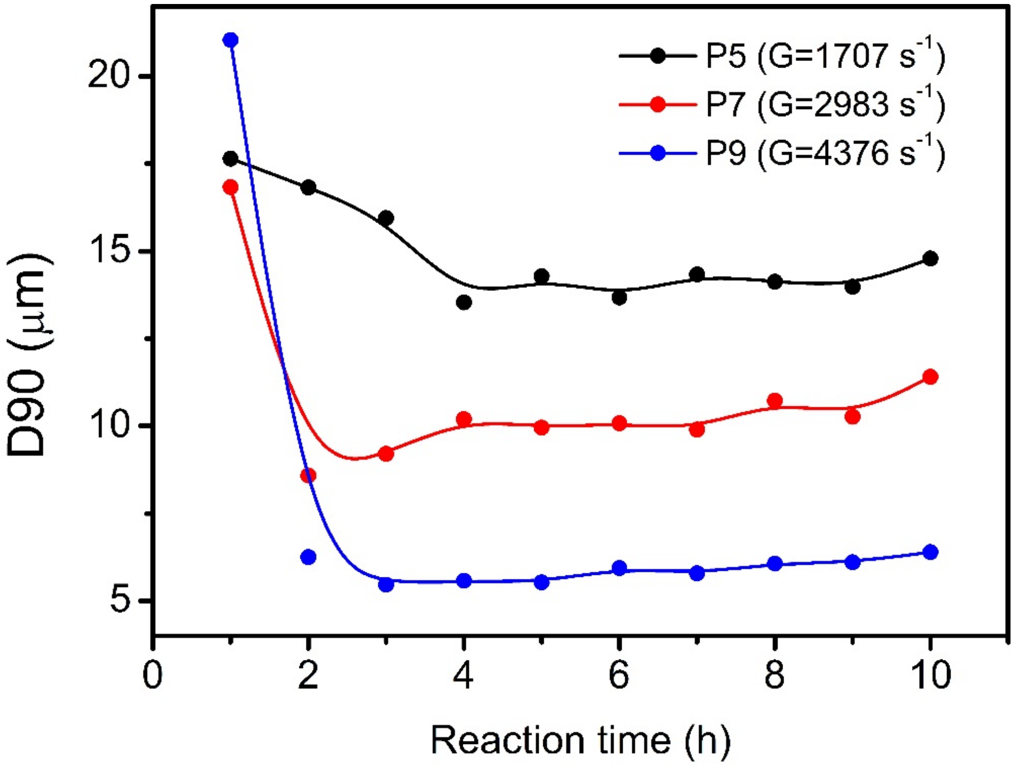

Figure 3-2. Reaction crystallization of NCM622 precursor in terms of different rotational speed, where the molar ratio of NH_3/MSO_4 is 1

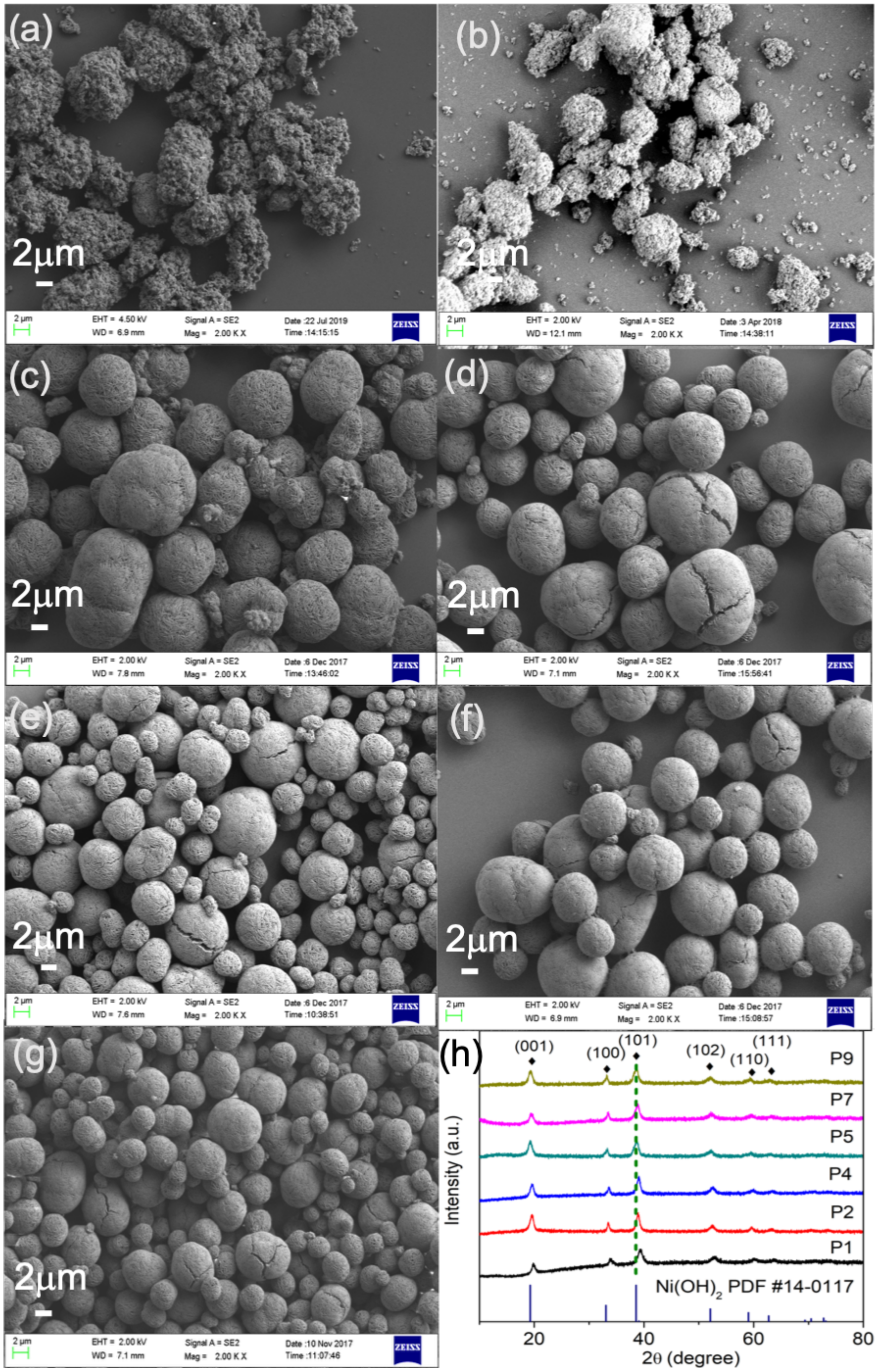

Figure 3-3.SEM images of NCM622 hydroxide prepared at different shear rate: (a) 855 S^{-1} (b) 1127 S^{-1} (c) 1707 S^{-1} (d) 2328 S^{-1} (e) 2983 S^{-1} (f) 3668 S^{-1} and (g) 4376 S^{-1} , (h) XRD patterns of precursor

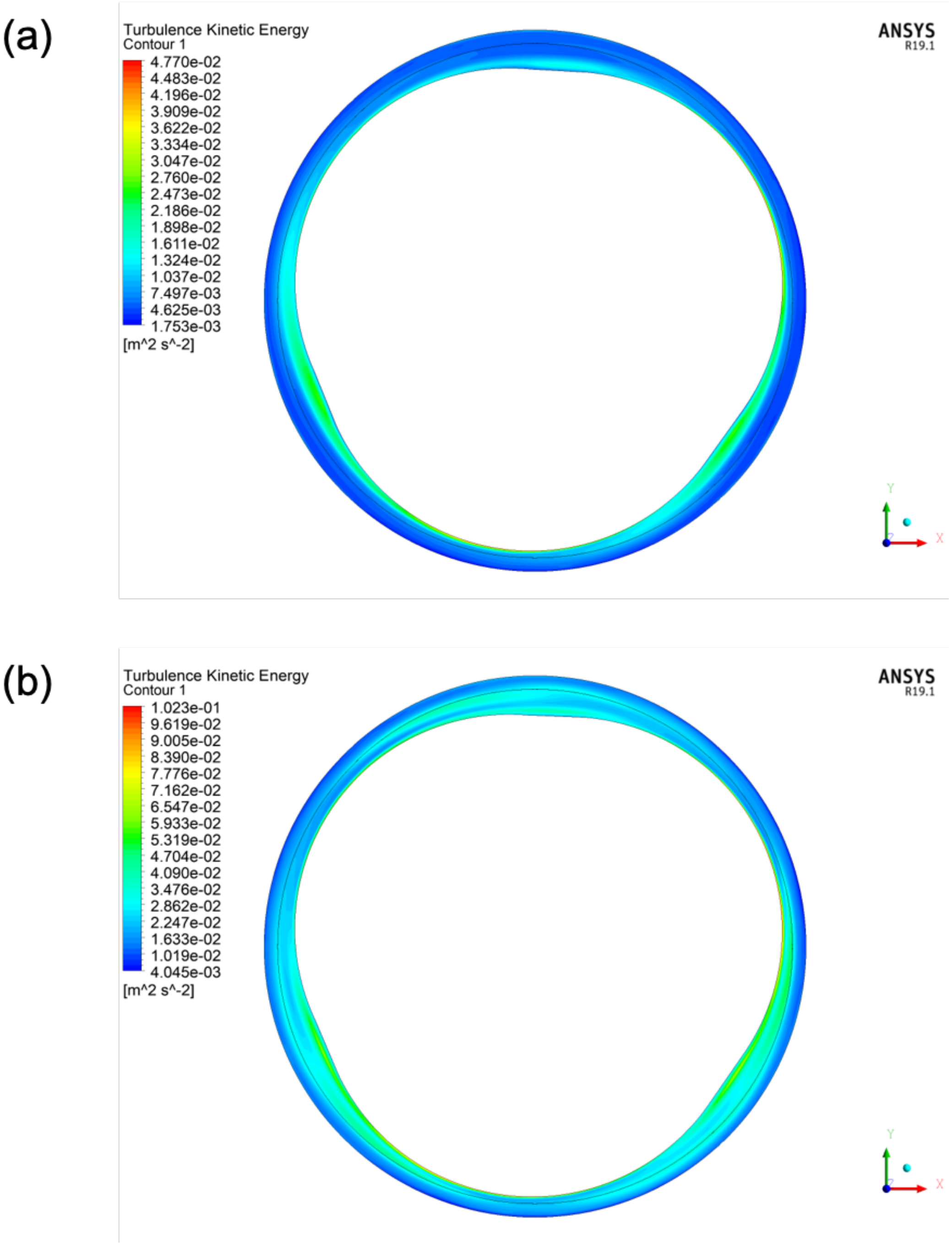
(a)
Turbulence Kinetic Energy
Contour 1
4.770e-02
4.483e-02
4.196e-02
3.909e-02
3.622e-02
3.334e-02
3.047e-02
2.760e-02
2.473e-02
2.186e-02
1.898e-02
1.611e-02
1.324e-02
1.037e-02
7.497e-03
4.625e-03
1.753e-03
[m^2 s^-2]
ANSYS
R19.1
Y
X
(b)
Turbulence Kinetic Energy
Contour 1
1.023e-01
9.619e-02
9.005e-02
8.390e-02
7.776e-02
7.162e-02
6.547e-02
5.933e-02
5.319e-02
4.704e-02
4.090e-02
3.476e-02
2.862e-02
2.247e-02
1.633e-02
1.019e-02
4.045e-03
[m^2 s^-2]
ANSYS
R19.1
Y
X

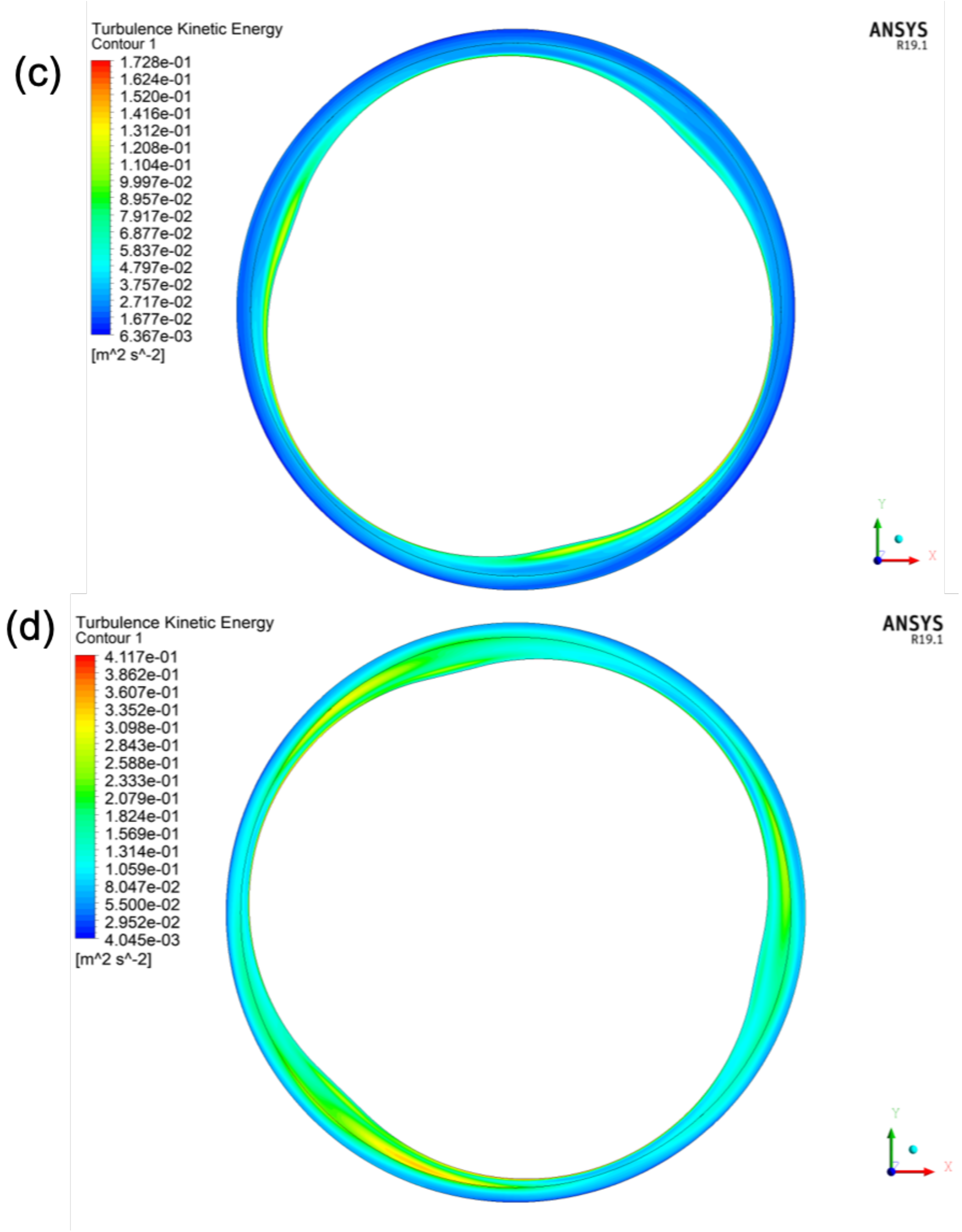

Figure 3-4. Turbulent kinetic energy and turbulent energy dissipation distributions in the cutting cross-section of the lobbed inner cylinder at different shear rate: (a) 600 s^{-1} (b) 1127 s^{-1} (c) 1707 s^{-1} (d) 2983 s^{-1}

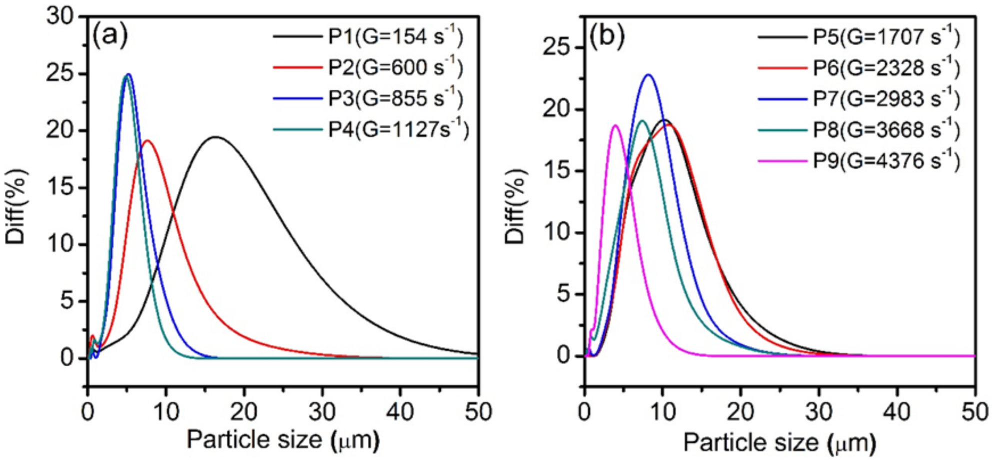

Figure 3-5. Typical particle size distribution (PSD) and particle size at different shear rate: (a) particle size distribution at a low shear rate, (b) particle size distribution at a high shear rate

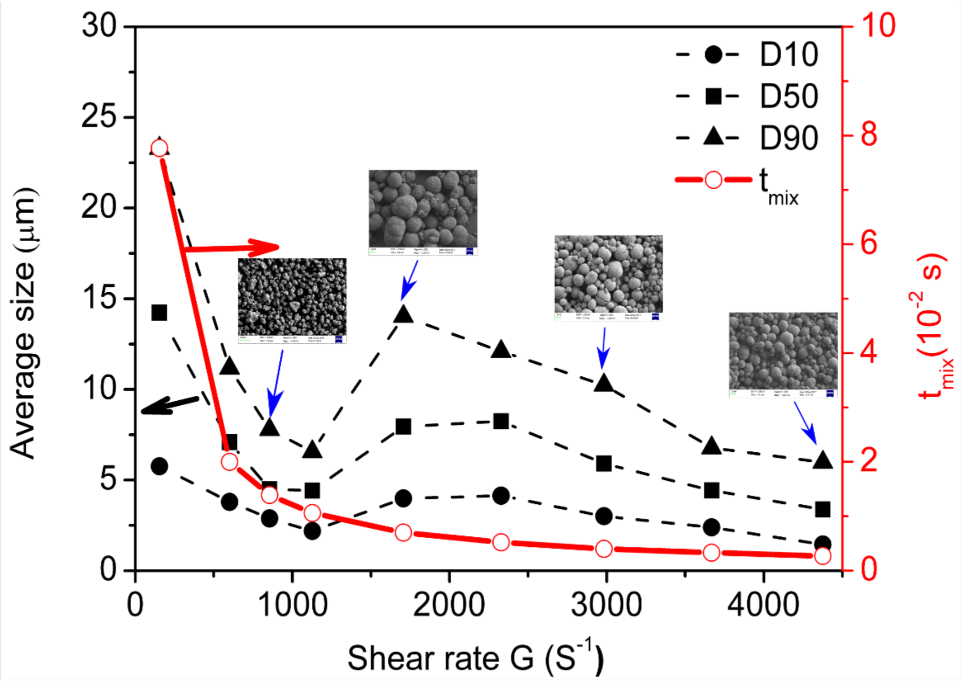

Figure 3-6. Particle size (left black scale) and mixing time (right red scale) as a function of the shear rate, insets shows morphologies of particle prepared at four different shear rates

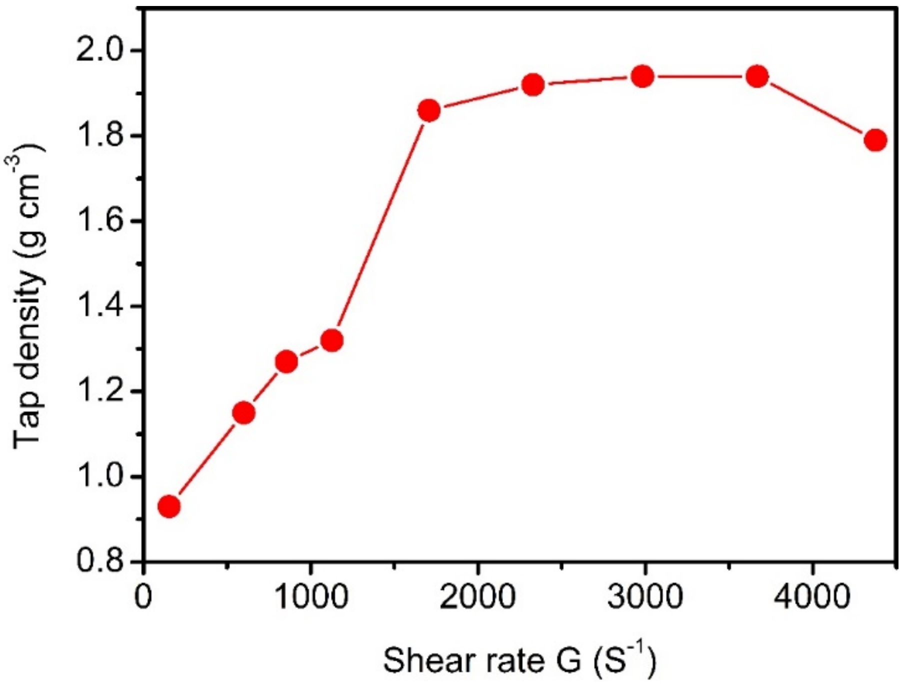

Figure 3-7. The tap density of particles as a function of the shear rate

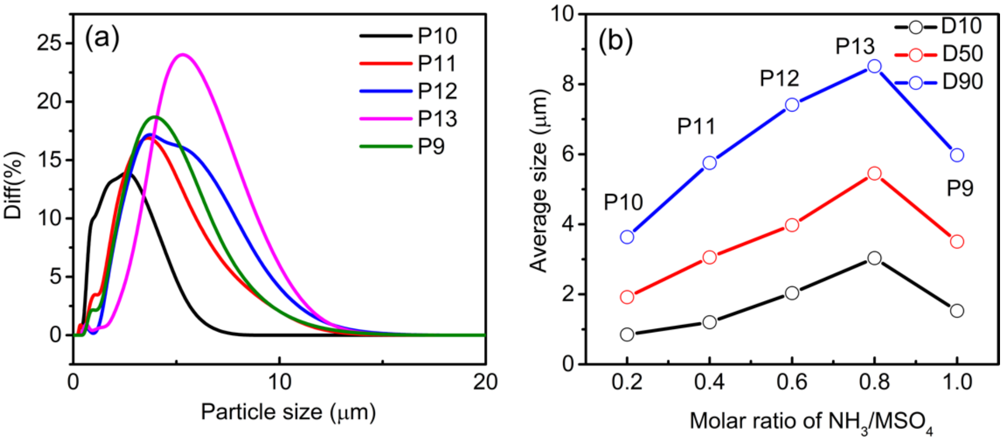

Figure 3-8. Particle size distribution (a) and particle size (b) of NCM622 precursor prepared at a different molar ratio of NH_3/MSO_4

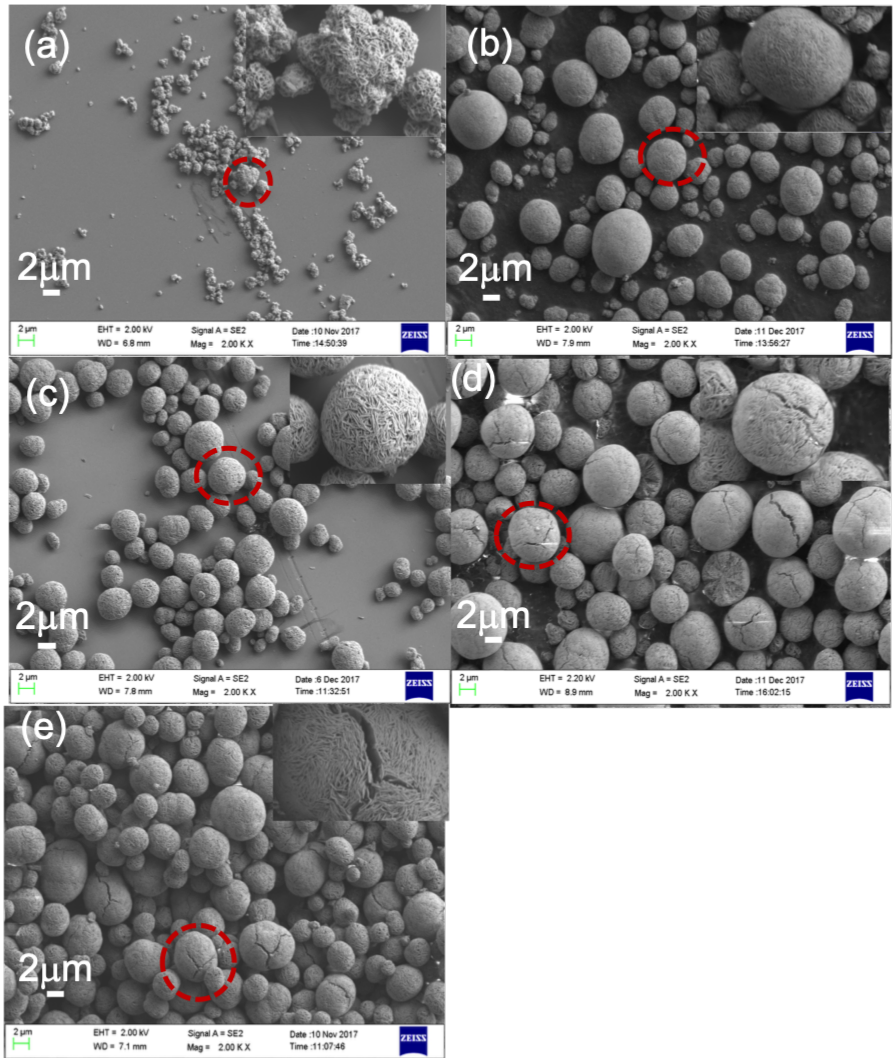

Figure 3-9.SEM images of NCM622 precursor at different molar ratio of NH_3/MSO_4: (a) 0.2, (b) 0.4, (c) 0.6, (d) 0.8 and (e) 1 prepared at shear rate of 4376 S^{-1}

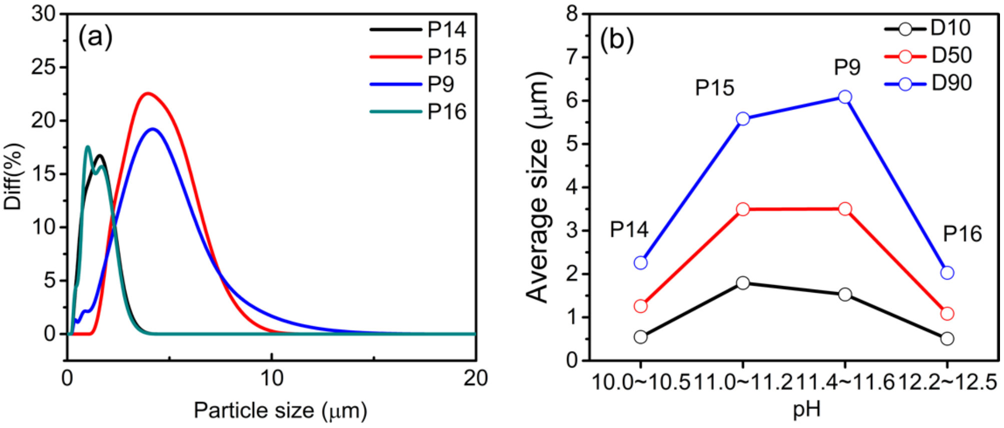

Figure 3-10. Particle size distribution (a) and particle size (b) of NCM622 precursor prepared at different pH

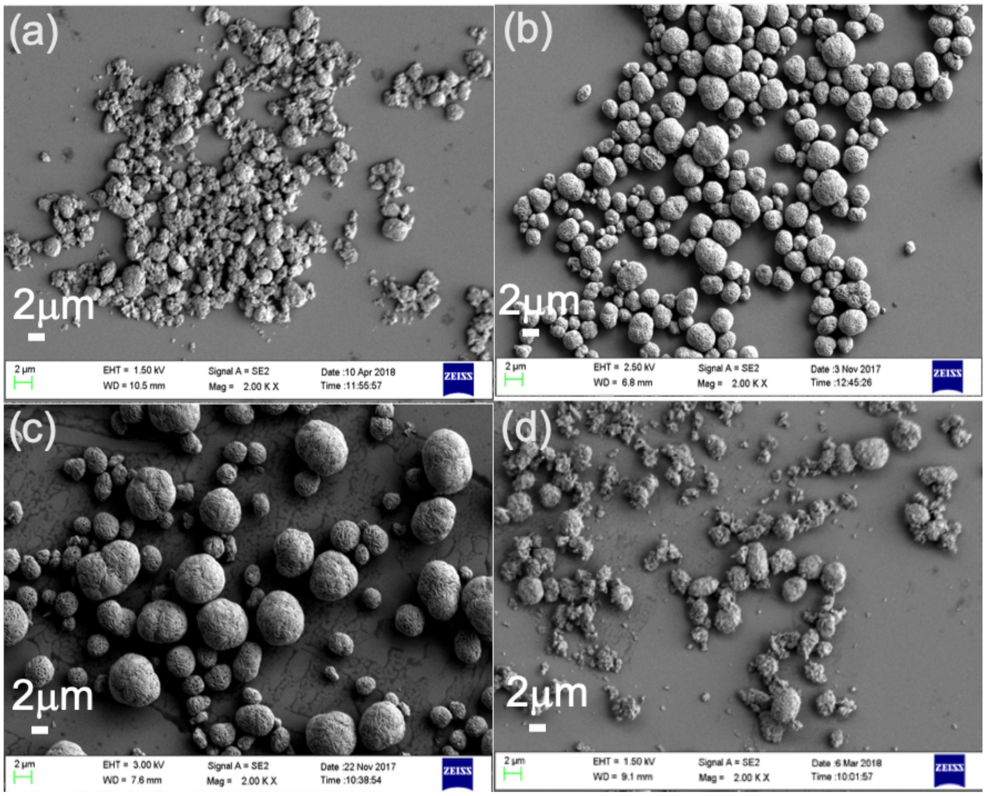

Figure 3-11. SEM images of $(Ni_{0.6}Co_{0.2}Mn_{0.2})(OH)_2$ precursor prepared at different pH (a) 10.0~10.5 (b) 11.0~11.2 (c) 11.4~11.6 (d) 12.2~12.5

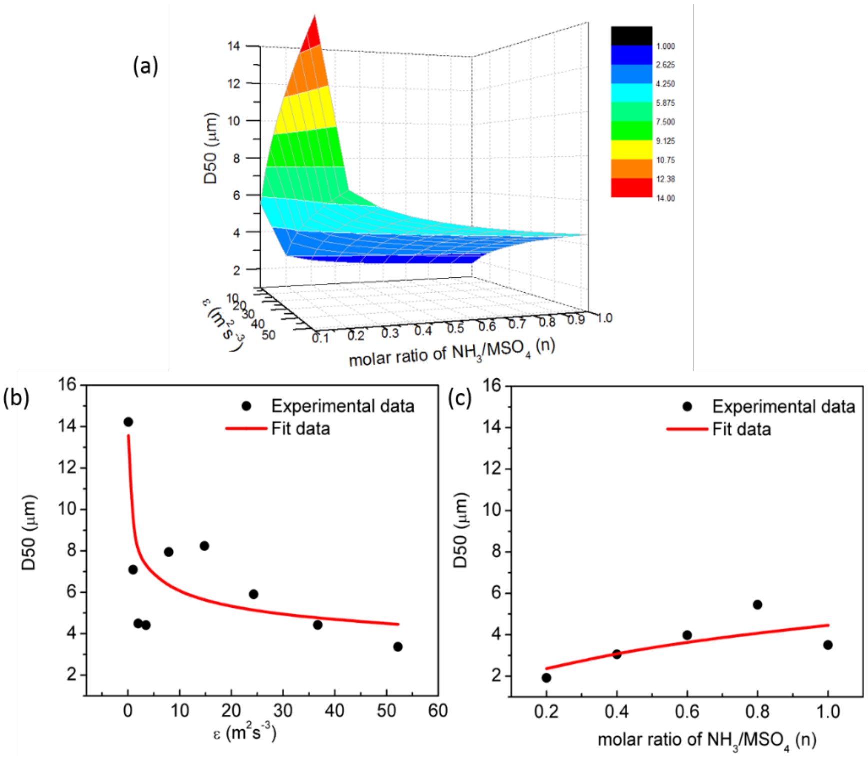

Figure 3-12. Model prediction of (a) surface relevance between turbulent energy dissipation ε and molar ratio of NH_3/MSO_4 -n; Comparison of model prediction with experimental data for agglomerate particle size (D_{50}): (b) at different turbulent energy dissipation ε, where molar ratio of NH_3/MSO_4 -n is 1; (c) at different molar ratio of NH_3/MSO_4 -n, where ε is 52.2 $m^2 s^{-3}$.

Tables

Table 3-1. Preparation conditions of NCM622 precursors in terms of the molar ratio of NH_3/MSO_4, rotational speed and pH

Sample Name	**molar ratio of NH_3/MSO_4**	**Rotational speed (rpm)**	**pH**
P1	1	100	11.4~11.6
P2	1	300	11.4~11.6
P3	1	400	11.4~11.6
P4	1	500	11.4~11.6
P5	1	700	11.4~11.6
P6	1	900	11.4~11.6
P7	1	1100	11.4~11.6
P8	1	1300	11.4~11.6
P9	1	1500	11.4~11.6
P10	0.2	1500	11.4~11.6
P11	0.4	1500	11.4~11.6
P12	0.6	1500	11.4~11.6
P13	0.8	1500	11.4~11.6
P14	1	1500	10.0~10.5
P15	1	1500	11.0~11.2
P16	1	1500	12.2~12.5

Table 3-2. The value of shear rate (G) used in the experiment and corresponding angular velocities (ω), Reynolds numbers (Re) , energy dissipation rate (ε), Reynold number ratios (R) and Kolmogorov length scale (λ)

Sample Name	**Rotational speed (rpm)**	**G (s^{-1})**	**ω (rad s^{-1})**	**Re (-)**	**ε (W kg^{-1})**	**R (-)**	**λ (µm)**
P1	100	154	10.5	1281	0.1	9.8	133
P2	300	600	31.4	3842	1.0	29.4	67.4
P3	400	855	41.9	5123	2.0	39.2	56.5
P4	500	1127	52.4	6404	3.5	49	49.2
P5	700	1707	73.3	8965	7.9	68.5	40.0
P6	900	2328	94.2	11527	14.8	88.1	34.2
P7	1100	2983	115.2	14089	24.3	107.7	30.2
P8	1300	3668	136.1	16650	36.7	127.3	27.3
P9	1500	4376	157.1	19212	52.2	146.9	25.0

Table 3-3. Crystalline size of particles calculated according to the Scherrer's formula

PDF # 14-0117		P1		P2		P4		P5		P7		P9	
Pos. [°2Th.]	**h k l**	**Pos. [°2Th.]**	**Particle Size (nm)**	**Pos. [°2Th.]**	**Particle Size (nm)**	**Pos.[°2 Th.]**	**Particle Size (nm)**	**Pos. [°2Th.]**	**Particle Size (nm)**	**Pos. [°2Th.]**	**Particle Size (nm)**	**Pos.[°2 Th.]**	**Particle Size (nm)**
19.258	001	19.823	12.57	19.523	10.68	19.608	11.21	19.275	10.21	19.564	9.95	19.382	10.11
33.064	100	33.756	11.72	33.414	21.38	33.623	20.08	33.277	14.35	33.446	17.32	33.18	13.93
38.541	101	39.239	8.74	38.837	11.86	38.969	11.13	38.535	9.06	38.757	9.83	38.563	9.71
52.1	102	52.679	9.92	52.401	9.28	52.42	9.87	52.201	12.21	52.099	7.64	52.096	11.50
Average particle size			**10.74**		**13.30**		**13.07**		**11.46**		**11.18**		**11.31**

Table 3-4. ICP-MS of NCM622 precursor prepared at different pH

Sample Name	**pH**	**Metal ion (wt.%)**			**Moalr ratio of Ni：Co：Mn**
		Ni	**Co**	**Mn**	
P14	10.0~10.5	29.431	11.277	10.684	0. 501：0.191：0.194
P15	11.0~11.2	32.525	12.276	11.398	0.554：0.208：0.207
P9	11.4~11.6	35.108	11.938	10.762	0.598：0.203：0.196
P16	12.2~12.5	31.170	11.382	10.792	0.531：0.193：0.196

Chapter 4

Co-precipitation Synthesis of High-tap Density and Small Size of Spherical $(Ni_{0.6}Co_{0.2}Mn_{0.2})(OH)_2$ Precursor and Good Electrochemical Performance for Lithium Cathode Material Using a Lobed Taylor-Couette (TC) Reactor

Summary

In Chapter 3, the effects of hydrodynamics and physico-chemical conditions on the agglomerate shape and sizes of the particles prepared by a lobed Taylor-Couette (TC) reactor are investigated. This chapter will focus on the evaluation of its electrochemical performance for Lithium cathode material in terms of different preparation conditions. Layered $Li(Ni_{0.6}Co_{0.2}Mn_{0.2})O_2$ cathode materials were synthesized from spherical metal hydroxide $(Ni_{0.6}Co_{0.2}Mn_{0.2})(OH)_2$ of small size (3-8μm) which was prepared by co-precipitation method with a lobed Taylor-Couette flow reactor (LTC). The results show that the preparation of metal hydroxide is significantly influenced by synthetic conditions, such as pH, the molar ratio of NH_3/MSO_4 and stirring speed. The produced $(Ni_{0.6}Co_{0.2}Mn_{0.2})(OH)_2$ precursor has achieved a high tap density of 1.94 g cm^{-3} when operating under the optimized condition. Calcination of $(Ni_{0.6}Co_{0.2}Mn_{0.2})(OH)_2$ with LiOH at 860 ^{O}C has obtained a well-ordered layer structure with a high tap-density of 2.36 g cm^{-3}. The electrochemical tests have indicated that the material prepared at optimized conditions has initial electrochemical properties of 166.0 mAh g^{-1} at 0.1C. The first discharge capacity and the capacity in 40 cycles at 0.5C reach 164.4mAhg^{-}

^{1} and 145.4 mAh g^{-1}, with capacity retention of 88.4%. As for the rate performances, the average discharge capacities were found to have 175.0 mAh g^{-1}, 170.4 mAh g^{-1}, 159.0 mAh g^{-1}, 146.4 mAh g^{-1} and 125.1 mAh g^{-1} at 0.1 C, 0.2 C, 0.5 C, 1 C and 2 C, respectively. The experiments have confirmed that the optimized stirring speed, calcination temperature, molar ratio of NH_3/MSO_4, pH are 1500 rpm, 860^{O}C, 0.8, 11.4~11.6.

4.1 Introduction

Increasing demands for portable electronic devices and the use of electrical vehicles (EVs) for green transport require high energy density batteries. As one of the most promising members, Lithium-ion batteries are well known for their excellent electrochemical performances such as high energy and power densities. As a composition, Lithium cathode material plays an important role in terms of high energy and power densities for Lithium-ion material (Manthiram *et al*., 2013; Wang *et al*., 2015; Yang *et al*., 2012). So far, the application of layered structured compounds of $LiMO_2$ (M=transitional metal elements: Ni/Co/Mn) for fabrication of Lithium cathode material has been well studied. Liu *et al*. (1999) first synthesized $LiNi_xCo_yMn_zO_2$ (NCM, $0 \leq x, y, z \leq 1$) and reported it as a kind of important and promising cathode material for large capacity and its good reversibility in capacity, lower cost and environmental-friendly. To date, there have existed several commercialized and well developed Lithium-ion cathode materials available such as $LiNi_{1/3}Co_{1/3}Mn_{1/3}O_2$ (NCM333) and $LiNi_{0.5}Co_{0.2}Mn_{0.3}O_2$ (NCM523). However, the capacities of these materials are usually in the range of 150~160 mAh g^{-1}, which cannot meet the demand for high energy density in many cases. Consequently, the adoption of Nickel-rich ($Ni \geq 0.6$) materials that have been recognized to have a high specific capacity has received much attention.

The preparation of $Ni_xMn_yCo_{1-x-y}(OH)_2$ precursor can employ different approaches including co-precipitation (Tang *et al*., 2016, Wu *et al*., 2012), sol-gel method (Chen *et al*., 2005), solid-state reaction (Liang *et al*., 2014) andspray drying (Yue *et al*., 2011b). Co-precipitation is a popular technology and mostly used in industry as it is relatively simply realized for obtaining $Ni_xMn_yCo_{1-x-y}(OH)_2$ precursor with homogeneous composition (Tang *et al*., 2016; Wu *et al*., 2012). However, when the tap density higher than 1.8 g cm^{-3} is required, most of these ternary precursors are synthesized in a batch mixing tank crystallizer or continuous stirred tank reactor (CSTR), which a long reaction time of 12~40 h is usually imposed (Tang *et al*., 2016). In such operation condition, the agglomerate size, size distribution and morphology are hard to predict due to the random turbulent eddies in the mixing (Dong *et al*., 2017; Yang *et al*., 2017; Lee *et al*., 2004). Furthermore, it has been reported that the electrochemical properties of $LiNi_xCo_yMn_{1-x-y}O_2$ are interrelated to the properties of precursors prepared by co-precipitation. Many previous studies have revealed that the electrochemical properties of the final product $LiNi_xCo_yMn_{1-x-y}O_2$ are dependent on the morphology, structure, size of primary and secondary particles, size distribution of precursors (Atsumi, 2001; Tang *et al*., 2016, Nie *et al*., 2015). In particular, it has been found that particle size has an effect on surface features, current density and lithium-ion diffusion used as electrode active material. It is noticed here that the average size of secondary particles prepared by traditional crystallizers is generally around 10~15 μm (Luo *et al*., 2006; Liang *et al*., 2014; Liu *et al*., 2012; Park *et al*., 2008; Lee *et al*., 2004). Study on the precursors with small size (<10 μm) and its relevant electrochemical properties is still limited.

Taylor-Couette (TC) reactor with an excellent micromixing performance and periodic fluid motion properties is considered as a promising technology in the area of preparation of uniform ultra-fine particles. It also possesses the potential application for the preparation of precursors as lithium cathode materials. Kim *et al*. (2015) have reported that they synthesized a series of narrowly distributed and spherical Ni-rich hydroxide $(Ni_{0.90}Co_{0.05}Mn_{0.05})(OH)_2$ with a particle size in the range of 3~7 μm using the traditional TC reactors. However, they did not go further to prepare cathode materials based on the synthesized precursor and measured the electrochemical properties of the samples prepared with the material (Thai *et al*., 2015; Mayra and Kim, 2015; Kim *et al*., 2011). Feridun *et al*. (2016) synthesized $Ni_{0.6}Mn_{0.2}Co_{0.2}(OH)_2$ precursors, also using the Taylor vortex reactor, and obtained the tap densities of 1.77-1.98 g cm^{-3} and 2.02-2.24 g cm^{-3} for the active materials, delivering 173-186 mAh g^{-1} discharge capacities at the first cycle of 0.1C when cycled between 4.3V-3.0V. To the best of our knowledge, there are still limited results published with respect to the electrochemical properties of $LiNi_xCo_yMn_{1-x-y}O_2$ prepared by using TC reactors. It has been recognized that the use of the specific profile of the cross-section for the inner cylinder could deform Taylor vortices, effectively reducing the regions of low velocity and shear rate in the TC reactor (Li *et al*., 2015). High shear rate may be beneficial to the formation of spherical precursor with narrow size distribution (Thai *et al*., 2015).

In the present study, the co-precipitation method will be adopted to prepare $Ni_{0.6}Co_{0.2}Mn_{0.2}(OH)_2$ precursor by using a lobed TC reactor. Spherical $LiNi_{0.6}Co_{0.2}Mn_{0.2}O_2$ cathode material was synthesized by the mixture of the precalcined precursor with LiOH at high temperature calcination. The effect of preparation conditions such as pH, stirring speed and molar ratio of

NH_3/MSO_4on the morphology of precursors and their physical and electrochemical properties of $LiNi_{0.6}Co_{0.2}Mn_{0.2}O_2$ will be investigated.

4.2 Experimental

4.2.1 Synthesis Method

For the formation of $(Ni_{0.6}Co_{0.2}Mn_{0.2})(OH)_2$ precursor, a specially designed lobed Taylor-Couette flow reactor (LTC) (shown in Figure 4-1) with a lobed inner cylinder (volume-630 ml) was used, where the inner cylinder was rotational and the outer cylinder was stationary. The inner cylinder was driven by a variable speed driver with a torque meter. The LTC was placed horizontally in order to prevent the effects of the hydrostatic pressure gradient. The metal sulfate solution (MSO_4) was prepared using $NiSO_4 \cdot 6H_2O$ (>98%, Jinchuan Group co., LTD), $MnSO_4 \cdot H_2O$ (>96%, Shanghai nanwei chemicals co., Ltd), $CoSO_4 \cdot 7H_2O$ (>98%, Sinopharm Chemical Reagent Co., Ltd) as raw materials. The molar ratio of nickel sulfate, cobalt sulfate, and manganese sulfate in the feed solution was kept constant at 0.6:0.2:0.2 and its feed concentration was kept unchanged at 2 mol L^{-1}. 4 M of Sodium hydroxide (>96%, Tianjin zhiyuan chemicals co., Ltd) was used as hydroxyl reactant and a certain concentration of ammonia (25~28%, Sinopharm Chemical Reagent Co., Ltd) was used as chelating agent for crystallization of $(Ni_{0.6}Co_{0.2}Mn_{0.2})(OH)_2$ precursor. Before reaction, the LTC (hereafter also referred to as crystallizer) was initially filled with distilled water and the temperature was kept at $55^{O}C$.

During the reaction, the metal sulfate solution, sodium hydroxide and ammonia were continuously feed into the LTC reactor using the peristaltic pumps through three ports mounted on the surface of the left end of the LTC reactor. The mean residence time of operation for the precursor synthesis process was controlled to be 60 mins. After that, the collected final precipitate was filtered using a vacuum pump and was washed several times with distilled water until the pH of the product attains 7. The precipitate was then subsequently dried in a circulation oven at 80^{O}C for 24 hours.

$LiNi_{0.6}Co_{0.2}Mn_{0.2}O_2$ cathode material was calcined by a combination of $(Ni_{0.6}Co_{0.2}Mn_{0.2})(OH)_2$ precursor and LiOH where the molar ratio of Li/metal (Ni, Co, and Mn) was 1.05. Excess lithium was added to compensate for loss due to the evaporation of lithium salt at the high temperature during the calcination process. The mixture of precursor and LiOH were calcined at 500^{O}C for 4 hours at the first stage and then further calcinated at high temperature of 760°C-910 °C for 12 hours in the air. Without special instructions, the calcination temperature is 860^{O}C.

4.2.2 Material Characterization

XRD analyses were conducted in a Bruker-AXS D8 advance powder diffractometer using Cu-Ka radiation (λ=1.5406 Å) and power of 40kv×20Ma, where diffraction pattern was recorded in the range 2θ=10-80^{o} with a step size of 0.01^{o}. The morphologies of synthesized powders were observed using SEM produced from ZEISS ZIGMA 174C CZ. A particle size analyzer (Bettersize 2000 Intelligent Laser Particle Size Analyzer, Bettersize instruments Ltd.) was used to determine the particle size and size distribution of aggregates. The tap density of particles was measured by putting a known mass of powder in a vertical tube and tapping for 15 mins on a lab bench. The volume after tapping the powder was determined and the tap density was calculated. Each measurement have been repeated three times.

4.2.3 Electrochemical Measurement

Electrochemical performance was measured with a CR2032 coin-type cell. The cell is composed of a lithium metal anode, $LiNi_{0.6}Co_{0.2}Mn_{0.2}O_2$ cathode and Celgard 2400 microporous membrane. The cathode consists of 80 wt.% of $LiNi_{0.6}Co_{0.2}Mn_{0.2}O_2$, 10 wt.% of Super P as a conducting agent and 10 wt.% of polyvinylidene fluoride (PVDF) as a binder. All these materials were dispersed in N-methyl pyrrolidinone (NMP) and stirred for 8 hours to make the slurry. The prepared slurry was coated uniformly onto an aluminum foil and then dried in an oven for 8h at 80 °C. After drying, the electrodes are cut in the form of 12 mm diameters disks. The electrolyte is a mixture of 1M $LiPF_6$ resolved in ethylene carbonate (EC) and ethyl methyl carbonate (EMC) (3:7, v/v). The assembly of all cells is carried out in an argon-filled glove box. These charge-discharge characteristics were measured between 2.7–4.3 Vat room temperature (vs. Li/Li^+) at a desired current density (1 C=160 mAh g^{-1}) using CT2001A land instrument. The cyclic voltammetry (CV) were evaluated by electrochemical work station PARSTAT MC (multi-channel) from Princeton, USA at the scan rate of 0.1 mVs^{-1} between 2.7 V and 4.3 V.

4.3 Results and Discussion

4.3.1 Characterization of $Ni_{0.6}Co_{0.2}Mn_{0.2}(OH)_2$Precursor

Co-precipitation of $Ni_{0.6}Co_{0.2}Mn_{0.2}(OH)_2$ was carried out continuously in the lobed Taylor-Couette reactor (shown in Figure 4-1) and the morphology change of the products was monitored regularly with certain time intervals by SEM images. Figure 4-2 shows the SEM images of $Ni_{0.6}Co_{0.2}Mn_{0.2}(OH)_2$ hydroxide prepared on the condition of the inner cylinder rotating at 1500 rpm (P2) while adopting different reaction time. It has been generally accepted that the use of time 10 times of the periodic toroidal motion of Taylor vortices would be sufficient for the continuous preparation of NCM precursor as the turbulent eddies embedded in such Taylor vortices will effectively interact with the entrapped aggregated particles formed by crystal nuclei. At the beginning of the reaction (Figure 4-2a), primary fine particles are formed and then combine with each other to form large irregular-shaped aggregates due to high supersaturation of reaction. These aggregates collide and may redistribute as the result of local shear caused by turbulent dissipated eddies that have a Kolmogorov scale, forming micro-sized agglomerates (Figure 4-2c and Figure 4-2d) which consist of needle-like microcrystalline grains (shown in Figure 4-2e). It can be seen from the figure that the particles grow gradually and develop a smooth and uniform spherical morphology as the crystallization has achieved an equilibrium with the effect of the local shear due to the turbulent eddies.

The XRD pattern of $Ni_{0.6}Co_{0.2}Mn_{0.2}(OH)_2$ precursor of P2 is displayed in Figure 4-2f, which clearly confirms that the precursor has a typical spectrum similar to that of $Ni(OH)_2$ (PDF # 14-0117) (Tian *et al.*, 2016). All the diffraction lines are indexed to indicate that a hexagonal structure with a space group of $P\overline{3}m1$ is formed. The ICP-OES result shows that the composition of Ni:Co:Mn in P2 is 0.598:0.202:0.196, which can be regarded as a molar ratio of 0.6Ni, 0.2Co and 0.2Mn of the initial designed composition. Based on the results of SEM, XRD and ICP-OES, it can be judged that the prepared spherical $Ni_{0.6}Co_{0.2}Mn_{0.2}(OH)_2$ precursor has been well synthesized using the continuous co-precipitation method in the lobed TC reactor.

In chapter 3, the effects of various factors such as stirring speed, the molar ratio of NH_3H_2O/MSO_4 and pH on particle size, size distribution and morphology were studied systematically. The main conclusions are as follows. The tap densities of the samples are listed in Table 4-1. It has been confirmed by many previous studies that pH is a crucial factor during the co-precipitation process. It should be controlled carefully to fall into a suitable range of values for the synthesis of NCM622 precursor because Nickle ions prefer to precipitate at a high pH, while Co and Mn require a low range of pH due to their different Ksp for Ni-rich materials. Thus, the pH should be increased to fall into the range in which manganese hydroxide is not precipitated (Lee *et al.*, 2004). The values of pH used in the present experiments were chosen to be 11.0~11.2, 11.4~11.6 and 12.0~12.2. Figure 4-3 (a-c) shows the SEM images of NCM powders of P1, P2 and P3, synthesised at different pH values respectively. When the pH is in the range of 11.0~11.6, the particles are all spherical in shape. However, the tap density of P2 (1.77 g cm^{-3}) is slightly higher than that of P1 (1.75 g cm^{-3}).

When the pH is increased to 12.0~12.2, the particles exhibit irregular shapes. Accordingly, the pH of 11.4~11.6 has been chosen for the subsequent experiments.

The stirring speed also affects the formation of spherical particles. Enhancement of stirring speed can enhance the shear rate especially the local shear due to the turbulence. The high shear rate induced by the velocity gradient acted on the agglomerates, intensifying the collision and redispersion among the particles, and may also promote the breakage of aggregated particles. Mayra and Kim (2015) have indicated that the higher shear rate, the smaller particle size is obtained. Figure 4-3(d-f) shows SEM images of the NCM622 powders of P4, P5 and P6 prepared at 500, 700 and 1100 rpm. At low stirring speed (500 rpm), the formed agglomerated particles are irregular (see Figure 3d). When the stirring speed increases to 700 rpm, the primary particles pack closely and form a dense secondary particle. Further increasing the stirring speed to 1100 rpm, the morphology of particle looks better sphericity and the particle out surface is smooth. Compared with the case of particles (P2) in the range of 5~6 μm prepared at 1500 rpm (shown in Figure 4-3b), the particle sizes for P5 and P6 are about ~10 μm. The secondary particle size distribution of precursors with different stirring speed was also observed as shown in Figure 4-4. The detailed measured parameters are listed in Table 4-2. It can be seen that all samples have presented a uniform and symmetrical particle distribution and no significant difference between the cases was identified. It should be noted here, however, that the particle size distribution of precursors become much narrower when increasing the stirring speed from 700 rpm (P5) to 1500 rpm (P2). The $D_{10}/D_{50}/D_{90}$ of P5 is 4.333/8.068/14.333 μm and $D_{10}/D_{50}/D_{90}$ of P2 is 1.415/3.169/5.788 μm, as shown in Table 4-2. This is in accordance with the SEM observation as shown in Figure 4-3. Case P4 also shows the appearance of small sizes of aggregates with irregular nonspherical morphology. The tap-densities of P5 and P6 are 1.86 g cm^{-3} and 1.94 g cm^{-3}, respectively, which are higher than that of P2, consistent with the observations observed by Dahn and co-workers where they reported that larger particles will have a higher tap-density (Jouanneau et al., 2003).

The effect of the molar ratio of NH_3/MSO_4 on the morphology can be seen from the SEM images shown in Figure 4-3. It can be clearly observed that the particles of P4 are composed of various fine primary grains, which are piled loosely to form the structure. As the molar ratio of NH_3/MSO_4 increased from 0.4 to 1, the uniform and spherical particles start to form. It has been well recognised that NH_4^+ ion plays an important role in promoting the formation of dense sphere-like hydroxide. In the metallic hydroxide preparation, NH_3H_2O, a chelating agent, can effectively prevent from the phase separation and form the impurity phase such as $Ni(OH)_2$, $Co(OH)_2$ or $Mn(OH)_2$ during the reaction. The spherical particles in P7 have attained a tap-density as high as 1.91 g cm^{-3}, the highest among all the particles in terms of different molar ratio of NH_3/MSO_4.

It seems that the pH values in the range of 11.4~11.6, the molar ratio of NH_3/MSO_4 in the range of 0.4~1 and stirring speed in the range of 700~1500 rpm are the ideal conditions for the formation of high tap density (>1.8 g cm^{-3}) of spherical ternary NCM622 precursor by using the lobed TC reactor.

4.3.2 Electrochemical Properties of $LiNi_{0.6}Co_{0.2}Mn_{0.2}O_2$Cathode Materials

4.3.2.1 Effect of Calcination Temperature

The calcination temperature plays an important role in the structure formation and electrochemical properties of Li cathode materials. Liang et al (Liang *et al*., 2014) found $LiNi_{0.6}Co_{0.2}Mn_{0.2}O_2$ calcined at 820 °C for 12 h has the best electrochemical properties. Xia et al (Xia *et al*., 2015) reported that the$LiNi_{0.6}Co_{0.2}Mn_{0.2}O_2$ synthesized at 780 °C for 12h has the best structural and electrochemical performance. Zhang *et al*. (2006) investigated that the optimum calcination temperature of $LiNi_{0.6}Co_{0.2}Mn_{0.2}O_2$ synthesized by carbonate co-precipitation method is 850–900 °C. This indicates the calcination temperature usually varies with different precursors.

The XRD patterns of $LiNi_{0.6}Co_{0.2}Mn_{0.2}O_2$ (LP7) calcinated at different temperature are shown in Figure 4-5. All the sample shows the same α-$NaFeO_2$ structure with R-3m space group (No.166) and no extra diffraction peaks from related secondary phases or impurities exist. All the XRD patterns show a clear split between the 006/012 and 108/110 peaks, indicating that the hexagonal structures are preserved among the materials (Deng *et al*., 2010, Yue *et al*., 2011a). However, the split becomes much clearer with increasing the calcination temperature. The intensity of diffraction line calcinated at 860^{O}C and 910^{O}C is higher than that of sample calcinated at 710 ^{O}C and 810 ^{O}C, which indicates high crystallinity of samples calcinated at high temperatures. The lattice parameters of $LiNi_{0.6}Co_{0.2}Mn_{0.2}O_2$ calcinated at different temperature are also shown in Table 3. The intensity ratio of I_{003}/I_{104} is an important parameter to predict the cation mixing effect in the lattice of the layered oxide. The value of $I_{(003)}/I_{(104)}$ lower than 1.2 is an indication of high cation mixing due to the occupancy of ions in the lithium regions (3b sites). The intensity ratio of I_{003}/I_{104} of all samples are higher than 1.2, showing that the lattice distortion does not occur. The value of I_{003}/I_{104} for the sample calcinated at $860^{O}C$ is the highest, which indicates a low cation mixing among all samples. The values of c/a are indicators of the extent of hexagonal ordering (Cheralathan *et al*., 2010). The values of c/a for all samples are relatively high, indicating the formed precursors have a well ordered layered structure. It was also found that the value of c/a decreases with increasing calcination temperature. This indicates that calcinated temperature at $810^{O}C$-$860^{O}C$ are proper temperature to obtain $LiNi_{0.6}Co_{0.2}Mn_{0.2}O_2$ with good electrochemical properties. In this temperature range, the sample calcinated at $860^{O}C$ shows lower crystalline size than that of sample calcinated at 810 ^{O}C, hence, we considered that the temperature of 860 ^{O}C is a proper temperature for calcination since the increase of crystalline size has the tendency to reduce the charging capacity of the material.

The effect of calcination temperature on the morphology of $LiNi_{0.6}Mn_{0.2}Co_{0.2}O_2$is shown in Figure 4-6. It can be clearly seen that the spherical morphology of precursor remained after sintering. However, the initial needle-like primary particle structure of precursor has completely changed to square shape or rectangle shape with the particle size in the range of 200-300 nm. According to the theory of crystal growth, increasing the calcinated temperature could facilitate the formation of primary particles, that is, the crystallite size will be increased (Cao *et al*., 2005). This is in accordance with the results of SEM observations. It also can be found that the size of primary particles calcinated at 910^{O}C is much larger than that of the other three samples calcinated at 760 ^{O}C, 810 ^{O}C and 860 ^{O}C. As we know, the diffusion of Li^+ is proportional to the particle size. However, if the particle size is too large, the diffusion of Li^+ needs much more time, especially at the end of the charge or discharge process. This will lead to the deterioration of electrochemical property. Thence, the sample calcinated at 910 ^{O}C indicates a worse electrochemical properties compared with other samples. The atomic ratio of Li:Ni:Co:Mn for the sample of $LiNi_{0.6}Co_{0.2}Mn_{0.2}O_2$ (860^{O}C) is determined to be 1.04:0.58:0.21:0.21, which is consistent with the theoretical composition of $Li_{1.05}Ni_{0.6}Co_{0.2}Mn_{0.2}O_2$.

The cycling performance of $LiNi_{0.6}Co_{0.2}Mn_{0.2}O_2$ at the current rate of 0.1 C (1C=160mAh g^{-1}) for the first three cycles and 0.5C for the last 40 cycles are shown in Figure 4-7a. With increasing calcination temperature from 760 ^{O}C to 860 ^{O}C, the initial delivered discharge capacities at 0.1C are improved from 122.2 mAh g^{-1} to 166.0 mAh g^{-1}. Further increasing the calcination temperature to 910 ^{O}C, its initial delivered discharge capacity at 0.1C decreased to 155.8 mAh g^{-1}. The initial delivered discharge capacity of samples sintered at 760 ^{O}C, 810 ^{O}C, 860 ^{O}C, 910 ^{O}C at 0.5C are 125.3 mAh g^{-1}, 130.9 mAh g^{-1}, 161.1 mAh g^{-1}, 128.3 mAh g^{-1} respectively. The sample calcinated at 760 ^{O}C delivers a lower initial discharged capacity than that the samples calcinated at other temperatures, the cells of former exhibits stable cyclability with high capacity of 124.8 mAh g^{-1} at 0.5C at the end of 40 cycles with a capacity retention of 99.6%. While the sample calcinated at 810 ^{O}C, 860 ^{O}C, 910 ^{O}C, about 90% of the initial discharge capacities for each sample are remained after 40 cycles.

EVs and renewable energy storage applications require LIBs with high rate capability (Fu *et al.*, 2014). The rate capacity of $LiNi_{0.6}Co_{0.2}Mn_{0.2}O_2$ prepared at various C-rates are presented in Figure 4-7b. The cells are firstly charged to 4.3V at 0.1C and then discharged at 0.1C, 0.2C, 0.5C, 1C and 2C for each 5 cycles. With increasing of the current density, the discharge capacity of all samples is decreased due to the function of polarization (Chen *et al.*, 2014).

The discharge capacity of sample LP7 calcinated at 860^{o}C shows the best rate electrochemical performance, where its average discharge capacities are 175.0 mAh g^{-1}, 170.4 mAh g^{-1}, 159.0 mAh g^{-1}, 146.4 mAh g^{-1} and 125.1 mAh g^{-1} at 0.1 C, 0.2 C, 0.5 C, 1 C and 2 C respectively. Sample calcinated at 810^{o}C shows better electrochemical properties at 0.1C and 0.2C than that of sample calcinated at 910 ^{o}C, while at a high rate (0.5C, 1C and 2C), the trends of electrochemical properties are quite similar. Sample calcinated at 760^{o}C shows the poorest electrochemical performances with 130.6 mAh g^{-1}, 125.2 mAh g^{-1}, 111.3 mAh g^{-1}, 96.3 mAh g^{-1} and 76.9 mAh g^{-1} at 0.1C, 0.2C, 0.5C, 1C and 2C respectively.

Based on the cycling performance and rate capacity of $LiNi_{0.6}Co_{0.2}Mn_{0.2}O_2$ prepared at different temperatures, the sample calcinated at $860^{O}C$ shows the best electrochemical performances, which is in agreement with the analysis of crystal structure. Figure 4-7c shows the cyclic voltammograms of $LiNi_{0.6}Co_{0.2}Mn_{0.2}O_2$ for different sintering temperature at third cycle. It can be seen that there is only one redox couple exhibits in the CV curve and the redox reaction is mainly attributed to redox transition of Ni^{2+}/Ni^{4+} (Yang et al., 2014), indicating that structure change from hexagonal to monoclinic does not happen between 2.7 and 4.3V. The electrochemical reversibility can be characterized by the voltage difference (ΔE_p) by the voltage difference between the anodic peak and cathodic peak (Zhao et al., 2015). The ΔE_p for the $LiNi_{0.6}Co_{0.2}Mn_{0.2}O_2$ sintered at 760 ^{O}C, 810 ^{O}C, $860^{O}C$ and $910^{o}C$ are 0.3626V, 0.4854V, 0.3424V and 0.5509V, respectively. $LiNi_{0.6}Co_{0.2}Mn_{0.2}O_2$ sintered at 860 ^{o}C exhibiting smallest ΔE_p implies that the layered structure of $LiNi_{0.6}Co_{0.2}Mn_{0.2}O_2$ can be stabilized and the polarization could be restrained at this sintering temperature, which also indicates that the sample has the best electrochemical performance. All these observations are consistent with its electrochemical performance as discussed earlier.

4.3.2.2 Effect of stirring speed

Figure 4-8 shows the XRD patterns of $LiNi_{0.6}Co_{0.2}Mn_{0.2}O_2$ cathode materials with various stirring speed. Based on all the diffraction peaks, the prepared $LiNi_{0.6}Co_{0.2}Mn_{0.2}O_2$ samples exhibit α-$NaFeO_2$ structure R-3m space group (No.166). The sharp peaks indicate all the samples have good crystallinity and no extra diffraction peaks from related secondary phases or impurities exist. All the XRD patterns show a clear split between the 006/012 and 108/110 peaks, indicating that the hexagonal structures are preserved among the materials. Table 4-3 summarized all the unit cell parameters, the intensity ratio of $I_{(003)}/I_{(104)}$ of $LiNi_{0.6}Co_{0.2}Mn_{0.2}O_2$. As the stirring speed is increased from 500 rpm to 1500 rpm, the value of c/a does not change much, indicating that a well-defined hexagonal layered structure was kept for all samples at a high value of c/a. The intensity ratio of $I_{(003)}/I_{(104)}$ exhibited that the samples prepared at 500 rpm (LP4) to 1100 rpm (LP6) except for LP2 has a certain level of cation mixing. The highest value of $I_{(003)}/I_{(104)}$ is 1.218 for the sample of LP2. This indicates that the small size of precursors could decrease the level of cation mixing. It is known that cation mixing can deteriorate the electrochemical properties of $LiNi_{0.6}Co_{0.2}Mn_{0.2}O_2$. The crystallite size of the above samples was also calculated according to XRD patterns using the Scherer equation.

$$D = \frac{0.89\lambda}{\beta COS\theta} \tag{4-1}$$

Where D is the crystallite size (nm), λ is the wavelength of the X-ray radiation (1.5418 Å), β is the full width half maximum and θ is the angle of diffraction. Here, the calculated crystallite sizes are based on the lattice plane of (003), (104) and (101). It can be seen that the crystallite sizes decreased from 57.6 nm to 33.6 nm with the increase of stirring speed from 500 rpm to 1500 rpm. Hence, we can expect that the best electrochemical performances can be got for the sample of LP2 because of its small crystallite size and low cation mixing.

The particle size distributions of $LiNi_{0.6}Co_{0.2}Mn_{0.2}O_2$ cathode materials prepared with different stirring speeds are observed in Figure 4-9 and detailed parameters are revealed in Table 4-5. A slight size increase phenomenon of all samples was observed after calcination process in comparison with the sizes of the precursors. This is due to the crystal growth during the calcination process. The samples of LP2, LP5 and LP6 have a uniform and symmetrical particle distribution after the calcination process. The particle size distribution of LP4 is more broader than other samples, indicating a slight aggregation happened after calcination. It was also concluded that the calcination process does not change the sizes of $LiNi_{0.6}Co_{0.2}Mn_{0.2}O_2$ so much. The sizes of LP2 still shows the lowest among all the samples.

Figure 4-10 shows the initial charge/discharge process of all samples prepared with different stirring speed and its cycle performances are evaluated at 0.1C and 0.5C. Table 4-6 lists a series of electrochemical data tested from Figure 4-10. As the stirring speed is increased from 500 rpm to 1500 rpm, the initial discharge capacity of $LiNi_{0.6}Co_{0.2}Mn_{0.2}O_2$ material increases correspondingly. The cycling performance of $LiNi_{0.6}Co_{0.2}Mn_{0.2}O_2$ material at 0.1 C rate for the first three cycles, and then 40 cycles at 0.5 C in order to investigate its retention capacity. As shown in Figure 4-9 and Table 4-5, the first cycle charge–discharge capacities of sample LP4 at 0.1 C is found to be 226 (144.8) mAh g^{-1}. And the first cycle discharge capacity of LP4 at 0.5 C is 121.7 mAh g^{-1}, After 40 cycles, the specific capacity of LP4 is 98.2 mAh g^{-1}, which corresponds to 80.7% of the initial capacity retention. Increasing the stirring speed from 500 rpm to 700 rpm, the initial columbic efficiency of LP5 is 89.7%, which is the highest among the samples. The relevant capacity retention at 0.5C was about 94.5 %, decreasing the discharge capacity from 149.7 (first cycle) to 141.5 mAh g^{-1} (40 cycles). It was also observed from Figure 10b that the capacity increased from 30 cycles and then declined. This is because of the following reasons. At the beginning of the reaction, the electrolyte has difficulty to enter into the particle due to its bigger particle size. However, after a dozen of the charge-discharge process, the electrolytes are fully soaked in the electrode, an increased capacity is obtained. This observation is also observed in the researches of Nie *et al* (2015). For the sample of LP6, the first cycle charge-discharge capacities at 0.1C are 177.2 (151.2) mAh g^{-1}. The discharge capacity at 0.5 C gradually decreases from 146.5 mAh g^{-1} to 123.2 mAh g^{-1}, which corresponds to 84.1% of capacity retention at the end of 40 cycles. However, for the sample LP2, the specific charge-discharge capacity at 0.1 C is 248.0 (176.0) mAh g^{-1}. The relevant capacity retention was about 85.5%, decreasing the discharge capacity from 176.3 to 150.8 mAh g^{-1} after 40 cycles. The higher initial discharge capacity and excellent rate capability could be attributed to its nano-sized primary particles and smaller micro-sized secondary particle, which are a favor for the lithium ion diffusion kinetics. As a higher stirring speed results in smaller primary particles, i.e. smaller crystallite size. As we discussed in the former section, the diffusion length of Li^+ is proportional to the particle size, that is, if the crystallite size of $LiNi_{0.6}Co_{0.2}Mn_{0.2}O_2$ is larger, the time for Li^+ to diffuse is much longer, especially at the end of charge or discharge (Zhang *et al*., 2010). Thence, LP2 shows the best charge/discharge capacity.

4.3.2.3 Effect of molar ratio of NH_3/MSO_4

Figure 4-11 shows the cycling performances of $LiNi_{0.6}Co_{0.2}Mn_{0.2}O_2$ cathode material prepared at the molar ratio of NH_3/MSO_4 cycled at 0.1C and 0.5C. The first three cycles are tested at 0.1C and the other 40 cycles are tested at 0.5C. Table 4-7 lists its relevant electrochemical data shown in Figure 4-11. It can be seen that the initial discharge capacity of $LiNi_{0.6}Co_{0.2}Mn_{0.2}O_2$ at 0.1C increases correspondingly with increasing the molar ratio of NH_3/MSO_4. However, the columbic efficiencies of powders at the high molar ratio of NH_3/MSO_4 are larger than that of powders at low molar ratio of NH_3/MSO_4. The columbic efficiencies of samples LP2 and LP7 are 71.0% and 64.4%, while the columbic efficiencies of samples of LP8, LP9 and LP10 are 83.6%, 89.3%, 85.3%, respectively. As for the cycling performances at 0.5C, all the samples show a gradual capacity fading during cycling. The discharge capacity of $LiNi_{0.6}Co_{0.2}Mn_{0.2}O_2$ also increased with the increasing of molar ratio of NH_3/MSO_4. The initial discharge capacity of LP2 and LP8 are 176.3 mAh g^{-1} and 158.6 mAh g^{-1}, with capacity retention rate of 85.3% and 82.2%. By contrast, the discharge capacity of LP9 and L10 are just 141.4 mAh g^{-1} and 130.8 mAh g^{-1}. In a comparison of all samples, LP7 shows the best cycling performances at 0.5 C rate in terms of capacity retention. According to the above results, it can be seen clearly that NH_3H_2O concentration does have an effect on the electrochemical performance of $LiNi_{0.6}Co_{0.2}Mn_{0.2}O_2$. NH_3H_2O could prevent phase separation and promote the formation of homogeneous ternary metal hydroxide. A proper NH_3H_2O concentration facilitates the formation of precursors with high purity and well crystallinity, which benefits the electrochemical performances of $LiNi_{0.6}Co_{0.2}Mn_{0.2}O_2$(Deng *et al*., 2010).

4.4 Conclusions

$Li(Ni_{0.6}Co_{0.2}Mn_{0.2})O_2$ have been prepared from LiOH and co-precipitated $Ni_{0.6}Co_{0.2}Mn_{0.2}(OH)_2$ precursors. The preparation conditions such as pH, themolar ratio of NH_3/MSO_4 and stirring speed adopted during the co-precipitation process have been examined. The main conclusions drawn from the investigations can be summarised as follows:

(1) The selection of pH, molar ratio of NH_3/MSO_4 and stirring speed is crucial and has a significant impact on the particle morphology and tap density. pH ranging between 11.4 to 11.6, the molar ratio of NH_3/MSO_4in the range of 0.4~1, stirring speed in the range of 700 rpm and 1500 rpm are deemed to be proper conditions for the formation of high tap density (>1.8 g cm^{-3}) of spherical ternary NCM622 precursor when using the lobed TC reactor.

(2) The electrochemical tests indicate that the synthesised material calcinated at 860°C has the best electrochemical properties. The particles prepared with smaller size show less cation mixing degree, which is beneficial to their electrochemical properties.

(3) This work has further demonstrated that the preparation of $Ni_{0.6}Co_{0.2}Mn_{0.2}(OH)_2$ precursor with a lobed TC reactor may provide a

promising route to obtain high performance cathode materials with good cycling performance and rate capability.

References

ATSUMI, T. N., Y.; KOBAYAKAWA, K.; NEGISHI, K.; YAMAZAKI, N.; SATO, Y. 2001. Particle size effect of $LiCoO_2$ powders on discharge performance of lithium ion batteries. *Electrochemistry Communications,* 69**,** 603-607.

CAO, H., ZHANG, Y., ZHANG, J. & XIA, B. 2005. Synthesis and electrochemical characteristics of layered $LiNi_{0.6}Co_{0.2}Mn_{0.2}O_2$ cathode material for lithium ion batteries. *Solid State Ionics,* 176**,** 1207-1211.

CHEN, C.-H., WANG, C.-J. & HWANG, B.-J. 2005. Electrochemical performance of layered $Li[Ni_xCo_{1-2x}Mn_x]O_2$ cathode materials synthesized by a sol–gel method. *Journal of Power Sources,* 146**,** 626-629.

CHEN, Y., ZHANG, Y., CHEN, B., WANG, Z. & LU, C. 2014. An approach to application for $LiNi_{0.6}Co_{0.2}Mn_{0.2}O_2$ cathode material at high cutoff voltage by TiO_2 coating. *Journal of Power Sources,* 256**,** 20-27.

CHERALATHAN, K. K., KANG, N. Y., PARK, H. S., LEE, Y. J., CHOI, W. C., KO, Y. S. & PARK, Y.-K. 2010. Preparation of spherical $LiNi_{0.80}Co_{0.15}Mn_{0.05}O_2$ lithium-ion cathode material by continuous co-precipitation. *Journal of Power Sources,* 195**,** 1486-1494.

DENG, C., ZHANG, S., FU, B. L., YANG, S. Y. & MA, L. 2010. Synthetic optimization of nanostructured $Li[Ni_{1/3}Mn_{1/3}Co_{1/3}]O_2$ cathode material prepared by hydroxide coprecipitation at 273K. *Journal of Alloys and Compounds,* 496**,** 521-527.

DONG, B., HUANG, X., YANG, X., LI, G., XIA, L. & CHEN, G. 2017. Rapid preparation of high electrochemical performance $LiFePO_4/C$ composite cathode material with an ultrasonic-intensified micro-impinging jetting reactor. *Ultrasonic Sonochemistry,* 39**,** 816-826.

FERIDUNA, O. K., SHINA, Y. & KRUMDICKA, G. 2016. Nickel-rich cathode precursor synthesis by taylor vortex reactor. *ECS meeting abstracts,* 03**,** 526.

FU, C., LI, G., LUO, D., LI, Q., FAN, J. & LI, L. 2014. Nickel-rich layered microspheres cathodes: lithium/nickel disordering and electrochemical performance. *ACS Applied Materials & Interfaces,* 6**,** 15822-15831.

JOUANNEAU, S., EBERMAN, K. W., KRAUSE, L. J. & DAHN, J. R. 2003. Synthesis, characterization, and electrochemical behavior of improved $Li[(Ni_xCo_{1-2x}Mn_x]O_2$ ($0.1 \leq x \leq 0.5$). *Journal of The Electrochemical Society,* 150**,** A1637-A1642.

KIM, J.-M., CHANG, S.-M., CHANG, J. H. & KIM, W.-S. 2011. Agglomeration of nickel/cobalt/manganese hydroxide crystals in Couette–Taylor crystallizer. *Colloids and Surfaces A: Physicochemical and Engineering Aspects,* 384**,** 31-39.

LEE, M.-H., KANG, Y.-J., MYUNG, S.-T. & SUN, Y.-K. 2004. Synthetic optimization of $Li[Ni_{1/3}Co_{1/3}Mn_{1/3}]O_2$ via co-precipitation. *Electrochimica Acta,* 50**,** 939-948.

LI, G., YANG, X. & YE, H. 2015. CFD simulation of shear flow and mixing in a taylor–couette reactor with variable cross-section inner cylinders. *Powder Technology,* 280**,** 53-66.

LIANG, L., DU, K., PENG, Z., CAO, Y., DUAN, J., JIANG, J. & HU, G. 2014. Co–precipitation synthesis of $Ni_{0.6}Co_{0.2}Mn_{0.2}(OH)_2$ precursor and characterization of $LiNi_{0.6}Co_{0.2}Mn_{0.2}O_2$ cathode material for secondary lithium batteries. *Electrochimica Acta,* 130**,** 82-89.

LIU, Q., DU, K., HU, G.-R., PENG, Z.-D., CAO, Y.-B. & LIU, W.-M. 2012. Characterization of $LiNi_{0.9}Co_{0.05}[Mn_{1/2}Mg_{1/2}]_{0.05}O_2$ solid solution for secondary lithium ion batteries. *Solid State Ionics,* 227**,** 23-29.

LIU, Z., YU, A & LEE, J. Y. 1999. Synthesis and characterization of $LiNi_{1-x-y}Co_xMn_y O_2$ as the cathode materials of secondary lithium batteries. *Journal of Power Sources,* 81-82**,** 416-419.

LUO, X., WANG, X., LIAO, L., GAMBOA, S. & SEBASTIAN, P. J. 2006. Synthesis and characterization of high tap-density layered $Li[Ni_{1/3}Co_{1/3}Mn_{1/3}]O_2$ cathode material via hydroxide co-precipitation. *Journal of Power Sources,* 158**,** 654-658.

MANTHIRAM, A., FU, Y. & SU, Y.-S. 2013. In charge of the world: electrochemical energy storage. *Journal of Physical Chemistry Letters,* 4**,** 1295-1297.

MAYRA, Q.-P. & KIM, W.-S. 2015. Agglomeration of Ni-rich hydroxide in reaction crystallization: effect of taylor vortex dimension and intensity. *Crystal Growth & Design,* 15**,** 1726-1734.

NIE, M., XIA, Y.-F., WANG, Z.-B., YU, F.-D., ZHANG, Y., WU, J. & WU, B. 2015. Effects of precursor particle size on the performance of $LiNi_{0.5}Co_{0.2}Mn_{0.3}O_2$ cathode material. *Ceramics International,* 41**,** 15185-15192.

PARK, S. H., KANG, S. H., BELHAROUAK, I., SUN, Y. K. & AMINE, K. 2008. Physical and electrochemical properties of spherical $Li_{1+x}(Ni_{1/3}Co_{1/3}Mn_{1/3})_{1-x}O_2$ cathode materials. *Journal of Power Sources,* 177**,** 177-183.

TANG, Y., LU, Y. & LUO, G. 2016. Controllable hydrothermal conversion from Ni-Co-Mn carbonate nanoparticles to microspheres. *Crystals,* 6**,** 156-168.

THAI, D. K., MAYRA, Q.-P. & KIM, W.-S. 2015. Agglomeration of Ni-rich hydroxide crystals in Taylor vortex flow. *Powder Technology,* 274**,** 5-13.

TIAN, J., SU, Y., WU, F., XU, S., CHEN, F., CHEN, R., LI, Q., LI, J., SUN, F. & CHEN, S. 2016. High-rate and cycling-stable nickel-rich cathode materials with enhanced Li^+ diffusion pathway. *ACS Applied Materials & Interfaces,* 8**,** 582-587.

WANG , Y., YANG , Z., QIAN , Y., GU, L. & ZHOU, H. 2015. New insights into improving rate performance of Lithium-rich cathode material. *Advanced Materials,* 27**,** 3915-3920.

WU, K., WANG, F., GAO, L., LI, M.-R., XIAO, L., ZHAO, L., HU, S., WANG, X., XU, Z. & WU, Q. 2012. Effect of precursor and synthesis temperature on the structural and electrochemical properties of Li($Ni_{0.5}Co_{0.2}Mn_{0.3}$)O_2. *Electrochimica Acta,* 75**,** 393-398.

XIA, Y.-F., NIE, M., WANG, Z.-B., YU, F.-D., ZHANG, Y., ZHENG, L.-L., WU, J. & KE, K. 2015. Structural, morphological and electrochemical investigation of $LiNi_{0.6}Co_{0.2}Mn_{0.2}O_2$ cathode material synthesized in different sintering conditions. Ceramics International, 41, 11815-11823.

YANG, S., WANG, X., YANG, X., LIU, Z., WEI, Q. & SHU, H. 2012. High tap density spherical Li[$Ni_{0.5}Mn_{0.3}Co_{0.2}$]O_2 cathode material synthesized via continuous hydroxide coprecipitation method for advanced Lthium-ion batteries. *International Journal of Electrochemistry,* 2012**,** 1-9.

YANG, X.-G., LENG, Y., ZHANG, G., GE, S. & WANG, C.-Y. 2017. Modeling of lithium plating induced aging of lithium-ion batteries: Transition from linear to nonlinear aging. *Journal of Power Sources,* 360**,** 28-40.

YANG, Z., LU, J., BIAN, D., ZHANG, W., YANG, X., XIA, J., CHEN, G., GU, H. & MA, G. 2014. Stepwise co-precipitation to synthesize $LiNi_{1/3}Co_{1/3}Mn_{1/3}O_2$ one-dimensional hierarchical structure for lithium ion batteries. *Journal of Power Sources,* 272**,** 144-151.

YUE, P., WANG, Z., PENG, W., LI, L., CHEN, W., GUO, H. & LI, X. 2011a. Spray-drying synthesized $LiNi_{0.6}Co_{0.2}Mn_{0.2}O_2$ and its electrochemical performance as cathode materials for lithium ion batteries. *Powder Technology,* 214**,** 279-282.

YUE, P., WANG, Z., PENG, W., LI, L., GUO, H., LI, X., HU, Q. & ZHANG, Y. 2011b. Preparation and electrochemical properties of submicron $LiNi_{0.6}Co_{0.2}Mn_{0.2}O_2$ as cathode material for lithium ion batteries. *Scripta Materialia,* 65**,** 1077-1080.

ZHANG, S., DENG, C., FU, B. L., YANG, S. Y. & MA, L. 2010. Synthetic optimization of spherical Li[$Ni_{1/3}Mn_{1/3}Co_{1/3}$]O_2 prepared by a carbonate co-precipitation method. *Powder Technology,* 198**,** 373-380.

ZHANG, Y., CAO, H., ZHANG, J. & XIA, B. 2006. Synthesis of $LiNi_{0.6}Co_{0.2}Mn_{0.2}O_2$ cathode material by a carbonate co-precipitation method and its electrochemical characterization. Solid State Ionics, 177**,** 3303-3307.

ZHAO, J., WANG, Z., GUO, H., LI, X., HE, Z., LI, T., 2015. Synthesis and electrochemical characterization of Zn-doped Li-rich layered Li[$Li_{0.2}Mn_{0.54}Ni_{0.13}Co_{0.13}$]$O_2$ cathode material. Ceramics International, 41**,** 11396–11401.

Figures

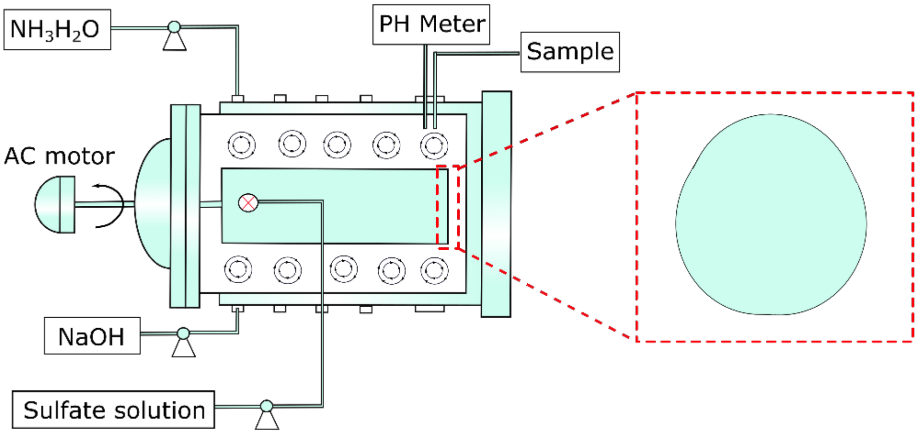

Figure 4-1. Schematic diagram of experimental system used for reaction crystallization of $(Ni_{0.6}Co_{0.2}Mn_{0.2})(OH)_2$ precursor by a TC reactor with a lobed inner cylinder

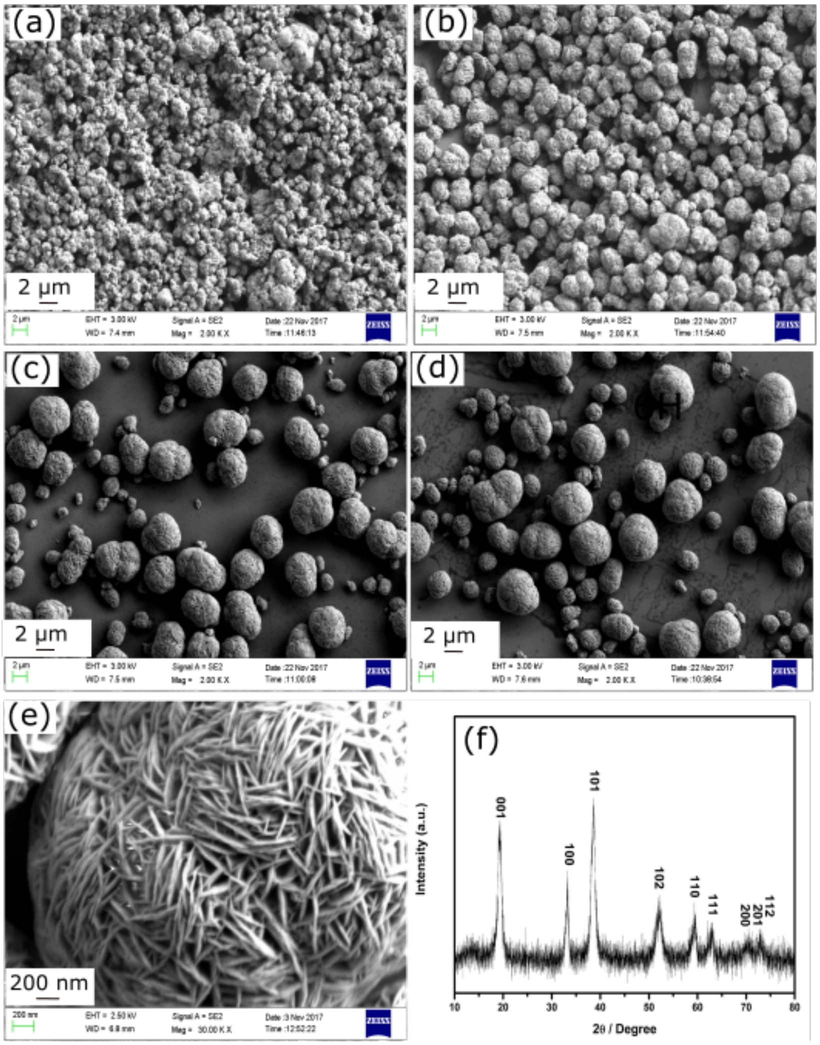

Figure 4-2. SEM images of $Ni_{0.6}Co_{0.2}Mn_{0.2}(OH)_2$ hydroxide prepared at 1500 rpm in terms of different reaction times: (a) 1h; (b) 2h; (c) 5h; (d) 6h; (e) Inner structure; XRD patterns of (f) the precursor P2

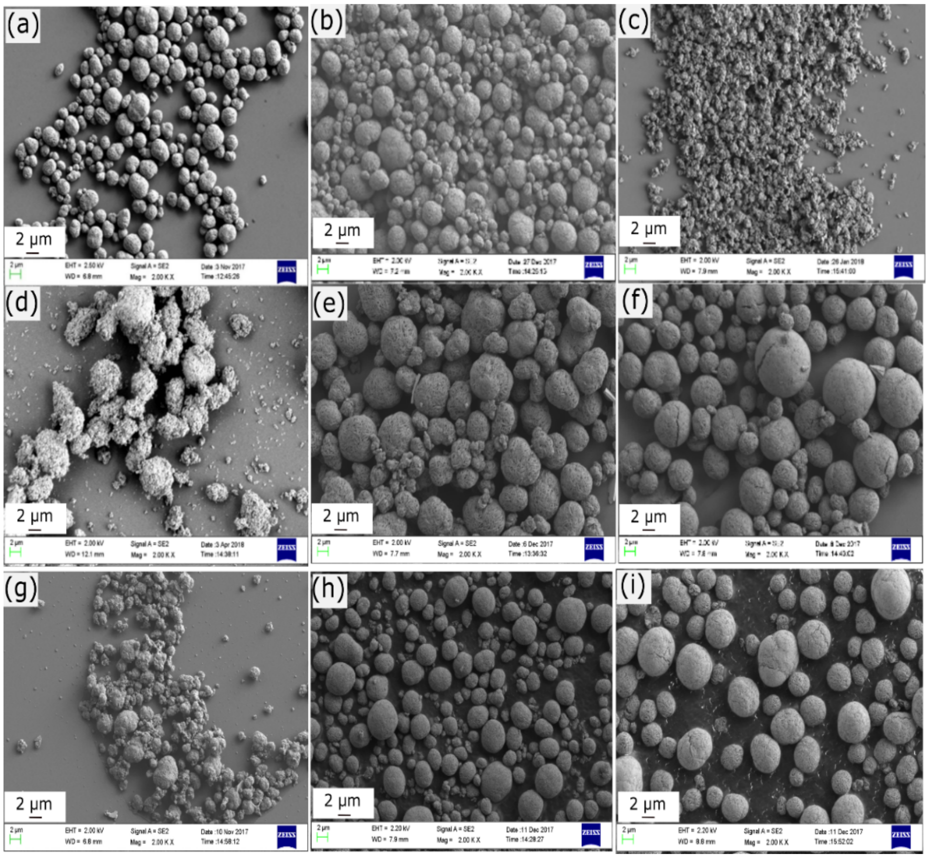

Figure 4-3.SEM images of $Ni_{0.6}Co_{0.2}Mn_{0.2}(OH)_2$ hydroxide prepared at different conditions: (a) pH= 11.0~11.2, 1500 rpm, molar ratio of NH_3/MSO_4 of 1; (b) pH= 11.4~11.6, 1500 rpm, molar ratio of NH_3/MSO_4 of 1;(c) pH= 12.0~12.2, 1500 rpm, molar ratio of NH_3/MSO_4 of 1; (d) pH= 11.4~11.6, 500 rpm, molar ratio of NH_3/MSO_4 of 1; (e) pH= 11.4~11.6, 700 rpm, molar ratio of NH_3/MSO_4 of 1; (f) pH= 11.4~11.6, 1100 rpm, molar ratio of NH_3/MSO_4 of 1;(g) pH= 11.4~11.6, 1500 rpm, molar ratio of NH_3/MSO_4 of 0.2; (h) pH= 11.4~11.6, 1500 rpm, molar ratio of NH_3/MSO_4 of 0.4;(i) pH= 11.4~11.6, 1500 rpm, molar ratio of NH_3/MSO_4 of 0.8

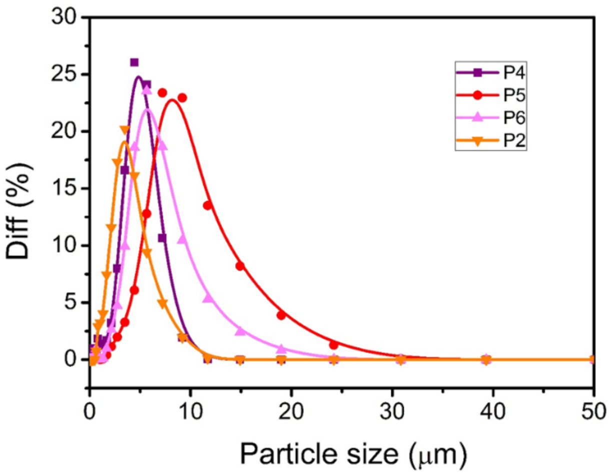

Figure 4-4. Particle size distribution of $Ni_{0.6}Co_{0.2}Mn_{0.2}(OH)_2$ precursor prepared with different stirring speed

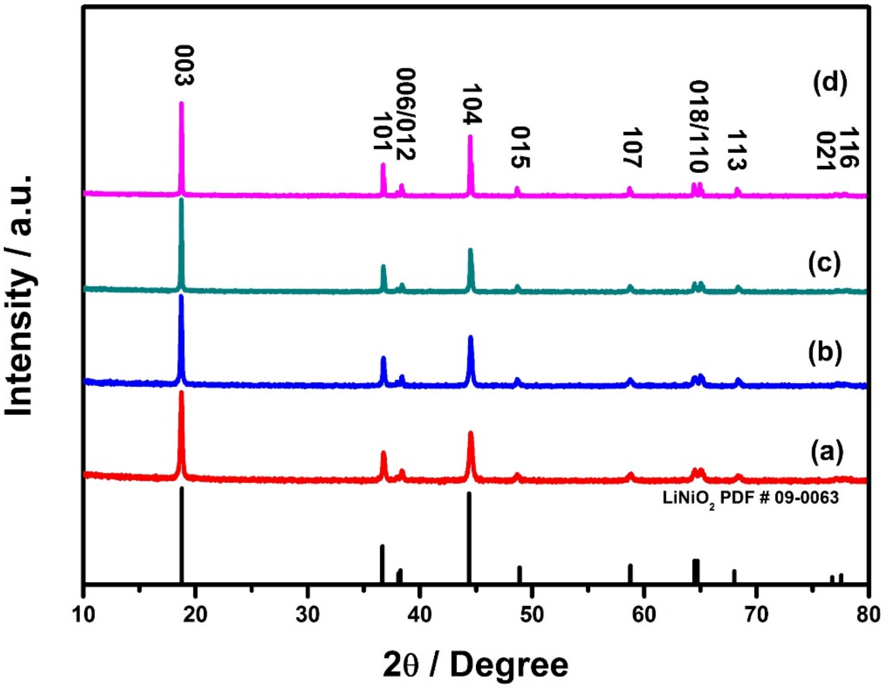

Figure 4-5. XRD patterns of $LiNi_{0.6}Co_{0.2}Mn_{0.2}O_2$ (LP7) calcinated at different temperature: a) 760^{O}C b) 810 ^{O}C c) 860^{O}C d) 910 ^{O}C

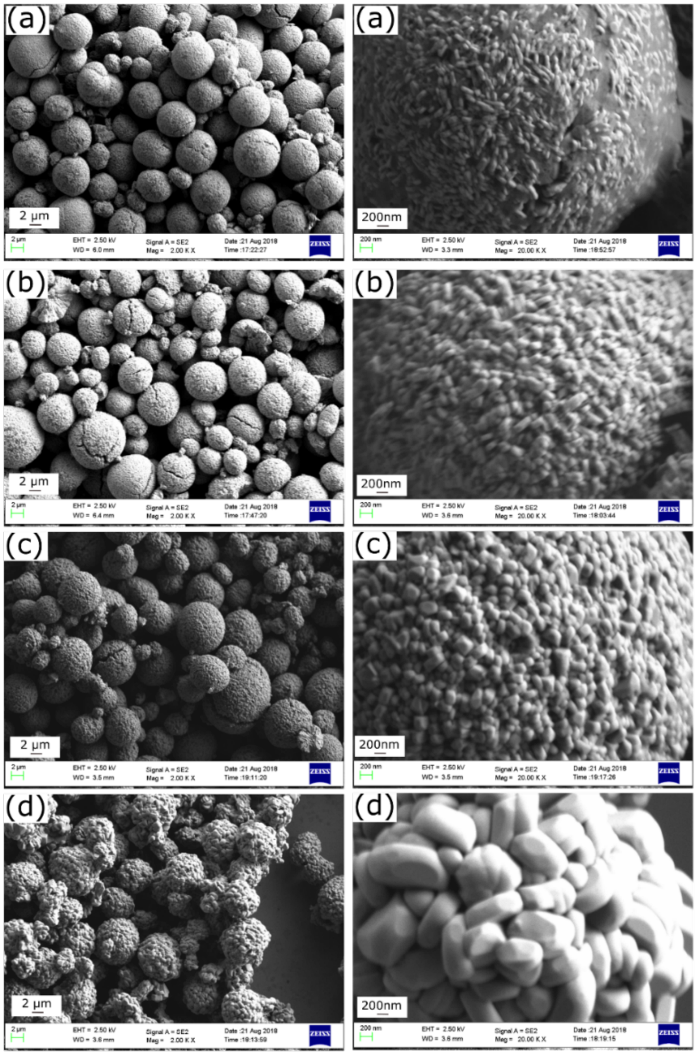

Figure 4-6. SEM images of $LiNi_{0.6}Co_{0.2}Mn_{0.2}O_2$ obtained at different calcinated temperature: a) 760^{O}C; (b) 810^{O}C; (c) 860^{O}C; (d) 910^{O}C (magnification: I=2000x and II=20, 000x)

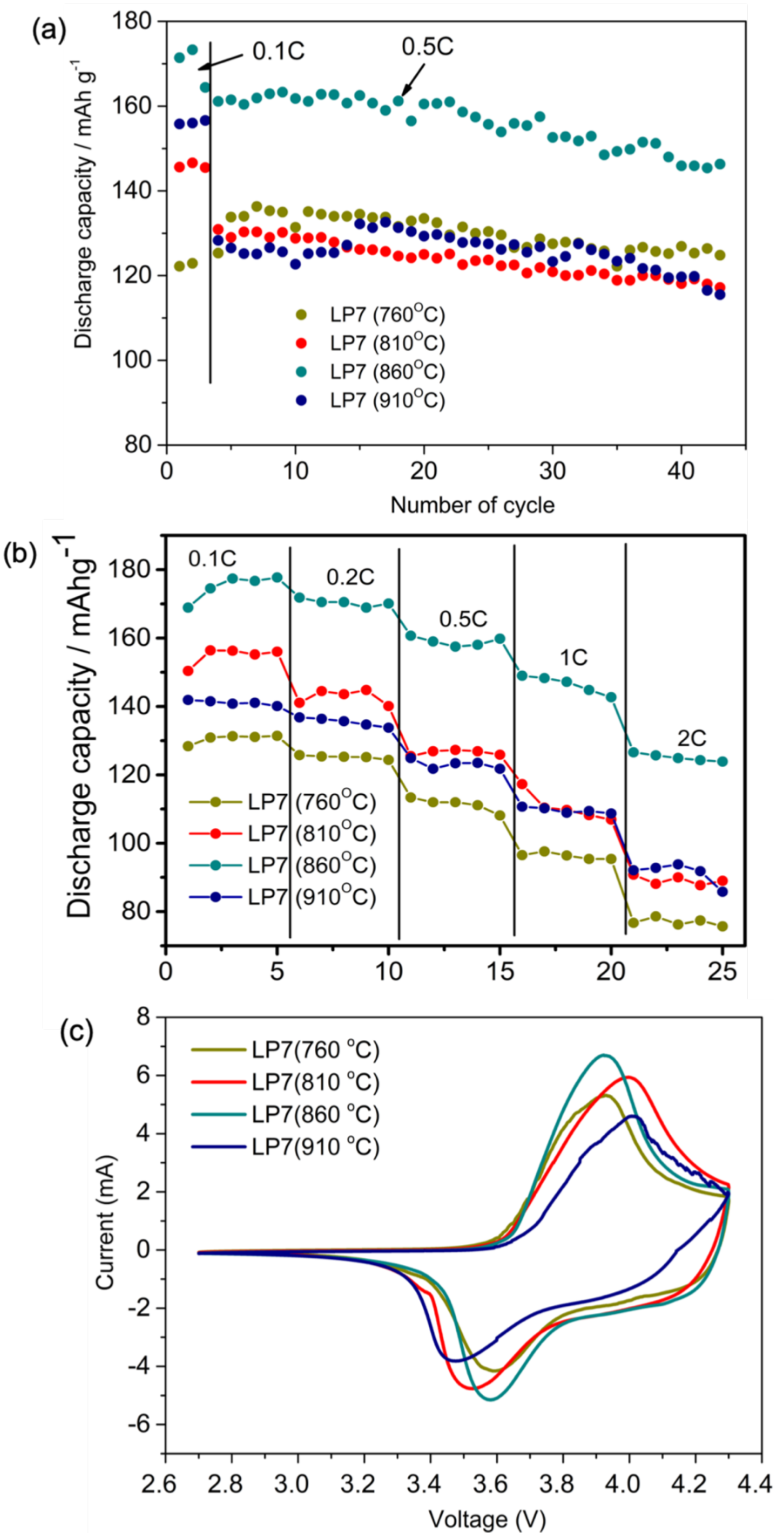

Figure 4-7. The Cycling performance of (a) $LiNi_{0.6}Co_{0.2}Mn_{0.2}O_2$ at 0.1 C and 0.5C; (b) rate capacity of $LiNi_{0.6}Co_{0.2}Mn_{0.2}O_2$ prepared at various C-rates; (c) cyclic voltammograms of $LiNi_{0.6}Co_{0.2}Mn_{0.2}O_2$ for different sintering temperature at third cycle

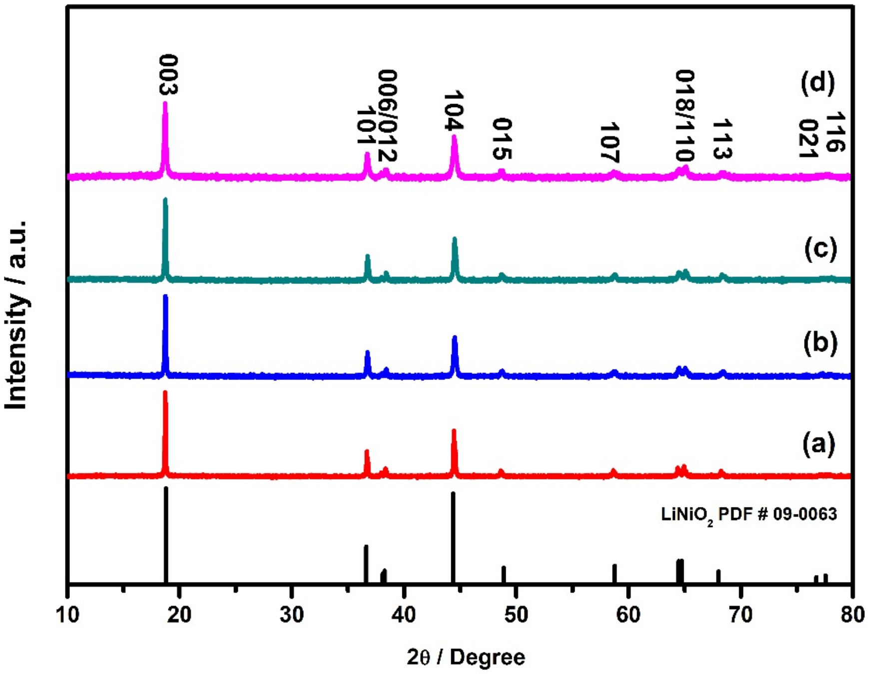

Figure 4-8. XRD patterns of $LiNi_{0.6}Co_{0.2}Mn_{0.2}O_2$ cathode materials with various stirring speeds: (a) 500 rpm (b)700 rpm (c) 1100 rpm (d) 1500 rpm

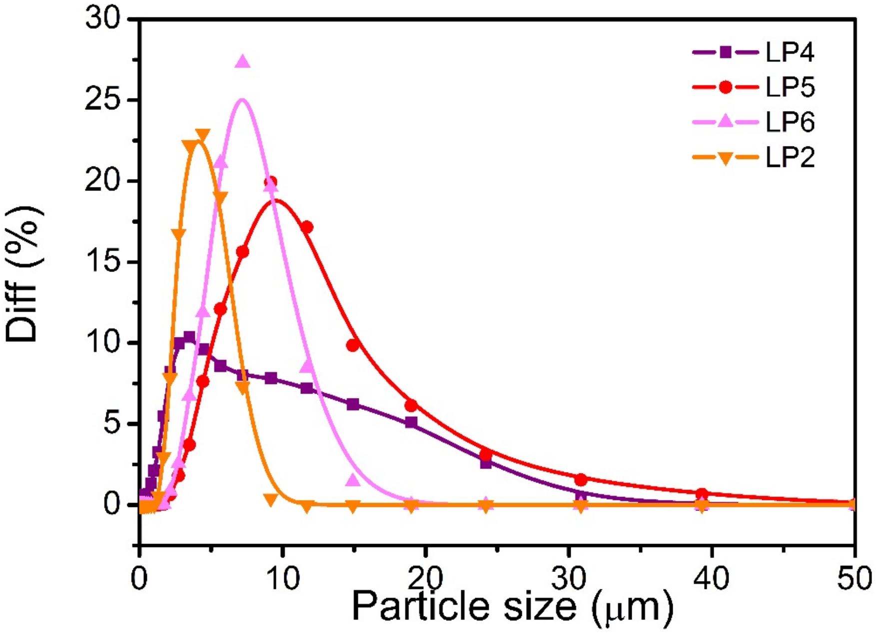

Figure 4-9. Particle size distribution of $LiNi_{0.6}Co_{0.2}Mn_{0.2}O_2$ cathode materials prepared with different stirring speed.

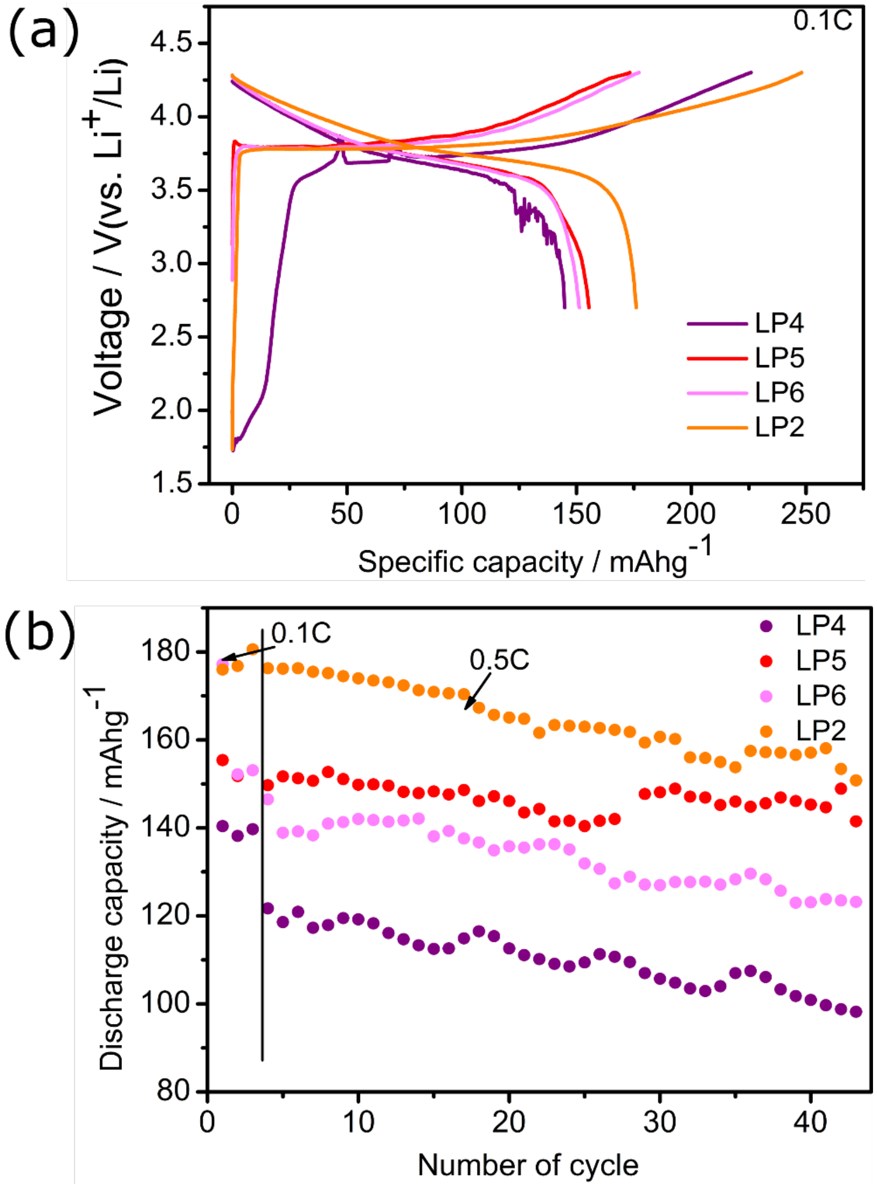

Figure 4-10. The initial charge-discharge curves of (a) LiNi$_{0.6}$Co$_{0.2}$Mn$_{0.2}$O$_2$ at 0.1 C; Cycling performance of (b) LiNi$_{0.6}$Co$_{0.2}$Mn$_{0.2}$O$_2$ at 0.1 C and 0.5C

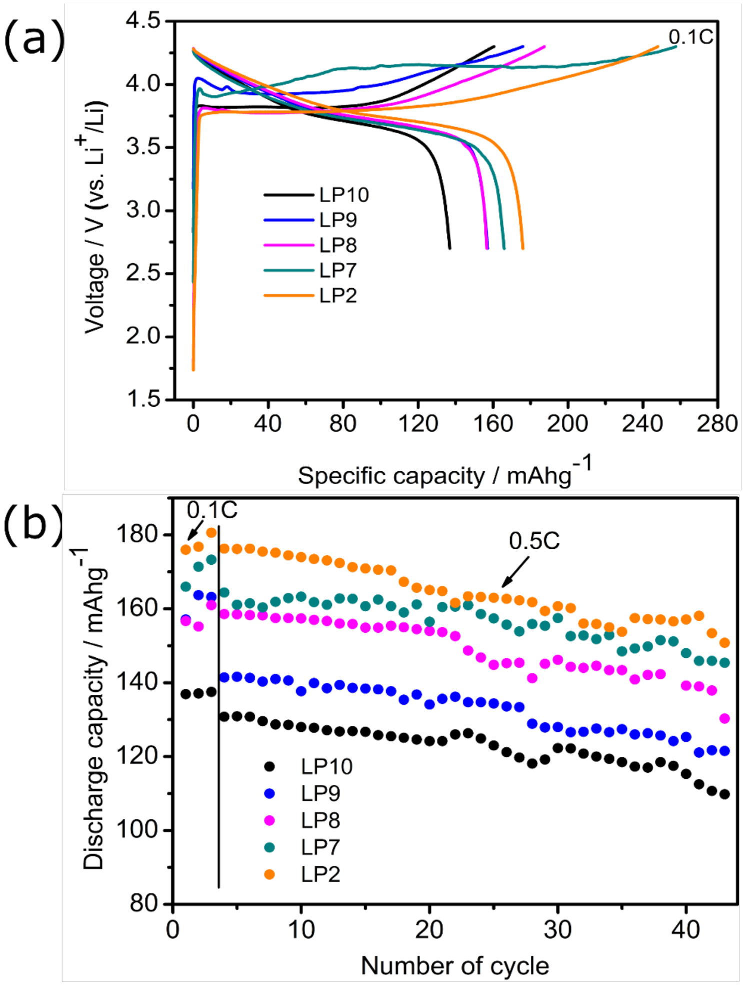

Figure 4-11. Cycling performance of $LiNi_{0.6}Co_{0.2}Mn_{0.2}O_2$ at different molar ratio of NH_3/MSO_4

Tables

Table 4-1. Detailed preparation conditions of $Ni_{0.6}Co_{0.2}Mn_{0.2}(OH)_2$ precursor

Precursor Name	**Calcinated Sample**	**Molar ratio of NH_3/MSO_4**	**Rotational Speed (rpm)**	**pH**	**Tap density of Precursor （cm^3 g^{-1}）**	**Tap density of $LiNi_{0.6}Co_{0.2}Mn_{0.2}O_2$ （cm^3 g^{-1}）**
P1	LP1	1	1500	11.0~11.2	1.75	--
P2	LP2	1	1500	11.4~11.6	1.79	2.18
P3	LP3	1	1500	12.0~12.2	1.45	--
P4	LP4	1	500	11.4~11.6	1.32	1.68
P5	LP5	1	700	11.4~11.6	1.86	2.11
P6	LP6	1	1100	11.4~11.6	1.94	2.32
P7	LP7	0.8	1500	11.4~11.6	1.91	2.36
P8	LP8	0.6	1500	11.4~11.6	1.88	2.21
P9	LP9	0.4	1500	11.4~11.6	1.76	2.09
P10	LP10	0.2	1500	11.4~11.6	1.53	1.86

Table 4-2. Particle size distribution parameters of $Ni_{0.6}Co_{0.2}Mn_{0.2}(OH)_2$ precursor prepared with different stirring speed

Precursor	**Stirring speed (rpm)**	**Size of Precursor**		
		D10 (µm)	**D50 (µm)**	**D90 (µm)**
P2	1500	1.415	3.169	5.788
P4	500	2.015	4.430	6.643
P5	700	4.333	8.068	14.333
P6	1100	3.037	5.585	9.893

Table 4-3. Unit cell parameters, the intensity ratio of $I_{(003)}/I_{(104)}$ and R-factor of $LiNi_{0.6}Co_{0.2}Mn_{0.2}O_2$

Sample Name	**Calcinated temperature （°C）**	**a**	**c**	**c/a**	**V/Å^3**	**I_{003}/I_{104}**
LP7	760	2.8652	14.2035	4.9572	100.98	1.264
LP7	810	2.8661	14.2077	4.9572	101.07	1.213
LP7	860	2.8657	14.2017	4.9558	101.01	1.290
LP7	910	2.8687	14.2047	4.9516	101.23	1.201

Table 4-4. Unit cell parameters, the intensity ratio of $I_{(003)}/I_{(104)}$ and R-factor of $LiNi_{0.6}Co_{0.2}Mn_{0.2}O_2$ prepared at different stirring speed

Sample Name	**Stirring speed (rpm)**	***a*/Å**	***c*/Å**	**V/Å^3**	***c/a***	**$I_{(003)}$ /$I_{(104)}$**	**Crystalline size (nm)**
LP2	1500	2.8723	14.2270	101.65	4.953	1.218	33.6
LP4	500	2.8713	14.2206	101.53	4.953	1.062	57.6
LP5	700	2.8708	14.2225	101.51	4.954	1.158	51.8
LP6	1100	2.8696	14.2285	101.47	4.958	1.073	51.9

Table 4-5. Particle size distribution parameters of $LiNi_{0.6}Co_{0.2}Mn_{0.2}O_2$ prepared with different stirring speed

Sample Name	**Stirring speed (rpm)**	**Size of Calcinated Sample**		
		D10 (µm)	**D50 (µm)**	**D90 (µm)**
LP2	1500	2.327	3.890	6.136
LP4	500	1.448	4.484	15.514
LP5	700	4.480	8.986	17.609
LP6	1100	3.881	6.740	10.269

Table 4-6. Electrochemical data of $LiNi_{0.6}Co_{0.2}Mn_{0.2}O_2$ prepared at different stirring speed at 0.1 C and 0.5 C-rate charge/discharge cycling

Sample Name	Stirring speed (rpm)	Initial charge capacity at 0.1C (mAh g^{-1})	Initial discharge capacity at 0.1C (mAh g^{-1})	Initial columbic efficiency (%)	First discharge capacity at 0.5 C	40th discharge capacity (mAh g^{-1}) at 0.5C	Capacity retention after 40 cycles (%)
LP2	1500	248.0	176.0	71.0	176.3	150.8	85.5
LP4	500	226.0	144.8	64.1	121.7	98.2	80.7
LP5	700	173.2	155.4	89.7	149.7	141.5	94.5
LP6	1100	177.2	151.2	85.3	146.5	123.2	84.1

Table 4-7. Electrochemical data of $LiNi_{0.6}Co_{0.2}Mn_{0.2}O_2$ prepared at molar ratio of NH_3/MSO_4 at 0.1 C and 0.5 C-rate charge/discharge cycling

Sample Name	**Molar ratio of NH_3/MSO_4**	**Initial charge capacity at 0.1C (mAh g^{-1})**	**Initial discharge capacity at 0.1C (mAh g^{-1})**	**Initial coulombic efficiency (%)**	**First discharge capacity at 0.5 C**	**40th discharge capacity (mAh g^{-1}) at 0.5C**	**Capacity retention after 40 cycles (%)**
LP2	1	248.0	176.0	71.0	176.3	150.8	85.5
LP7	0.8	257.6	166.0	64.4	164.4	145.4	88.4
LP8	0.6	187.4	156.7	83.6	158.6	130.3	82.2
LP9	0.4	176	157.1	89.3	141.4	121.5	85.9
LP10	0.2	160.5	136.9	85.3	130.8	109.8	83.9

Chapter 5

Numerical Prediction of the Electrochemical Properties of $LiNi_{0.6}Co_{0.2}Mn_{0.2}O_2$Cathode Material During the Discharge Process

Summary

Chapter 4 analyses the electrochemical property of $LiNi_{0.6}Co_{0.2}Mn_{0.2}O_2$ prepared at different conditions. From this chapter, the effects of calendaring and particle sizes on the physical and electrochemical properties of $LiNi_{0.6}Co_{0.2}Mn_{0.2}O_2$ cathode were investigated using numerical modelling approach. An electrochemical Pseudo 2D model accounted for the electrochemical reactions has been employed for numerical prediction of the electrochemical properties of the assembled coin cell. To validate the predictions, open circuit potential was obtained by fitting the experimental results of discharge at a low rate (0.1C) with the cell operating at the room temperature. Based on the SEM images obtained for $LiNi_{0.6}Co_{0.2}Mn_{0.2}O_2$ cathode materials, a suitable compaction load acting on the electrode for preparation of the cell should be in the range of 5~10 mpa. A relationship between the compaction load P and the porosity of the coating ε_l used in the equation of diffusion was obtained by fitting the experimental data with an exponential function. The numerical predictions show that the the first discharge capacities of the samples with applying the compaction load of 0, 5, 10, 15 and 20 MPa are 95.0, 181.1, 161.9, 212.4 and 137.6 mAh g^{-1}, respectively, at 0.1C rate, consistent with the experimental data. The discharge curves based on the numerical predictions indicate that the discharge capacity drops rapidly when the compaction load changes 15 to 20 MPa. The simulation results reaffirm that the discharge capacity increases with reduction of the particle radius. The consequence of reduction in the particle size of active materials is the improvement on the solid phase diffusion. The parameters obtained from the numerical modelling can serve as the references for the determination of the electrochemical properties of the coin battery cell of different discharge capacities when using the numerical modelling.

Keywords: calendaring, $LiNi_{0.6}Co_{0.2}Mn_{0.2}O_2$, compaction load, solid phase diffusion coefficient

5.1 Introduction

High specific energy density Lithium-ion batteries (LIBs) means the needs for the development of high rate LIBs. Such developments require the optimisation of the design parameters such as the thickness of electrode, porosity and particle size. As these design parameters are also variable for different LIBs cathode materials, it will be time-consuming and expensive to optimise these design parameters via experimental approach. Adoption of suitable mathematical modelling and numerical simulation may provide guidelines for obtaining the best design parameters so that decent electrochemical performance of the battery can be attained. Consequently, the number of required experiments can be significantly reduced. The current chapter attempts to use an electrochemical Pseudo 2D model that has accounted for the electrochemical reactions for numerical prediction of the electrochemical properties of the assembled coin cell.

A number of researchers have studied the effects of various design parameters on LIBs by employing experimental and simulation-based optimization methods. Meyer *et al.* (2017, 2018) have reported that by controlling the compaction process, the performance-optimized pore structure in the LIBs can be determined. They obtained an exponential relation between the porosities of electrodes and applied line load. Hosseinzadeh *et al.* (2018) adopted a multi-layered porosity model based on 3D electrochemical-thermal model to study the thickness and height of the electrode on a Lithium-ion battery. Their results have shown that a multi-layered porosity distribution across the thickness of the electrode has better battery performance than the case of porosity changes along the electrode height. Newman and Tiedemann (1975) have developed a porous electrode theory in order to maximize the energy density in their pioneer work. In the work, the activation and concentration polarization were neglected in the derivation for the constant-current discharging of an electrode. The maximum energy density is found to be associated with the existence of higher fraction of active material. Doyle *et al.* proposed a Pseudo-two-dimensional (P2D) model for simulation of LIBs based on the combination porous electrode theory with concentrated solution theory (Doyle *et al*. 1993; Darling and Newman;1997; Darling and Newman, 1998). The model now has been well accepted for simulation of the electrochemical reaction of LIBs and is used for prediction of the performance of the battery and for estimation of the parameters at different conditions with high accuracy. Based on the P2D model, Yang *et al*. (2016) further proposed an electrochemical-thermal Li-ion battery model to investigate the charging polarization characteristics. The influence factors such as $LiPF_6$ concentration, particle radius was evaluated according to the polarization properties. Appiah *et al*. (2016) also proposed the use of a nonlinear least squares technique to study the effect of cathode thickness and porosity on Li transport. They found that thicker electrodes with a lower porosity requires a longer time for discharge than that of thinner electrodes with high porosity. Ashwin *et al*. (2017) proposed a battery pack model to predict the cell variation under constant voltage charging and discharging. The model has integrated the effects such as ageing, thermal and porosity of the precursor materials. Based on their model, it was found that the individual cells develop uniform SEI growth without significant split current variation (Ashwin *et al*., 2017). The use of 3D microstructure-based models to simulate the battery performance can be also found in the literature (Stephenson *et al*., 2011).

In spite of the previous studies and attempts on the numerical simulation and experiments, reliable prediction of the electrochemical performance of the nickel-rich $LiNi_{0.6}Co_{0.2}Mn_{0.2}O_2$ cathode remains challengeable. The current chapter is thus to attempt to study the calendaring effects on the physical and electrochemical properties of $LiNi_{0.6}Co_{0.2}Mn_{0.2}O_2$ cathode by means of numerical simulation and experimental validation. A relationship between the coating porosity and compaction load was proposed through the parameter estimation. Adoption of the P2D model that incorporates our parameters for numerical simulation of the electrochemical performance of the assembled coin cells has demonstrated a high accuracy in prediction of the electrochemical behaviours for discharge process. The effect of particle size on the solid phase diffusion of LIBs was also studied in this chapter.

5.2 Mathematical Modelling and Numerical Simulation

5.2.1 Mathematical Model Description

In order to model its galvanostatic discharge curve, Figure 5-1 shows the computational domain of the three main components of the NCM622 half-cell battery: the lithium foil as an anode electrode, the separator and the NCM622 as a cathode electrode. The following assumptions have been introduced for P2D model and the numerical simulation:

(1) The positive electrode is a porous medium which includes electrolyte and porous active particles in a solid phase.

(2) The active materials are simplified as uniform spherical particles.

(3) During the discharge process, the Li-ion transports from the Lithium metal to the positive electrode. It was also assumed that Li-ions move from the surface of the particle of the positive electrode towards the entre along the radius direction (r) of the particle.

(4) The transport of Li^+ is along the x-direction in the electrolyte phase. The electrons only transport in the conductive phase between the current collector and the active material.

The electrochemical reactions at the negative and positive electrode can be described by:

For Negative electrode

$$L_i \rightarrow L_i^+ + e^- \tag{5-1}$$

For Positive electrode:

$$\mathrm{Li}_{x-1}\mathrm{MO}_2 + Li^+ + e^- \rightarrow \mathrm{Li}_x\mathrm{MO}_2 \tag{5-2}$$

Where M is the total transition metal NCM; *x* is the number of moles of lithium present in the cathode.

5.2.2 Governing Equations

Based on the assumptions in subsection 5.2.1, the Pseudo two-dimensional model (P2D) adopted in this chapter is basically similar to that proposed by Newman *et al.* (1975) while the models with modifications can be also found, for example, in the work of Marc Doyle (1993) and, Xu and Wang (2017) amomg others. The model couples the equations of charge conservation, mass conservation, and electrochemical reactions. The charge conservation in both the solid phase and the electrolyte phase obeys the rule of Ohm's law. The mass conversation describes the diffusion of Li ion in the solid phase and migration of Li ion in the electrolyte phase. The diffusion process of Li ions is driven by concentration gradient whilst the migration process is driven by potential gradient. Since the electrochemical reaction only takes place at the surface of the negative lithium metal, the effect of thickness of the model geometry can be ignored as the electronic conductivity of the lithium metal is very high. The electrochemical reaction kinetics is described by the Butler-Volmer equation which can be used to determine the local reaction rate and potential.

Charge conservation.- The electrical current density (i_s) flowing through the solid phase can be described by Ohm's law as follows:

$$i_s = \sigma_s \varepsilon_s^{\beta_s} \frac{\partial \varphi_s}{\partial x} \tag{5-3}$$

Where i_s is the electrical current density in the solid phase, σ_s is the electrical conductivity, β_s is the Bruggeman's constant for the conductive phase. φ_s is the electrical potential in the solid phase. The ionic current density (i_l) passing through the electrolyte phase (assuming one-dimensional case) can also be expressed according to Ohm's law, given by

$$i_l = k_{l,eff} \frac{\partial \varphi_l}{\partial x} + k_{D,eff} \frac{\partial ln c_l}{\partial x} \tag{5-4}$$

$$k_{l,eff} = k_l \varepsilon_l^{\beta} \tag{5-5}$$

$$k_{D,eff} = \frac{2RTk_{l,eff}}{F}(n_+ - 1)(1 + \frac{\partial lnf_\pm}{\partial c_l}) \quad (5\text{-}6)$$

Where $k_{l,eff}$is the effective ionic conductivity of electrolyte phase, $k_{D,eff}$ is the effective diffusional conductivity as defined in the concentrated solution theory, k_l is the ionic conductivity of the electrolyte, ε_l is the porosity of the electrode, and β is the Bruggeman porosity exponent,$\varphi_l$describes the potential in the electrolyte phase, c_l is the concentration of lithium ions in the electrolyte phase, $f_\pm$ is the average molar activity coefficient, which is assumed to be constant, R is the universal gas constant, T is the absolute temperature, n_+ is the transferring number of lithium ions in the electrolyte phase.

The conservation of charge in the electrode can be expressed if the dimensional aspect ratio is large for the electrolyte

$$\frac{\partial i_s}{\partial x} = -S_a j_n \quad (5\text{-}7)$$

$$\frac{\partial i_l}{\partial x} = S_a j_n \quad (5\text{-}8)$$

Where j_n is the local charge transfer current density per unit area of the solid-electrolyte interface, and S_a stands for the volume-specific surface area. $S_a j_n$ can be thought of the volume-specific rate of reaction.

The reference potential at the separator/negative electrode and the conservation boundary condition for the ionic current density throughout the electrode can be specified as

$$\varphi_s|_{x=0} = 0 \tag{5-9}$$

$$k_{l,eff}\frac{\partial\varphi_l}{\partial x} + k_{D,eff}\frac{\partial lnc_l}{\partial x}|_{x=0} = k_{l,eff}\frac{\partial\varphi_l}{\partial x} + k_{D,eff}\frac{\partial lnc_l}{\partial x}|_{x=L_{sep}} = \frac{I_{app}}{\mathrm{A}} \tag{5-10}$$

Where I_{app} is the applied current of 1D computational domain, and A is the surface area of the electrode, which can be measured experimentally. As the electron cannot transport from the positive electrode to the separator due to the property of separator, one has the boundary condition which can be expressed as

$$\sigma_{s,eff}\frac{\partial\varphi_s}{\partial x}|_{x=L_{sep}} = 0 \tag{5-11}$$

Also, zero electrolyte current exists at the current collector:

$$k_{l,eff}\frac{\partial\varphi_l}{\partial x}|_{x=L_{sep}+L_{pos}} = k_{D,eff}\frac{\partial lnc_l}{\partial x}|_{x=L_{sep}+L_{pos}}=0 \tag{5-12}$$

Mass conservation.- In the solid phase, the mass conservation of Li^+ in the active material satisfies the Fick's second law of diffusion. Under the spherical coordinates, this can be expressed as

$$\frac{\partial c_s}{\partial t} = \frac{D_s}{r^2}\frac{\partial}{\partial r}(r^2\frac{\partial C_s}{\partial r}) \tag{5-13}$$

Where $c_s(x,r,t)$ is the concentration of lithium in the active material particles of the electrode, t is the time, $D_{s,eff}$ represents the effective diffusion coefficient of lithium in the solid phase, r is the radial coordinate inside a spherical particle. Here, D_s is independent of the radial coordinate r if the active material is homogeneous. The zero mass flux of lithium ions at the center of the spherical particle (r=0) gives the boundary condition

$$D_s\frac{\partial c_s}{\partial r}|_{r=0} = 0 \tag{5-14}$$

While the Li^+ at particle surface (r=R) gives another boundary condition

$$D_s \frac{\partial c_s}{\partial r}|_{r=R} = -\frac{j_n}{F} \quad (5\text{-}15)$$

On the other hand, the mass conservation of lithium ion in the electrolyte can be described by Eq. 5-16.

$$\varepsilon_l \frac{\partial c_l}{\partial t} = \frac{\partial}{\partial t}\left(D_{l,eff} \frac{\partial c_l}{\partial x}\right) + \frac{1-n_+}{F} j_n \quad (5\text{-}16)$$

$$D_{l,eff} = D_l {\varepsilon_l}^{\beta} \quad (5\text{-}17)$$

where $c_l(x,t)$ is the concentration of lithium ions in the electrolyte phase, ε_l is the porosity, n_+ is the transference number of lithium ions, $D_{l,eff}$ is the effective diffusion coefficient of lithium ions in the electrolyte phase, D_l is the reference coefficient, and β is the Bruggeman porosity exponent. That the porosity ε_l is independent of the concentration of lithium ions in the electrolyte phase has been assumed here. It should be noted here that no mass flux of lithium ions takes place in the electrolyte at cathode or anode, i,e, current collector interface, which yields the boundary condition:

$$\frac{\partial c_l}{\partial x}|_{x=0} = \frac{\partial c_l}{\partial x}|_{x=L_{sep}+L_{pos}} = 0 \quad (5\text{-}18)$$

The initial electrolyte concentration $c_{l,0}$, and the initial concentration of the NMC cathode $c_{s,0}$ have been set 1000 mol m^{-3} and 16560 mol m^{-3}, respectively.

Electrochemical reaction kinetics and the interface.- The local charge transfer current density (j_n) can be estimated based on the Butler-Volmer equation for electrode kinetics:

$$j_n = F k_0 c_l^{\alpha_a} (c_{s,max} - c_{s,surf})^{\alpha_a} c_{s,surf}^{a_c} \left\{exp\left(\frac{\alpha_a F\eta}{RT}\right) - exp\left(\frac{-\alpha_c F\eta}{RT}\right)\right\} \quad (5\text{-}19)$$

where k_0 is the reaction rate constant, $c_{s,max}$ is the maximum lithium ion concentration in the solid phase, $c_{s,surf}$ is the lithium ion concentration at the particle surface. α_a and α_c are the anodic and cathodic charge transfer coefficients, η is the local surface potential and F denotes the Faraday constant. The local surface potential η can be estimated by

$$\eta = \varphi_s - \varphi_l - U_{eq} - j_n R_{film} \tag{5-20}$$

where U_{eq} is the open circuit potential ($U_{eq} = U_{eq}(\frac{C_{s,surf}}{C_{s,max}})$), R_{film} is film resistance.

5.2.3 Numerical Simulation

COMSOL Multiphysics 5.3 has been used to solve the Pseudo 2D electrochemical model presented in section 5.2.2. The dependent variables of the model, the potential distribution $\varphi_s(x,t)$, $\varphi_l(x,t)$, concentration distributions $c_s(x,t)\, c_l(x,t)$ in the solid phase and electrolyte phase, are solved, which are subsequently used to evaluate the cell voltage according to the following expression:

$$V_{cell}(t) = \varphi_s\left(L_{sep} + L_{pos}, t\right) - \varphi_s(0,t) \tag{5-21}$$

5.3 Parameter estimation

Table 1 lists the parameters for the mathematical model including either transport, kinetic, or design parameters. The parameters were obtained either from the literature or from the experimental validation measurement. Those kinetic values were selected based on the comparisons to those reported in the literature. The Li-ion diffusion coefficients for all the cathodes were obtained by fitting the data of discharge voltage with different thickness of cathodes. For the positive electrode, all the particles are assumed to have the same size.

5.3.1 Concentration Dependent Parameters

Equilibrium potential: To validate the model, the potential based on the electrochemical performance of NCM622 at the 0.1C rate is served as the open circuit potential (OCP) of the battery as shown in Figure 5-2. The fitting of the OCP can be approximated by

$$U_{eq}(\mathrm{NCM622}) = -100.5x^{10} + 257.0x^{8} - 246.0x^{6} + 110.0x^{4} - 23.77x^{2} + 5.957 \ (0.3 < x < 1) \quad (5\text{-}22)$$

Relation (5-22) is similar to the work reported by Ramadass *et al.* (2004) and Li *et al.* (2013).

Liquid conductivity: The concentration dependent liquid conductivity was estimated from the conductivity of the liquid electrolyte (1M $LiPF_6$) resolved in ethylene carbonate (EC) and ethyl methyl carbonate (EMC) (3:7, v/v)) in COMSOL database, which takes the following empirical expression:

$$\kappa_l = 1.036\left(\frac{1.25(c_l/1000)}{0.7301+0.7547(c_l/1000)^3-0.1518(c_l/1000)^4}\right) \quad (5\text{-}23)$$

where c_l is the concentration in electrolyte and κ_l is the electrolyte conductivity. Here, the changes in the Li electrolyte conductivity have been described to be associated with the ion liquid concentration (Appiah *et al.*, 2016).

5.3.2 Estimation of Porosity

When the volume of pores in the electrode is filled with electrolyte, the electrode porosity $\varepsilon_l$is defined as the porosity (volume fraction of electrolyte) relative to the volume of the bulk electrode, ε_s is volume fraction of the solid phase relative to the volume of the bulk electrode. Both volume fractions can be defined according to

$$\varepsilon_l = \frac{V_l}{V} \tag{5-24}$$

$$\varepsilon_s = \frac{V_s}{V} \tag{5-25}$$

$$\varepsilon_l + \varepsilon_s = 1 \tag{5-26}$$

$$V = V_l + V_s \tag{5-27}$$

Where V is the total volume of the electrode consisting of the volume of electrolyte V_l and volume occupied by active material V_s. There are several microstructural parameters such as particle size, particle packing, particle shape and the distribution of particle sizes that affect the porosity. A common assumption imposed in present is to simplify the solid electrode material as a collection of spheres with identical size. Under this assumption, the volume of the active material (solid phase) can be estimated:

$$V_s = \frac{m_s}{\rho_s} \tag{5-28}$$

Where the terms m_s and ρ_s denote the mass and density of the active material, respectively.

V can be defined by

$$V = A \cdot L \tag{5-29}$$

with A the area of the electrode (m^2) and L the thickness of the electrode coating. The SEM images of the NCM materials before and after compaction are shown in Figure 5-3. As can be seen from Figure 5-3a that the spherical NCM particles distribute randomly in the cathode after compacting and stack together with Super P and PVDF. It has been observed that the aggregated primary particles have an average size of 200~300 nm, which is formed from the large secondary particles. The D_{50} of NCM materials was found to be about 6.471 µm, as can be seen from Figure 5-3j. The voids among the primary particles decrease when the compression is applied, which benefits the penetration of electrolyte. The compaction process results in decreasing in the thickness of the coating. Based on the observation on the cross sections of NCM cathodes shown in Figure 5-3e to Figure 5-3f, the original thickness of NCM cathode decreases from 47 µm to 20.4 µm as the compaction loading is increased from 0 to 5 MPa. Increasing the compacting loading from 10 to 20 MPa gives out an increase in the thickness of the coating, from 33.3 30.4 µm. When the compaction loading is further increased from 15 and 20 MPa, the surface of materials starts to crack, different from the other three materials with less compaction loading. During the process of compaction, particles are experiencing the deformation in a means of particle-particle rearrangement which is associated with particle friction (Meyer *et al.*, 2017). When the compaction forces exceed the critical value, the material cannot stand and the crack takes place. The observation based on the SEM images obtained in the present work suggests that a suitable range of compaction loading for the electrode will be 5~10 MPa.

It is expected that the thickness of the coating is related to the compaction loading. Considering the surface density of the electrode, the porosity of the electrode can be estimated using equations (5-24) to (5-29). The estimated porosity of the coating (ε_l) is plotted against the compaction loading as shown in Figure 5-4. An empirical relationship between the compaction loading P and porosity of the coating ε_l is obtained by fitting the experimental data of Meyer *et al* (2018), given by

$$\varepsilon_l = 0.7848 + 0.09542e^{(-0.6278P)} \tag{5-30}$$

As listed in Table 5-2, when the compaction loading increases from 0 to 5 MPa, the coating porosity decreases from 0.8802 to 0.7891. While the compaction loading increases from 10 to 20 MPa, the coating porosity changes little. The ultimate coating porosity is estimated to be about 0.7850, applicable for the range of compaction loading of 5 to 20 MPa.

5.4 Model Validation

Electrochemical performance (charge voltage) of $LiNi_{0.6}Co_{0.2}Mn_{0.2}O_2$ was measured in CR2032 coin-type cells. All the coin cells are composed of a lithium metal anode, $LiNi_{0.6}Co_{0.2}Mn_{0.2}O_2$ cathode and Celgard 2400 microporous membrane. The cathode consists of 80 wt.% of $LiNi_{0.6}Co_{0.2}Mn_{0.2}O_2$, 10 wt.% of Super P as a conducting agent and 10 wt.% of polyvinylidene fluoride (PVDF) as a binder. All these materials were dispersed in N-methyl pyrrolidinone (NMP) and stirred for 8 hours to make the slurry. The prepared slurry was coated uniformly onto an aluminium foil and then dried in an oven for 8h at 80 ^{O}C. After drying, the electrodes were cut into the form of 12 mm diameters disks. Calendaring of electrodes was performed by a compaction machine (shown in Figure 5-5) with stainless steel disc of 90 mm in diameter. The electrodes were compressed by stainless steel disc with different compaction loads. The assembly of all the cells is carried out in an argon-filled glove box. These charge-discharge characteristics were measured between 2.7–4.3 V at a desired current density (1C=160 mAh g^{-1}) using CT2001A land instrument.

Model validation in the present work was conducted by a wide range of C-rates for the coin cell samples prepared at different compaction load. Figure 5-6 shows the comparisons of the discharging voltage at 0.1C, 0.2C, 0.5C, 1C and 2C among the coin cell samples with compaction loading of 5 and 10 MPa between the experimental data obtained at room temperature and simulated results. As mentioned in Section 5.3.2, an estimation of porosity has been performed based on the compaction load. The input parameters for the model used for numerical simulation of the discharge voltage using two typical samples with compaction loading of 5 and 10 MPa are given in Table 5-1 and 5-3. For the sample with compaction loading of 5 MPa (shown in Figure 5-6a), the prediction agrees well with the experimental data at 0.1C, 0.2C, 0.5C and 1C. However, simulation data at 0.5C and 1C shows more rapid voltage decay at 2.9 V than the experimental data. At 2C, the discrepancy of the cell voltage between the prediction and experimental data becomes remarkable, greater than the other cases. For sample with compaction loading of 10 MPa as shown in Figure 5-6b, the predicted cell voltage and capacity at 0.2C, 0.5C and 1C are accorded with the experimental data but the consistence at 2C becomes very poor, similar to the case of compaction loading of 5 MPa. The discrepancy between the predicted and measured discharge voltage at a high rate is very likely caused by the high sensitivity of cell performance to the actual material properties, operating conditions and cell design parameters. When a cell discharges at a high rate, the cell becomes strong polarization. Based on the comparisons between the predicted and experimental data on discharge voltage of the cell at different rate, it can be said that the use of the presented P2D model can well predict the rate effect on the discharge voltage of the cell working at room temperature, especially for low rates (0.1C~0.5C), and the prediction is generally reasonable for moderate rates (1C~2C).

5.5 Results and Discussion

The cycling performance of $LiNi_{0.6}Co_{0.2}Mn_{0.2}O_2$ with different compaction load at a current rate of 0.1 C for the first three cycles and 0.2 C for the last 50 cycles in the voltage of 2.7-4.3V, obtained from the validation experiment, is shown in Figure 5-7. The first discharge capacities of the samples without compaction and with applying compaction load of 5, 10, 15 and 20 MPa are 95, 181.1, 161.9, 212.4, 137.6 mAh g^{-1}, respectively, at 0.1C rate. Under cycling at a 0.2C rate for 50 cycles, the sample with compaction load of 5 MPa and 10 MPa show a similar capacity retention (86.6%). The sample without compaction shows the discharge capacity of 66.1 mAh g^{-1} at the end of 25 cycles, while for the other two samples with 15 MPa and 20 MPa, the discharge specific capacity changes with remarkable fluctuations while the capacity value drops greatly. The results can be attributed to the morphology change of the

Lithium ternary material, which may be resulted from the internal porosity change of the material. In contrast, for the sample without compaction, the combination between inactive and active materials is very weak. As the calendaring process helps to bind all the materials together and improves the adhesion, the consequence is that the active particles are easy to contract and expand during the Li de-insertion and insertion process. It can be postulated that application of a high compaction load leads to high internal stress, which may bring about the structural destruction of the electrode, such as crack or fatigue fracture generation and propagation (Zheng *et al.*, 2012) and result in the electrochemical performance deterioration of the electrode.

Figure 5-8 shows the simulated and experimental discharge curve in terms of different particle radius (D_{50}) at the 0.5C current rate. The corresponding radii of samples S_2, S_3, S_4 and S_5 are 6.470, 8.986, 6.740 and 3.890μm, respectively. As all the samples are compacted by applying the same load (10 MPa), it can be reasonably assumed these samples to have the same porosity. Since the mass of electrodes for different samples varies, the individual thickness of electrodes was predicted using equations (5-24) to (5-29). It can be seen from the figure that the simulated cell discharge voltage for the coin cell assembled with the particles of different radius. The discharge cell voltage increases when the particle radius is reduced. It is reckoned that the smaller the particle size, the shorter of Li^+ insertion and dis-insertion distance. As a result, it will take shorter time to reach the equilibrium for Li-ion concentration between the surface and the center. According to the electrochemical models presented in section 5.2.2, the solid phase diffusion coefficient (Ds) for different cases is estimated as shown in Table 5-4 and the values of the diffusion coefficient are found to be the same order. A decrease in the particle size of the active material can only cause a slight increase in the solid phase diffusion coefficient (Ds). This is consistent with the observation on the predicted electrochemical performance.

5.6 Conclusions

Design of a suitable calendaring process is crucial for manufacturing $LiNi_{0.6}Co_{0.2}Mn_{0.2}O_2$ cathode with different pore structures and porosities of the electrode, which has a significant impact on the final electrochemical performance of fabricated Lithium battery. To better understand the calendaring process, an electrochemical P2D model has been employed to simulate the electrochemical reactions occurring in the assembled cell and to predict the electrochemical performance of the battery under different conditions. The main conclusions drawn from the numerical simulations can be summarized as follows:

(1) Numerical predictions indicate that the electrodes prepared with compaction load of 5~10 mpa have little difference in capacity retention. Application of higher compaction load will lead to degrading of the electrochemical performance.

(2) Based on the SEM images obtained for both the calendared and uncalendared electrodes the relationship between the compaction load P and porosity of the coating ε_l was obtained by fitting the experimental results and

implemented into the numerical modelling. It was found that the suitable range of compaction load should be 5~10 MPa and equilibrate of coating porosity is about 0.7850.

(3) The numerical simulation reaffirms that the size of the active material particle has a significant impact on solid phase diffusion. A reduction in the particle size of active materials can benefit the solid phase diffusion. Although the numerical predictions were conducted based on a thinner electrode obtained from the actual experiments, the results and parameters may also be useful for determination of the optimal porosity of a thick electrode with a good electrochemical properties.

References

APPIAH, W. A., PARK, J., SONG, S., BYUN, S., RYOU, M.-H. & LEE, Y. M. 2016. Design optimization of $LiNi_{0.6}Co_{0.2}Mn_{0.2}O_2$/graphite lithium-ion cells based on simulation and experimental data. *Journal of Power Sources,* 319**,** 147-158.

ASHWIN, T. R., MCGORDON, A. & JENNINGS, P. A. 2017. Electrochemical modelling of Li-ion battery pack with constant voltage cycling. *Journal of Power Sources,* 341**,** 327-339.

DARLING, R. & NEWMAN, J. 1997. Modeling a porous intercalation electrode with two characteristic particle sizes. *Journal of The Electrochemical Society,* 144**,** 4201-4208.

DARLING, R. & NEWMAN, J. 1998. Modeling side reactions in composite $LiMn_2O_4$ electrodes. *Journal of The Electrochemical Society,* 145**,** 990-998.

HOSSEINZADEH, E., MARCO, J. & JENNINGS, P. 2018. The impact of multi-layered porosity distribution on the performance of a lithium ion battery. *Applied Mathematical Modelling,* 61**,** 107-123.

JI, Y., ZHANG, Y. & WANG, C.-Y. 2013. Li-ion cell operation at low temperatures. *Journal of The Electrochemical Society,* 160**,** A636-A649.

DOYLE, M., FULLER, T. F. & NEWMAN, J. 1993. Modelling of galvanostatic charge and discharge of the Lithium/polymer/insertion cell. Journal of The Electrochemical Society, 140, 1526-1533.

MEYER, C., BOCKHOLT, H., HASELRIEDER, W. & KWADE, A. 2017. Characterization of the calendering process for compaction of electrodes for lithium-ion batteries. *Journal of Materials Processing Technology,* 249**,** 172-178.

MEYER, C., KOSFELD, M., HASELRIEDER, W. & KWADE, A. 2018. Process modelling of the electrode calendering of lithium-ion batteries regarding variation of cathode active materials and mass loadings. *Journal of Energy Storage,* 18**,** 371-379.

NEWMAN, J. & TIEDEMANN, W. 1975. Porous-electrode theory with battery applications. *AlChE Journal,* 21**,** 25-41.

RAMADASS, P., HARAN, B., GOMADAM, P. M., WHITE, R. & POPOV, B. N. 2004. Development of first principles capacity fade model for Li-ion cells. *Journal of The Electrochemical Society,* 151**,** A196-A203.

STEPHENSON, D. E., WALKER, B. C., SKELTON, C. B., GORZKOWSKI, E. P., ROWENHORST, D. J. & WHEELER, D. R. 2011. Modelling 3D microstructure and ion transport in porous Li-ion battery electrodes. *Journal of The Electrochemical Society,* 158**,** A781-A789.

XU, M. & WANG, X. 2017. Electrode thickness correlated parameters estimation for a Li-ion NMC battery electrochemical model. *ECS Transactions,* 77**,** 491-507.

YANG, F., QIAO, Y., GAO, B., DUAN, P. & ZHU, Y. 2016. Investigation on Li-ion battery charging polarization characteristics and influence factors. *Ionics,* 22**,** 1603-1610.

ZHENG, H., TAN, L., LIU, G., SONG, X. & BATTAGLIA, V. S. 2012. Calendering effects on the physical and electrochemical properties of Li[$Ni_{1/3}Mn_{1/3}Co_{1/3}$]O_2 cathode. *Journal of Power Sources,* 208**,** 52-57.

Figures

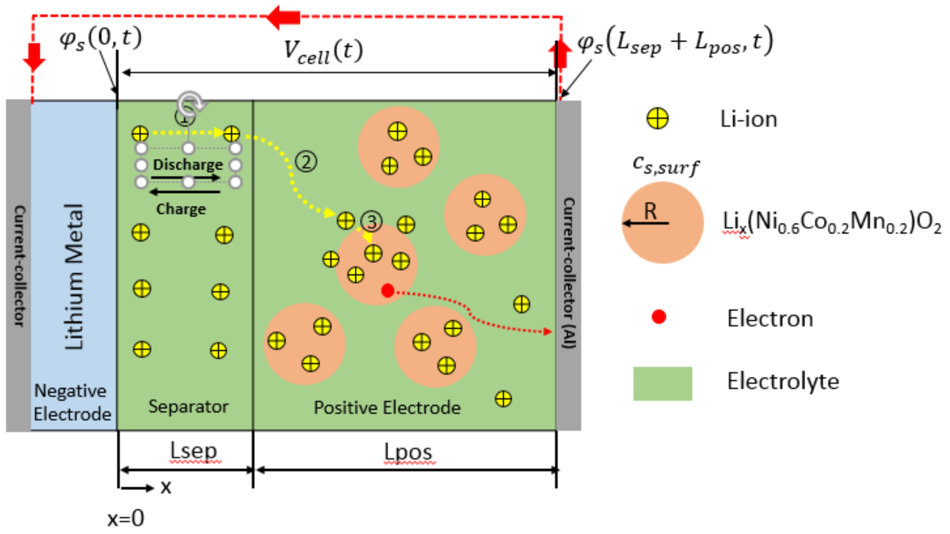

Figure 5-1.P2D model of the NCM622

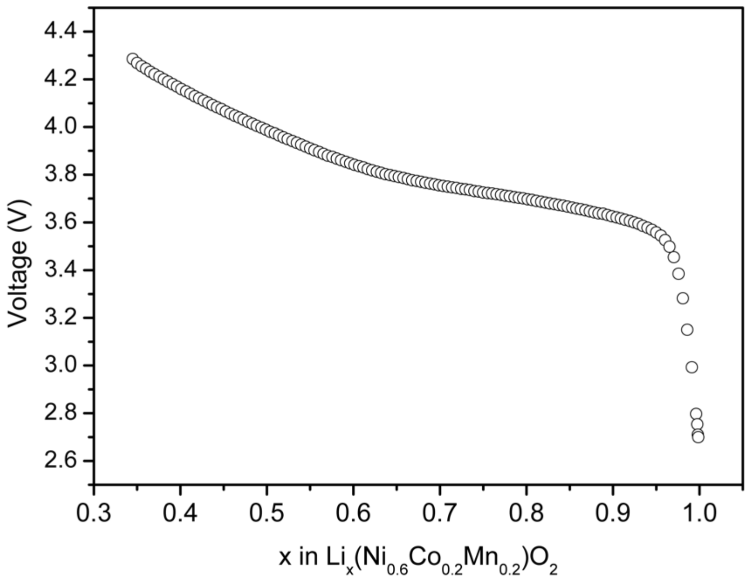

Figure 5-2. The initial stages of charge (SOC) for $Li_xNi_{0.6}Co_{0.2}Mn_{0.2}O_2$ cathode electrode

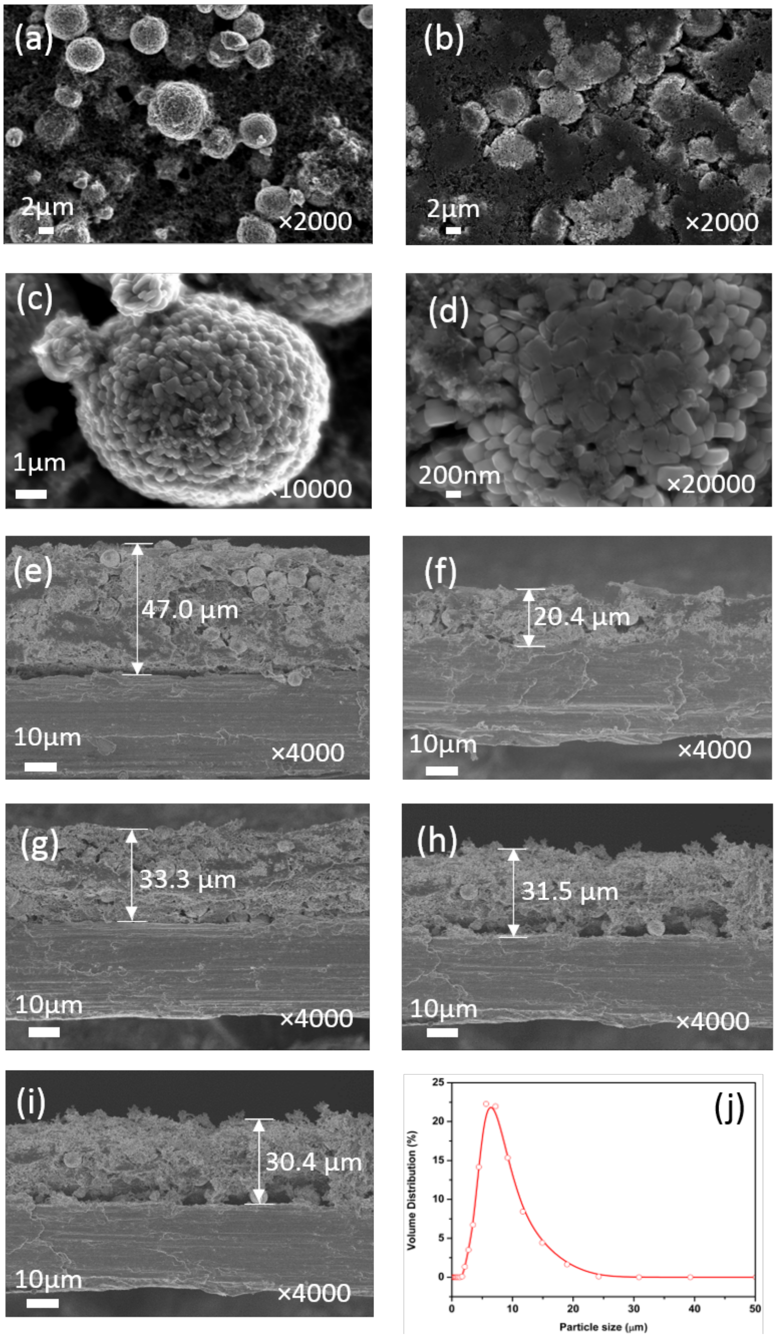

Figure 5-3.SEM images of the NCM materials before and after compaction

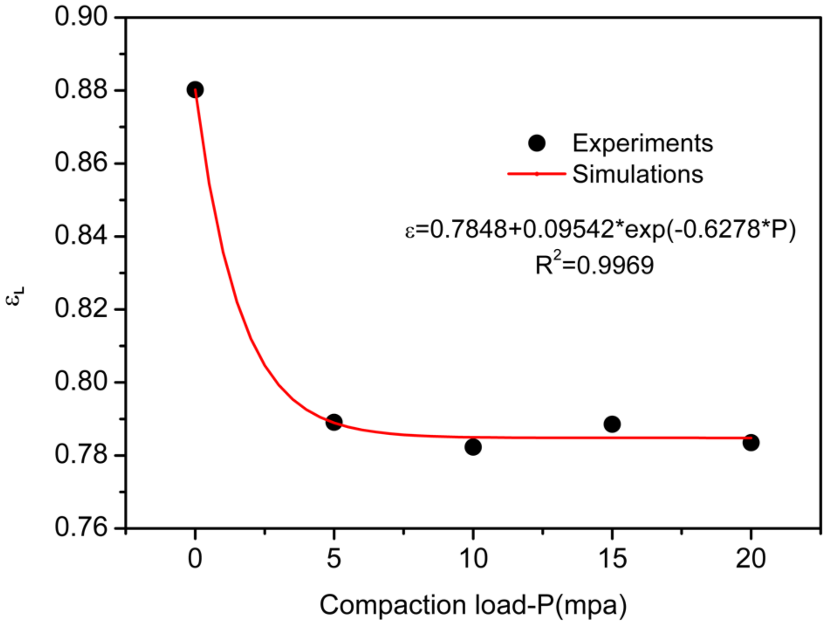

Figure 5-4. Calculated porosity of the coating (ε_l) against the compaction load P

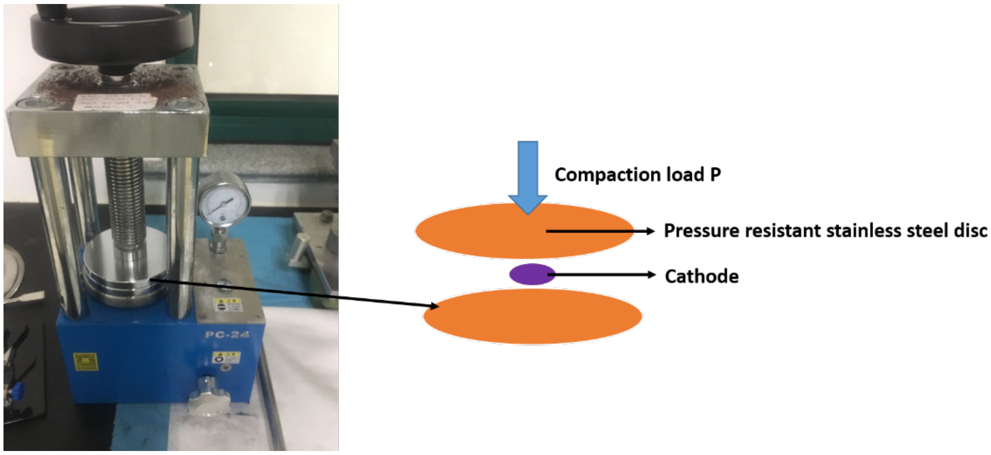

Figure 5-5.A compaction machine with stainless steel disc

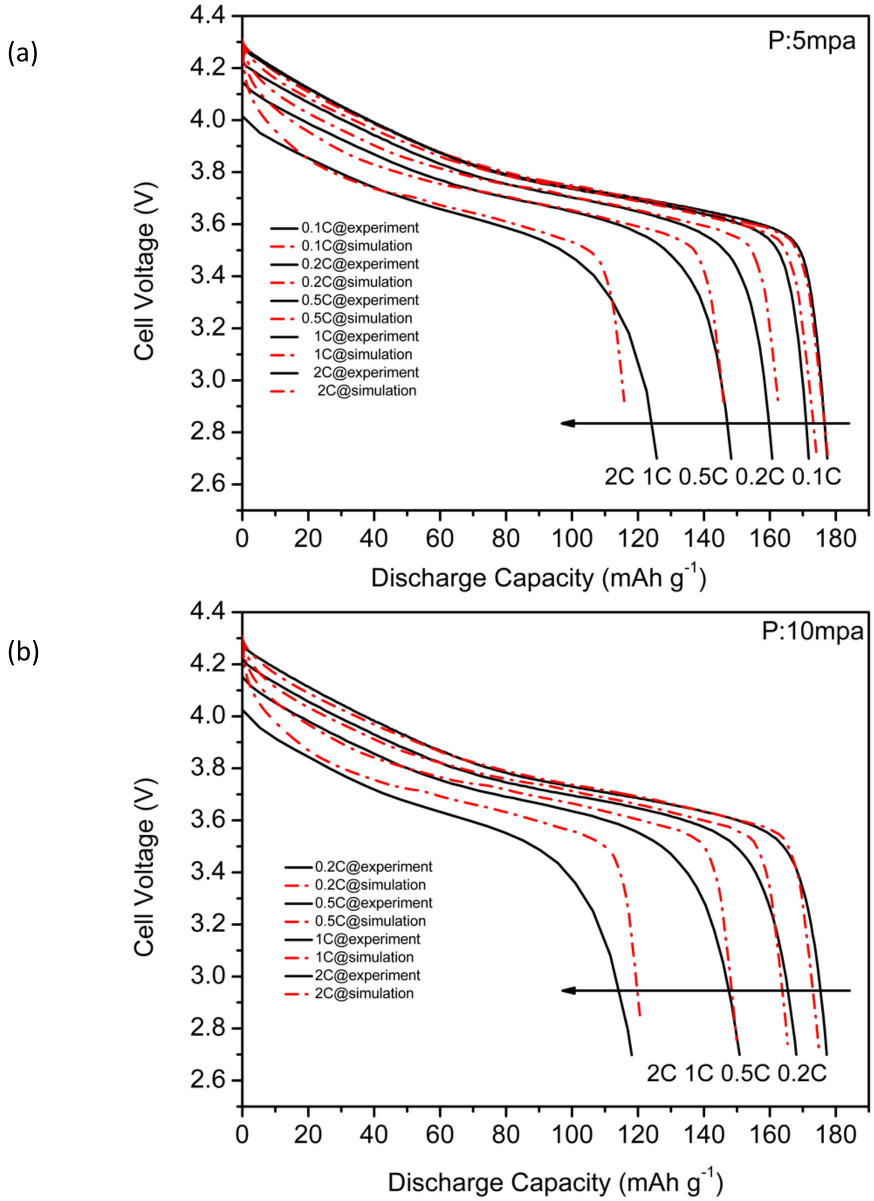

Figure 5-6. Discharging curves at 0.1C-2C for the samples between the experimental data and simulated results: (a) the compaction load of 5 mpa; (b) the compaction load of 10 mpa

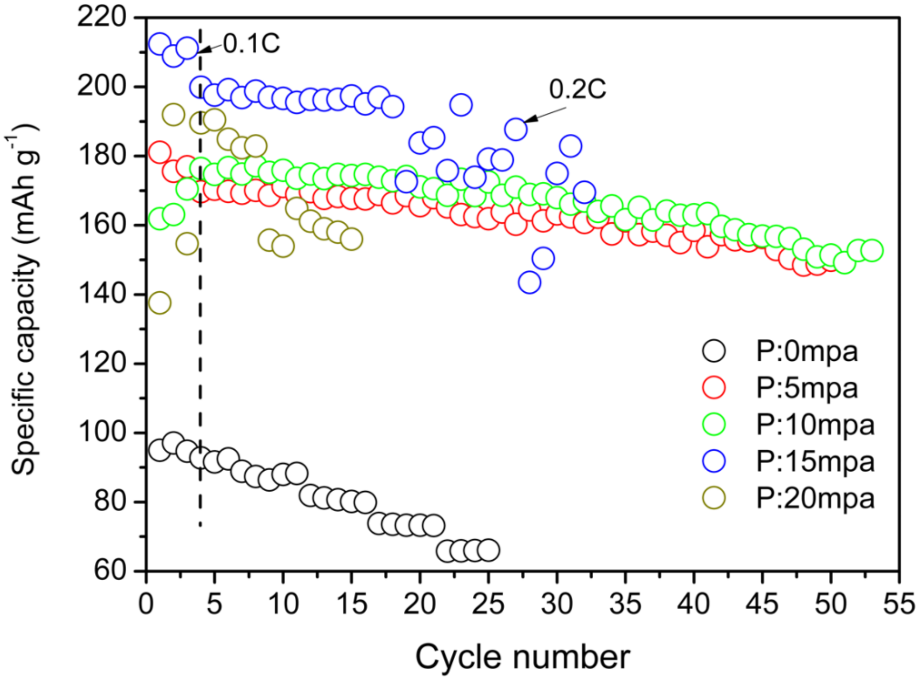

Figure 5-7. Cycling performance of $LiNi_{0.6}Co_{0.2}Mn_{0.2}O_2$ with different compaction load at 0.1 C and 0.2 C

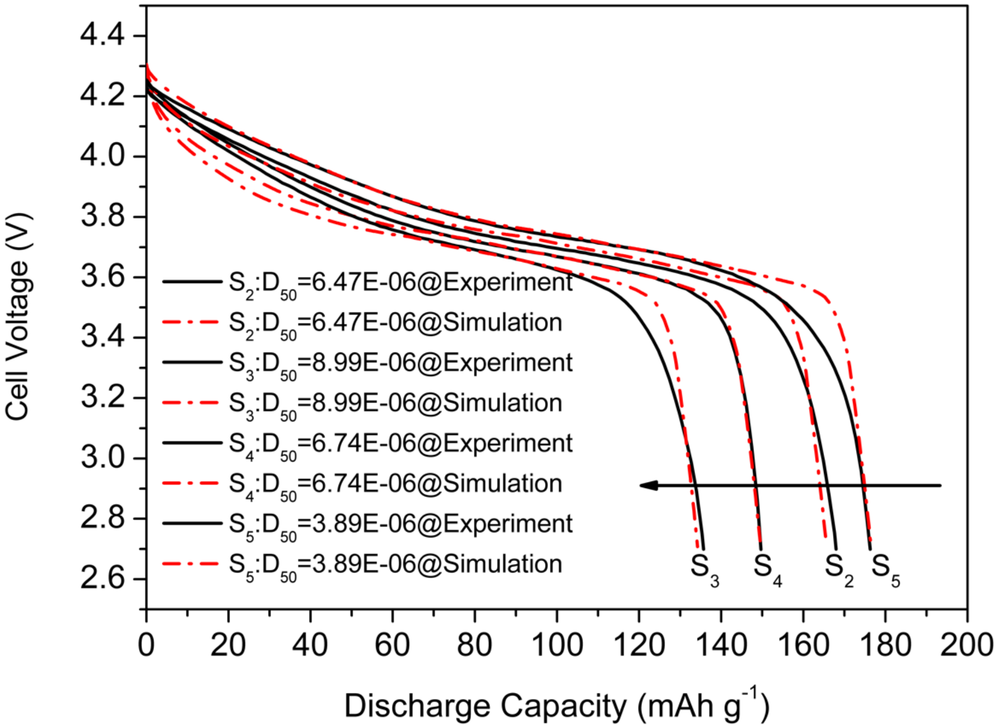

Figure 5-8. The simulated and experimental discharge curve in terms of different particle radius (D_{50}) at the 0.5C current rate

Tables

Table 5-1. Model parameters for NCM622 cells with different conditions

Parameters	**Symbol**	**Unit**	**Value**	**Ref**
Positive electrode thickness	L_{pos}	µm	Varing	b
Separator thickness	L_{sep}	µm	25	a
Radius of the particle	R	µm	Varing	a
Volume fraction of electrolyte	ε_l		Varing	b
Volume fraction of active material	ε_s		Varing	b
Maximum solid phase concentration	$c_{s,max}$	mol m^{-3}	49000	c
Minimum solid phase concentration	$c_{s,min}$	mol m^{-3}	16560	c
Reaction rate constant of cathode electrode	k_0	$m^{2.5}mol^{-0.5}s^{-1}$	3.94E-11	c
Density of NCM particle	ρ_s	g cm^{-3}	4.8	c
Area of the electrode plate	A	cm^2	1.131	a
Electronic conductivity	σ_s	S m^{-1}	11.6	a
Transfer coefficient for anodic current	a_a		0.5	c
Transfer coefficient for the catholic current	a_c		0.5	c
Gas constant	R	J $mol^{-1}K^{-1}$	8.314	c
Faraday constant	F	C mol^{-1}	96485	c
Bruggeman porosity exponent	β		1.5	c
Film resistance	R_{SEI}	$\Omega\, m^2$	0.001	c

Transference number of Li-ion in the electrolyte phase	t_+		0.363	c
Li-ion diffusion coefficient of NMC	$D_{s,ref}$	m^2s^{-1}	Varying	b
Li-ion diffusion coefficient in the electrolyte phase	$D_{l,ref}$	m^2s^{-1}	3.8E-10	c

a Value set in cell design; b Parameters calculated from cell design (Xu and Wang, 2017, Appiah *et al.*, 2016); c Parameters from Literature or Comsol database

Table 5-2. Results summary for compaction load, active material, measured thickness and porosity

Compaction load (mpa)	**Active material (mg)**	**Measured thickness (µm)**	**Calculated** ε_l
0	3.056	47.0	0.8802
5	2.336	20.4	0.7891
10	3.936	33.3	0.7823
15	3.616	31.5	0.7885
20	3.056	26.0	0.7835

Table 5-3. Cell design parameters of the NCM622 positive electrode with different compaction load

Sample Name	Compaction load (mpa)	D_{50} (µm)	ε_l	Active material (mg)	Calculated thickness (µm)	1C (Ah)	Current density i-1C (Ah/m^2)	D_s (m^{2}s^{-1})
S_1	5	6.471	0.7891	4.1760	36.4737	6.7E-04	5.92	3.8E-15
S_2	10	6.471	0.7850	2.0160	17.2722	3.0E-04	2.65	3.8E-15

Table 5-4. Cell design parameters of the NCM622 positive electrode with different particle size

Sample Name	Compaction load (mpa)	D_{50} (µm)	ε_l	Active material (mg)	Calculated thickness (µm)	1C (Ah)	Current density i-1C (Ah/m^2)	Ds (m^{2}s^{-1})
S_2	10	6.470	0.7850	2.0160	17.2722	3.0E-04	2.6525	3.8E-15
S_3	10	8.986	0.7850	1.2960	11.1036	2.0E-04	1.7949	3.8E-15
S_4	10	6.740	0.7850	1.8560	15.9014	2.9 E-04	2.5553	1.4E-15
S_5	10	3.890	0.7850	1.5360	13.1598	2.3E-04	2.0248	5.0E-15

Chapter 6

Improvement of Electrochemical Performance of $LiNi_{0.6-x}Co_{0.2}Mn_{0.2}Mg_xO_2$ Positive Electrode Materials by Doping Metal Mg

Summary

In Chapter 4, the electrochemical performance of $LiNi_{0.6}Co_{0.2}Mn_{0.2}O_2$ cathode material prepared by different conditions has been evaluated in detail. The Li/Ni mixing has been found to be a common phenomenon in the high nickel cathode materials. It has been reported in the open literature thatthe use of doping can improve the structural stability of high nickel cathode materials. This chapter will investigate the adoption of doping Mg onto $LiNi_{0.6}Co_{0.2}Mn_{0.2}O_2$ for improvement its electrochemical performance. $LiNi_{0.6-x}Co_{0.2}Mn_{0.2}Mg_xO_2$ (x=0, 0.02, 0.04 and 0.06) samples are prepared in a lobed Taylor-Couette reactor by co-precipitation and high-temperature solid state method. Effects of the Mg doping for Ni on the structure and electrochemical properties of $LiNi_{0.6-x}Co_{0.2}Mn_{0.2}MgxO_2$ positive electrode samples are characterized by XRD, SEM and electrochemical measurements. The XRD patterns show that all materials have a α-$NaFeO_2$ structure and no impurities are detected. The best electrochemical performance is achieved when the substitution fraction of Mg is 0.02. The fabricated samples have exhibited the initial discharge of capacities to be 153.1 mAh g^{-1} and 148.1 mAh g^{-1} at 0.1 C and 0.2 C, respectively. After 48 cycles of cycling at 0.2 C, those samples can still have a discharge capacity of 128.6 mAh g^{-1} with the capacity retention of

about 86.8 %. The average rate capability of $LiNi_{0.6-x}Co_{0.2}Mn_{0.2}Mg_xO_2$ (x=0.02) electrodes has attained 151.9 mAh g^{-1}, 150.3 mAh g^{-1}, 138.6 mAh g^{-1}, 126.7 mAh $g^{-1}$and 109.4 mAh g^{-1}measured at the current rate of 0.1 C, 0.2 C, 0.5 C, 1 C and 2 C rate, respectively. The cyclic voltammetry (CV) of $LiNi_{0.6-x}Co_{0.2}Mn_{0.2}Mg_xO_2$ (x=0.02) shows the smallest potential gap of 0.2847 V when compared with the cases of x=0.04 and 0.06, indicating a significantly enhanced electrochemical performance.

6.1 Introduction

Improvement of energy efficiency performance of Electric vehicles (EVs), hybrid vehicles (HEVs) and large electric energy storage devices (Cho *et al*., 2013; Kang and Ceder, 2009; Wang *et al*., 2015) has imposed the needs to develop the cathode materials with high energy and power density, which can lead to broaden the applications of these types of energy storage devices (Fu *et al*., 2014). As one of the most promising cathode materials, $LiNi_{0.6}Co_{0.2}Mn_{0.2}O_2$ has been intensively studied thus far due to its lower cost, higher capacity and environmentally friendly characteristics in comparison to $LiCoO_2$ electrodes (Chen *et al*., 2014). However, $LiNi_{0.6}Co_{0.2}Mn_{0.2}O_2$ still has some drawbacks such as low initial coulombic efficiency, poor rate capacity and unsatisfactory cycling performance (Xu *et al*., 2011, Zou *et al*., 2014). These problems related to poor cycling characteristics are likely caused by the cation mixing of Li/Ni during the synthesis process and structural transition into NiO-type rock salt phase (Belharouak *et al*., 2006).

It has been recognised that the substitution of metal ions can be effective in improving the electrochemical performance of cathode material. The popular substitution of metals is realised by substituting the following elements such as Mg (Liao *et al*., 2008; Liu *et al*., 2012), Al (Belharouak *et al*., 2006), Zn (Lu *et al*., 2013), Ca (Xiao *et al*., 2015), Fe (Cao *et al*., 2005), Ga (Xiao *et al*., 2015), Ti(Lu *et al*., 2013) and Cr (Li *et al*., 2012). It is generally accepted that the Mg substitution can reduce the cation mixing and act as pillars to improve structural stability (Liao *et al*., 2008; Liu *et al*., 2012). Also, Mg substitution can lead to the alleviation of phase change during lithium-ion insertion and extraction and enhancement of the thermal stability at every delithiated state (Kim *et al*., 2006). The consequence of Mg substitution has a positive impact on the final electrochemical performance of electrodes. Recently, Liu *et al*. (2012) have reported that $LiNi_{0.9}Co_{0.05}[Mn_{1/2}Mg_{1/2}]_{0.05}O_2$ can deliver an initial discharge capacity of 191.5 mAh g^{-1} at 0.2 C and the discharge capacity to be maintained more than 93% of the initial discharge capacity after 50 cycles. Wang *et al*. (2015) have demonstrated that doping 4% of Mg into $Li[Li_{0.16}Mg_{0.04}Co_{0.13}Ni_{0.13}Mn_{0.54}]O_2$ electrode can yield an initial discharge capacity of 272 mAh g^{-1} and 114 mAh g^{-1} at 8 C. In the meantime, the excellent cycling stability with 93.3% of capacity retention after 300 cycles was achieved. Huang *et al*. (2015) also found that the initial coulombic efficiency and cycling stability could be increased by substituting Mg for Mn in layered $LiNi_{0.6}Co_{0.2}Mn_{0.2-x}Mg_xO_2$. These studies have clearly indicated that Mg substitution is an effective route for improvement of electrochemical performance of $LiNi_{0.6-x}Co_{0.2}Mn_{0.2}Mg_xO_2$ positive electrode materials in addition to a well prepared and controllable synthesis of $(Ni_{0.6-x}Co_{0.2}Mn_{0.2}Mg_x)(OH)_2$ precursor particles.

To achieve controllable synthesis of $(Ni_{0.6-x}Co_{0.2}Mn_{0.2}Mg_x)(OH)_2$ precursor particles, the use of Taylor-Couette (TC) flow reactor has been considered to be promising as this type of reactor has a relatively better micromixing behaviours than other types of reactors such as mixing tanks, while the local interactions between turbulent eddies embedded in the formed Taylor vortices can be beneficial to the preparation of uniform ultra-fine particles (Kim *et al.*, 2011) due to a uniform local shear distribution. In the present chapter, the effect of Mg^{2+} ion substitution on Ni^{2+} in $LiNi_{0.6-x}Co_{0.2}Mn_{0.2}Mg_xO_2$ (x=0, 0.02, 0.04, 0.06) will be investigated. The Rietveld refinement will be used to verify the cation mixing and structural change. The electrochemical properties of the prepared samples will be measured and compared with and without addition of different Mg^{2+} concentrations. The experimental results have reaffirmed that significant enhancement of the electrochemical performance of the samples can be attained by properly applying Mg substitution.

6.2 Experimental

6.2.1 Material Synthesis

For the formation of Mg-doped $(Ni_{0.6-x}Co_{0.2}Mn_{0.2}Mg_x)(OH)_2$ (x=0, 0.02, 0.04, 0.06) precursor, a lobed Taylor-Couette flow reactor (volume-630 ml) (LTC) was used. The inner cylinder is rotating while the outer cylinder is stationary. The inner cylinder is driven by a variable speed drive with a torque-meter, as shown in Figure 6-1. The reactor (herewith so referred to as crystallizer as well) is placed horizontally in order to prevent the hydrostatic pressure effect. The metal sulfate solution was prepared using $NiSO_4{\cdot}6H_2O$ (>98%, Jinchuan Group co., LTD), $MnSO_4{\cdot}H_2O$ (>96%, Shanghai nanwei chemicals co., Ltd), $CoSO_4{\cdot}7H_2O$ (>98%, Sinopharm Chemical Reagent Co., Ltd), $MgSO_4$ (Sinopharm Chemical Reagent Co., Ltd.) as raw materials, here the feed concentration was always fixed at 2 mol L^{-1}. The molar ratio of Ni, Co, Mn and Mg is (0.6-x):0.2:0.2:x, where x is 0, 0.02, 0.04, 0.06 respectively. 4 M of

Sodium hydroxide (>96%, Tianjin zhiyuan chemicals co., Ltd) was used as hydroxyl reactant and 6 M of ammonia (25~28%, Sinopharm Chemical Reagent Co., Ltd) was used as a chelating agent for crystallization of $(Ni_{0.6}Co_{0.2}Mn_{0.2})(OH)_2$ precursor. All the reagents used in the experiments are in industry grade and were used without further purification. Before reaction, the LTC flow reactor (crystallizer) was initially filled with distilled water and the reaction temperature was kept at 55°C. During the reaction, the metal sulfate solution, sodium hydroxide and ammonia were continuously injected using separate peristaltic pumps through three ports located at the front axial part of the reactor. The mean residence time of agglomeration was controlled to be 60 mins. After the reaction, the final precipitate was filtered using a vacuum pump and washed several times with distilled water until the sample attains the pH value of 7. The sample precipitates $((Ni_{0.6-x}Co_{0.2}Mn_{0.2}Mg_x)(OH)_2)$ were subsequently dried in a circulation oven at 80°C overnight.

$LiNi_{0.6-x}Co_{0.2}Mn_{0.2}Mg_xO_2$(x=0, 0.02, 0.04, 0.06) cathode material (synthesised powder) was obtained by calcination method through the combination of $(Ni_{0.6-x}Co_{0.2}Mn_{0.2}Mg_x)(OH)_2$ precursor with LiOH, for which the molar ratio of Li/metal(Ni, Co, Mn and Mg) was kept to be 1.05. Excess lithium was added to compensate for the loss during the calcination process. The obtained precursor and LiOH were preheated at 500°C for 4 h and then further calcined at 860 °C for 12 h under atmosphere.

6.2.2 Material Characterization and Electrochemical Measurement

XRD analyses were conducted using a Bruker-AXS D8 advance powder diffractometer with the settings of Cu-Ka radiation (λ=1.5406 Å) and the power of 40kv×20Ma. Diffraction pattern was recorded in the range 2θ=10-80 ° with a step size of 0.01°. The collected XRD intensity data were analyzed using GSAS package software (Toby, 2001). The morphologies of synthesized powder were observed using SEM produced from ZEISS ZIGMA 174C CZ. Electrochemical performance was characterized by measuring a CR2032 coin-type cell assembled using the synthesized powder. The cell is composed of a lithium metal negative electrode and a $LiNi_{0.6}Co_{0.2}Mn_{0.2}O_2$ positive electrode that is separated by a microporous polypropylene film. The cathode consists of 80 wt.% of $LiNi_{0.6}Co_{0.2}Mn_{0.2}O_2$, 10 wt.% of Super P as a conducting agent and 10 wt.% of polyvinylidene fluoride (PVDF) as a binder. All these samples were dispersed in N-methyl pyrrolidinone (NMP) and stirred for 8 hours to make the slurry. The prepared slurry was coated uniformly onto an aluminum foil and dried in an air dry oven at 80 °C for 8 hours to form the electrodes. After drying, the electrodes were then cut into the disks of 12 mm in diameter. The typical cathode electrode disk mass load through the measurement was found to be about 2 mg cm^{-2}. The electrolyte was a mixture of 1 M $LiPF_6$ resolved in ethylene carbonate (EC) with ethyl methyl carbonate (EMC) (3:7, v/v). Assembly of the cells was carried out in an argon-filled glove box. These charge-discharge characteristics were measured between 2.7–4.3 V at room temperature (vs. Li/Li^+) at a desired current density (1 C=160 mAh g^{-1}) using

CT2001A land instrument. The electrochemical work station used in the test is PARSTAT MC (multi-channel) (made in Princeton, USA).

6.3 Results and Discussion

6.3.1 Characterization of $LiNi_{0.6-x}Co_{0.2}Mn_{0.2}Mg_xO_2$

XRD patterns of $LiNi_{0.6-x}Co_{0.2}Mn_{0.2}Mg_xO_2$ (x=0, 0.02, 0.04 and 0.06) are displayed in Figure 6-2. The detected peaks in the patterns obtained for all the samples can be indexed as α-$NaFeO_2$ structure (space group: $R\overline{3}m$). No other impurities were observed with increasing the doping concentration of Mg element. An apparent split between peaks (006)/(012) and (018)/(110) occurring in all the samples clearly indicates that a well-ordered layer structure is formed (Deng *et al*., 2010; Yue *et al*., 2011). The unit cell parameters (shown in Table 6-1), *a* and *c* decrease initially but subsequently increase with increase of the content of Mg. The details of changes in the structure will be further discussed in the following section focusing on XRD Rietveld refinement. The integrated intensity ratio (I_{003}/I_{104}) of peaks (003) and (104) can be considered as an indicator for cation mixing degree. With a small amount of Mg doping (x=0.02), the ratio of I_{003}/I_{104} increases from 0.93 (x=0) to 1.02 (x=0.02), which indicates the decrease of the degree of cation mixing. However, further increasing the content of Mg from 0.02 to 0.06, the degree of cation mixing increases. Since the extent of cation mixing is closely related to the electrochemical performance of materials, the lower cation mixing means the better electrochemical performance (Cheralathan *et al*., 2010). Thus, one can expect that the best electrochemical performance can be achieved for the sample of $LiNi_{0.6-x}Co_{0.2}Mn_{0.2}Mg_xO_2$ with the addition of 0.02 of Mg concentration.

Table 6-2 shows the nominal and measured chemical composition of $LiNi_{0.6-x}Co_{0.2}Mn_{0.2}Mg_xO_2$ (x=0, 0.02, 0.04, 0.06) determined by ICP-OES. The measured compositions of synthesized samples are close to those of setting values, suggesting that the Mg element is not lost during the synthesis process. It can be claimed that the synthesised samples based on the design have been well synthesised.

In order to further study the relationship between the structure and properties of the samples, the structural refinement (Rietveld refinements) have been performed by using GSAS program. The composition of Li, Co, Ni, Mn and Mg used in the Rietveld refinements are acquired from results of ICP-OES. It can be seen from the results that the ionic radius of Mg^{2+} (0.72 Å) is close to that of Li^+ (0.76 Å) and Ni^{2+} (0.69 Å), indicating a high possibility for Mg to occupy in the Li layer at the sites of 3a and 3b. For the refinements, it is assumed that $Li_1/Ni_1/Mg_1$ locates at site 3a (0,0,0), $Li_2/Ni_2/Co_1/Mn_1/Mg_2$ occupies at site 3b (0,0,0.5) and the O occupies at site 6c (0,0, z), with $z \approx 0.24$ (Huang *et al.*, 2015). For the other two elements, Co^{3+} (r=0.545 Å) and Mn^{4+} (r=0.53 Å), it was found that their ionic radii are much smaller than the radius of Li^+. It should be noted here that the incorporation of $Co^{3+}$and Mn^{4+} into the Li layer is not considered here. On the basis of the above analysis, the set formula of $LiNi_{0.6-x}Co_{0.2}Mn_{0.2}Mg_xO_2$ can be assumed to have such format, i.e. $[Li_{1-y}Ni_{y-x}Mg_z]_{3a}[Li_yNi_{0.6-y}Co_{0.2}Mn_{0.2}Mg_{x-z}]_{3b}O_2$.

The quality of observed and calculated results can be evaluated by two factors, R_{wp} and R_{p}, given by (Liu *et al.*, 2012)

$$R_P = \frac{\sum_{i=i,n} |Y_i - Y_{C,i}|}{\sum_{i=i,n} Y_i} \times 100 \tag{6-1}$$

$$R_{wP} = \frac{\sum_{i=1,n} w_i |Y_i - Y_{C,i}|^2}{\sum_{i=i,n} w_i Y_i^2} \times 100 \tag{6-2}$$

It should be noted that if the values for both R_{p} and R_{wp} are lower than 15%, the results of Rietveld Refinement can be treated to be reliable.

Figure 6-3 presents the comparative Rietveld XRD plots for the samples. It can be seen from the Figure 6-3 and Table 6-3 that after the refinements are made, R_{wp} and R_{p} for all the samples are lower than 15%, thus implying our refinement results to be reliable. In particular, 5.18% of Ni ions are located at lithium 3a sites for the sample without Mg doping while only 3.36% of Ni ions occupy at lithium 3a sites for the case of Mg substitution (x=0.02). This fully indicates that a small amount of Mg addition to $LiNi_{0.6-x}Co_{0.2}Mn_{0.2}Mg_xO_2$ can effectively inhibit the Ni^{2+} into Li (3a) layer. As a result, it has a positive effect on the reduction of the cation mixing of Li/Ni for the $LiNi_{0.6}Co_{0.2}Mn_{0.2}O_2$. Further increasing Mg substitution from 0.04 and 0.06, however, the cation mixing increases again, corresponding to the Ni^{2+} occupancy of 8.40% and 6.59% in Li (3a) layer, respectively. It can be said that excess Mg addition increases the chance of which Li^+ enters into the 3b site. Similar results were also observed in Mg doped $LiNi_{0.6}Co_{0.2}Mn_{0.2-x}Mg_xO_2$ (Huang *et al.*, 2015). It is noticed that the amount of Mg addition also affects the bonding distance of Li-O and M-O as observed the smallest bonding distance of Li-O and M-O occurs for the case of Mg doping (x=0.02). At 298K, the bond dissociation energy of Mg-O is larger than that of Ni-O, as reported by Lange's Handbook of Chemistry (Dean, 1990). Thus, when a small amount of Mg is doped, the enhanced bonding ability for Mg-O facilitates the structural stability of the material. As for the calculated unit cell parameters *a* and *c* (as listed in Table 6-1), it can also be analysed according to the Rietveld results. When doping a small amount of Mg^{2+} (x=0.02), it was observed that the amount of Ni^{2+} occupied in the Li layer reduces. As the radius of Ni^{2+} is 0.69 Å**,** slightly larger than that of Ni^{3+} (0.56 Å), less occupancy of Ni^{2+} may reduce the lattice parameters. It can be concluded that increasing the amount of Mg^{2+} content will promote more Mg^{2+} ions to enter into the bulk lattice. As the ionic radius of Mg^{2+} (0.72 Å) is also larger than that of Ni^{2+}, the unit cell dimensions will be enlarged again. It should be pointed out that the addition of Mg can act as pillars to provide extra structural stability and prevent the structural collapse inside the inter-slab such as Ni^{2+} ions as reported in the literature (Liu *et al*., 2012, Woo *et al*., 2009, Barsoukova *et al*., 2003). Nevertheless, the present work reveals that a small amount of Mg^{2+} addition (x=0.02) can indeed have an enhanced effort for layered structural stability so that one can expect an improvement of the electrochemical properties for this type of samples.

Figure 6-4 shows the SEM micrographs of the four samples prepared in this work. It can be seen that there is no obvious size difference between the pristine and Mg-substituted compounds. The particle sizes are around 200~300 nm, indicating that the morphology is not affected by the Mg-doping. However, the particles look quite fuzzy when the addition of Mg is increased to 0.06.

6.3.2 Electrochemical Performance of $LiNi_{0.6}Co_{0.2}Mn_{0.2}O_2$ cathode material

The initial charge and discharge profiles of $LiNi_{0.6-x}Co_{0.2}Mn_{0.2}Mg_xO_2$ (x=0, 0.02, 0.04 and 0.06) at 0.1 C (1 C=160 mAh g^{-1}) are plotted in Figure 6-5. It can be seen from the figure that the pristine $LiNi_{0.6}Co_{0.2}Mn_{0.2}O_2$ delivers a relatively high capacity of 145.2 mAh g^{-1}. With increasing Mg additive concentration from 0.0 to 0.02, the discharge capacity at 0.1 C increases to 153.1 mAh g^{-1}. Further increasing the content of Mg, however, has a negative impact on the discharge capacity of samples at 0.1 C as the obtained discharge capacities for x=0.04 and 0.06 are only 121.5 mAh g^{-1} and 122.7 mAh g^{-1}, respectively. It seems that the sample prepared with x =0.02 exhibits the highest initial capacity compared with the other samples. One of the explanations can be based on the following arguments. It has been recognised that Ni ions play an important role in the redox reaction during the delithiation process for the nickel-based cathode materials. When Ni^{2+} ions in the Li slab oxidise during the first intercalating and de-intercalating process, this can result in a collapse of inter-slab space so that lithium diffusion and de-intercalating in the inter-slab become difficult (Pouillerie *et al.*, 2000). However, a small amount of Mg addition into $LiNi_{0.6}Co_{0.2}Mn_{0.2}O_2$ will weaken the bonding of Li-O and M-O, as discussed in the preceding subsection for Rietveld refinement results. Consequently, the electrochemically inactive Mg^{2+}located in the Li slab can prevent from collapsing of the inter-slab space, thus reducing the irreversible capacity loss. This explains why the irreversible capacity is reduced by the excess addition of Mg into $LiNi_{0.6}Co_{0.2}Mn_{0.2}O_2$. In fact, for a large amount of Mg additions, the charge compensation is mainly realised by two-step oxidation of Ni^{2+} ions, i.e. Ni^{2+} to Ni^{3+} occurs during 3-3.9 V and then Ni^{3+} to Ni^{4+} takes place in the higher voltage range of 3.9-4.5V (Liao *et al.*, 2008). It can be inferred that the electrochemically inactive Mg substitution for active Ni ions will cause a decrease of capacity.

Figure 6-6 shows the cycling performance of $LiNi_{0.6-x}Co_{0.2}Mn_{0.2}Mg_xO_2$ (x=0, 0.2, 0.4 and 0.6) electrodes at 0.1 C and 0.2 C rate. The measurement was conducted for the first two cycles at 0.1 C and for the other 48 cycles at 0.2 C. The initial discharge capacity of pristine $LiNi_{0.6}Co_{0.2}Mn_{0.2}O_2$ at 0.2 C is 132.7 mAhg^{-1}. After experiencing 48 charge/discharge cycles, the pristine $LiNi_{0.6}Co_{0.2}Mn_{0.2}O_2$ delivers a discharge capacity of 96.6 mAh g^{-1} with capacity retention of 72.8%. In contrast, the electrode (x=0.02) delivers a first discharge capacity of 148.1 mAh g^{-1} while the discharge capacity is 128.6 mAh g^{-1} after 48 cycles with a discharge capacity retention about 86.8 %, which is much higher than that of the pristine electrode. It is interesting to note that the initial discharge capacities of the samples (x=0.04 and 0.06) at 0.2 C are 124.4 and 102 mAh g^{-1}, respectively. After taking 48 charge/discharge cycles, the discharge capacities of the sample for x=0.04 and 0.06 are only 111.8 mAh g^{-1} and 70.8 mAh g^{-1} with corresponding capacity retention of 89.9 % and 69.4 %. One can clearly see that improved cycling stability can be achieved by adopting a small amount of Mg substitution (Mg=0.02) for Ni ions in $LiNi_{0.6}Co_{0.2}Mn_{0.2}O_2$. The consequence is that an improvement on cycling properties is attained since the Mg^{2+} ions can migrate from the 3b site (transition metal) to the 3a site (lithium site), leading to the decrease in lattice dimensions, crystallite volume variations and cation mixing.

It should be noted that from power storage application point of view, the rate capacity is one of the most important indices that can be used to characterize the performance of Lithium-ion battery. Figure 6-7 presents the rate capacities of $LiNi_{0.6-x}Co_{0.2}Mn_{0.2}Mg_xO_2$ electrodes for x=0, 0.02, 0.04 and 0.06, which were obtained by measuring for continued 5 cycles at the current rate of 0.1 C, 0.2 C, 0.5 C, 1 C and 2 C rate. The results indicate that the discharge capacity decreases with discharge rate for all the samples. This may be attributed to the effect of polarization (Chen *et al*., 2014). However, the sample with Mg addition possesses a higher discharge capacity than the pristine sample at a higher rate. For example, the average capacity of the sample for x=0 at 0.1 C is 129.1 mAh g^{-1} but 151.9 mAh g^{-1} for x=0.02, 129.7 mAh g^{-1} for x=0.04 and 85.7 mAh g^{-1} for x=0.06, respectively. At 1 C/2 C, only 80.3/41.8 mAh g^{-1} can be delivered for x=0, but 126.7/109.4 mAh g^{-1} for x=0.02, 95.3/80.4 mAh g^{-1} for x=0.04. The capacity for x=0.06 decreases dramatically. These again illustrate that the use of small additives of Mg can improve the rate capacity because Mg doping can restrain the Li/Ni disorder so that the stable structure can be still maintained at a high rate, a finding consistent with the results reported by Liao *et al* (2008).

Cyclic voltammetry (CV) of $LiNi_{0.6-x}Co_{0.2}Mn_{0.2}Mg_xO_2$ (x=0, 0.02, 0.04 and 0.06) measured at a scan rate of 0.1 mV s^{-1} for the first two cycles are shown in Figure 6-8. It can be observed that only one redox couple exhibits in the CV for all the samples, indicating no multiphase reactions to take place (from hexagonal to monoclinic) within this voltage range. The redox peaks occurred during the charge/discharge process are caused by the oxidation of Ni^{2+} to Ni^{3+}/Ni^{4+} (Yang *et al.*, 2014). It can be seen from the figure that the all the redox peaks during the charge process and discharge process are around 4.0 V and 3.6 V. As the potential gap (ΔE_p) between redox peaks represents the degree of electrochemical reversibility (Huang *et al.*, 2015), better electrochemical reversibility can be obtained when ΔE_p is small. Notice that the obtained potential gap between redox peaks of the samples in our experiments are 0.4204 V (x=0), 0.2847 V (x=0.02), 0.3826 V (x=0.04) and 0.4718 V (x=0.06) based on the first cycle. Samples for Mg addition of 0.02 and 0.04 show small electrochemical polarization, while the sample for Mg (x=0.02) has the smallest electrochemical polarization among three conditions of Mg addition, indicating that the sample has the best electrochemical performance. When Mg addition x=0.06, the ΔE_p is greater than the pristine sample with worsen electrochemical properties. All these observations are consistent with the sample electrochemical performance as discussed earlier.

6.4 Conclusions

In the current chapter, we report the work on improvement of electrochemical performance of $LiNi_{0.6-x}Co_{0.2}Mn_{0.2}Mg_xO_2$ positive electrode materials by doping metal Mg. $LiNi_{0.6-x}Co_{0.2}Mn_{0.2}Mg_xO_2$(x=0, 0.02, 0.04 and 0.06) samples have been prepared using a co-precipitation in a LTC reactor and high-temperature calcination method for fabrication of the particles. Effects of the molar ratio fractions of Mg addition for Ni on its structure and electrochemical performance were investigated. The main conclusions reached as the results of the current study can be summarised:

(1) The XRD results showed that the cation mixing is reduced as the consequence of the content of Mg addition being increased from 0 to 0.02. However, a further increase in the content of Mg leads to an increase of cation mixing. A similar tendency was also observed to take place in the lattice parameters.

(2) The Rietveld refinement has shown that addition of a small amount of Mg to $LiNi_{0.6-x}Co_{0.2}Mn_{0.2}Mg_xO_2$ can inhibit the Ni^{2+} into Li (3a) layer, lowering the bonding distance of Li-O and M-O and increasing the structural stability of the material.

(3) It was also revealed that by doping a small amount of Mg can enhance the initial coulomb efficiency and reduce the capacity retention. The substitution of Mg (x=0.02) can effectively improve the electrochemical performance of the Ni-based positive electrode materials.

(4) The cyclic voltammetry (CV) obtained the conducted experiments show that $LiNi_{0.6-x}Co_{0.2}Mn_{0.2}Mg_xO_2$ (x=0.02) has the smallest potential

gap ΔE_p comparing with the cases of x=0.04 and 0.06, indicating that it has the best electrochemical performance.

References

BARSOUKOVA, E., KIM, D. H., LEE, H.-S., LEE, H., YAKOVLEVA, M., GAO, Y. & ENGEL, J. F. 2003. Comparison of kinetic properties of $LiCoO_2$ and $LiTi_{0.05}Mg_{0.05}Ni_{0.7}Co_{0.2}O_2$ by impedance spectroscopy. *Solid State Ionics,* 161**,** 19-29.

BELHAROUAK, I., LU, W., VISSERS, D. & AMINE, K. 2006. Safety characteristics of $Li(Ni_{0.8}Co_{0.15}Al_{0.05})O_2$ and $Li(Ni_{1/3}Co_{1/3}Mn_{1/3})O_2$. *Electrochemistry Communications,* 8**,** 329-335.

CAO, H., ZHANG, Y., ZHANG, J. & XIA, B. 2005. Synthesis and electrochemical characteristics of layered $LiNi_{0.6}Co_{0.2}Mn_{0.2}O_2$ cathode material for lithium ion batteries. *Solid State Ionics,* 176**,** 1207-1211.

CHEN, Y., ZHANG, Y., CHEN, B., WANG, Z. & LU, C. 2014. An approach to application for $LiNi_{0.6}Co_{0.2}Mn_{0.2}O_2$ cathode material at high cutoff voltage by TiO_2 coating. *Journal of Power Sources,* 256**,** 20-27.

CHERALATHAN, K. K., KANG, N. Y., PARK, H. S., LEE, Y. J., CHOI, W. C., KO, Y. S. & PARK, Y.-K. 2010. Preparation of spherical $LiNi_{0.80}Co_{0.15}Mn_{0.05}O_2$ lithium-ion cathode material by continuous co-precipitation. *Journal of Power Sources,* 195**,** 1486-1494.

CHO, Y., OH, P. & CHO, J. 2013. A new type of protective surface layer for high-capacity Ni-based cathode materials: nanoscaled surface pillaring layer. *Nano Letters,* 13**,** 1145-1152.

DEAN, J. 1990. Lange's handbook of chemistry. *material and manufacturing process,* 5**,** 678-688.

DENG, C., ZHANG, S., FU, B. L., YANG, S. Y. & MA, L. 2010. Synthetic optimization of nanostructured $Li[Ni_{1/3}Mn_{1/3}Co_{1/3}]O_2$ cathode material prepared by hydroxide coprecipitation at 273K. *Journal of Alloys and Compounds,* 496**,** 521-527.

FU, C., LI, G., LUO, D., LI, Q., FAN, J. & LI, L. 2014. Nickel-rich layered microspheres cathodes: lithium/nickel disordering and electrochemical performance. *ACS Applied Materials & Interfaces,* 6**,** 15822-15831.

HUANG, Z., WANG, Z., ZHENG, X., GUO, H., LI, X., JING, Q. & YANG, Z. 2015. Structural and electrochemical properties of Mg-doped nickel based cathode materials $LiNi_{0.6}Co_{0.2}Mn_{0.2-x}Mg_xO_2$ for lithium ion batteries. *RSC Advances,* 5**,** 88773-88779.

KANG, B. & CEDER, G. 2009. Battery materials for ultrafast charging and discharging. *Nature,* 458**,** 190-193.

KIM, G.-H., MYUNG, S.-T., KIM, H.-S. & SUN, Y.-K. 2006. Synthesis of spherical $Li[Ni_{(1/3-z)}Co_{(1/3-z)}Mn_{(1/3-z)}Mg_z]O_2$ as positive electrode material for lithium-ion battery. *Electrochimica Acta,* 51**,** 2447-2453.

KIM, J.-M., CHANG, S.-M., CHANG, J. H. & KIM, W.-S. 2011. Agglomeration of nickel/cobalt/manganese hydroxide crystals in couette–taylor crystallizer. *Colloids and Surfaces A: Physicochemical and Engineering Aspects,* 384**,** 31-39.

LI, L.-J., WANG, Z.-X., LIU, Q.-C., YE, C., CHEN, Z.-Y. & GONG, L. 2012. Effects of chromium on the structural, surface chemistry and electrochemical of layered $LiNi_{0.8-x}Co_{0.1}Mn_{0.1}Cr_xO_2$. *Electrochimica Acta,* 77**,** 89-96.

LIAO, P.-Y., DUH, J.-G. & SHEU, H.-S. 2008. Structural and thermal properties of $LiNi_{0.6-x}Mg_xCo_{0.25}Mn_{0.15}O_2$ cathode materials. *Journal of Power Sources,* 183**,** 766-770.

LIU, Q., DU, K., HU, G.-R., PENG, Z.-D., CAO, Y.-B. & LIU, W.-M. 2012. Characterization of $LiNi_{0.9}Co_{0.05}[Mn_{1/2}Mg_{1/2}]_{0.05}O_2$ solid solution for secondary lithium ion batteries. *Solid State Ionics,* 227**,** 23-29.

LU, H., ZHOU, H., SVENSSON, A. M., FOSSDAL, A., SHERIDAN, E., LU, S. & VULLUM-BRUER, F. 2013. High capacity $Li[Ni_{0.8}Co_{0.1}Mn_{0.1}]O_2$ synthesized by sol–gel and co-precipitation methods as cathode materials for lithium-ion batteries. *Solid State Ionics,* 249-250**,** 105-111.

POUILLERIE, C., CROGUENNEC, L., BIENSAN, P., WILLMANN, P. & DELMAS, C. 2000. Synthesis and characterization of new $LiNi_{1-y}Mg_yO_2$ positive electrode materials for Lithium-ion batteries. *Journal of The Electrochemical Society,* 147**,** 2061-2069.

TOBY, B. H. 2001. EXPGUI a graphical user interface for GSAS. *Journal of Applied Crystallography,* 34**,** 210-213.

WANG, Y. X., SHANG, K. H., HE, W., AI, X. P., CAO, Y. L. & YANG, H. X. 2015. Magnesium-doped $Li_{1.2}[Co_{0.13}Ni_{0.13}Mn_{0.54}]O_2$ for Lithium-ion battery cathode with enhanced cycling stability and rate capability. *ACS Applied Materials & Interfaces,* 7**,** 13014-13021.

WOO, S.-W., MYUNG, S.-T., BANG, H., KIM, D.-W. & SUN, Y.-K. 2009. Improvement of electrochemical and thermal properties of $Li[Ni_{0.8}Co_{0.1}Mn_{0.1}]O_2$ positive electrode materials by multiple metal (Al, Mg) substitution. *Electrochimica Acta,* 54**,** 3851-3856.

XIAO, Z.-W., ZHANG, Y.-J. & WANG, Y.-F. 2015. Synthesis of high-capacity $LiNi_{0.8}Co_{0.1}Mn_{0.1}$ O_2 cathode by transition metal acetates. *Transactions of Nonferrous Metals Society of China,* 25**,** 1568-1574.

XU, B., FELL, C. R., CHI, M. & MENG, Y. S. 2011. Identifying surface structural changes in layered Li-excess nickel manganese oxides in high voltage lithium ion batteries: a joint experimental and theoretical study. *Energy & Environmental Science,* 4**,** 2223-2233.

YANG, Z., LU, J., BIAN, D., ZHANG, W., YANG, X., XIA, J., CHEN, G., GU, H. & MA, G. 2014. Stepwise co-precipitation to synthesize $LiNi_{1/3}Co_{1/3}Mn_{1/3}O_2$ one-dimensional hierarchical structure for lithium ion batteries. *Journal of Power Sources,* 272**,** 144-151.

YUE, P., WANG, Z., PENG, W., LI, L., CHEN, W., GUO, H. & LI, X. 2011. Spray-drying synthesized $LiNi_{0.6}Co_{0.2}Mn_{0.2}O_2$ and its electrochemical performance as cathode materials for lithium ion batteries. *Powder Technology,* 214**,** 279-282.

ZOU, G., YANG, X., WANG, X., GE, L., SHU, H., BAI, Y., WU, C., GUO, H., HU, L., YI, X., JU, B., HU, H., WANG, D. & YU, R. 2014. Improvement of electrochemical performance for Li-rich spherical $Li_{1.3}[Ni_{0.35}Mn_{0.65}]O_{2+x}$ modified by Al_2O_3. *Journal of Solid State Electrochemistry,* 18**,** 1789-1797.

Figures

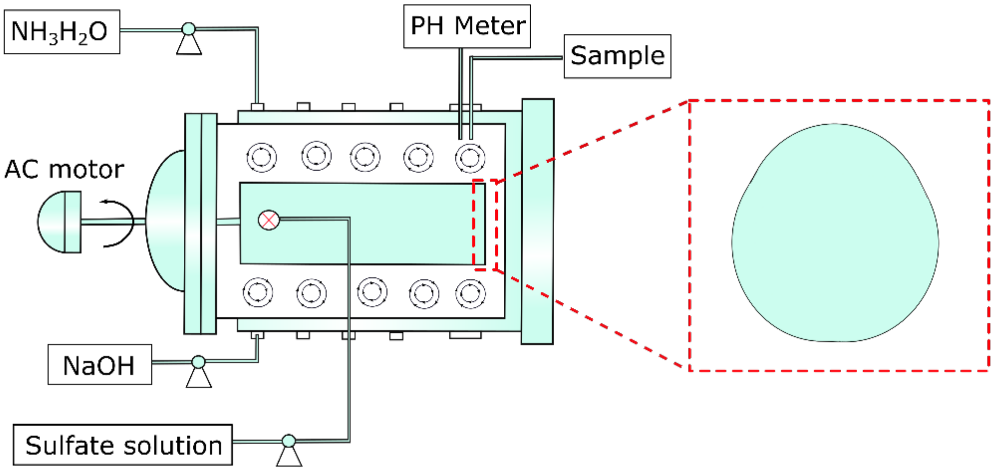

Figure 6-1. Schematic diagram of (a) experimental system used for reaction crystallization of $(Ni_{0.6}Co_{0.2}Mn_{0.2})(OH)_2$ precursor and (b) Inner structure of lobed Taylor-Couette unit

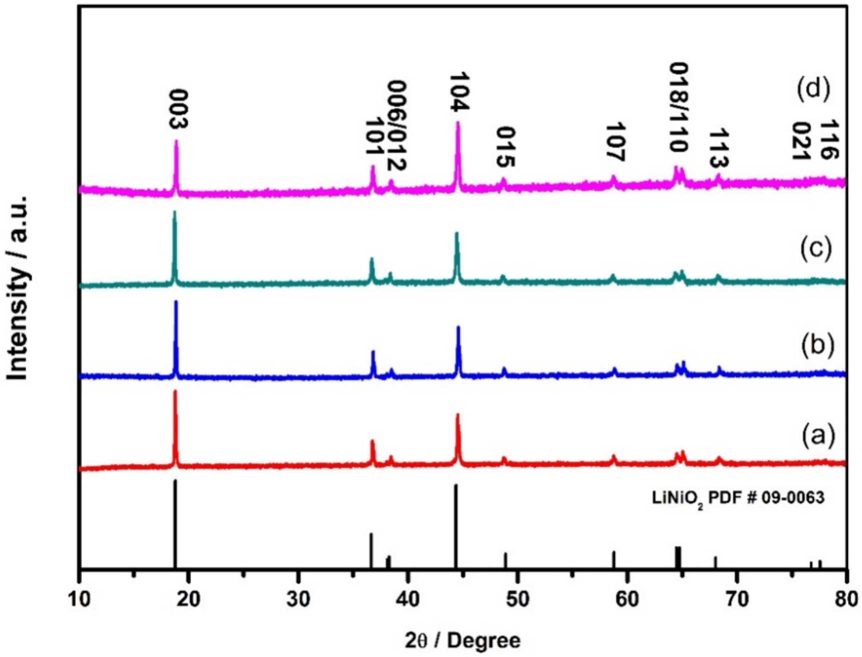

Figure 6-2.XRD pattern of the $LiNi_{0.6-x}Co_{0.2}Mn_{0.2}Mg_xO_2$: (a) x=0.0; (b) 0.02; (c) 0.04; (d) 0.06

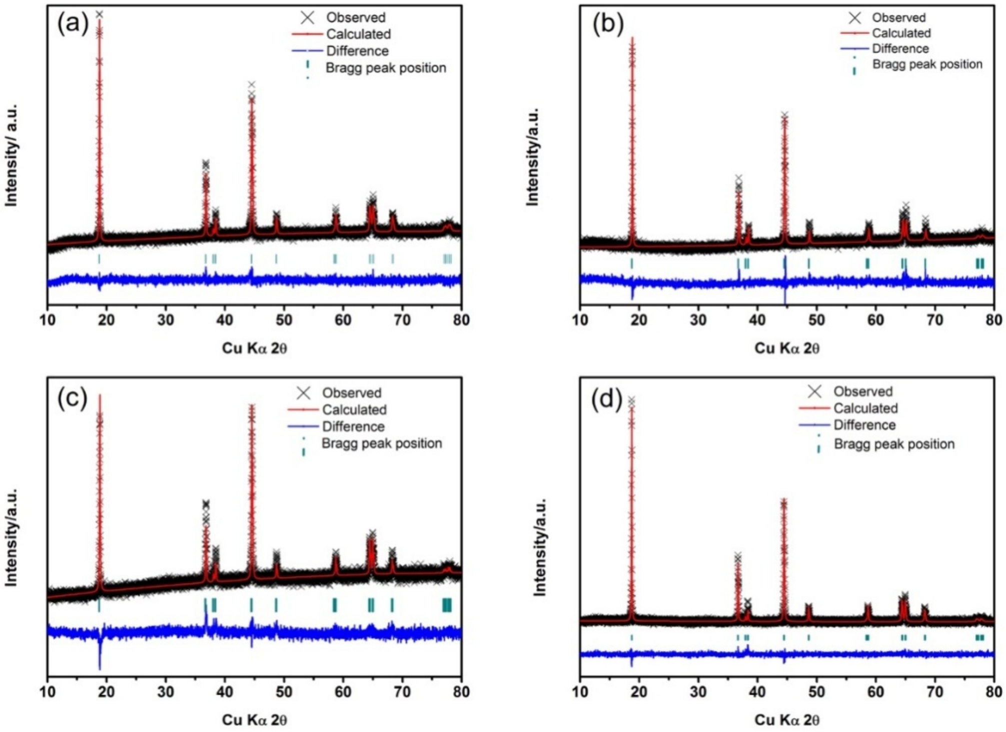

Figure 6-3. X-ray Rietveld refinement patterns for $LiNi_{0.6-x}Co_{0.2}Mn_{0.2}Mg_xO_2$ material: (a) x=0; (b) x=0.02; (c) x=0.04; (d) x=0.06

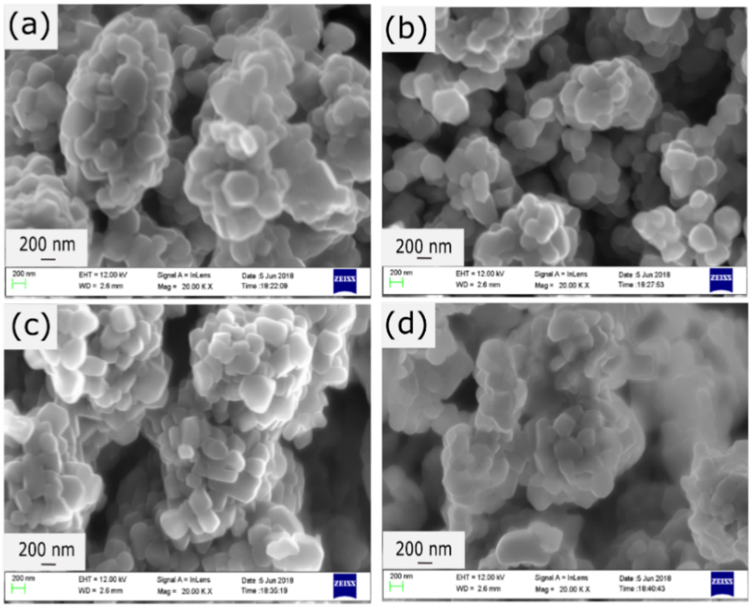

Figure 6-4. SEM images of $LiNi_{0.6-x}Co_{0.2}Mn_{0.2}Mg_xO_2$ material samples (a) x=0, (b) 0.02, (c) 0.04 and (d) 0.06

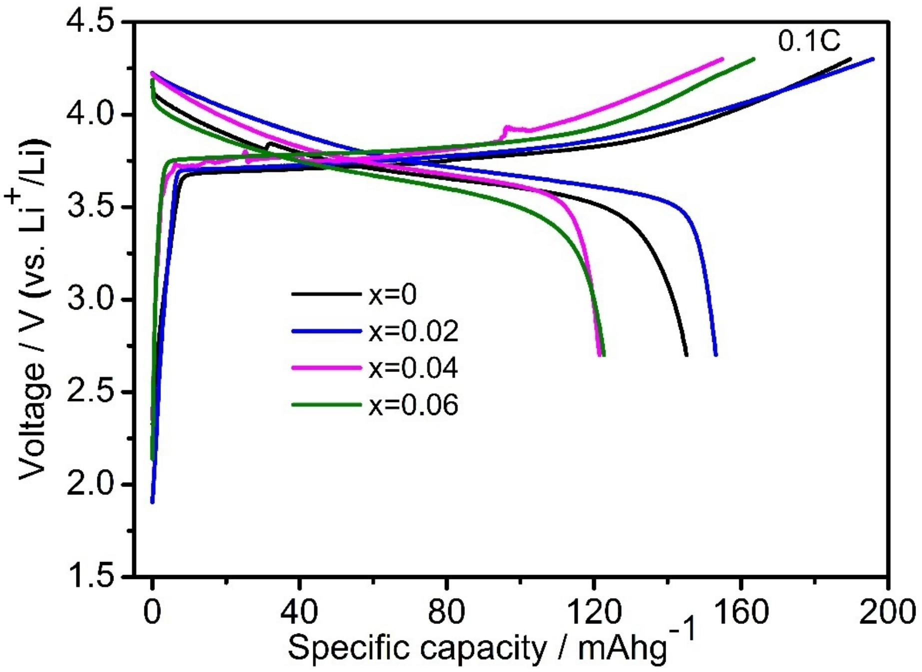

Figure 6-5. The initial charge and discharge profiles of $LiNi_{0.6-x}Co_{0.2}Mn_{0.2}Mg_xO_2$ (x=0, 0.2, 0.4 and 0.6) at 0.1 C

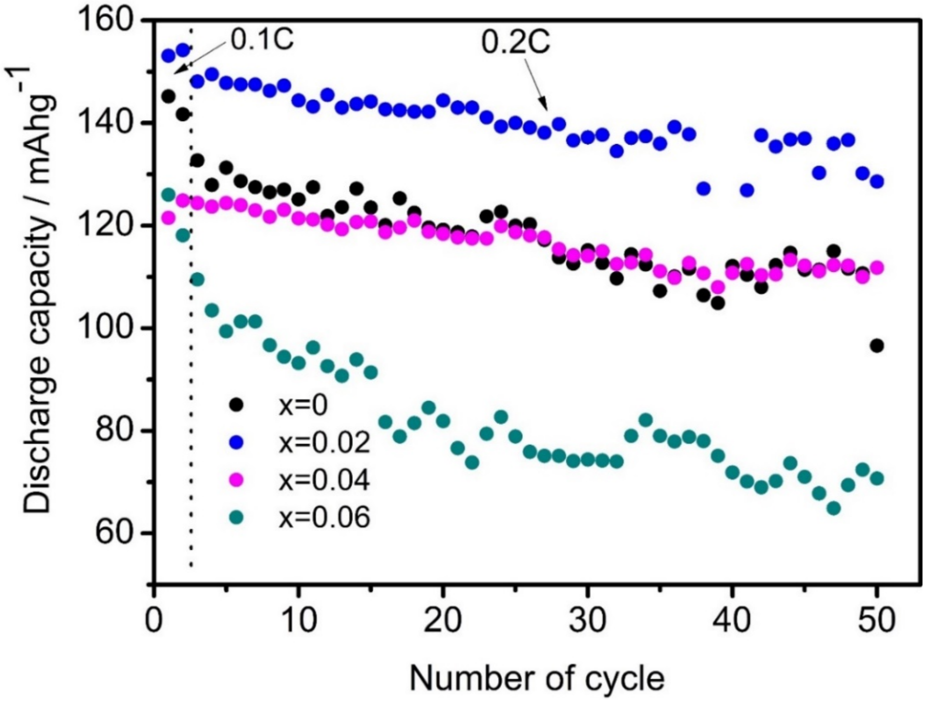

Figure 6-6. Cycle performance of $LiNi_{0.6-x}Co_{0.2}Mn_{0.2}Mg_xO_2$ (x=0, 0.2, 0.4, 0.6) at 0.2 C

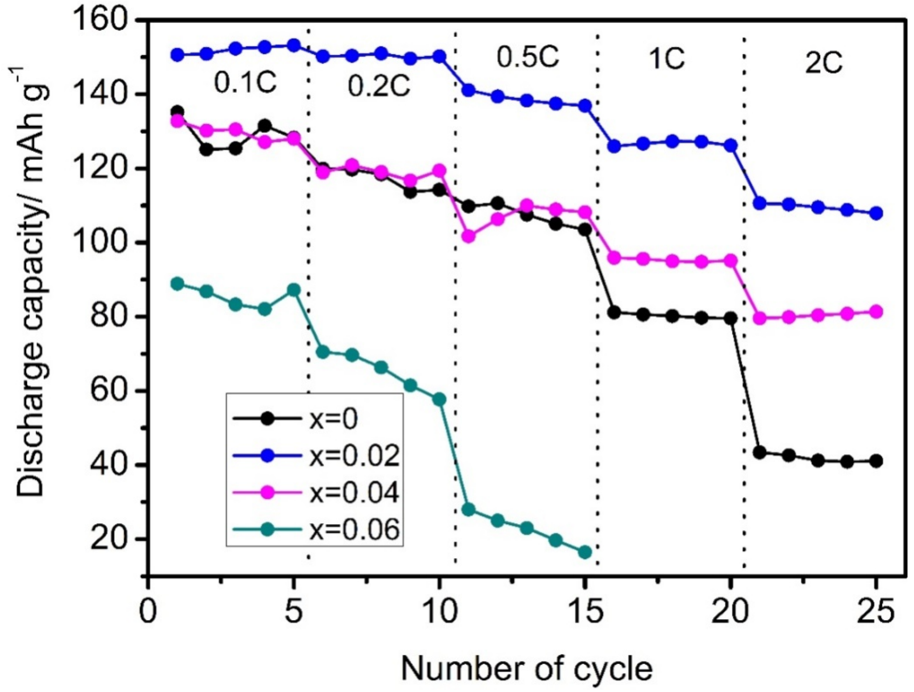

Figure 6-7. Rate capability of $LiNi_{0.6-x}Co_{0.2}Mn_{0.2}Mg_xO_2$ (x=0, 0.02, 0.04, 0.06) electrodes

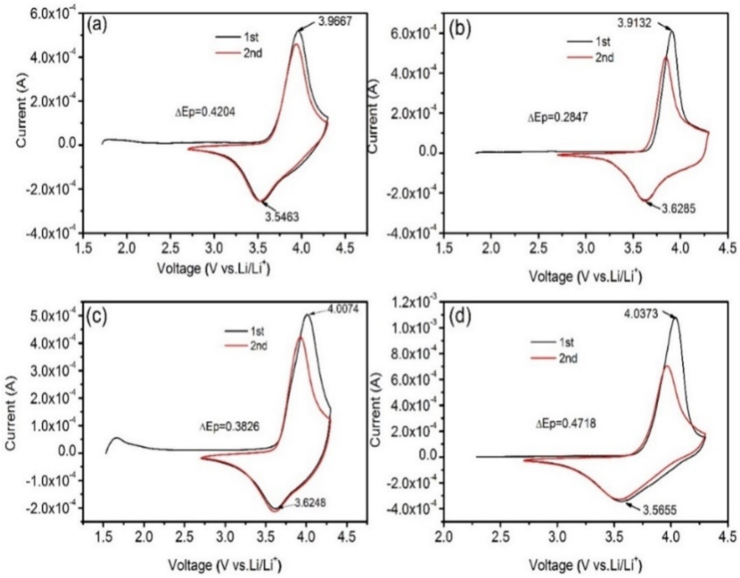

Figure 6-8. CV curves for the first two cycles of $LiNi_{0.6-x}Co_{0.2}Mn_{0.2}Mg_xO_2$ (x=0, 0.02, 0.04 and 0.06)

Tables

Table 6-1. Unit cell parameters, the intensity ratio of $I_{(003)}/I_{(104)}$ of $LiNi_{0.6-x}Co_{0.2}Mn_{0.2}Mg_xO_2$ (x=0, 0.02, 0.04, 0.06)

Addition of Mg	**a**	**c**	**c/a**	**V (Å^3)**	**I_{003}/I_{104}**
x=0	2.8702	14.1897	4.9438	101.23	0.93
x=0.02	2.8669	14.1877	4.9488	100.98	1.02
x=0.04	2.8736	14.2376	4.9546	101.80	0.86
x=0.06	2.8719	14.1941	4.9424	101.40	0.61

Table 6-2. The setting and analyzed composition of $LiNi_{0.6-x}Co_{0.2}Mn_{0.2}Mg_xO_2$ (x=0, 0.02, 0.04 and 0.06)

Nominal chemical formula	**Analyzed chemical formula**
$LiNi_{0.6}Co_{0.2}Mn_{0.2}O_2$	$Li_{0.994}Ni_{0.588}Co_{0.202}Mn_{0.20}$
$LiNi_{0.58}Co_{0.2}Mn_{0.2}Mg_{0.02}O_2$	$Li_{1.08}Ni_{0.594}Co_{0.217}Mn_{0.215}Mg_{0.022}$
$LiNi_{0.56}Co_{0.2}Mn_{0.2}Mg_{0.04}O_2$	$Li_{0.994}Ni_{0.537}Co_{0.212}Mn_{0.200}Mg_{0.036}$
$LiNi_{0.54}Co_{0.2}Mn_{0.2}Mg_{0.06}O_2$	$Li_{0.951}Ni_{0.562}Co_{0.222}Mn_{0.215}Mg_{0.063}$

Table 6-3. Structural analysis obtained from X-ray Rietveld refinement and interatomic distances of $LiNi_{0.6-x}Co_{0.2}Mn_{0.2}Mg_xO_2$ material (x=0, x=0.02, x=0.04, x=0.06) sample

Atom	site	Occ (x=0)	Occ (x=0.02)	Occ (x=0.04)	Occ (x=0.06)
Li1	3a	0.9482	0.9628	0.9035	0.9219
Ni1	3a	0.0518	0.0336	0.0840	0.0659
Mg1	3a		0.0036	0.0125	0.0122
Li2	3b	0.0518	0.0372	0.0965	0.0781
Ni2	3b	0.5482	0.5464	0.4500	0.4710
Co1	3b	0.2020	0.2025	0.2060	0.2010
Mn1	3b	0.1980	0.1975	0.2100	0.2021
Mg2	3b		0.0164	0.0275	0.0478
O	6c	1	1	1	1
Rwp(%)		4.70	6.17	5.51	4.37
Rp(%)		3.71	4.86	4.27	3.35
χ^2		1.169	1.684	1.388	1.404
Li–O (Å)		2.11307 (7)	2.11217 (7)	2.11456 (4)	2.11573 (2)
M–O (Å)		1.96491 (5)	1.96397 (6)	1.96635 (4)	1.96732 (2)

Table 6-4. Electrochemical Data of $LiNi_{0.6}Co_{0.2}Mn_{0.2}O_2$ prepared at different Mg addition at 0.1 C and 0.2 C-rate charge/discharge cycling

Addition of Mg	**Initial charge capacity at 0.1C (mAh g^{-1})**	**Initial discharge capacity at 0.1C (mAh g^{-1})**	**Initial coulombic efficiency (%)**	**First discharge capacity at 0.2 C**	**48th discharge capacity (mAh g^{-1}) at 0.2 C**	**Capacity retention after 48 cycles (%)**
0	189.6	145.2	76.6	132.7	96.6	72.8
0.02	195.8	153.1	78.2	148.1	128.6	86.8
0.04	154.8	121.5	78.4	124.4	111.8	89.9
0.06	163.4	122.7	75.1	102	70.8	69.4

Recapitulation and Recommendation for Future Work

7.1 Recapitulation

A series of nickel rich $LiNi_{1-x-y}Co_xMn_yO_2$(NCM) materials (Ni≥0.6) for Lithium cathode materials have been considered as promising candidates for the next generation of commercial materials due to its higher specific capacity and lower cost. Among them, $LiNi_{0.6}Co_{0.2}Mn_{0.2}O_2$ has been widely recognised as a potential candidate material. The preparation of this material is usually realised by using both co-precipitation and high-temperature solicitation. Co-precipitation method is mainly used for the preparation of NCM precursor. Spherical precursor with a high tap density is beneficial to the improvement of the electrochemical performance of the precursor materials. The properties of the spherical precursors such as particle size, size distribution and morphology are strongly related to the hydrodynamic conditions and physical-chemical conditions. Normally, the influence of hydrodynamic conditions on the co-precipitation method is investigated under random turbulent eddy flow using an impeller or propeller. A problem encountered when using this method is that it usually takes a long time to obtain the particle size with a high tap density. As such, an effective approach is to use the optimisation in the process of the preparation process. The current project has employed a Taylor vortex flow reactor for synthesis of NCM precursor as this type of the reactor can easily realise the control on the agglomeration of nickel, cobalt and manganese hydroxide. The synthesis process occurring inside such reactor has the features that characterised by the synthesised spherical precursor particles having a narrow size distribution and a high tap density. However, the successful synthesis itself is still subjected to various factors such as reactor internal configuration and adopted operating conditions. A Taylor-couette reactor with the lobed inner cylinder (LTC) has been employed throughout the present study for synthesising the NCM622 precursor. Unlike other conventional Taylor-couette reactors with the circular inner cylinder, the hydrodynamics in the LTC reactor presents the deformed Taylor vortices in circumferential direction, which enhances the turbulent kinetic energy generation and turbulent energy dissipation and consequently reduces the regions of low Reynolds shear stresses. As a result, the mixing in the LTC reactor allows the particles to undergo an environment with a slightly high shear rate but more uniform shear rate distribution, thus being beneficial to the synthesis of particles.

In Chapter 3, we first studied the hydrodynamics in the LTC reactor and physical-chemical conditions to prepare a series size of NCM622 particles. In general, the particle sizes of the precursors in LTC reactor depend to a great extent on the shear rate, the molar ratio of NH_3H_2O and pH. It has been found that the particle size decreases with increasing the shear rate. The micromixing in the LTC reactor can be intensified with increasing the local shear rate, which can be realized by adjusting the lobed inner cylinder rotational speed. Consequently, the morphology of particle also changes from irregular to spherical-like and synthesized particles become compact at the high shear rate. The size and size distribution are also influenced by the molar ratio of NH_3/MSO_4. An appropriate molar ratio of NH_3/MSO_4 (0.4~1) would be desirable for getting spherical precursors. A correlation between turbulent energy dissipation and the molar ratio of NH_3/MSO_4 is subsequently established to evaluate the synthesized particle sizes.

Based on the synthesis process of NCM622 precursors using the LTC reactor, Chapter 3 mainly focuses on the effects of controlling the hydrodynamics and physical-chemical properties. However, the implications of these effects on the actual performance of Lithium battery were not discussed. The electrochemical performances of $LiNi_{0.6}Co_{0.2}Mn_{0.2}O_2$ have been evaluated in Chapter 4. $Li(Ni_{0.6}Co_{0.2}Mn_{0.2})O_2$ cathode materials have been prepared from calcination of co-precipitated $Ni_{0.6}Co_{0.2}Mn_{0.2}(OH)_2$ precursors and LiOH at high temperature. By comparing the calcination temperature, it was found that the calcination temperature of 860^{o}C is a suitable temperature for synthesising the cathode material with the best electrochemical performance. The particles prepared with smaller size show less cation mixing degree, which is beneficial to their electrochemical properties. The obtained results have provided guidelines for obtaining high-performance cathode materials with decent cycling performance and rate capability.

Achieving the desired electrochemical properties, however, usually needs to conduct the expensive and time-consuming physical experiments. Using a physically-based predictive model can assists more reasonable utilization of the synthesis for the required materials and allow for a real-time control of the synthesis process according to the predicted electrochemical performance of the synthesised LIBs (here the assembled coin cell is concerned). In Chapter 5, A pseudo-two-dimensional (P2D) model has been applied to simulate the electrochemical reactions of the $LiNi_{0.6}Co_{0.2}Mn_{0.2}O_2$ and predict the electrochemical behaviour at different conditions. The detailed analysis of a suitable calendaring process provides a forecasting for manufacturing $LiNi_{0.6}Co_{0.2}Mn_{0.2}O_2$ cathode with different pore structures and porosities of the electrode. It was revealed based on the simulations that the electrodes prepared with compaction load of 5~10 mpa have little difference in capacity retention. Higher compaction load will lead to the crack of particles, degrading of the electrochemical performance. Based on the SEM images obtained for both the calendared and uncalendared electrodes the relationship between the compaction load P and porosity of the coating ε_l was obtained by fitting the experimental results and implemented into the numerical modelling. It was found that equilibrate of coating porosity is about 0.7850. The numerical simulation also confirms that a reduction in the particle size of active materials can benefit solid phase diffusion.

The Mg doped NiCoMn precursor has also been synthesised by the LTC reactor and the electrochemical performances of the samples were evaluated. $LiNi_{0.6-x}Co_{0.2}Mn_{0.2}Mg_xO_2$ (x=0, 0.02, 0.04 and 0.06) has been prepared by co-precipitation in the LTC reactor and using high-temperature calcination method. The XRD results indicate that addition of a small amount of Mg (x=0.02) is beneficial to lowering of the Li/Ni cation mixing. A similar tendency was also observed to take place in the lattice parameters. Rietveld refinement results show that addition of small amount of Mg (x=0.02) could inhibit the Ni^{2+} into Li (3a) layer, lowering the bonding distance of Li-O and M-O and increasing the structural stability of the material. As for the electrochemical performances, the electrochemical performance has also been improved for a small amount of Mg doping onto $LiNi_{0.6}Co_{0.2}Mn_{0.2}O_2$.

There are still a couple of issues remaining to be resolved in in the present study:

(1) Controlling the reactor is a difficult problem during the reaction. In our experiment, LTC reactor is placed horizontally so that the effect of hydrostatic pressure can be disregarded. However, this has brought out bubble accumulation in the top region in contact with the outer cylinder of the Taylor-Couette flow reactor in the duration of the operation. Consequently, the reaction and mixing may take place in a gas-liquid two-phase flow system, resulting in the process to become uncertain. In such case, Taylor vortices structure may change and deform significantly, influencing both the synthesised particle size and morphology. It is expected that for industrial scale applications, this issue will become critical. This influence has to be considered in the reactor scale-up. In other words, the effect of gravity needs to be accounted when using the large size Taylor-Couette flow reactor to prepare different types of particles.

(2) Though the tap density of spherical NCM622 prepared by the LTC reactor meets the requirement for industrial application, the electrochemical properties reported in this work are based on the limited data. Multiple cycle stability and high rate capacity of the samples need to be improved further.

(3) It has been found that the assembled Li-ion sample coin cells in this study suffer substantial energy and power loss when being operated at lower temperatures. The low-temperature performance is also related to the cell structure design. Thus, the thermal effect should be considered in the numerical simulation of the electrochemical performance of the LIBs.

7.2 Recommendation for Future Work

Detailed studies on the preparation of NCM622 using an LTC reactor have been conducted as reflected in the preceding chapters of this thesis. It has been clearly demonstrated that the hydrodynamics in the LTC reactor is crucial for synthesis of NCM precursor particles while suitable controlling the operation parameters that affect the hydrodynamics can be intentionally used for synthesis of NCM series precursors. To promote a wider application of continuous crystallization of NCM materials (here with referring to the use of LTC reactor) in industry, more efforts should be made in various aspects, in particular (1) adaptability for large scale reactor; (2) better control on the reactor operation and chemical reaction; (3) better design of internal configuration of the LTC reactor so that the mixing and hydrodynamics can be improved to ensure to obtain the required distribution of particles and high tap density. Although the preparation of NCM precursor particles by using the Taylor vortex flow reactor is not the mainstream in the Lithium battery manufacturing industry at the present, it is expected with certain confidence that the use of Taylor vortex flow reactor will become well recognised preparation process for synthesis of NCM precursor materials as Taylor vortex flow can provide the advantages of hydrodynamics much superior to the conventional mixing tank reactors.

The electrochemical performance of $LiNi_{0.6}Co_{0.2}Mn_{0.2}O_2$ in this work has been evaluated in terms of calcination temperature, particles sizes and the molar ratio of NH_3/MSO_4. There still exist many inadequacies which need to be improved, for example, the structural stability of material and cycling stability for electrochemical properties. Surface modification has been demonstrated to be an effective way to improve the electrochemical behavior of NCM materials. In considering the differences between NCM series precursor materials, the synthesis should be treated individually. Element doping has been shown to be an appropriate route to improve the structural stability of the material. It should be pointed out that applying different voltages, the electrochemical properties of the materials with different elemental modifications change significantly. Thus, it is necessary to explore the appropriate doping elements and their doping function effects on the electrochemical properties of NCM materials. Surface coating of the positive electrode precursor material can stabilise the surface, minimize the side reaction and increase the thermal stability. A hybrid coating method would be a promising way for improving the electrical and ionic conductivity of the lithium batteries. In order to further understand the fundamentals of the reaction, numerical modelling of the LIBs ion diffusion process is highly recommended, the employment of 2D or 3D models should take different preparation processes of electrode and particle into consideration. The development of a simplified P2D model suitable for high discharge rate for Li simulation may be necessary but the model should have the features of simple and fast estimation and also take into account the thermal stability of the battery.

Appendix

Appendix A

This appendix details the relationship between supersaturation and molar ratio of NH_3/MSO_4 (n). For ionic crystal precipitation, the solubility can be represented in terms of the solubility product, as shown in the following example:

$$A^{2+} + 2B^{-} = AB_2(\mathrm{s}) \qquad \text{[A-1]}$$

$$K_{sp} = [A^{2+}]_{eq}[B^{-}]_{eq}^{2} \qquad \text{[A-2]}$$

where A^{2+} and $B^{-}$are the ionic concentrations of components A and B in solution at equilibrium, respectively. The saturation ratio, S, for this example can be written as

$$S = \frac{c'}{c^*} \qquad \text{[A-3]}$$

wherec' is the original solute concentration and c^* is the equilibrium solubility of the solute at the temperature and pressure of the system; from this, the supersaturation ratio σ can be defined as

$$\sigma = \frac{c-c^*}{c^*} = S - 1 \qquad \text{[A-4]}$$

For component AB_2, c^* can be calculated according to the following equation:

$$c^* = (K_{sp}/4)^{1/3} \qquad \text{[A-5]}$$

Coprecipitation synthesis using NH_3H_2O starts from the formation of a metal–ammonium complex (Eq. A-6 to A-8), where metal cations are coordinated to the ligands of ammonia ions. Then, the ammonia anions are slowly replaced by hydroxide anions coming from NaOH. The main reactions of formation of metal–ammonium complexes are listed as follows:

$$\mathrm{M + L = ML} \qquad \beta_1 \qquad [\mathrm{ML}] = \beta_1[\mathrm{M}]\cdot[\mathrm{L}] \qquad \text{[A-6]}$$

$$\mathrm{M + 2L = 2ML} \qquad \beta_2 \qquad [\mathrm{ML_2}] = \beta_2[\mathrm{M}]\cdot[\mathrm{L}] \qquad \text{[A-7]}$$

$$\cdots$$

$$\mathrm{M} + \mathrm{mL} = \mathrm{ML} \qquad \beta_{\mathrm{m}} \qquad [\mathrm{ML}_{\mathrm{m}}] = \beta_{\mathrm{m}}[\mathrm{M}] \cdot [\mathrm{L}] \qquad \text{[A-8]}$$

Where M is the metal ion of Ni, Co, Mn; L is ammonium (NH_3); m is the ion number of complex (m=1~6); $\beta_1, \beta_2, \ldots \beta_m$ is the equation equilibrium constant.

When NH_3H_2O is utilized as chelating agent, the supersaturation of solution will be changed. Thence, c^*can be calculated according to the following equation:

$$c^*(M) = (K_{sp} a_{MLm}/4)^{1/3} \qquad \text{[A-9]}$$

$$a_{ML_m} = 1 + \beta_1[\mathrm{NH_3}] + \beta_2[\mathrm{NH_3}]^2 \ldots + \beta_m[\mathrm{NH_3}]^m \qquad \text{[A-10]}$$

Chemical equilibrium reaction used for the calculation is listed in Table A-1. The variation of the concentration of metal–ammonium is obtained by solving the equilibrium equations that are pH-dependent dissociation of ammonium in water. In our system, the pH data during the coprecipitation process is 11.4~11.6, To further simplify the calculation, an averaged pH data of 11.5 is used. Using reaction 3, 15 and 28 in Table A-1, the equilibrium concentration of Ni^{2+}, Co^{2+} and Mn^{2+} in solution are calculated as the following.

$$[\mathrm{Ni}^{2+}] = \frac{\mathrm{K}_3}{(\mathrm{K}_2 \cdot 10^{-\mathrm{pH}})^2} = 5.49\mathrm{E} - 11$$

$$[\mathrm{Co}^{2+}] = \mathrm{K}_{19}/(\mathrm{K}_2 \cdot 10^{-\mathrm{pH}})^2 = 5.89\mathrm{E} - 10$$

$$[\mathrm{Mn}^{2+}] = \mathrm{K}_{28}/(\mathrm{K}_2 \cdot 10^{-\mathrm{pH}})^2 = 1.91\mathrm{E} - 08$$

According to conservation of mass, the original concentration of NH_3 equals to the total concentration of free NH_3, NH_4^+, NH_3 in metal-ammonia complex.

$$[\mathrm{N}] = [\mathrm{NH_3}]\{1 + \mathrm{K}_1 \cdot 10^{-\mathrm{pH}} + [\mathrm{Ni}^{2+}] \cdot \mathrm{K}^{9+}[\mathrm{Co}^{2+}] \cdot \mathrm{K}_{22} + [\mathrm{Mn}^{2+}] \cdot \mathrm{K}_{34}\}$$

$$+[\mathrm{NH_3}]^2\{2[\mathrm{Ni}^{2+}] \cdot \mathrm{K}_{10} + 2[\mathrm{Co}^{2+}] \cdot \mathrm{K}_{23} + 2[\mathrm{Mn}^{2+}] \cdot \mathrm{K}_{35}\}$$

$$+[\mathrm{NH_3}]^3\{3[\mathrm{Ni}^{2+}] \cdot \mathrm{K}_{11} + 3[\mathrm{Co}^{2+}] \cdot \mathrm{K}_{24} + 3[\mathrm{Mn}^{2+}] \cdot \mathrm{K}_{36}\}$$

$$+[\mathrm{NH_3}]^4\{4[\mathrm{Ni^{2+}}]\cdot \mathrm{K_{12}} + 4[\mathrm{Co^{2+}}]\cdot \mathrm{K_{25}} + 4[\mathrm{Mn^{2+}}]\cdot \mathrm{K_{37}}\}$$

$$+[\mathrm{NH_3}]^5\{5[\mathrm{Ni^{2+}}]\cdot \mathrm{K_{13}} + 5[\mathrm{Co^{2+}}]\cdot \mathrm{K_{26}}\}$$

$$+[\mathrm{NH_3}]^6\{6[\mathrm{Ni^{2+}}]\cdot \mathrm{K_{14}} + 6[\mathrm{Co^{2+}}]\cdot \mathrm{K_{27}}\}$$

$$= 1.01 * [\mathrm{NH_3}] + 4.84\ \mathrm{E}-05 * [\mathrm{NH_3}]^2 + 2.72\ \mathrm{E}-03 * [\mathrm{NH_3}]^3 + 5.25\ \mathrm{E}-02 * [\mathrm{NH_3}]^4 + 3.58\mathrm{E}-01 * [\mathrm{NH_3}]^5 + 4.57\ \mathrm{E}-01 * [\mathrm{NH_3}]^6 \quad [\text{A-11}]$$

The concentration of metal–ammonium complex can be written as

$$[Ni(NH_3)_m]^{2+} = [\mathrm{Ni^{2+}}]^* \alpha_{[Ni(NH_3)_m]}{}^{2+}$$

$$= [\mathrm{Ni^{2+}}]\{1 + [\mathrm{NH_3}]\cdot \mathrm{K_9} + [\mathrm{NH_3}]^2\cdot \mathrm{K_{10}} + [\mathrm{NH_3}]^3\cdot \mathrm{K_{11}} + [\mathrm{NH_3}]^4\cdot \mathrm{K_{12}} + [\mathrm{NH_3}]^5\cdot \mathrm{K_{13}} + [\mathrm{NH_3}]^6\cdot \mathrm{K_{14}}\}$$

$$= [\mathrm{Ni^{2+}}]\{1 + 6.31\mathrm{E}+02 * [\mathrm{NH_3}] + 1.10\mathrm{E}+05 * [\mathrm{NH_3}]^2 + 5.89\mathrm{E}+06 * [\mathrm{NH_3}]^3 + 9.12\mathrm{E}+07 * [\mathrm{NH_3}]^4 + 5.13\mathrm{E}+08 * [\mathrm{NH_3}]^5 + 5.50\mathrm{E}+08 * [\mathrm{NH_3}]^6\} \quad [\text{A-12}]$$

$$[Co(NH_3)_m]^{2+} = [\mathrm{Co^{2+}}]^* \alpha_{[Co(NH_3)_m]}{}^{2+}$$

$$= [\mathrm{Co^{2+}}]\{1 + [\mathrm{NH_3}]\cdot \mathrm{K_{22}} + [\mathrm{NH_3}]^2\cdot \mathrm{K_{23}} + [\mathrm{NH_3}]^3\cdot \mathrm{K_{24}} + [\mathrm{NH_3}]^4\cdot \mathrm{K_{25}} + [\mathrm{NH_3}]^5\cdot \mathrm{K_{26}} + [\mathrm{NH_3}]^6\cdot \mathrm{K_{27}}\}$$

$$= [\mathrm{Co^{2+}}]\{1 + 1.29\mathrm{E}+02 * [\mathrm{NH_3}] + 5.50\mathrm{E}+03 * [\mathrm{NH_3}]^2 + 6.17\mathrm{E}+04 * [\mathrm{NH_3}]^3 + 3.55\mathrm{E}+05 * [\mathrm{NH_3}]^4 + 5.37\mathrm{E}+05 * [\mathrm{NH_3}]^5 + 1.29\mathrm{E}+05 * [\mathrm{NH_3}]^6\} \quad [\text{A-13}]$$

$$[Mn(NH_3)_m]^{2+} = [\mathrm{Mn}^{2+}]^* \alpha_{[Mn(NH_3)_m]}{}^{2+}$$

$$= [\mathrm{Mn}^{2+}]\{1 + [\mathrm{NH_3}] \cdot \mathrm{K}_{34} + [\mathrm{NH_3}]^2 \cdot \mathrm{K}_{35} + [\mathrm{NH_3}]^3 \cdot \mathrm{K}_{36}$$

$$+ [\mathrm{NH_3}]^4 \cdot \mathrm{K}_{37}\}$$

$$= [\mathrm{Mn}^{2+}]\{1 + 6.31 * [\mathrm{NH_3}] + 2.0\mathrm{E} + 01 * [\mathrm{NH_3}]^2 + 5.01\mathrm{E} + 01 *$$

$$[\mathrm{NH_3}]^3 + \quad 2.0\mathrm{E} + 01 * [\mathrm{NH_3}]^4\} \qquad \text{[A-14]}$$

Based on the above equations, Table 2-4 list the value of the molar ratio of NH_3/MSO_4, $[NH_3]$ concentration, the original metal concentration, S and σ during the experiment.

The final relationship between supersaturation σ and molar ratio of NH_3/MSO_4 (n) can be defined as:

$$\sigma = k_1 n\text{^}(-k_2) \qquad \text{[A-15]}$$

Table A-1. Chemical equilibrium reactions and equilibrium constants used in the solubility calculations

Number	Reaction	lgKn	Number	Reaction	lgKn
1	$NH_3+H^+=NH_4^+$	$lgK_1=9.246$	20	$2Co^{2+}+OH^-= Co_2(OH)^{3+}$	$lgK_{20}=2.7$
2	$H_2O=H^++OH^-$	$lgK_2=-14$	21	$4Co^{2+}+4OH^-= Co_4(OH)_4^{4+}$	$lgK_{21}=25.6$
3	$Ni(OH)_2(s)=Ni^{2+}+2OH^-$	$lgK_3=-15.26$	22	$Co^{2+}+NH_3=Co(NH_3)^{2+}$	$lgK_{22}=2.11$
4	$Ni^{2+}+OH^-= Ni(OH)^+$	$lgK_4=4.97$	23	$Co^{2+}+2NH_3=Co(NH_3)_2^{2+}$	$lgK_{23}=3.74$
5	$Ni^{2+}+2OH^-= Ni(OH)_2$	$lgK_5=8.55$	24	$Co^{2+}+3NH_3=Co(NH_3)_3^{2+}$	$lgK_{24}=4.79$
6	$Ni^{2+}+3OH^-= Ni(OH)_3^-$	$lgK_6=11.33$	25	$Co^{2+}+4NH_3=Co(NH_3)_4^{2+}$	$lgK_{25}=5.55$
7	$2Ni^{2+}+OH^-= Ni_2(OH)^{3+}$	$lgK_7=3.3$	26	$Co^{2+}+5NH_3=Co(NH_3)_5^{2+}$	$lgK_{26}=5.73$
8	$4Ni^{2+}+4OH^-= Ni_4(OH)_4^{4+}$	$lgK_8=28.3$	27	$Co^{2+}+6NH_3=Co(NH_3)_6^{2+}$	$lgK_{27}=5.11$
9	$Ni^{2+}+NH_3=Ni(NH_3)^{2+}$	$lgK_9=2.8$	28	$Mn(OH)_2(s)=Mn^{2+}+2OH^-$	$lgK_{28}=-12.72$
10	$Ni^{2+}+2NH_3=Ni(NH_3)_2^{2+}$	$lgK_{10}=5.04$	29	$Mn^{2+}+OH^-= Mn(OH)^+$	$lgK_{29}=3.9$
11	$Ni^{2+}+3NH_3=Ni(NH_3)_3^{2+}$	$lgK_{11}=6.77$	30	$Mn^{2+}+3OH^-= Mn(OH)_3^-$	$lgK_{30}=8.3$
12	$Ni^{2+}+4NH_3=Ni(NH_3)_4^{2+}$	$lgK_{12}=7.96$	31	$Mn^{2+}+4OH^-= Mn(OH)_4^{2-}$	$lgK_{31}=7.7$
13	$Ni^{2+}+5NH_3=Ni(NH_3)_5^{2+}$	$lgK_{13}=8.71$	32	$2Mn^{2+}+OH^-= Mn_2(OH)^{3+}$	$lgK_{32}=3.4$
14	$Ni^{2+}+6NH_3=Ni(NH_3)_6^{2+}$	$lgK_{14}=8.74$	33	$2Mn^{2+}+3OH^-= Mn_2(OH)_3^+$	$lgK_{33}=17.1$
15	$Co(OH)_2(s)=Co^{2+}+2OH^-$	$lgK_{15}=-14.23$	34	$Mn^{2+}+NH_3=Mn(NH_3)^{2+}$	$lgK_{34}=0.8$
16	$Co^{2+}+OH^-= Co(OH)^+$	$lgK_{16}=3.3$	35	$Mn^{2+}+2NH_3=Mn(NH_3)_2^{2+}$	$lgK_{35}=1.3$
17	$Co^{2+}+2OH^-= Co(OH)_2$	$lgK_{17}=9.2$	36	$Mn^{2+}+3NH_3=Mn(NH_3)_3^{2+}$	$lgK_{36}=1.7$
18	$Co^{2+}+3OH^-= Co(OH)_3^-$	$lgK_{18}=10.5$	37	$Mn^{2+}+4NH_3=Mn(NH_3)_4^{2+}$	$lgK_{37}=1.30$
19	$Co^{2+}+4OH^-=Co(OH)_4^{2-}$	$lgK_{19}=10.2$			

Table A-2. Summary of molar ratio of NH_3/MSO_4, $[NH_3]$ concentration, Ni^{2+} concentration,$\alpha[\mathrm{N_i}(\mathrm{NH_3})_\mathrm{m}]^{2+}$S and σ

Molar ratio of NH_3/MSO_4 (n)	**[N] (mol L^{-1})**	**$[NH_3]$ (mol L^{-1})**	***c (Ni^{2+})* (molL^{-1})**	$\boldsymbol{\alpha_{[N_i(NH_3)_m]^{2+}}}$	**c* （mol/L）**	**S**	$\boldsymbol{\sigma}$
0.2	0.4	0.39	1.20	9.04E+06	1.07E-03	1116.38	1115.38
0.4	0.8	0.68	1.20	1.53E+08	2.76E-03	434.56	433.56
0.6	1.2	0.84	1.20	4.70E+08	4.01E-03	299.14	298.14
0.8	1.6	0.95	1.20	8.63E+08	4.91E-03	244.23	243.23
1	2	1.02	1.20	1.29E+09	5.62E-03	213.51	212.51

Table A-3. Summary of molar ratio of NH_3/MSO_4, $[NH_3]$ concentration, Co^{2+}concentration, $\alpha[\mathrm{C_O}(\mathrm{NH_3})_\mathrm{m}]^{2+}$,S and σ

Molar ratio of NH_3/MSO_4 (n)	**[N] (mol L^{-1})**	**$[NH_3]$ (mol L^{-1})**	***c(Co^{2+})* (molL^{-1})**	$\boldsymbol{\alpha_{[C_O(NH_3)_m]^{2+}}}$	**c* （mol/L）**	**S**	$\boldsymbol{\sigma}$
0.2	0.4	0.39	0.40	1.81E+04	2.98E-04	1340.23	1339.23
0.4	0.8	0.68	0.40	1.92E+05	6.56E-04	609.66	608.66
0.6	1.2	0.84	0.40	4.99E+05	9.02E-04	443.25	442.25
0.8	1.6	0.95	0.40	8.43E+05	1.07E-03	372.23	371.23
1	2	1.02	0.40	1.19E+06	1.21E-03	331.37	330.37

Table A-4. Summary of molar ratio of NH_3/MSO_4, $[NH_3]$ concentration, Mn^{2+} concentration, $\alpha[\mathrm{M_n(NH_3)_m}]^{2+}$,S and σ

Molar ratio of NH_3/MSO_4 (n)	**[N] (mol L^{-1})**	**$[NH_3]$ (mol L^{-1})**	***c(Mn^{2+})* (molL^{-1})**	$\boldsymbol{\alpha_{[Mn(NH_3)_m]^{2+}}}$	**c* （mol/L）**	**S**	$\boldsymbol{\sigma}$
0.2	0.4	0.39	0.40	9.98	7.79E-05	5132.41	5131.41
0.4	0.8	0.68	0.40	34.89	1.19E-04	3376.87	3375.87
0.6	1.2	0.84	0.40	60.94	1.43E-04	2804.02	2803.02
0.8	1.6	0.95	0.40	83.42	1.58E-04	2525.33	2524.33
1	2	1.02	0.40	103.11	1.70E-04	2353.08	2352.08

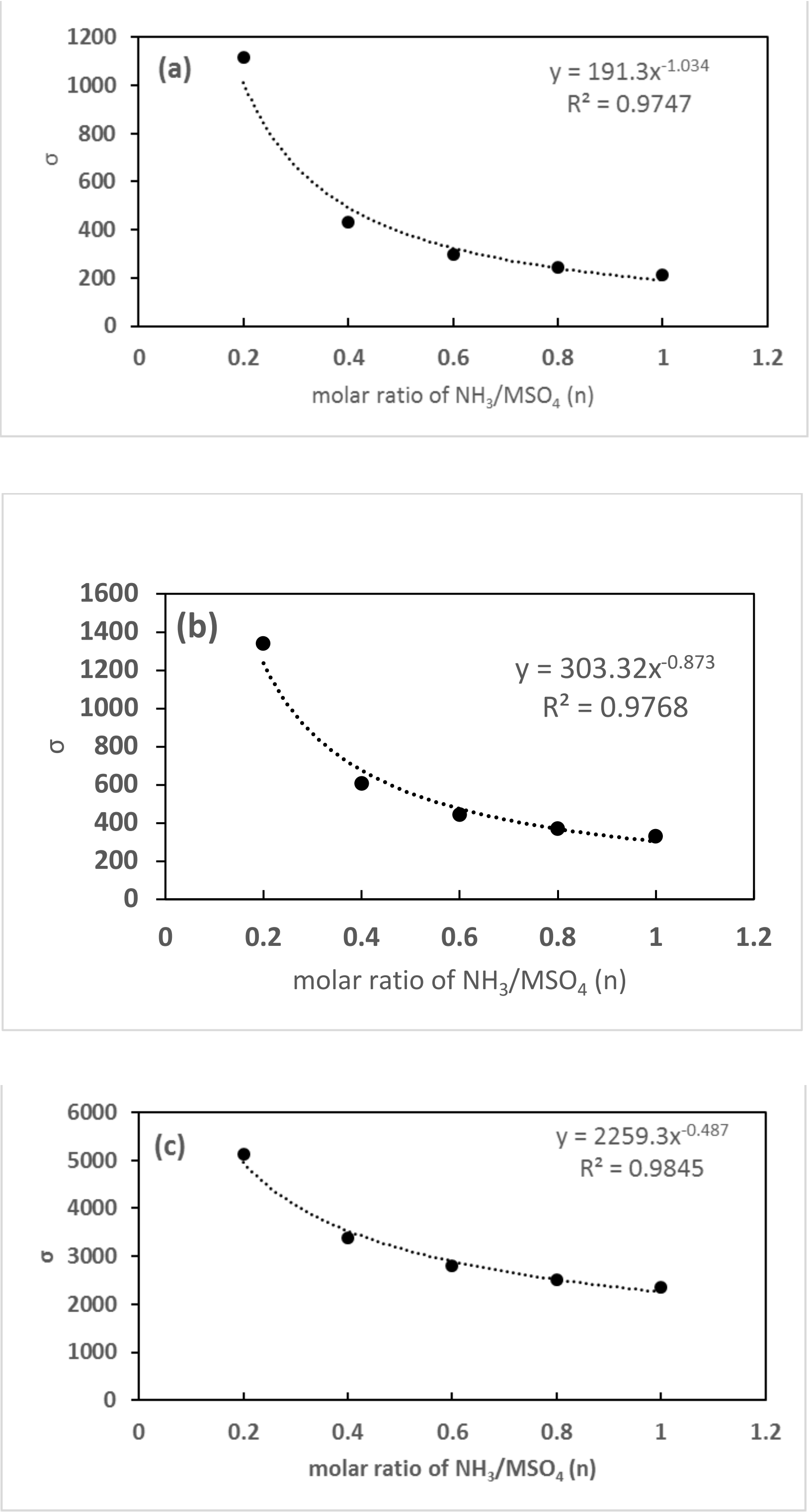

Figure A-1 The relationship between supersaturation σ and molar ratio of NH_3/MSO_4 with metal–ammonium complex: (a) $\alpha_{[N_i(NH_3)_m]^{2+}}(b)\alpha_{[C_O(NH_3)_m]^{2+}}\alpha_{[M_n(NH_3)_m]^{2+}}$

List of Publications

Journal papers:

HUANG, X., YANG, X., LI, G., EZEH, C. I., SUN, C. & SNAPE, C. Hybrid two-step preparation of nano-sized MgAl layered double hydroxides for CO_2 adsorption (Submitted Under Review).

HUANG, X., LIU, L., DONG, B., XUE, C., LI, G. & YANG, X. Preparation of Spherical-like $(Ni_{0.6}Co_{0.2}Mn0_{.2})(OH)_2$ precursor using a lobed Taylor-Couette reactor: Effect of shear rate, molar ratio of NH_3/MSO_4 and pH on precursor particle size and morphology (Submitted Under Review).

Book chapter

YANG, X., LIU, L., HUANG, X., XUE, C. & LI, G. Effects of fluid dynamics on the shapes of barium sulfate particles precipitated in a lobed inner cylinder Taylor-Couette flow reactor ISBN 978-953-5